FABRICATION AND CHARACTERIZATION OF FEW-MODE FIBER BRAGG GRATINGS FOR MODE CONVERSION AND SENSING APPLICATIONS

MUHAMMAD MAHMOOD ALI

INSTITUTE OF GRADUATE STUDIES
UNIVERSITY OF MALAYA
KUALA LUMPUR

2016

FABRICATION AND CHARACTERIZATION OF FEW-MODE FIBER BRAGG GRATINGS FOR MODE CONVERSION AND SENSING APPLICATIONS

MUHAMMAD MAHMOOD ALI

THESIS SUBMITTED IN FULFILMENT OF THE REQUIREMENTS FOR THE DEGREE OF DOCTOR OF PHILOSOPHY

INSTITUTE OF GRADUATE STUDIES
UNIVERSITY OF MALAYA
KUALA LUMPUR

2016

UNIVERSITY OF MALAYA

ORIGINAL LITERARY WORK DECLARATION

Name of Candidate: MUHAMMAD MAHMOOD ALI

Registration/Matric No: HHE120004

Name of Degree: DOCTOR OF PHILOSOPHY

Title of Thesis ("this Work"): FABRICATION AND CHARACTERIZATION OF FEW-MODE FIBER BRAGG GRATINGS FOR MODE CONVERSION AND SENSING APPLICATIONS

Field of Study: PHOTONICS ENGINEERING

I do solemnly and sincerely declare that:

(1) I am the sole author/writer of this Work;
(2) This Work is original;
(3) Any use of any work in which copyright exists was done by way of fair dealing and for permitted purposes and any excerpt or extract from, or reference to or reproduction of any copyright work has been disclosed expressly and sufficiently and the title of the Work and its authorship have been acknowledged in this Work;
(4) I do not have any actual knowledge nor do I ought reasonably to know that the making of this work constitutes an infringement of any copyright work;
(5) I hereby assign all and every rights in the copyright to this Work to the University of Malaya ("UM"), who henceforth shall be owner of the copyright in this Work and that any reproduction or use in any form or by any means whatsoever is prohibited without the written consent of UM having been first had and obtained;
(6) I am fully aware that if in the course of making this Work I have infringed any copyright whether intentionally or otherwise, I may be subject to legal action or any other action as may be determined by UM.

Candidate's Signature Date:

Subscribed and solemnly declared before,

Witness's Signature Date:

Name:

Designation:

ABSTRACT

Few-mode fibers (FMFs) have unveiled a new horizon to find various applications in new photonic devices. Currently, they have gained a great interest in optical communication and sensing technologies, particularly in the field of space division multiplexing technology to increase the transmission bandwidth and to overcome the capacity limitations of standard SMF-28 fiber. FMF offer several distinct features from single mode fibers and multimode fibers, in terms of medium core size which is capable of accommodating several transverse modes (2-6 modes) and supporting multiple transmission channels through mode-division multiplexing (MDM). The inscription of grating structure in FMF produces intriguing grating device that offers more than one Bragg wavelength where each wavelength can be associated to one or two transverse modes in the fiber. Therefore, it is essential to investigate and precisely characterize the several properties of these modes such as coupling between modes and their sensitivities to the ambient environment, with their applications. In this thesis, the fabrication of Bragg gratings (FM-FBGs) on two-mode (2MF) and four-mode (4MF) step index fibers will be discussed. It is mentioned that the environmental effects such as pre-stress conditions during fabrication, can alter the grating period which may be slightly deviate from the period of phase mask. Therefore a non-destructive approach based on Optical Imaging Technique (OIT) is proposed for measuring the period of an FBG. OIT has been used for the accurate measurement of grating period of FBGs inscribed in single mode fiber and in few-mode fibers before experimental characterization. Thereafter the FM-FBGs are analysed experimentally through selective mode excitation using binary phase plates. The reflected mode intensity profiles at each resonant Bragg wavelength under different mode excitation conditions are analysed to confirm the involved resonant

spatial modes. The mode coupling, such as self-mode and cross-mode coupling, occurring inside the fabricated FM-FBGs, is investigated. The measured transmission and reflection spectra are compared with the simulation results. Cross-mode coupled wavelengths offer the feature of conversion between the two associated modes and the conversion efficiency can be associated with the grating strength. Thereafter, the modal sensitivities of FM-FBGs to temperature and refractive index change have been investigated. Chemical etching technique is performed to remove the cladding of FM-FBG and to enhance the sensitivity of to the ambient refractive index change.

ABSTRAK

Beberapa mod gentian telah muncul sebagai satu potensi baru untuk kepelbagaian aplikasi dalam peranti fotonik. Pada masa ini, ianya digunakan secara menyeluruh dalam teknologi komunikasi dan alat penderia optik, terutamanya dalam bidang teknologi angkasa melalui pemultipleksan yang bertujuan meningkatkan jalur lebar penghantaran seterusnya mengatasi had kapasiti gentian piawai SMF-28. Gentian beberapa mod (FMF) menawarkan berbagai ciri yang berbeza berbanding gentian mod tunggal dan gentian multi-mod, dari segi saiz teras sederhana yang mampu menampung beberapa mod melintang (2-6 mod) dan menyokong saluran penghantaran berganda melalui mod-bahagian pemultipleksan (MDM). Pembentukan struktur grating dalam FMF menghasilkan peranti grating menarik yang menawarkan lebih daripada satu jarak gelombang Bragg di mana setiap jarak gelombang berkaitan dengan satu atau dua mod melintang dalam gentian. Oleh itu, adalah penting untuk menyiasat melalui pencirian yang tepat akan sifat-sifat mod ini, antaranya kesan kombinasi gandingan mod dan sensitiviti mereka terhadap suasana persekitaran, melalui aplikasi tertentu. Dalam tesis ini, proses fabrikasi grating Bragg (FM-FBGs) melalui dua mod (2MF) dan empat mod (4MF) indeks gentian akan dibincangkan. Dengan kesan persekitaran melalui keadaan pra-tekanan semasa fabrikasi, menyebabkan perubahan tempoh bagi parutan yang berbeza sedikit dari tempoh fasa-mask. Oleh itu dengan menggunakan cara-tanpa-musnah berdasarkan Teknik Pengimejan Optik (OIT) untuk pengukuran tempoh FBG telah dicadangkan. OIT telah digunakan untuk pengukuran yang tepat bagi tempoh FBG sepertimana terbentuk dalam gentian mod tunggal dan dalam gentian beberapa mod sebelum pencirian eksperimen dijalankan. Selepas itu FM-FBGs dianalisa secara eksperimental melalui pengujaan mod terpilih menggunakan plat fasa binari.

Pantulan profil mod meningkatkan pengujaan alunan bagi setiap panjang gelombang Bragg pada kadar mod yang berbeza seterusnya dianalisa untuk mengesahkan penglibatan alunan mod spatial. Gandingan mod, seperti mod diri dan gandingan mod rentasan yang berlaku di dalam FM-FBGs turut disiasat. Pengukuran transmisi serta pantulan spektrum turut dibandingkan melui keputusan simulasi. Jarak gelombang bagi gandingan mod lintang menawarkan ciri-ciri penukaran bagi kedua-dua mod bersekutu yang mana kecekapan penukaran adalah berkenaan dengan kekuatan parutan. Seterusnya, penyiasatan terhadap sensitiviti modal FM-FBGs kepada suhu persekitaran dan perubahan indeks biasan turut dijalankan. Teknik punaran kimia dijalankan untuk menyingkirkan gumpalan FM-FBG dan meningkatkan sensitivitinya terhadap perubahan indeks biasan persekitaran.

DEDICATION

I dedicate my Ph.D. thesis to my beloved grandparents, parents, respected teachers and Dr. Rabeea Sadaf, because I could never have done this work without their faith, support, unconditional love and constant encouragement; May they always be blessed and cherished here and the hereafter (Ameen)!

ACKNOWLEDGEMENTS

All praises and glory to Almighty Allah (ﷻ) for bestowing countless blessings, including physical robustness in me, on account of which I was able to complete this dissertation. I humbly offer salutations upon all Prophets, the source of guidance and knowledge to all mankind.

I am grateful and highly indebted to my research advisors, Distinguished Prof. Datuk Dr. Harith Ahmad (Director, Photonics Research Centre, University of Malaya) and Dr. Kok Sing Lim (Senior Lecturer, Photonics Research Centre, University of Malaya). I extend my heartfelt respect for their unflagging encouragement and diligent supervision. Their co-operative and amiable nature is indeed exemplary.

I would also like to extend my sincerest gratitude to Prof. Dato' Dr. Mohd Amin Jalaludin (Vice-Chancellor, University of Malaya), Prof. Dr. Fauza Abdul Ghaffar (Dean, Institute of Graduate Studies), Prof. Dr Mohamed Kheireddine Taieb Aroua (Deputy Dean, Institute of Graduate Studies), Distinguished Prof. Datuk Dr. Harith Ahmad (Director, Photonics Research Centre (PRC), University of Malaya) and Mdm. Sarinah Sallip (Senior Principal Assistant Registrar (Manager), Bright Sparks Unit (BSU)) for providing excellent research-oriented environment and high-tech equipment at University Malaya. Also, it has been a great pleasure to interact and learn from the faculty members of UM, PRC and outside faculty members from other Universities.

I have many thanks for my fellows and friends for cooperation and providing enjoyable moments especially Dr. Qayyum Zafar, Dr. Zubair, Md. Rajibul Islam, Shahid Bashir Baig, Dr. Tipu Sultan and Moinuddin Muhammad Quazi.

Finally would pay my heartiest gratitude to the most precious and divine relations of life, my ideal my father Abdul Ghaffar Naz and mother Sardar Mai, my beloved and kind mother, my sweet brother Muhammad Masood Ali and his wife and kids (Abeeha, Mustehsan and Zainab), and dear sisters Saira, Humaira and Shumaila for their unflagging love, numerous sacrifices and support throughout my life and their thoughts and prayers gave me strength and motivation with positive energy to prosper myself in the life. In the end, I acknowledge the role of those important characters whose names could not be displayed in the words but will always remain in my memories.

Muhammad Mahmood Ali

TABLE OF CONTENTS

LIST OF FIGURES

LIST OF TABLES

LIST OF SYMBOLS AND ABBREVIATIONS

°C	:	Degree centigrade
AOMC	:	Acousto-optic mode converter
ArF	:	Argon Fluoride
ASE	:	Amplified spontaneous emission
BOTDR	:	Brillouin optical time domain reflectometry
BS	:	Beam Splitter
CCD	:	Charge-coupled device
CMT	:	Coupled mode theory
CW	:	Continuous wave
dB	:	Decibel
dBm	:	Decibel with reference power as 1 milli Watt (mW)
DIC	:	Differential interface contrast
DMGD	:	Dispersion modal group delay
DMs	:	Dichroic mirrors
DSP	:	Digital signal processing
EDFA	:	Erbium doped fiber amplifier
ER	:	Extinction ratio
FMF	:	Few-mode fiber
FM-FBG	:	Few-mode fiber Bragg grating
FPM	:	Four photon mixing
FWHM	:	Full width at half maximum
GFF	:	Gain flattening filters
GIF	:	Graded index fiber
KrF	:	Krypton Fluoride

LP	:	Linearly polarized
LPG	:	Long period grating
MCF	:	Multi-core fiber
MDL	:	Mode dependent loss
MDM	:	Mode division multiplexing
MGD	:	Modal group delay
MIMO	:	Multi-input multi-output
NA	:	Numerical aperture
OAM	:	Orbital angular momentum
OIT	:	Optical imaging technique
OIT	:	Optical imaging technique
OPA	:	Optical parametric amplifier
OSA	:	Optical spectrum analyzer
PC	:	Polarization controller
PCF	:	Photonic crystal fiber
PMF	:	Polarization maintaining fiber
RI	:	Refractive index
RIU	:	Refractive index unit
SDM	:	Space division multiplexing
SMF	:	Single mode fiber
TDM	:	Time division multiplexing
UV	:	Ultraviolet
WDM	:	Wavelength division multiplexing
$\mu\varepsilon$	:	Micro strain

CHAPTER 1: INTRODUCTION

Optical fiber is a cylindrical dielectric waveguide made from low-loss silica glass or plastic materials and used to transfer data in the form of light modulation without any distortion, attenuation, and delay. This technology is an important breakthrough because of its numerous applications in telecommunications, industries, structural health monitoring, military, environment, and biomedical domains (Agrawal, 2012; Kirkendall & Dandridge, 2004; H.-N. Li, Li, & Song, 2004; Méndez & Morse, 2011; S. Miller, 2012; Udd & Spillman Jr, 2011). Over the past few decades, continuous research efforts have led to significant breakthroughs in the development of economical and compact optical-fiber-based devices with improved performance. A brief overview of the classification, historical development, and fiber Bragg gratings of optical fiber devices is presented.

1.1 Introduction and Historical Background

In the 1790s, the first "optical telegraph" was invented by the French Chappe brothers by fixing a series of lights on towers to transmit messages from one tower to the next at a distance of 400 m (Burns, 2004). Afterward, a British physicist named John Tyndall demonstrated in the 1850s that light signals can be bent by guiding the light through a curved stream of water; in this way, he came up with the concept on how total internal reflection can guide the light along flowing liquid (Hecht, 2004). After many developments in the field of guided optics, CV Boys fabricated the finest glass thread in 1887 for the first time (Boys, 1887), and in one of his lectures, he revealed the significance of fibers (Boys, 1889).

"I do not believe if any experimentalist had been promised by a good fairy that he might have anything he desired, that he would have ventured to ask for any one thing with so many valuable properties as these fibers possess."

The transmission of light through a bundle of transparent rods was first reported by Heinrich Lamm in 1930 (Hecht, 2004), and several experiments on bare fibers were performed by Holger Moeller and Abraham van Heel in the 1950s. While working on a periscope project, van Heel and Willem Brouwer found that transparent fibers with mirror coatings would be more efficient rather than thin reflective tubes. Hence, they drew the first glass fibers the same way Boys had done 60 years before and made plastic fibers with high loss of transmission light. In 1953, van Heel was the first to introduce the cladding part of an optical fiber. Elias Snitzer provided a theoretical description of single-mode fibers (SMFs) in 1961, which can guide a single mode with small core size (Snitzer, 1961; Snitzer & Osterberg, 1961).

In the early 1960s, the transmission loss of glass-clad fiber was reported to be 1 dB/m, which was suitable for medical applications but unfeasible for communication technology. In 1970, the scientists from Corning Glass Works reported the loss to be 20 dB/km by doping silica glass with titanium for SMF. Since then, continuous research has been conducted to improve the transmission bandwidth of SMFs and reduce the transmission loss, nonlinearity effects, and dispersion. As such, fiber optic technology had been transformed from multimode fibers to standard SMFs and then to various specialty fibers. These specialty fibers are optical fibers designed to achieve special characteristics that cannot be accomplished by standard single-mode or multimode fibers in telecommunication. Graded index fiber (GIF), polarization-maintaining fiber (PMF), multicore fiber (MCF), hollow core fiber, photonic crystal fiber (PCF), and few-mode fiber (FMF) are examples of specialty fibers. These fibers are currently used in various technologies, such as telecommunication and sensing applications. The cross-sectional view of some optical fibers is shown in Figure 1.1.

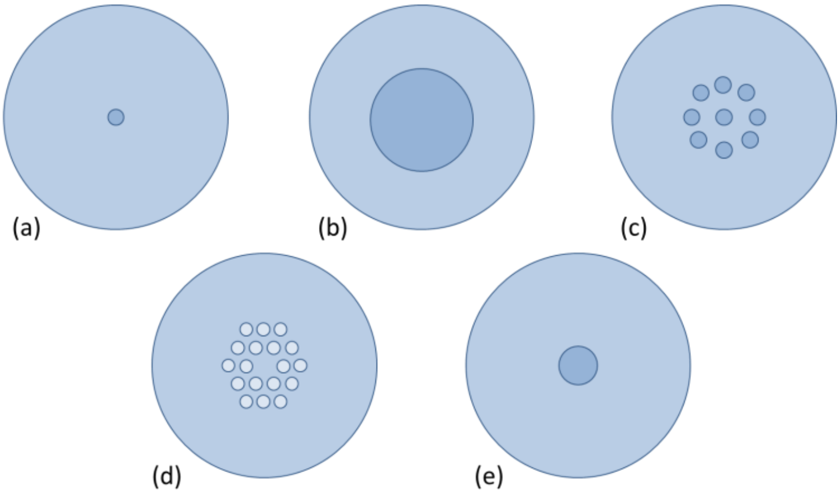

Figure 1.1: Cross sectional view of various optical fibers. (a) Single-mode fiber, (b) multimode fiber, (c) multicore fiber, (d) photonic crystal fiber, (e) FMF.

Since the 1980s, different approaches have been adopted to enhance the channel capacity of standard single-mode optical fibers. Transmission capacity multiplies approximately 10-fold every 4 years (Figure 1.2) (Richardson, Fini, & Nelson, 2013). Thus, the exponential increase of transmission data capacity has been achieved by recent technologies, such as wavelength division multiplexing (WDM) and high spectral efficiency coding with reasonable operating cost, via the same transmitting fiber/channel by changing the fiber end equipment. However, the fibers used in real networks are predicted to reach capacity limits in the near future, which can be explained by Shannon's theory for nonlinear fiber channels under several assumptions (Essiambre & Tkach, 2012; Mitra & Stark, 2001). The standard SMF exhibits data capacity limits of up to 100 Tbits/s, which correspond to filling the C and L amplification bands of an erbium-doped fiber amplifier (EDFA) at a spectral efficiency of approximately 10 bits/s/Hz. Before the "capacity crunch" occurs, further innovations should be developed to meet the increasing data traffic demands. One of the most feasible solutions is space division multiplexing (SDM) technology, which not only increases the channel capacity but also improves the economical productivity in terms of cost per bit and energy efficiency (Winzer, 2011). By using SDM technology, light is propagated through spatially distinguishable data paths in the optical fiber, which can be achieved using either MCFs or multimode fibers with small core sizes such as FMFs. MCFs with coupled multiple cores can increase the core density and/or large core effective areas, whereas FMFs can minimize the nonlinear effects (Pan, Weng, & Wang, 2015; Randel, Magarini, et al., 2011). Many researchers have investigated that combining the approaches of FMFs and MCFs to enhance channel capacity is possible (Qian et al., 2012; Katsuhiro Takenaga et al., 2012; K. Takenaga et al., 2012; Xia et al., 2012).

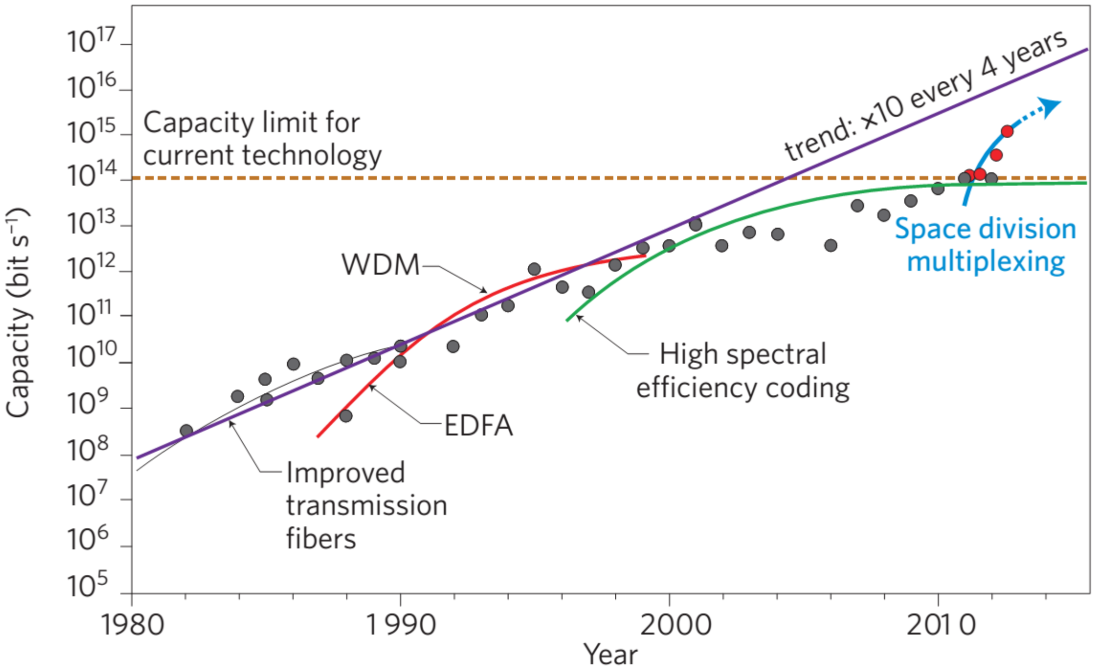

Figure 1.2: Channel capacity enhancement evolution for standard SMF by using various technologies with capacity limits, such as WDM and high spectral efficiency coding; red markers represent the reported capacities enabled by space division technology (Richardson et al., 2013).

FMF-based devices have exhibited promising potential in numerous applications, including optical communications and industrial sensors for temperature, refractive index, chemistry, biomedicine, and pressure. FMFs offer several distinct features in terms of medium core size unlike SMFs and multimode fibers; FMFs can accommodate several transverse modes (2–6 modes) and support multiple transmission channels through mode-division multiplexing (MDM). The simulated spatial intensity profiles for different modes in FMFs are shown in Figure 1.3. Moreover, by taking advantage of optical fibers as sensing elements, FMFs may be used for multi-parameter sensing, and the sensitivity for each mode can be investigated (A. Li, Wang, Hu, & Shieh, 2015). Recently, fiber Bragg grating (FBG) structure inscribed in FMFs has been regarded as one of the most feasible devices that can be used as a discriminative or multi-parameter sensor to investigate modal sensitivities.

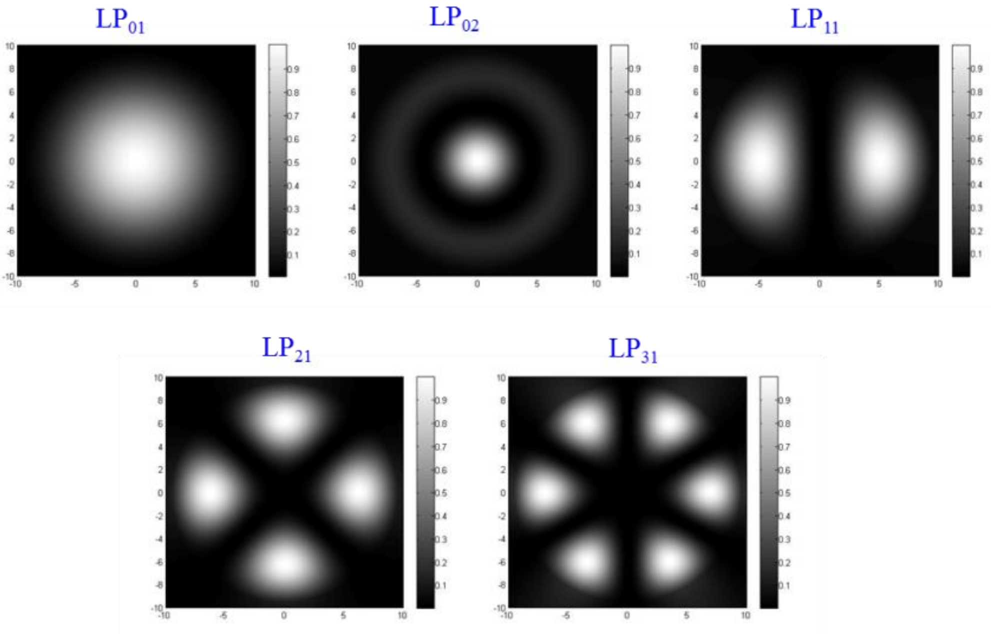

Figure 1.3: Simulated optical field intensity of different modes such as LP_{01}, LP_{02}, LP_{11}, LP_{21}, and LP_{31} at the cross-section of normal FMF.

The present work mainly focuses on few-mode devices based on fiber Bragg grating (FM-FBG). This research primarily aims to enrich the understanding about FM-FBGs, from the precise measurements of grating period and mode-coupling characteristics to the theoretical investigations and fabrication of FM-FBG-based devices, such as mode converters and cladless FM-FBG multi-parameter sensors.

1.2 Recent Developments on FMF-based Devices

In the development of FMF-based devices, as well as on the exploration of their characteristics and potential in optical communication and sensing applications, numerous studies have been carried out. MODE-GAP is one of the major efforts in the development of FMFs and SDM technologies (A. D. Ellis & Suibhne, 2012). Ellis et al. (A. Ellis & Doran, 2013) reported the possibility of using FMF as a solution for capacity crunch. The mode-coupling effect on the mode-dependent loss of FMFs has been reported in the literature (Lobato et al., 2012; Lobato Polo et al., 2012) and has been discussed in detail by many researchers (Ali et al., 2015; Grüner-Nielsen et al., 2012; Kumar, Goel, & Varshney, 2001; K. S. Lim, Ali, Loo, Chong, & Ahmad, 2014; Schulze, Brüning, Schröter, & Duparré, 2015; Vuong et al., 2015). Moreover, the behavior of soliton and nonlinear pulse propagation in FMFs has been discussed in the literature (Mac Suibhne et al., 2012; Suibhne et al., 2012). FMFs have been characterized by phase-sensitive optical low-coherence interferometry (Gabet et al., 2014; Hamel, Jaouen, Gabet, & Ramachandran, 2007; Ma et al., 2009). Various researchers have introduced several devices using FMFs, such as band selection optical filters (Siddharth Ramachandran, Ghalmi, Wang, & Yan, 2002; Siddharth Ramachandran, Wang, & Yan, 2002), add/drop multiplexers (X. Chen, Li, Ye, Al Amin, & Shieh, 2013; Fang & Jia, 2014b; G. Li, Bai, Zhao, & Xia, 2014; D. A. B. Miller, 2013), long distance transmission channels (Hanzawa et al., 2011; Yaman, Bai, Zhu, Wang, & Li, 2010), FMF modal couplers (Ismaeel, Lee, Oduro, Jung, & Brambilla, 2014; Y Jung et al., 2013), and FMF amplifiers (Yongmin Jung, Kang, et al., 2014; Yongmin Jung, Lim, et al., 2014). In addition, the role of mode converters with FMFs are important for all fiber SDM technology systems (J. Dong & Chiang, 2015; Grüner-Nielsen & Nicholson, 2012). Therefore, FBGs inscribed in FMFs can exhibit mode conversion properties at cross-coupling wavelengths, which can be tuned by adjusting the temperature or applied strain (Ali et al., 2015).

Numerous efforts have been dedicated to develop FMF-based components for mode conversions. For instance, bidirectional mode conversion with FM-FBGs has been characterized using the following: selective mode excitation with phase plate (Ali et al., 2015; Chuang et al., 2012; Lee & Erdogan, 2001; Siddharth Ramachandran, Wang, et al., 2002; Suzuki, Schülzgen, & Peyghambarian, 2008), short piece of multimode fiber spliced with SMF for multimode interference (MMI)-based beam shapers (Zhu et al., 2010), long period grating induced by mechanical periodic micro-bending (Pradhan et al., 2015; S. Ramachandran, Kristensen, & Yan, 2009), temperature-insensitive LPG written CO_2 laser (J. Dong & Chiang, 2015), electromagnetic-induced LPG (Sakata, Sano, & Harada, 2014), and rectangular core fiber under pressure for mode conversion (Bullington et al., 2012). The mode conversion for the characterization of FMFs can also be achieved using binary phase plates (SeGall, Divliansky, Jollivet, Schülzgen, & Glebov, 2015; SeGall, Divliansky, & Glebov, 2013; SeGall et al., 2012).

Signals comprising more than one mode and propagating via FMFs through multiple coupled paths will arrive at the receiver end with modal group delay (MGD) as a result of modal dispersion. Therefore, in the FMF-based MDM system, the complexity of the computational load for MDM multi-input multi-output (MIMO) optical digital signal processing (DSP) is generally proportional to MGD. Consequently, FMFs with proper modal dispersion properties should be designed and fabricated. Ramachandran introduced a dispersion-tailored FMF by fabricating LPG with UV laser (Siddharth Ramachandran, 2005); dispersion-compensated fibers have also been reported by many researchers (Grüner-Nielsen et al., 2005; R Ryf et al., 2012). In addition, FMFs with low dispersion modal group delay (DMGD), FMFs with positive and negative DMGD concatenated, and strongly coupled fibers are few approaches that can reduce the effective computational load for MIMO signal processing in SDM systems (Ferreira, Fonseca, & da Silva, 2014; G. Li et al., 2014).

Most FMF-based devices have exhibited promising functionalities in various applications (S Ramachandran, 2003), such as multi-parameter/discriminative sensors (Qiu, Cheng, Luo, Zhang, & Zhu, 2013; H. Z. Yang et al., 2015) and fiber lasers (Feng, Liu, Fu, Yuan, & Dong, 2004; Moon, Paek, & Chung, 2004). FMF-based optical fiber sensors are inexpensive, highly sensitive, and capable of discrimination, making them preferable for most researchers (Vengsarkar, Michie, Jankovic, Culshaw, & Claus, 1994). Optical sensing of different parameters through FMFs can be performed using modal interference (Kumar et al., 2001) and mode reflections through FM-FBGs (Mizunami, Djambova, Niiho, & Gupta, 2000). FM-FBG sensors exhibit different modal sensitivities for concentration/refractive index and solution temperature by enhancing the evanescent field of the device by through removal of the cladding using chemical etching (H. Z. Yang et al., 2015). These sensors can be applied in chemical industries, oil and gas industries, and biomedical applications for multi-parameter sensing because of the previously mentioned advantages (S Ramachandran, 2003).

1.3 Motivation

In the field of telecommunications, standard SMF has been used in accordance with Moore’s law (Smit, Van der Tol, & Hill, 2012), and the internet traffic has maintained its exponential growth by increasing computer processing power. To date, WDM systems (Bosco, Carena, Curri, Poggiolini, & Forghieri, 2010; Cai et al., 2011; T. Li, 1993) and other assisted technologies such as advanced modulation format with digital coherent reception (Kikuchi, 2006; Koizumi, Toyoda, Yoshida, & Nakazawa, 2012), polarization multiplexing (Savory, Gavioli, Killey, & Bayvel, 2007), and forward error correction techniques (Mizuochi, 2006) have fulfilled the spectral bandwidth of the channels. Data transmission with over 100-Tbit/s capacity in laboratory experiments has been reported (Qian et al., 2011; Sano et al., 2012). To maintain signal-to-noise ratio (SNR), the input power of all WDM channels should be more than 1 watt. However, because of increasing bandwidth applications, Shannon capacity limits, and light-induced catastrophic damage limitation of standard SMFs, a bottleneck trend is predicted to develop (Essiambre, Kramer, Winzer, Foschini, & Goebel, 2010; Essiambre & Tkach, 2012; Kahn & Ho, 2004; R Kashyap & Blow, 1988). Spatial dimension can be considered as the fifth dimension of data transmission in addition to time, wavelength, polarization, and phase, which can be used to overcome the capacity limit problem through SDM (Richardson et al., 2013). FMFs are feasible to implement MDM because they can support multiple modes with high capacities and flexibilities (Igarashi, Souma, Takeshima, & Tsuritani, 2015; A. Li, Al Amin, Chen, & Shieh, 2011; Richardson et al., 2013; Roland Ryf, Randel, et al., 2011; Salsi et al., 2011). Transmission experiments using FMFs have already been reported by many researchers (Ip et al., 2014; Randel et al., 2012; Randel, Ryf, et al., 2011; R Ryf et al., 2014; Roland Ryf et al., 2013; Vincent Sleiffer et al., 2012). Therefore, we are motivated to explore the possible applications of FMFs in optical communication. In addition to the utilization of FMFs, the fundamental mode should be converted to higher order modes by using modal converters before these modes are coupled with FMFs (Fontaine, Ryf, Bland-Hawthorn, & Leon-Saval, 2012; S. Leon-Saval, Birks, Bland-Hawthorn, & Englund, 2005; S. G. Leon-Saval et al., 2014; Soma, Takeshima, Igarashi, & Tsuritani, 2014). Furthermore, FM-FBG is one of the most feasible methods to characterize the FMF for each mode, in addition to mode coupling and mode conversion at cross-coupled wavelengths of FM-FBG. The addition of the spatial dimension as the fifth dimension in FMFs may also be useful for optical sensors (B. Y. Kim, Blake, Huang, & Shaw, 1987; Vengsarkar, Michie, et al., 1994).

The structures of core and cladding for FMFs are quite similar to those of SMFs, thereby making their fabrication process compatible with that of SMFs and more economic than the fabrication process of conventional PMF or PCF (X. Dong, Tam, & Shum, 2007). For instance, PMFs and two-mode fibers with elliptical core have been used to characterize and measure temperature and strain (Y. H. Kim & Song, 2014; Zou, He, & Hotate, 2009), but the system is costly and difficult to fabricate.

The motivation and aim of the present work are to identify ways to accurately measure the grating period and to characterize the mode coupling and modal sensitivities of FM-FBG. Mode conversion can be achieved through phase plates, but in-fiber mode converters should be fabricated for all fiber SDM networks to reduce optical power loss through the optical setup of phase plates. Additionally, FMF modes exhibit different sensitivities for physical parameters; thus, they have been characterized using cladless FM-FBG by sensing the refractive index and temperature of the solution. Sensing parameter, sensitivity, cost efficiency, and sensing element are the factors influencing the performance of different optical fibers used for sensing applications (Chester, Martellucci, & Scheggi, 2012; A. Li et al., 2015). Interestingly, FM-FBGs can be used for mode conversions and multi-parameter sensing.

1.4 Objectives

The significance of FBGs in various technologies such as in optical communication and sensing applications necessitates the development of tools for analysis, synthesis, and characterization of FBGs to make them efficient in performance. For example, a suitable mathematical model is crucial when designing gratings to understand the relationship between the spatial grating structure and the reflection and transmission spectra. This work aims to elucidate the fabrication techniques, understand the characteristics, and explore the potential applications of FM-FBG-based devices. The main objectives of this research are explained as follows:

i. to inscribe the FBGs in FMF and investigate Bragg grating period by using optical imaging technique;
ii. to analyze modal coupling in FM-FBGs with the aid of theory and experiment;
iii. to investigate and characterize FM-FBGs for mode conversions; and
iv. to investigate and characterize the modal sensitivities of FM-FBGs for discriminative sensing, such as cladless few-mode grating sensor for simultaneous measurement of temperature and refractive index.

The work begins with the fabrication of good quality FM-FBGs. An optical imaging technique is developed to investigate the grating period. Other aspects such as pre-strain conditions and placement angle during the image acquisition of gratings are considered to ensure that the measuring technique is accurate. In the analytical study and characterization of intermodal coupling and modal sensitivities of FM-FBGs, experimental data are quantitatively analyzed using several software tools, such as MATLAB and Microsoft Excel. The new applications of FM-FBGs, namely, mode converters and multi-parameter cladless FM-FBG sensors, are also explored and demonstrated on the basis of mode coupling and modal sensitivities.

1.5 Thesis Outline

This thesis presents an investigation about FM-FBGs and their applications. This work covers the fabrication of FBGs inside FMFs, as well as the corresponding applications. The fabrication and theoretical analysis of the characteristics of the FM-FBG-based devices are discussed in detail. The thesis outline is presented as follows.

Chapter 2 presents the theoretical and literature review, which provides an overview of the recent developments in the field of FBGs and FMF-based devices. Coupled mode theory has been adopted to analyze self-mode coupling and cross-mode coupling in FMFs, and the sensing mechanism of FM-FBGs is also presented. Moreover, the photosensitivity mechanism inside the fiber is discussed in this chapter.

Chapter 3 introduces FBGs in various fibers, and the experimental fabrication techniques are outlined; specifically, phase mask technique used for the devices in the present work is described. In addition, an accurate measurement technique for the grating period of FBGs inscribed in the standard single mode is presented, as well as in FMFs based on optical imaging technique.

Chapter 4 reports the experimental analysis of mode coupling that occurs inside the core of FM-FBGs. The presented FBGs are inscribed in two-mode and four-mode step-index fibers. Thereafter, under the selective input mode-launching conditions with the use of binary phase plates, the coupling between specific modes, such as self-coupling and cross-coupling at the associated resonant wavelengths, is studied with the observation of reflected mode intensity profiles. The findings in this chapter indicate that FM-FBGs can be used as reflective mode converters for MDM data transmission systems.

In Chapter 5, FM-FBGs as multi-parameter sensors are investigated. The output response of each 2M-FBG mode to the changes in ambient refractive index and temperature is presented and discussed in detail. In this work, chemical etching technique is used to develop cladless FM-FBGs for simultaneous measurement of temperature and refractive index because of the varying sensitivities of each Bragg wavelength. The property of cross sensitivity between temperature and refractive index is also considered and employed for discrimination measurement by using a characteristic matrix of order 3.

Finally, the work reported in this thesis is summarized in Chapter 6. An outlook on future research directions in this field is also suggested in the second section of this chapter.

CHAPTER 2: LITERATURE REVIEW AND THEORY

In this chapter, literature review and theories related to optical fibers are presented. Various optical fibers used for optical communication and sensing applications are presented, along with a brief review of the physics underlying the operation mechanism of optical fiber-based devices, such as FBGs. A brief overview of coupled mode theory for the FBG and modal coupling inside the optical fiber is explained, with a special focus on FM-FBGs. The significance of FMF in SDM technology is also presented. A brief review of optical communication-based applications, such as optical filters and mode converters, as well as the possible sensing applications of few-mode optical fibers, is studied. The important aspects to be considered while using FMF-based devices as multi-parameter or discriminative sensors are discussed.

2.1 Introduction

An optical fiber consists of a central glass core surrounded by a cladding layer, in which refractive index n_b is slightly lower than the core index n_a. Such fibers are generally referred to as step-index fibers to distinguish them from graded-index fibers, in which the refractive index of the core decreases gradually from the center to the core boundary; detailed theoretical analyses on these fibers can be found in the literature (Ghatak & Thyagarajan, 1998; Liao, 2012; Marcuse, 1974; Saleh & Teich, 2007). Figure 2.1 illustrates the cross-section and refractive index profiles of a step index fiber. The refractive index profile for the step index fiber can be mathematically expressed as

$$n(r) = \begin{cases} n_a & for \quad 0 < r \leq a \\ n_b & for \quad r > a \end{cases} \tag{2-1}$$

where $0 < r < a$ represents the core region, and $r > a$ represents the cladding region.

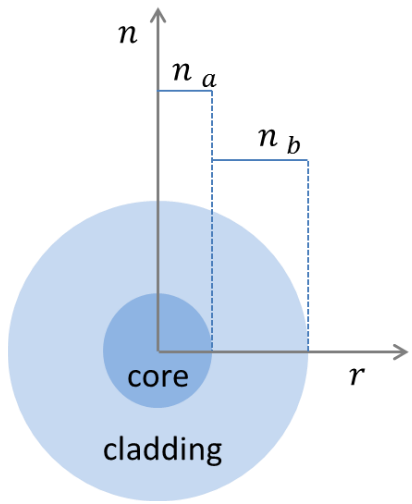

Figure 2.1: Illustration of refractive index profile of step index fiber.

The electric (E) and magnetic fields (H) in the optical fiber can generally be expressed as

$$\boldsymbol{E}(r, \phi, z, t) = \boldsymbol{E_0}\exp[i(\omega t - \beta z)] \quad \textbf{(2-2)}$$

$$\boldsymbol{H}(r, \phi, z, t) = \boldsymbol{H_0}\exp[i(\omega t - \beta z)] \quad \textbf{(2-3)}$$

where $\boldsymbol{E_0}$ and $\boldsymbol{H_0}$ are the field vectors that can be expressed in terms of unit vectors $\boldsymbol{a_r}$, $\boldsymbol{a_\phi}$, and $\boldsymbol{a_z}$ in the radial, azimuthal, and longitudinal directions, respectively.

$$E_0 = E_r\boldsymbol{a_r} + E_\phi\boldsymbol{a_\phi} + E_z\boldsymbol{a_z} \quad \textbf{(2-4)}$$

$$H_0 = H_r\boldsymbol{a_r} + H_\phi\boldsymbol{a_\phi} + H_z\boldsymbol{a_z} \quad \textbf{(2-5)}$$

The exact solution of field and modes existing inside the optical fiber can be investigated by solving the following Maxwell's equations:

$$\boldsymbol{\nabla} \times \boldsymbol{E} = -i\omega\mu_0\boldsymbol{H} \quad \textbf{(2-6)}$$

$$\boldsymbol{\nabla} \times \boldsymbol{H} = -i\omega\varepsilon_0\varepsilon_r\boldsymbol{E} = -i\omega\varepsilon\boldsymbol{E} \quad \textbf{(2-7)}$$

where ε represents the permittivity, and μ represents the permeability of the guided medium. ε and μ are related to their corresponding values in vacuum by $\varepsilon_0 = 8.854 \times$

10^{-12} F/m and $\mu_0 = 4\pi \times 10^{-7}$ H/m, which can be expressed as $\varepsilon = \varepsilon_0 \varepsilon_r = \varepsilon_0 n^2$ and $\mu = \mu_0$, respectively. By incorporating basic vector calculus to the Maxwell equations, the following equations can be achieved:

$$\frac{1}{r}\begin{vmatrix} \boldsymbol{a_r} & r\boldsymbol{a_\phi} & \boldsymbol{a_z} \\ \frac{\partial}{\partial r} & \frac{\partial}{\partial \phi} & \frac{\partial}{\partial z} \\ E_r & rE_\phi & E_z \end{vmatrix} = -i\omega\mu_0 (H_r \boldsymbol{a_r} + H_\phi \boldsymbol{a_\phi} + H_z \boldsymbol{a_z}) \tag{2-8}$$

$$\frac{1}{r}\frac{\partial E_z}{\partial \phi} + i\beta E_\phi = -i\omega\mu_0 H_r \tag{2-9}$$

$$-i\beta E_r - \frac{\partial E_z}{\partial r} = -i\omega\mu_0 H_\phi \tag{2-10}$$

$$\frac{1}{r}\frac{\partial (rE_\phi)}{\partial r} - \frac{1}{r}\frac{\partial E_r}{\partial \phi} = -i\omega\mu_0 H_z \tag{2-11}$$

$$\frac{1}{r}\frac{\partial H_z}{\partial \phi} + i\beta H_\phi = -i\omega\varepsilon E_r \tag{2-12}$$

$$-i\beta H_r - \frac{\partial H_z}{\partial r} = -i\omega\varepsilon E_\phi \tag{2-13}$$

$$\frac{1}{r}\frac{\partial (rH_\phi)}{\partial r} - \frac{1}{r}\frac{\partial H_r}{\partial \phi} = -i\omega\varepsilon E_z \tag{2-14}$$

After expressing the transverse components of the fields (E_r, E_ϕ, H_r, and H_ϕ) as functions of the longitudinal components (E_z and H_z), we can achieve the expression for E_r by adding (2-10)$\times\, \beta$ with (2-12)$\times\, \omega\mu_0$ as

$$E_r = \frac{-i}{(k_0 n)^2 - \beta^2}\left(\beta \frac{\partial E_z}{\partial r} + \frac{\omega\mu_0}{r}\frac{\partial H_z}{\partial \phi}\right) \tag{2-15}$$

The expression for E_ϕ can also be achieved by adding (2-9)$\times\, \beta$ with (2-13) $\times\, \omega\mu_0$ as

$$E_\phi = \frac{-i}{(k_0 n)^2 - \beta^2}\left(\frac{\beta}{r} \frac{\partial E_z}{\partial \phi} - \omega\mu_0 \frac{\partial H_z}{\partial r}\right) \tag{2-16}$$

Similarly, the expression for H_r can be achieved by adding (2-9)$\times\, \omega\varepsilon$ with (2-13)$\times\, \beta$ as

$$H_r = \frac{-i}{(k_0 n)^2 - \beta^2}\left(\beta \frac{\partial H_z}{\partial r} - \frac{\omega\varepsilon}{r}\frac{\partial E_z}{\partial \phi}\right) \tag{2-17}$$

and the expression for H_ϕ is achieved by adding (2-10**)** $\times\ \omega\varepsilon$ with (2-12**)** $\times\ \beta$ as

$$H_\phi = \frac{-i}{(k_0 n)^2 - \beta^2}\left(\frac{\beta}{r}\frac{\partial H_z}{\partial \phi} + \omega\varepsilon\frac{\partial E_z}{\partial r}\right) \qquad \textbf{(2-18)}$$

where k_0 is the free space number defined as $k_0 = \sqrt{\epsilon_0 \mu_0}$ or as $k_0 = \frac{\omega}{c} = \frac{2\pi}{\lambda_0}$, where λ_0 is the free space wavelength. By incorporating equations (2-17) and (2-18) into equation (2-14**)** we can obtain

$$\frac{\partial^2 E_z}{\partial r^2} + \frac{1}{r}\frac{\partial E_z}{\partial r} + \frac{1}{r^2}\frac{\partial^2 E_z}{\partial \phi^2} + \left({k_0}^2 n^2 - \beta^2\right)E_z = 0 \qquad \textbf{(2-19)}$$

Similarly, by using equations (2-15**)** and (2-16) into equation (2-11**)**, the following equation is achieved:

$$\frac{\partial^2 H_z}{\partial r^2} + \frac{1}{r}\frac{\partial H_z}{\partial r} + \frac{1}{r^2}\frac{\partial^2 H_z}{\partial \phi^2} + \left({k_0}^2 n^2 - \beta^2\right)H_z = 0 \qquad \textbf{(2-20)}$$

Given that equations (2-19) and (2-20) are similar, each equation can generally be expressed in terms of arbitrary function ψ, which represents both field functions E_z and H_z. Thus, the equation (2-4) can be written in a cylindrical coordinate system as

$$\frac{\partial^2 \psi}{\partial r^2} + \frac{1}{r}\frac{\partial \psi}{\partial r} + \frac{1}{r^2}\frac{\partial^2 \psi}{\partial \phi^2} + \left({k_0}^2 n^2 - \beta^2\right)\psi = 0 \qquad \textbf{(2-21)}$$

The variable separable method can be used to solve equation (2-21). Thus, $\psi(r,\phi)$ can be written as

$$\psi(r,\phi) = R_z(r)\Phi_z(\phi \qquad \textbf{(2-22)}$$

By substituting equation (2-22) into equation (2-21) and by dividing the result by $\psi(r,\phi)/r^2$, we can obtain the following system of equations:

$$\frac{r^2}{R}\left(\frac{d^2R}{dr^2}+\frac{1}{r}\frac{dR}{dr}\right)+r^2\left({k_0}^2n^2-\beta^2\right)=-\frac{1}{\Phi}\frac{d^2\Phi}{d\phi^2}=+l^2 \quad \textbf{(2-23)}$$

The cylindrical and radial parts of equation (2-23) can be rewritten as

$$\frac{d^2\Phi}{d\phi^2}+l^2\Phi=0 \quad \textbf{(2-24)}$$

$$r^2\frac{d^2R}{dr^2}+r\frac{dR}{dr}+\left\{\left({k_0}^2n^2(r)-\beta^2\right)r^2-l^2\right\}R=0 \quad \textbf{(2-25)}$$

where l is a constant and must be an integer for the function Φ to obtain a single value. The ϕ dependence will be of the form $\cos(l\phi+\varphi)$ or $\sin(l\phi+\varphi)$, with φ as an initial phase angle, whereas the negative values of l will correspond to the same field distribution. As such, two independent states of polarization can exist for each value of l. The modes with $l=0$ are ϕ independent with twofold degeneracy, whereas the modes with $l\geq 1$ exhibit a fourfold degeneracy, that is, corresponding to two orthogonal polarization states and to the ϕ dependence being $\cos l\phi$ or $\sin l\phi$.

By substituting equation (2-1) into equation (2-25), we can obtain

$$r^2\frac{d^2R}{dr^2}+r\frac{dR}{dr}+\left\{\left({k_0}^2{n_a}^2-\beta^2\right)r^2-l^2\right\}R=0 \quad for\ 0<r<a \quad \textbf{(2-26)}$$

$$r^2\frac{d^2R}{dr^2}+r\frac{dR}{dr}+\left\{\left({k_0}^2{n_b}^2-\beta^2\right)r^2-l^2\right\}R=0 \quad for\ \ r>a \quad \textbf{(2-27)}$$

Assuming that

$$U^2=\left({k_0}^2{n_a}^2-\beta^2\right)a^2 \quad \textbf{(2-28)}$$

and

$$W^2=\left(\beta^2-{k_0}^2{n_b}^2\right)a^2 \quad \textbf{(2-29)}$$

where both U and W are real, the guided mode condition for the optical fiber can be obtained as

$$k_0{}^2 n_b{}^2 < \beta^2 < k_0{}^2 n_a{}^2 \quad \textbf{(2-30)}$$

and the normalized *V*-parameter for the optical fiber can be written as

$$V = \sqrt{U^2 + W^2} = \sqrt{\left(k_0{}^2 n_a{}^2 - k_0{}^2 n_b{}^2\right) a^2} = k_0 a \sqrt{\left(n_a{}^2 - n_b{}^2\right)} \quad \textbf{(2-31)}$$

Furthermore, equations (2-26) and (2-27) can be rewritten as

$$r^2 \frac{d^2R}{dr^2} + r\frac{dR}{dr} + \left\{U^2\left(\frac{r}{a}\right)^2 - l^2\right\}R = 0 \quad for \;\; 0 < r < a \quad \textbf{(2-32)}$$

$$r^2 \frac{d^2R}{dr^2} + r\frac{dR}{dr} - \left\{W^2\left(\frac{r}{a}\right)^2 + l^2\right\}R = 0 \quad for \;\; r > a \quad \textbf{(2-33)}$$

The above equations are the standard forms of Bessel's equation (Zaitsev & Polyanin, 2002). Their solutions must converge in each case and the field should be continuous at the discontinuity of refractive index at the core-cladding interface ($r = a$). Therefore, the radial wave function $R(r)$ in the core is the Bessel function of first kind, such as $J_l(\cdot)$. The radial wave function in the cladding is the modified Bessel function of first kind, such as $K_l(\cdot)$. After determining the solutions for equations (2-32) and (2-33), equation (2-22) can be written as

$$\psi(r,\phi) = R(r)\begin{pmatrix} sin(l\phi + \varphi) \\ cos(l\phi + \varphi) \end{pmatrix}$$

Therefore, the field components E_z and H_z can finally be written as

$$E_z(r,\phi) = \begin{cases} A\,J_l\left(U\frac{r}{a}\right) sin(l\phi + \varphi) & for \quad 0 < r < a \\ C\,K_l\left(W\frac{r}{a}\right) sin(l\phi + \varphi) & for \qquad r > a \end{cases} \quad \textbf{(2-34)}$$

$$H_z(r,\phi) = \begin{cases} B\,J_l\left(U\frac{r}{a}\right) cos(l\phi + \varphi) & for \quad 0 < r < a \\ DK_l\left(W\frac{r}{a}\right) cos(l\phi + \varphi) & for \qquad r > a \end{cases} \quad \textbf{(2-35)}$$

Hence, the expression for transverse field components both in core and cladding can be found by using the expression of equations (2-34) and (2-35) in equations (2-15**)** to (2-18) as follows:

$$E_r(r,\phi) = \begin{cases} \left[-A\frac{i\beta a}{U}\,J_l'\left(U\frac{r}{a}\right) + B\,\frac{i\omega\mu_0 a}{U^2}\frac{l}{(r/a)}J_l\left(U\frac{r}{a}\right)\right] sin(l\phi+\varphi) \quad for \quad 0<r<a \\ \left[C\frac{i\beta a}{W}\,K_l'\left(W\frac{r}{a}\right) - D\,\frac{i\omega\mu_0 a}{W^2}\frac{l}{(r/a)}K_l\left(W\frac{r}{a}\right)\right] sin(l\phi+\varphi) \quad for \quad r>a \end{cases} \tag{2-36}$$

$$E_\phi(r,\phi) = \begin{cases} \left[-A\frac{i\beta a}{U^2}\,\frac{l}{(r/a)}J_l\left(U\frac{r}{a}\right) + B\,\frac{i\omega\mu_0 a}{U}J_l'\left(U\frac{r}{a}\right)\right] cos(l\phi+\varphi) \quad for \quad 0<r<a \\ \left[C\frac{i\beta a}{W^2}\,\frac{l}{(r/a)}K_l\left(W\frac{r}{a}\right) - D\,\frac{i\omega\mu_0 a}{W}K_l'\left(W\frac{r}{a}\right)\right] cos(l\phi+\varphi) \quad for \quad r>a \end{cases} \tag{2-37}$$

$$H_r(r,\phi) = \begin{cases} \left[A\frac{i\omega {n_a}^2 a}{U^2}\,\frac{l}{(r/a)}J_l\left(U\frac{r}{a}\right) - B\,\frac{i\beta a}{U}J_l'\left(U\frac{r}{a}\right)\right] cos(l\phi+\varphi) \quad for \quad 0<r<a \\ \left[-C\frac{i\omega {n_b}^2 a}{W^2}\,\frac{l}{(r/a)}K_l\left(W\frac{r}{a}\right) + D\,\frac{i\beta a}{W}K_l'\left(W\frac{r}{a}\right)\right] cos(l\phi+\varphi) \quad for \quad r>a \end{cases} \tag{2-38}$$

$$H_\phi(r,\phi) = \begin{cases} \left[-A\frac{i\omega {n_a}^2 a}{U}J_l'\left(U\frac{r}{a}\right) + B\,\frac{i\beta a}{U^2}\,\frac{l}{(r/a)}J_l\left(U\frac{r}{a}\right)\right] sin(l\phi+\varphi) \quad for \quad 0<r<a \\ \left[C\frac{i\omega {n_b}^2 a}{W}J_l'\left(W\frac{r}{a}\right) - D\,\frac{i\beta a}{W^2}\,\frac{l}{(r/a)}J_l\left(W\frac{r}{a}\right)\right] sin(l\phi+\varphi) \quad for \quad r>a \end{cases} \tag{2-39}$$

By applying the boundary to make the field continuous at $r = a$,

$$E_z(a,\phi)|_{core} = E_z(a,\phi)|_{cladding} \tag{2-40}$$

$$E_\phi(a,\phi)\big|_{core} = E_\phi(a,\phi)\big|_{cladding} \tag{2-41}$$

$$H_z(a,\phi)|_{core} = H_z(a,\phi)|_{cladding} \tag{2-42}$$

$$H_\phi(a,\phi)\big|_{core} = H_\phi(a,\phi)\big|_{cladding} \tag{2-43}$$

The following can equation can be obtained:

$$\begin{bmatrix} J_l(U) & 0 & -K_l(W) & 0 \\ \frac{i\beta}{U^2}\frac{l}{(1/a)}J_l(U) & \frac{i\omega\mu_0 a}{U}J_l'(U) & -\frac{i\beta}{W^2}\frac{l}{(1/a)}K_l(W) & \frac{i\omega\mu_0 a}{W}K_l'(W) \\ 0 & J_l(U) & 0 & -K_l(W) \\ -\frac{i\omega {n_a}^2 a}{U}J_l'(U) & \frac{i\beta}{U^2}\frac{l}{(1/a)}J_l(U) & -\frac{i\omega {n_b}^2 a}{W}K_l'(W) & \frac{i\beta}{W^2}\frac{l}{(1/a)}K_l(W) \end{bmatrix}\begin{bmatrix} A \\ B \\ C \\ D \end{bmatrix} = 0 \tag{2-44}$$

As shown in the equation above, coefficients A, B, C, and D present nontrivial solutions; thus, the determinant of the principle matrix must be zero. After some mathematical manipulations, the resultant equation will be a characteristic or dispersion equation as follows:

$$\left(\frac{J_l'(U)}{UJ_l(U)} + \frac{K_l'(W)}{WK_l(W)}\right)\left(\frac{{n_a}^2}{{n_b}^2}\frac{J_l'(U)}{UJ_l(U)} + \frac{K_l'(W)}{WK_l(W)}\right) = l^2\left(\frac{1}{U^2} + \frac{1}{W^2}\right)\left(\frac{{n_a}^2}{{n_b}^2}\frac{1}{U^2} + \frac{1}{W^2}\right) \tag{2-45}$$

This equation gives the solutions for hybrid mode (EH or HE modes), for which $E_z \neq 0$ and $H_z \neq 0$. In addition, we can find the coefficients in terms of A from the boundary condition equations in (2-44) as

$$C = A\frac{J_l(U)}{K_l(W)} \tag{2-46}$$

$$D = B\frac{J_l(U)}{K_l(W)} \tag{2-47}$$

$$B = -A\frac{\beta l}{\omega\mu_0}\left(\frac{\frac{1}{U^2} + \frac{1}{W^2}}{\frac{J_l'(U)}{UJ_l(U)} + \frac{K_l'(W)}{WK_l(W)}}\right) \tag{2-48}$$

For $\boldsymbol{l = 0}$, equation (2-45**)** can be divided into two parts as

$$\left(\frac{J_l'(U)}{UJ_l(U)} + \frac{K_l'(W)}{WK_l(W)}\right) = 0 \tag{2-49}$$

$$\left(\frac{{n_a}^2}{{n_b}^2}\frac{J_l'(U)}{UJ_l(U)} + \frac{K_l'(W)}{WK_l(W)}\right) = 0 \tag{2-50}$$

Equation (2-49) represents the dispersion equation for TE_{0m} modes, for which $E_z = 0$ and (2-50) represent the TM_{0m} mode with $H_z = 0$.

The approximation $\frac{n_a}{n_b} \approx 1$ or $\frac{n_a - n_b}{n_a} \ll 1$ can be used to simplify the characteristic equations and consequently describe the model with loose confinement of light in the core (Okamoto, 2010). This approximation is commonly known as "weakly-guiding" approximation, in which the modes are considered nearly transverse and exhibiting the arbitrary state of polarization referred to as linearly polarized (LP) modes. The two independent sets of modes can be assumed as x-polarization and y-polarization, which exhibit the same propagation constants. On the basis of the "weakly-guiding" approximation, the characteristic equation (2-45) can be modified as

$$\frac{J_l'(U)}{UJ_l(U)} + \frac{K_l'(W)}{WK_l(W)} = \pm l\left(\frac{1}{U^2} + \frac{1}{W^2}\right) \quad \textbf{(2-51)}$$

where $l \geq 1$. By using the recurrent properties of Bessel function, equation (2-51) can be modified in two ways as follows:

$$U\frac{J_{l+1}(U)}{J_l(U)} = -W\frac{K_{l+1}(W)}{K_l(W)} \quad \textbf{(2-52)}$$

or can be written as

$$U\frac{J_{l-1}(U)}{J_l(U)} = W\frac{K_{l-1}(W)}{K_l(W)} \quad \textbf{(2-53)}$$

In Figure 2.2 the relationship between U and W for V = 4, has been illustrated for finding the LP_{lm} modes which can be further used to determine the effective refractive index of the modes.

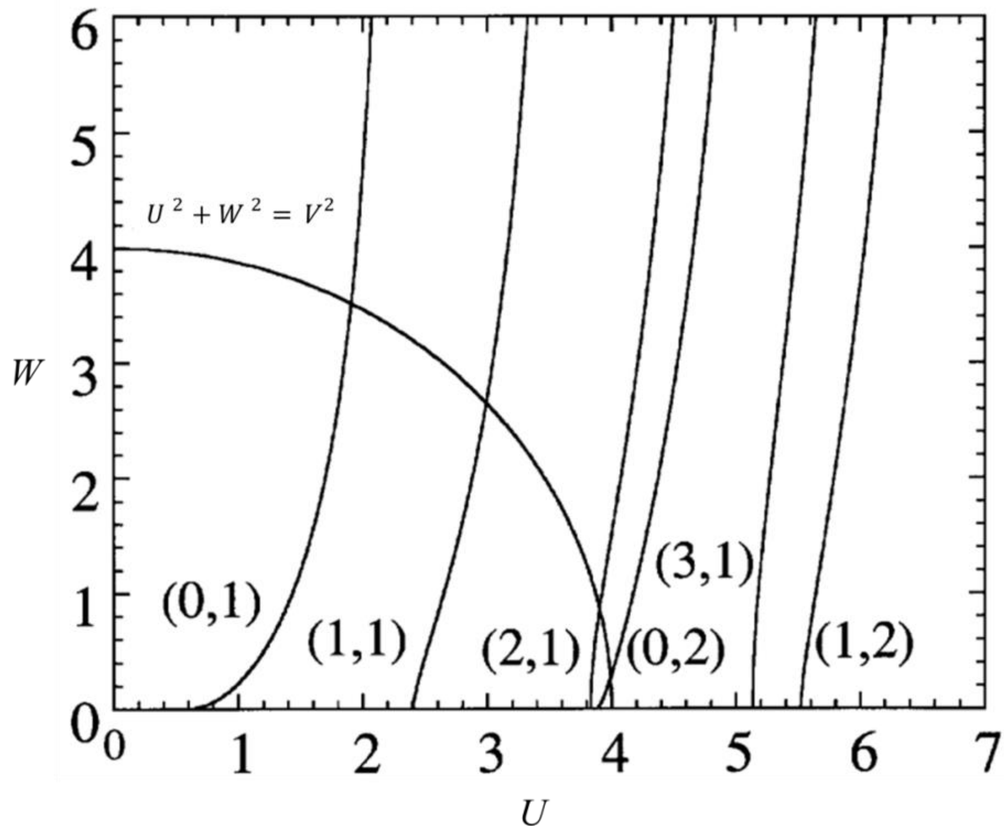

Figure 2.2: Graph illustrating the relationship between U and W for V = 4. The solution of circular curve $U^2 + W^2 = V^2$ and other vertical curves with the index (*m, l*) for LP$_{lm}$ mode provide the corresponding eigenvalues of the modes, which are further used to determine the effective refractive index of the modes (Kawano & Kitoh, 2004).

By defining the normalized propagation constant b as

$$b = \frac{{n_{eff}}^2 - {n_b}^2}{{n_a}^2 - {n_b}^2} = \frac{\frac{\beta^2}{{k_0}^2} - {n_b}^2}{{n_a}^2 - {n_b}^2} = \frac{W^2}{V^2} \qquad \textbf{(2-54)}$$

Equations (2-28) and (2-29) can be simplified as $W = V\sqrt{b}$ and $U = V\sqrt{1-b}$. The condition ${n_b}^2 < \left(\frac{\beta^2}{{k_0}^2} = {n_{\text{eff}}}^2\right) < {n_a}^2$ for guided modes is also rewritten as $0 < b < 1$. Hence, the characteristic equation can be defined in terms of normalized propagation constant b and V-number as

$$\begin{cases} V\sqrt{1-b}\dfrac{J_{l-1}\left(V\sqrt{1-b}\right)}{J_l\left(V\sqrt{1-b}\right)} = -V\sqrt{b}\dfrac{K_{l-1}\left(V\sqrt{b}\right)}{K_l\left(V\sqrt{b}\right)} & for \quad l \geq 1 \\ V\sqrt{1-b}\dfrac{J_1\left(V\sqrt{1-b}\right)}{J_0\left(V\sqrt{1-b}\right)} = V\sqrt{b}\dfrac{K_1\left(V\sqrt{b}\right)}{K_0\left(V\sqrt{b}\right)} & for \quad l = 0 \end{cases} \tag{2-55}$$

These equations are transcendental, and their solutions provide the characteristic curves representing b as a function of V. For single-valued l, a finite number of solutions exist, and the m^{th} solution is referred to as the LP_{lm} mode. The characteristics (dispersion) curves have been plotted for using equation (2-55) as shown in Figure 2.3.

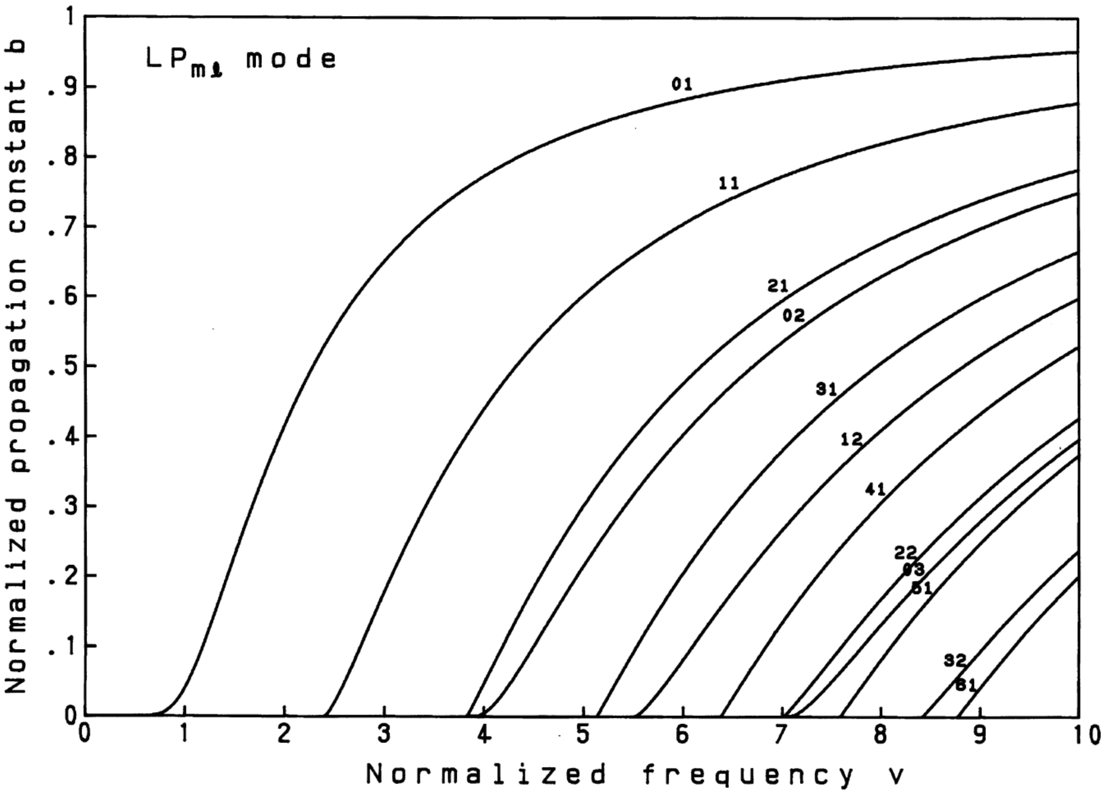

Figure 2.3: Dispersion (characteristic) curves of LP$_{ml}$ modes guided by step index optical fiber (Okamoto, 2010).

The total electric field component E_z can be written as

$$E_z = \sum_{l,m} E_{z,lm} \tag{2-56}$$

when $b = 0$, the cut-off condition of the mode can be derived from equation (2-54) as

$$\frac{\beta^2}{{k_0}^2} = {n_b}^2 \Rightarrow \beta = k_0 n_b$$

In addition, $W = 0$ and $U = V = V_c$, which is called cut-off V number. The guided modes no longer exist in the fiber core, and only the radiation modes will exist in the cladding.

The power propagating in the cylindrical optical fiber can be calculated using the averaged Poynting vector in the direction of propagation as follows:

$$\begin{aligned} P_a &= \int_0^{2\pi} \int_0^{\infty} \frac{1}{2} (E \times H^*) \cdot u_z \, r \, dr \, d\phi \\ &= \frac{1}{2} \int_0^{2\pi} \int_0^{\infty} \left(E_r {H_\phi}^* - E_\phi {H_r}^* \right) r \, dr \, d\phi \end{aligned} \tag{2-57}$$

In case of weakly guided LP modes, the expression for TE and TM modal power will be the same, whereas that for core region is given as

$$P_a = P_0 \int_0^{a} \int_0^{2\pi} |E|^2 r \, dr \, d\phi \tag{2-58}$$

$$P_a = \frac{P_0}{2} \pi a^2 \left(1 - \frac{J_{l-1}(U) J_{l+1}(U)}{{J_l}^2(U)} \right) \tag{2-59}$$

and for cladding region as

$$P_b = P_0 \int_a^{\infty} \int_0^{2\pi} |E|^2 r \, dr \, d\phi \tag{2-60}$$

$$P_b = \frac{P_0}{2} \pi a^2 \left(\frac{K_{l-1}(W) K_{l+1}(W)}{{K_l}^2(U)} - 1 \right) \tag{2-61}$$

where P_0 is the constant.

By using the expression of Equations (2-59) and (2-61), the total power can be calculated as

$$P_t = P_a + P_b = \frac{P_0}{2}\pi a^2 \frac{V^2}{U^2}\left(\frac{K_{l-1}(W)K_{l+1}(W)}{{K_l}^2(U)}\right) \tag{2-62}$$

Hence, the normalized power in the core is written as

$$\frac{P_a}{P_t} = \frac{W^2}{V^2} + \frac{U^2}{V^2}\left(\frac{{K_l}^2(U)}{K_{l-1}(W)K_{l+1}(W)}\right) \tag{2-63}$$

For weakly guided modes, the effective refractive index core for each mode at different wavelengths can be determined by solving b for each mode in equation (2-55) through numerical method. In this case, the solution of b for each mode can be expressed as a function of wavelength. Equation (2-55)can be written as

$$f(b_l) = V\sqrt{1-b_l}\frac{J_{l-1}\left(V\sqrt{1-b_l}\right)}{J_l\left(V\sqrt{1-b_l}\right)} + V\sqrt{b_l}\frac{K_{l-1}\left(V\sqrt{b_l}\right)}{K_l\left(V\sqrt{b_l}\right)} = 0 \tag{2-64}$$

By solving the function above with one of the standard numerical methods, such as Newton Raphson’s method, the values of b_{lm} can be obtained for different wavelengths. Thereafter, the effective refractive index for each mode can be achieved using equation (2-54) as

$$n_{eff,lm}(\lambda) = \sqrt{{n_b}^2 + b_{lm}(\lambda)\frac{V_{lm}(\lambda)}{k_0 a}} \tag{2-65}$$

2.2 Coupled Mode Theory

Coupled mode theory (CMT) is a commonly used to investigate the coupling between confined modes of optical fibers as a result of perturbation in the core refractive index (Yariv, 1973). The refractive index of a step index fiber with periodic perturbation can be modeled as

$$n(r,\phi,z) = \begin{cases} n_a + \delta n(r,\phi,z) & for \quad 0 < r < a \\ n_b & for \quad r > a \end{cases} \quad \textbf{(2-66)}$$

where n_a is the core refractive index in the unperturbed fiber that is uniform along z, n_b is the cladding refractive index of the fiber, a is the core radius of the fiber, and δn is the index perturbation assumed to be a periodic function with respect to z and within the range of the combined result of dc and ac changes in the refractive index, which is induced by UV illumination as follows:

$$\delta n(r,\phi,z) = \big(\delta n_{dc}(r,\phi,z) + \delta n_{ac}(r,\phi,z)\big)F(z) \quad \textbf{(2-67)}$$

where $F(z)$ is the apodization function. If the UV illumination is uniform across the cross-section of the optical fiber, the refractive index profile will be symmetric, and index perturbation will be the function of z alone, which can be written as

$$\delta n(z) = \big(\delta n_{dc}(z) + \delta n_{ac}(z)\big)F(z) \quad \textbf{(2-68)}$$

Furthermore, in the case of non-apodized or uniform gratings, the apodization function will be $F(z) = 1$, and the dc part of the refractive index will be $\delta n_{dc}(z) = c_1$. Here, c_1 is the constant derived by taking the spatial average of refractive index change over a grating period.

$$\delta n_{ac}(z) = \upsilon\, cos\left(2\pi \frac{z}{\Lambda}\right) \quad \textbf{(2-69)}$$

where υ is the fringe visibility of the refractive index change, and Λ is the perturbation period. Alternatively, various apodized gratings can be achieved, such as Gaussian-apodized and sinc-apodized gratings. The Gaussian apodization for induced refractive index can be formulated as (Sun et al., 2009),

$$F(z) = exp\left(-\frac{4\,ln(2)z^2}{FWHM^2}\right) \qquad for \qquad 0 < \ z < L \tag{2-70}$$

where FWHM is the full width at half maximum for induced refractive index function, and L is the grating length. Figure 2.4(a) and (b) show the induced index changes along the fiber axis for uniform and Gaussian-apodized grating structures, respectively.

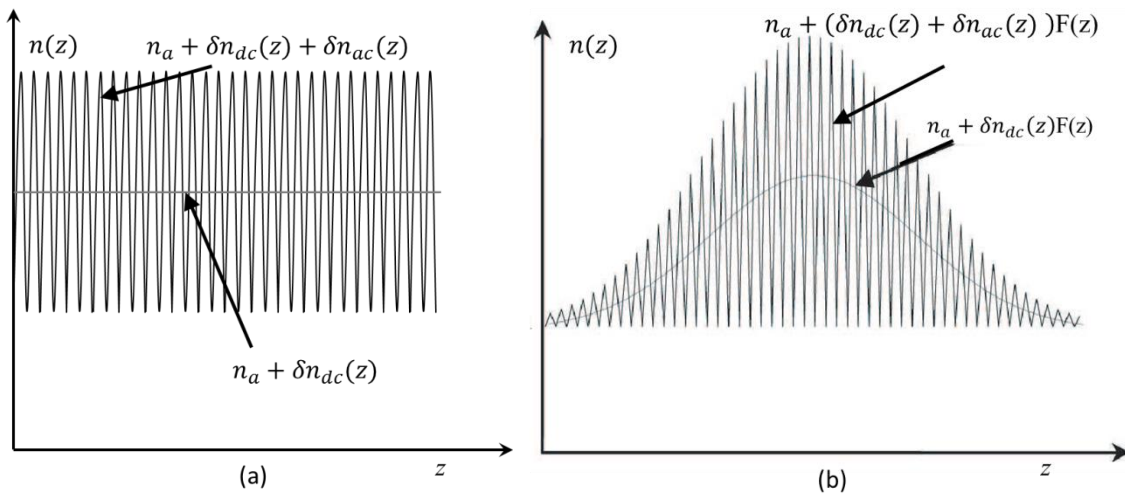

Figure 2.4: Illustrative diagram of the UV-induced refractive index changes in (a) uniform grating and (b) Gaussian-apodized grating with fringe visibility υ=1.

Assuming that the transverse field components ψ (representing either E or H fields) of the perturbed fiber can be written as a linear superposition of the LP modes of the unperturbed fiber (C. Lu & Cui, 2006),

$$\psi_t = \sum_{l,m} \psi_{lm}(r,\phi)\, exp(i\omega t)\,\{A_{lm}(z)\, exp(-i\beta_{lm}z) + B_{lm}(z)\, exp(i\beta_{lm}z)\} \tag{2-71}$$

where $A_{lm}(z)$ and $B_{lm}(z)$ are slowly varying amplitudes for the transverse mode fields traveling in the $+z$ and $-z$ directions, respectively. The subscript lm denotes the mode index of the LP modes, and ψ_{lm} is the field pattern of the corresponding LP mode. β_{lm} represents the corresponding propagation constant of the mode. When a dielectric perturbation exists in an optical fiber, an LP_{lm} mode can exchange energy with other

LP_{pq} modes. To simplify the mode index, different modes coupled with each other can be defined in such a way that the index lm is replaced by μ, and the index pq is replaced by ν; thus, the generalized coupled equation can be written as

$$\frac{dA_l}{dz} = i \sum_l e_l(r,\phi)\, exp(i\omega t)\, \{A_l(z)\, exp(-i\beta_l z) + B_l(z)\, exp(i\beta_l z)\} \tag{2-72}$$

$$\frac{dA_\mu}{dz} = i \sum_\nu A_\nu\left(\kappa_{\nu,\mu}^t + \kappa_{\nu,\mu}^z\right) exp\left[i\left(\beta_\nu - \beta_\mu\right)z\right] + i \sum_\nu B_\nu\left(\kappa_{\nu,\mu}^t - \kappa_{\nu,\mu}^z\right) exp\left[-i\left(\beta_\nu + \beta_\mu\right)z\right] \tag{2-73}$$

$$\frac{dB_\mu}{dz} = \sum_\nu A_\nu\left(\kappa_{\nu,\mu}^t - \kappa_{\nu,\mu}^z\right) exp\left[i\left(\beta_\nu + \beta_\mu\right)z\right] - i \sum_\nu B_\nu\left(\kappa_{\nu,\mu}^t + \kappa_{\nu,\mu}^z\right) exp\left[-i\left(\beta_\nu - \beta_\mu\right)z\right] \tag{2-74}$$

where $\kappa_{\nu,\mu}^t$ and $\kappa_{\nu,\mu}^z$ in equations (2-73) and (2-74) are the corresponding transverse and longitudinal coupling coefficients between the modes μ and ν. The coefficients $\kappa_{\nu,\mu}^z$ are usually neglected because the fiber modes follow the condition $\kappa_{\nu,\mu}^z \ll \kappa_{\nu,\mu}^t$, where $\kappa_{\nu,\mu}^t$ is defined as

$$\kappa_{\nu,\mu}^t(z) = \frac{\omega}{4} \int_0^{2\pi} \int_0^{\infty} \Delta\varepsilon\, \psi_\mu(r,\phi) \psi_\nu(r,\phi) r dr d\phi \tag{2-75}$$

where ω is the angular frequency, and $\Delta\varepsilon$ is the perturbation to the permittivity of the core of optical fiber. When solving for equation (2-75), the modes are considered as normalized such that the power carried by each LP mode is $\left|A_\mu\right|^2 + |A_\nu|^2$. The two mode-coupled equations for the LP_{01} and LP_{11} modes are given here for better illustration as

$$\frac{d}{dz}\begin{bmatrix} A_{01} \\ A_{11} \\ B_{01} \\ B_{11} \end{bmatrix} = M \begin{bmatrix} A_{01} \\ A_{11} \\ B_{01} \\ B_{11} \end{bmatrix} \tag{2-76}$$

$$M = i\begin{bmatrix} \kappa_{01-01}^{t} & \kappa_{01-01}^{t}exp(-i2\beta_{01}z) & \kappa_{11-01}^{t}exp(-i(\beta_{11}-\beta_{01})z) & \kappa_{11-01}^{t}exp(-i(\beta_{11}+\beta_{01})z) \\ \kappa_{11-01}^{t}exp(i(\beta_{01}-\beta_{11})z) & \kappa_{01-11}^{t}exp(-i(\beta_{11}+\beta_{01})z) & \kappa_{11-11}^{t} & \kappa_{11-11}^{t}exp(-i2\beta_{11}z) \\ -\kappa_{01-01}^{t}exp(i2\beta_{01}z) & \kappa_{01-01}^{t} & -\kappa_{11-01}^{t}exp(i(\beta_{11}+\beta_{01})z) & -\kappa_{11-01}^{t}exp(-i(\beta_{11}-\beta_{01})z) \\ -\kappa_{11-01}^{t}exp(i(\beta_{01}+\beta_{11})z) & -\kappa_{01-11}^{t}exp(-i(\beta_{11}-\beta_{01})z) & -\kappa_{11-11}^{t}exp(i2\beta_{11}z) & -\kappa_{11-11}^{t} \end{bmatrix}$$

(2-77)

Equation (2-76) can be further solved using any numerical methods, such as Runge-Kutta method, with the consideration of initial boundary value conditions (Sun et al., 2009). For the case above, the values of A_{01} and A_{11} at $\mathrm{z} = 0$ are considered as non-zero power of the input modes, whereas the values of B_{01} and B_{11} at $z = \mathrm{L}$ are considered zero.

2.3 Phase Modification in Optical Fiber

The sensitivity of the sensor depends on the rotational degree of the polarization induced by the measurand and on the minimal detectable rotation. The effect of the measurand on the state of polarization can be determined using the phase of a guided wave of μ^{th} mode of fiber with length L and expressed as

$$\varphi_{\mu} = \beta_{\mu}L = n_{eff,\mu}k_0L \qquad \textbf{(2-78)}$$

where β is the propagation constant of the mode, n_{eff} is the effective index of the mode, and k_0 is the wave vector in free space. The phase difference between two modes such as μ^{th} and ν^{th} modes guided by the fiber after length L is given by

$$\Delta\varphi_{\mu,\nu} = \Delta\beta_{\mu,\nu}L = \Delta n_{eff,\mu,\nu}k_0L \qquad \textbf{(2-79)}$$

where $\Delta n_{\text{eff},\boldsymbol{\mu},\boldsymbol{\nu}}$ is the difference between the effective indices of the two polarization modes.

2.3.1 Effect of Mechanical Strain (Elasto-optic Effect)

If the optical fiber is subjected to an externally applied mechanical strain (ε), a phase difference proportional to the length of the fiber under applied strain is produced. Mathematically, this relationship can be written as

$$\frac{1}{L}\frac{\partial(\Delta\varphi)}{\partial\varepsilon} = k_0\frac{\partial\left(\Delta n_{eff}\right)}{\partial n}\frac{\partial n}{\partial\varepsilon} + k_0\frac{\partial\left(\Delta n_{eff}\right)}{\partial D}\frac{\partial D}{\partial\varepsilon} + k\Delta n_{eff}\frac{1}{L}\frac{\partial L}{\partial\varepsilon} \quad \textbf{(2-80)}$$

where D and n are the transverse dimension and the index profile of the fiber, respectively.

The first term of equation (2-80) describes the photo-elastic effect, that is, the refractive index of a material varies according to the mechanical strain. In the case of a normal circular fiber, this variation can be calculated as

$$\frac{\partial n}{\partial\varepsilon} = \frac{-n^3}{2}\left[p_{12} - \tilde{\nu}(p_{11} + p_{12})\right] \quad \textbf{(2-81)}$$

where $\tilde{\nu}$ is the Poisson's ratio of silica, which is supposed to be identical for the core and the cladding layer; p_{11} and p_{12} are the elasto-optic coefficients of silica (Mondanos, Lloyd, Giles, Badcock, & Weir, 2000). The second term of equation (2-80) is related to the variation of the fiber's portion when it is subjected to a mechanical strain. Modifying the section will affect the effective indexes of the modes and their differences (Δn_{eff}). The modification does not considerably affect the variation of phase difference, which makes it negligible in practice. The last term of equation (2-80) describes the variation of the fiber's length as a result of mechanical strain.

2.3.2 Effect of Temperature (Thermo-optic Effect)

Similar to the elasto-optic effect, the modifications induced by temperature can also be analyzed. The variation of the phase difference as a result of temperature (T) can be written as

$$\frac{1}{L}\frac{\partial(\Delta\varphi)}{\partial T} = k_0\frac{\partial\left(\Delta n_{eff}\right)}{\partial n}\frac{\partial n}{\partial T} + k_0\frac{\partial\left(\Delta n_{eff}\right)}{\partial D}\frac{\partial D}{\partial T} + k\Delta n_{eff}\frac{1}{L}\frac{\partial L}{\partial T} \qquad \textbf{(2-82)}$$

Equation (2-82) presents the same first two terms in Equation (2-80). These terms are related to the modified opto-geometrical parameters (*n* and *D*) of the fiber, which induce the variation of Δn_{eff}. The variations of the refractive index result from the thermo-optic effect. The third term in equation (2-82) represents the compression of the thermal expansion, which is given as

$$\frac{\partial L}{\partial T} = \alpha L \qquad \textbf{(2-83)}$$

where α is the thermal dilatation coefficient.

The variations of phase difference are essentially caused by the modification of the refractive index according to temperature. Equations (2-80) and (2-82) are used to calculate the mechanical and thermal sensitivities of circular fibers. However, calculating the sensitivities of birefringent fibers is more complicated because the forms and materials comprising such fibers are more complex.

2.4 FMF Applications in SDM Networks

SDM or mode division multiplexing technology can be implemented using MCFPH (Hayashi, Taru, Shimakawa, Sasaki, & Sasaoka, 2011), multi-mode fiber (MMF), or FMF (Richardson et al., 2013; Roland Ryf et al., 2013) and photonic band-gap fiber (PBF) (Nielsen, Jacobsen, Mortensen, Folkenberg, & Simonsen, 2004). FMF is one of the most feasible and economical ways to implement SDM technology, as reported by many researchers (Roland Ryf et al., 2013; Roland Ryf, Randel, et al., 2011; Salsi et al., 2011). In this section, different devices that use FMFs to develop SDM technology are discussed briefly, such as FMF-based amplifiers, multiplexers, couplers, and mode converters.

2.4.1 FMF Transmission via Mode Division Multiplexing

The concept of MDM for optical fibers had been previously investigated (Berdagué & Facq, 1982) but not implemented in practical systems. However, MDM has become an essential part of the transmission system for the implementation of SDM technology nowadays. The MDM transmission system involves few-mode/multimode fibers, mode multiplexer/de-multiplexer, transmitter array, and receiver array. Although the existing multimode fibers support large numbers of guided modes, the modal dispersion, MDL, intermodal crosstalk, caused by fiber imperfections, bending, twisting, and signal processing complexities are very difficult to control. Therefore, most of the current MDM transmission systems comprise FMFs for long distances. Recently, many researchers have reported about FMF-based MDM transmission systems with low modal loss and low differential mode group delay (Hanzawa et al., 2011; Ip et al., 2014; M.-J. Li et al., 2012; Roland Ryf, Sebastian Randel, et al., 2012; Sillard, Bigot-Astruc, & Molin, 2014).

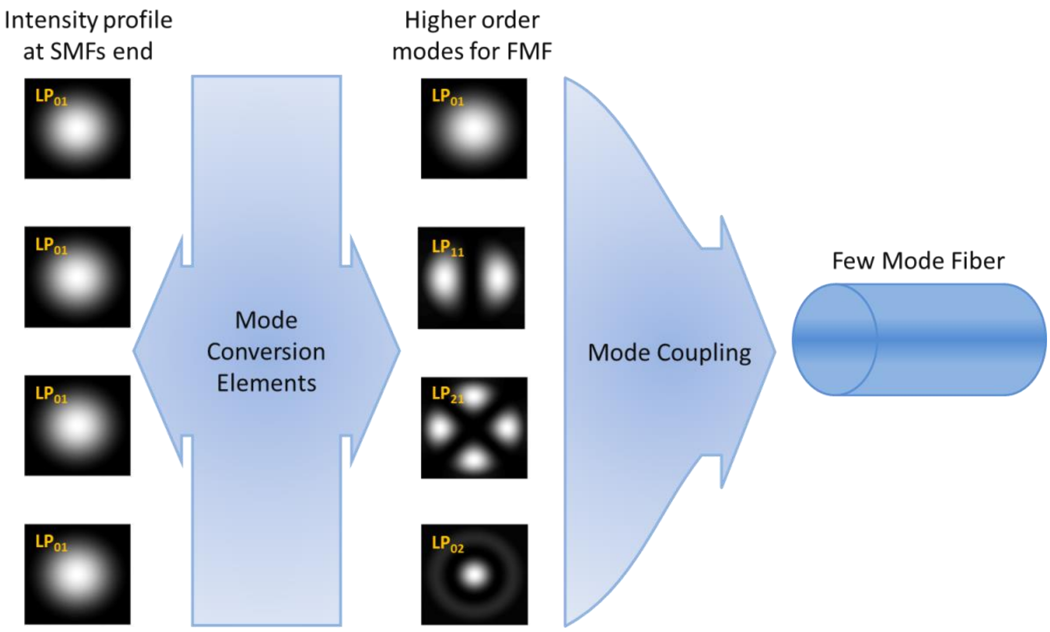

Figure 2.5: Illustrative diagram of mode-division multiplexing (MDM). De-multiplexing is simply the reverse of an MDM.

Mode multiplexing requires the conversion of fundamental mode intensity profiles of SMFs into higher order modes; thereafter, all the modes should be coupled to FMF for transmission. A basic illustrative diagram is shown in Figure 2.5. Mode conversions can be performed in different ways, such as LCoS chip or tunable spatial light modulators (Montero-Orille et al., 2013; Salsi et al., 2011), binary phase plates (Montero-Orille et al., 2013), tunable mechanical long-period gratings, and Bragg gratings inscribed in FMF (Ali et al., 2015; Pradhan et al., 2015; S. Ramachandran et al., 2009). The next important step in the MDM system involves the coupling of all modes to the FMF for transmission. Various methods have been developed to couple the higher order modes, including the use of space optics with the combination of beam splitters and lenses or through photonic lanterns (S. G. Leon-Saval et al., 2014; G. Li et al., 2014) and fiber couplers (Ismaeel et al., 2014; Y Jung et al., 2013), such as the dual-mode fused optical fiber coupler proposed by Jung *et al.* (Y Jung et al., 2013) and multi-spot based fiber mode coupler proposed by Ryf *et al.* (Roland Ryf, Miguel A Mestre, et al., 2012). However, multiplexers with mode converters and free space optics for FMF coupling exhibit inevitably high multiplexing loss because of passive combination loss. Mode multiplexers with low loss have been categorized into two types. The first type is based on the matching of the excited transverse field profile with the fiber modes, whereas the second is based on the matching of the excited modes to the fiber modes with respect to longitudinal propagation constants (G. Li et al., 2014). The loss-measuring parameters in the passive components of MDM systems include total insertion loss (TIL) and MDL, which can be written as

$$TIL = \left(\frac{1}{N}\sum_{n=1}^{N}|\lambda_n|^2\right)^{-1} \quad \textbf{(2-84)}$$

$$MDL = \frac{max(|\lambda_n|^2)}{min(|\lambda_n|^2)} \quad \textbf{(2-85)}$$

where N is the total number of orthogonal channels, and the term $|\lambda_n|^2$ represents the intensity transmission coefficient of the n^{th} channel.

2.4.2 FMF Amplifiers

The commercial viability of implementing SDM technology strongly depends on the feasibility of cost and energy-efficient optical amplification (Krummrich, 2012; G. Li et al., 2014). Raman amplification (Roland Ryf, Sierra, et al., 2011), parametric amplification (N. Zhao, Huang, Amezcua-Correa, Li, & Li, 2013), and erbium-doped fiber amplification (Bai et al., 2012; Bigot, Le Cocq, & Quiquempois, 2015; Yung et al., 2011) are the most promising techniques for modal amplification. Various approaches have been used to realize the preamplifier and booster stages with different types of fibers; however, FMFs present more potential in terms of cost and energy efficiency than other types of fibers, such as multi-core and photonic bandgap fibers.

2.4.2.1 Raman Amplification in FMF

Stimulated Raman scattering is used as the amplification effect in a back-propagating pump configuration. Depolarized pump laser is selectively coupled with the supported linearly polarized mode of the FMF, such as LP_{11} mode, to achieve the mode gain equalization inside the FMF (Roland Ryf, Sierra, et al., 2011). In Raman amplification, the pump laser power at wavelength λ_P is transferred to a signal of wavelength λ_S, and this process depends on polarization instead of phase. Therefore, the depolarized pump laser is used to allow the polarization independency of the gain. The m^{th} mode power S_m along the fiber can be formulated as (Roland Ryf, Essiambre, von Hoyningen-Huene, & Winzer, 2012)

$$\frac{dS_m}{dz} = -\alpha_S S_m + \gamma_R \left(\sum\nolimits_n f_{n,m} (P_n^+ + P_n^-) \right) S_m \qquad \textbf{(2-86)}$$

where γ_R is related to the cross section of spontaneous Raman scattering, α_S is the absorption coefficient at λ_S, and $f_{n,m}$ is the overlap integral of the m^{th} and n^{th} modes. The forward- and backward-propagating powers for mode *n* at λ_P can be written as

$$\frac{dP_n^\pm}{dz} = P_n^\pm \left(\mp\alpha_P \mp \frac{\lambda_S}{\lambda_P} \gamma_R \left(\sum\nolimits_n f_{n,m} S_m \right) \right) \qquad \textbf{(2-87)}$$

where α_P is the absorption coefficient at λ_P. In Equations (2-76) and (2-77), fast power averaging is assumed, which is only true when the amplifier's length is much larger than the mode beat length as a result of phase velocity differences. The beat lengths are found in the range of 1 m to 10 m for standard step-index FMF (Roland Ryf, Sierra, et al., 2011). Ryf *et al*. (Roland Ryf, Sierra, et al., 2011) reported two-mode fibers with gain of 8 dB for LP_{01} and LP_{11} modes by using a pump power of 1.25 W with equivalent noise figure (NF) of −1.5 dB at 1550 nm. This amplifier has been successfully used in six-channel mode division multiplexed MIMO transmission over 137 km long FMF.

2.4.2.2 Parametric Amplification in FMF

Optical materials exhibiting nonlinearities such as $\chi^{(2)}$ or $\chi^{(3)}$ can be used for parametric amplification (Choi, Li, Kim, & Kumar, 1997; Onishi et al., 1998). By using one or more intense pump waves, the optical parametric amplifier (OPA) is pumped to achieve the gains over two wavelength bands surrounding each of the pump wavelengths. An OPA shows a wideband and flat gain profile because the parametric gain is not dependent on energy transitions between energy states, which are considered more advantageous than the other optical fiber amplifiers. The working principle can be explained by four-photon mixing (FPM) theory, in which the relative phase is considered between four interacting photons (Agrawal, 2007; Cappellini & Trillo, 1991; Hansryd, Andrekson, Westlund, Li, & Hedekvist, 2002; Stolen & Bjorkholm, 1982). Fiber-based OPAs have been widely used to amplify SMFs; however, it will be very interesting if OPAs can be used for few-mode or multimode fibers in SDM technology. Some researchers have reported OPAs based on multimode fibers or FMFs (Annamalai & Vasilyev, 2012; N. Zhao et al., 2013). Achieving OPA in FMF has been found difficult because of the different dispersion properties of each mode and the challenge of satisfying the phase-matching conditions for all modes over a large wavelength range (N. Zhao et al., 2013). Zhao *et al.* (N. Zhao et al., 2013) proposed a FMF with similar modal dispersion such that both modal profiles are equally confined in the radial direction; moreover, the gain of 10 dB for OPA by using 1 km FMF was reported for LP_{01} and LP_{11} modes with bandwidth of 50 and 75 nm, respectively.

2.4.2.3 Erbium-Doped Fiber Amplification in FMF

Erbium-doped fiber amplifiers (EDFAs) are the most common devices used to achieve efficient amplification in both SMF and FMF cases (Bigot et al., 2015; Genevaux et al., 2016; Stacey & Jenkins, 2005). However, attaining the efficient and equalized amplification of the different modal or spectral channels in the case of multimode or few-mode systems is a considerable challenge. SDM technology needs to be compatible with the existing technologies of SMFs, such as WDM, polarization multiplexing, and advance modulation techniques; therefore, EDFA should be designed in FMFs, which can perform for modal as well as spectral (wavelengths) contents of the optical signal. Many researchers have reported the FM-EDFAs for SDM systems (Herbster & Romero, 2014; Ip et al., 2014; Ip, Li, Montero, & Yano, 2013; Yongmin Jung, Kang, et al., 2014; Yongmin Jung, Lim, et al., 2014; Vincent Sleiffer et al., 2012; VAJM Sleiffer et al., 2012). The gain required in EDFA is typically greater than 20 dB for all channels, which should be similar for all modes. To better illustrate the performance of FM-EDFA, the new parameter Differential Modal Gain (DMG) is introduced, which can be defined as

$$DMG(\lambda) = max\{|G(m,\lambda) - G(n,\lambda)|\} \; for \; m \neq n \qquad \textbf{(2-88)}$$

where G represents the gain in dB, m and n represent the mode numbers, and λ represents the wavelength. Equation (2-78) illustrates that in ideal cases, the DMG should be zero, and all the modes should exhibit the same gain over the C-band; therefore, gain flattening filters (GFFs) are used to achieve the same modal gain in practice (Ip et al., 2013). Moreover, all the high-order modes suffer losses, which means that FM-EDFA should compensate for the mode-dependent loss (MDL) by keeping the DMG nonzero. The simple block diagram of FM-EDFA is shown in Figure 2.6. Two laser diodes are installed for forward and backward pumping alongwith the modal content controllers so that the signal and pumps are combined using dichroic mirrors (DMs) and a piece of FM-EDF.

The first multimode EDFA was theoretically explained by Desurvire *et al.* (Desurvire, 2002), and Gong *et al.* (Gong et al., 2007) performed the numerical analysis of multimode EDFAs thereafter. The assumptions that have been made in the theoretical model of multimode EDFAs are for amplification in the Er ions; the electronic transition is a two-level system, the fiber is considered to be homogeneous in longitudinal direction, the EDF is considered to be weakly guided, and modes are considered as LP modes. Later on, these assumptions have been verified by numerical and experimental investigations (Kang et al., 2012; Le Cocq et al., 2012). Moreover, Jung *et al.* (Yongmin Jung, Lim, et al., 2014) proposed another way to realize the FM-EDFA by cladding pumped technique. However, in this technique, the reported FM-EDFA supports six spatial modes with more than 20 dB average modal gains between 1534 nm to 1565 nm with NF of about 6 dB to 7 dB, and the measured DMG was approximately 3 dB.

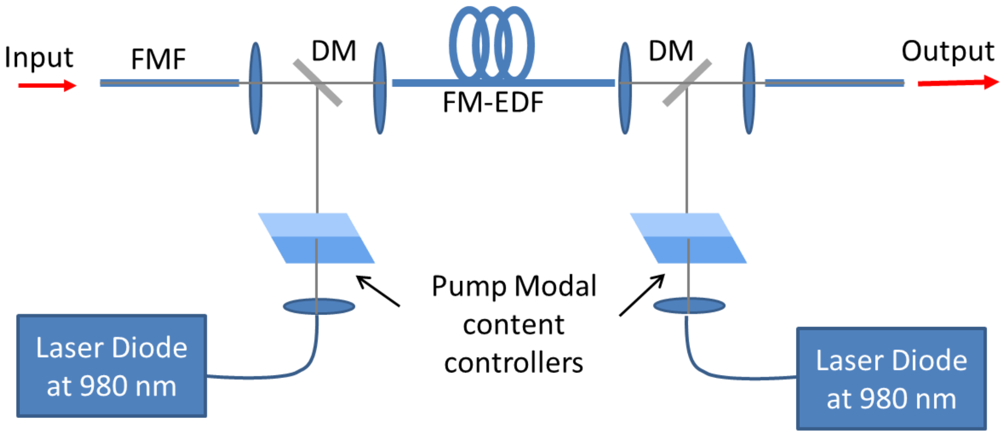

Figure 2.6: Block diagram of few-mode erbium-doped fiber amplifier (FM-EDFA) (G. Li et al., 2014).

2.4.3 FMF-based Mode Converters

An efficient, controllable, and stable mode converter is the core component of MDM systems. Various ways have been developed to realize mode converters; for instance, the binary phase plates, mechanically or thermally induced LPGs, integrated waveguide optics, free space optical setups, and all fiber mode converters have been used (Ali et al., 2015; Montero-Orille et al., 2013; Pradhan et al., 2015; S. Ramachandran et al., 2009; Salsi et al., 2011). When designing the mode converters, the characteristics that should be considered are modal purity, modal extinction ratio, and mode conversion efficiency. The details of mode conversion using binary phase plates are discussed in Chapter 4. Some examples of mode converters with FMFs, as proposed by different researchers, are listed in Table 2.1.

Table 2.1: Some examples of mode converters fabricated in FMF.

Reference	Device Type	Fabrication Method	LP Modes	Efficiency	Comments
(Andermahr & Fallnich, 2010)	LPG	Optically Induced by ns pulsed laser via Kerr effect	LP_{01} and LP_{11}	50%	The grating is instantaneously and temporally induced while the writing pulse is in the fiber.
(Siddharth Ramachandran, Wang, et al., 2002)	LPG	UV-induced LPG	LP_{01} and LP_{02}	99%	These gratings are polarization insensitive with the bandwidth of 63 nm and the insertion loss is less than 0.2 dB.
(Hellwig, Walbaum, & Fallnich, 2013)	LPG	Optically Induced by ns pulsed laser	LP_{01} and LP_{11}	>90%	Graded index FMF conversion range from 1160 nm up to 1700 nm.
(Hellwig, Schnack, Walbaum, Dobner, & Fallnich, 2014)	LPG	Optically Induced by fs pulsed laser	LP_{01} and LP_{02}	46%	Required pulse energies can be reduced to 120 nJ.
(Giles et al., 2012)	LPG	Mechanically induced LPG	LP_{01}, LP_{11}, LP_{21} and LP_{02}		LPGs in 2-MF and 4-MF have been investigated and method to separate and monitor the mode in real time is described
(Sakata et al., 2014)	LPG	Electromagnetic induced	LP_{01} and LP_{11}		Wavelength can easily be tuned by changing the pitch of coil spring. The bandwidth of mode converter can expand from 5 to 90 nm whereas the drive voltage can be decreased about half.
(Song, Su Park, Kim, & Song, 2014)	Acousto-optic mode-converter (AOMC)	Acousto-optic induced	LP_{01}, LP_{11}, LP_{21} and LP_{02}	>95%	The coupling efficiency higher than 95% and the extinction ratio greater than 10 dB are achieved for each higher-order mode.
(S. Li, Mo, Hu, Du, & Wang, 2015)	All-fiber orbital angular momentum mode converter	Thermally induced LPG (CO_2 laser) combined with mechanical rotator, metal flat slabs and polarization controller (PC)	LP_{01}, LP_{11}, and OAM		By adjusting the stressing, rotating, and twisting the mechanical devices to selectively convert LP_{01} mode from the SMF to the LP11a, LP11b, OAM−1, or OAM+1 mode using 2-MF
(J. Dong & Chiang, 2015)	LPG	Thermally induced LPG (CO_2 laser) with mechanical rotator, metal flat slabs and polarization controller (PC)	LP_{01} and LP_{11}	>99%	Mode converter has the bandwidth of 34 nm in the C-band.
(Y. Gao, Sun, Chen, & Sima, 2015)	Tilted FBG	UV induced Tilted FBG by phase mask	LP_{01}, LP_{11}, LP_{21} and LP_{02}	>99.5%	Tilted FM-FBG with the tilt angle is 1.6° the coupling between LP_{01} and higher order modes increase by increasing the tilt angle at certain value.
(Ali et al., 2015)	FBG	UV-induced FBG by phase mask	LP_{01}, LP_{11}, LP_{21} and LP_{02}	70% to 95%	Mode conversion occurs at the cross coupling wavelengths of FM-FBGs.

2.4.3.1 Long-Period Gratings in FMF for Mode Conversion

Long-period gratings (LPGs) in optical fibers arise from periodic perturbations of the refractive index, and the period lies in the range 100 µm to 1 mm (Hill et al., 1990; James & Tatam, 2003). In LPGs, the propagating modes of core and co-propagating modes of cladding are coupled with each other, which induce the attenuation at discrete wavelength bands of the transmission spectrum. If the beating length of two transverse modes is equal to grating period, mode conversion can occur and the fundamental mode can be converted to high-order modes (Andermahr & Fallnich, 2010). The illustrative diagram is shown in Figure 2.7. The LPGs can be induced in different ways, such as optically induced (Andermahr & Fallnich, 2010), electromagnetic induced (Sakata et al., 2014), mechanically induced, or thermally induced LPGs (Grüner-Nielsen & Nicholson, 2012; Pradhan et al., 2015).

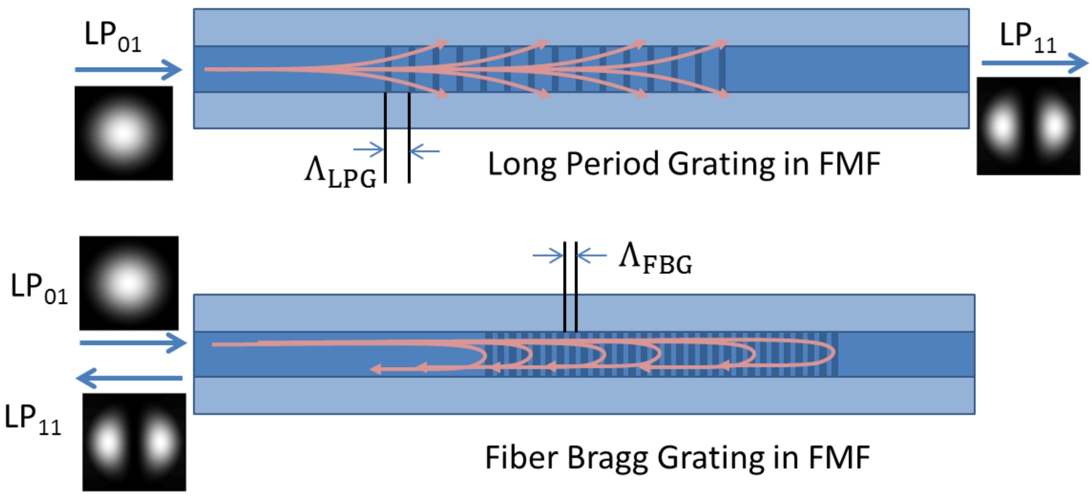

Figure 2.7: Illustrative diagram of mode conversion using LPG in FMF (above) and FBG in FMF (below). When the LPG period is matched with the beat length of modes, the mode conversion happens at the receiver-end, whereas the FM-FBG at cross-coupled wavelength mode conversion can be achieved at reflection side.

2.4.3.2 Fiber Bragg Gratings in FMF for Mode Conversion

The efficient mode conversion is the basic requirement for the realization of MDM systems. Therefore, an alternative way of mode conversion in addition to LPGs or free space optics using phase plates and beam splitters involves the use of FBGs inscribed in

FMF, as shown in Figure 2.7. An FBG is realized as a result of the periodic perturbations of core refractive index of fiber. Coupling between the modes occurred because of the phase matching of the forward- and backward-propagating modes of core; the coupling can be categorized into two types, namely, the self-mode coupling and the cross-mode coupling (Ali et al., 2015). Self-mode coupling and cross-mode coupling are shown in Figure 2.8 (a) and Figure 2-8(b) respectively.

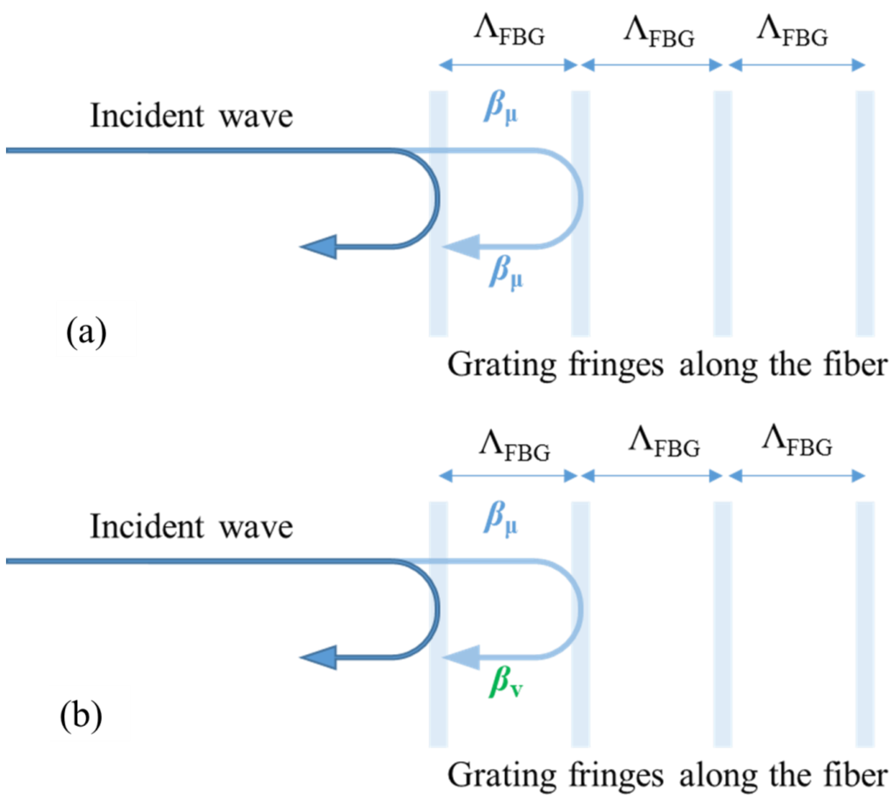

Figure 2.8: Concept of self-mode coupling in (a) and cross-mode coupling in (b) for FMF Bragg gratings.

The phase matching condition of self-mode coupling is given by

$$2\pi = \beta_\mu \Lambda_{FBG} + \beta_\mu \Lambda_{FBG} = 2\beta_\mu \Lambda_{FBG} \quad \textbf{(2-89)}$$

$$\lambda_\mu = 2n_\mu(\lambda_\mu)\Lambda_{FBG} \quad \textbf{(2-90)}$$

where β_μ and Λ_{FBG} are the propagation constants of the μ^{th} mode and Bragg grating period of FM-FBG. n_μ and λ_μ are the effective refractive index and Bragg wavelength of μ^{th} mode, respectively. The phase matching condition of cross-mode coupling between μ^{th} and v^{th} modes is given as

$$2\pi = \beta_\mu \Lambda_{FBG} + \beta_v \Lambda_{FBG} = (\beta_\mu + \beta_v)\Lambda_{FBG} \tag{2-91}$$

$$\lambda_\mu = [n_\mu(\lambda_{\mu,v}) + n_v(\lambda_{\mu,v})]\Lambda_{FBG} \tag{2-92}$$

At the cross-mode coupled wavelengths, stronger coupling of the two modes provides the higher mode conversion efficiency, and the cross-coupling can be increased to a certain level by enhancing the induced birefringence during UV-inscription FBG because of the non-uniform induced refractive indexed profile. The other way to enhance the cross-coupling for mode conversion is to fabricate the tilted FBG (Y. Gao et al., 2015). The details of coupling and mode conversions are presented in Chapter 4. The mode conversion bandwidth, which can be tuned by varying temperature and strain, is further discussed.

2.5 FMF Sensing Applications

The FMF can be used to sense more than one parameter by taking advantage of its more than one supporting modes. Given the thermo-optic and elasto-optic effects in optical fiber, all the FMF modes demonstrate unique sensitivities. Therefore, given the opportunity to sense more sensing parameters such as temperature, strain, and pressure in addition to removing the cladding of the FMF, the core modes become sensitive to the ambient environment and can be used to measure the refractive index of the liquid solution. For example, the block diagram of this sensor can measure the refractive index and temperature of the solution simultaneously; the detail of the sensitivity analysis is presented in Chapter 5. Examples of such sensors include OTDR and FBGs, and the modal interferometry in FMFs reported in the literature is presented in Table 2.2.

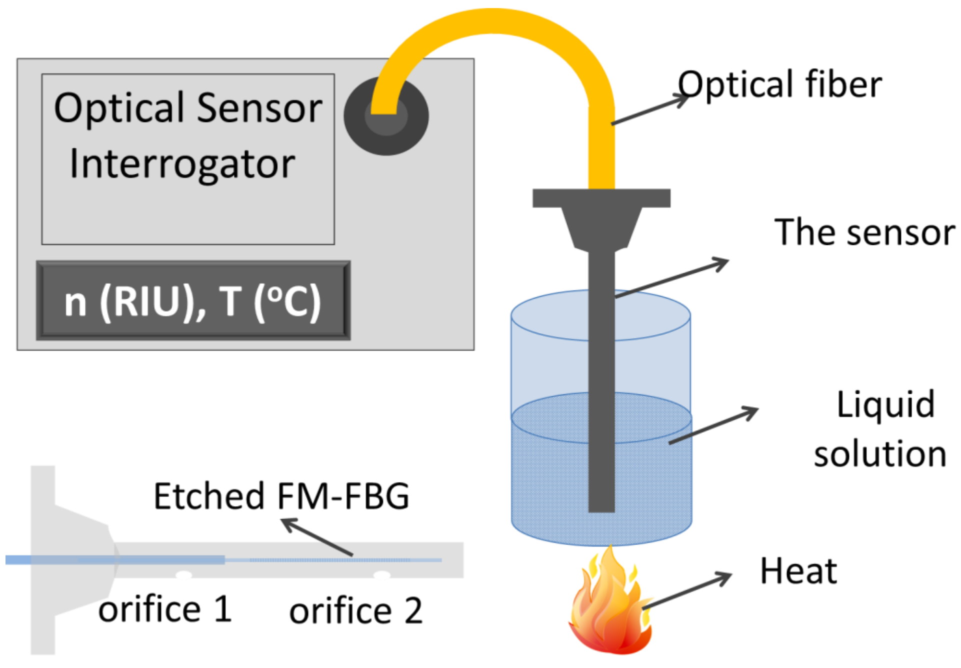

Figure 2.9: Block diagram of the FM-FBG sensor for the simultaneous measurement of refractive indeix and temperature.

Table 2.2: Examples of sensing applications of FMF devices.

Reference	Device Type	Sensing Parameters	Sensing Range	Sensitivity				Comments
(Weng, Ip, Pan, & Wang, 2015)	Brillouin optical time domain reflectometry (BOTDR)	Temperature and strain	−25 °C to 80 °C 0 to 3000 με	Mode	MHz/°C	kHz/με	με/ °C	It works on the principle of stimulated Brillouin scattering. The FMF with modified mode profile and doping concentration results in five-fold higher accuracy.
				LP_{01}	1.29	58.5	0.0241	
				LP_{11}	1.25	57.6	0.0236	
(P. Guo et al., 2013)	FBG	Temperature, strain and bending	20 °C to 120 °C 0 με to 1500 με 0 m^{-1} to 0.45 m^{-1}	Mode	pm/m^{-1}	pm/°C	pm/με	FBG have been written by UV-laser and tested for temperature, strain and bending.
				LP_{01}	–654.1	11.0	1.3 for all	
				LP_{01}-LP_{11}	–638.2	10.9		
				LP_{11}	–636.9	11.2		
(D. Chen, Wu, Tse, & Tam, 2011)	Modal interferometer	Hydrostatic pressure	0 MPa to 39 MPa	−23.7 pm/MPa				LP_{01} and LP_{11} modal interference in FMF for pressure sensing.
(A. Li et al., 2015)	Discrete FMF modal interferometer	Temperature	30 °C to 70 °C	−1.72 nm/°C				The device work on the basis of modal interference.
(A. Li et al., 2015)	Brillouin distributed FMF sensor	Mechanically induced LPG	25 °C to 90 °C 0 με to 1800 με	Mode	MHz/°C	MHz/με		The device works on the principle of Brillouin scattering in an FMF.
				LP_{01}	1.01690	0.05924		
				LP_{11}	0.99099	0.04872		
(Huang, Fu, Ke, Shum, & Liu, 2014)	FBG	Temperature and strain	27 °C to 65 °C 100 to 3900με	Mode	pm/°C	pm/με		FBG have been written by UV-laser and characterized by temperature and strain measurements.
				LP_{01}	11.5	~0.9 for both		
				LP_{11}	10.6			
(Qiu et al., 2013)	Few-mode polymer optical FBG	Temperature and strain	20 °C to 40 °C 0 to 15000με	Mode	pm/°C	pm/με		Few-mode Polymer optical fiber (POF) has been used to inscribe FBG and was characterized for temperature and strain.
				LP_{01}	−98	1193		
				LP_{11}	−103	1189		
				LP_{21}	−105	1186		
				LP_{02}	−111	1163		
(H. Z. Yang et al., 2015)	Cladless FM-FBG	Temperature and refractive index	22 °C to ~75 °C 1.3159 to 1.3595 RIU	Mode	pm/°C	nm/RIU		FM-FBG was fabricated and then chemically etched for simultaneous sensing of temperature and refractive index.
				LP_{01}	9.62 ± 0.08	1.183		
				LP_{11}	9.52 ± 0.13	4.816		

2.6 Summary

The optical fiber theory used for the presented research work has been discussed and characteristics equation has been developed for optical fiber for finding the effective refractive indices of the supported modes of FMF. A brief overview of coupled mode theory for the FBG and modal coupling inside the optical fiber was explained, with a special focus on FM-FBGs. Various optical fiber devices used for optical communication such as optical filters and mode converters and sensing applications were presented, along with a brief review of the physics underlying the operation mechanism of optical fiber-based devices, such as FBGs. The important aspects to be considered while using FMF-based devices as multi-parameter or discriminative sensors were discussed.

CHAPTER 3: FABRICATION OF FEW-MODE FIBER BRAGG GRATINGS AND PRECISE MEASUREMENT OF GRATING PERIOD

In this chapter, the fabrication of FBGs using phase mask technique is presented in detail. The grating period of fabricated FBG is an important factor that should be measured more accurately. Therefore a new approach based on optical imaging technique is presented for the period measurement of FBG. The proposed technique is a simple and direct approach that involves a differential interface contrast (DIC) microscope and a high-resolution CCD camera. Image processing is performed on the microscope images to obtain low noise grating profiles and grating periods. Uncertainty can be reduced by adopting a large image sample size during the image processing. In the investigation, the FBGs of different grating periods are fabricated by pre-straining the photosensitive fibers during UV-writing process. A good linearity between the measured Bragg wavelengths and grating periods is observed and the measured strain-optics coefficient is found to be in agreement with reported literature.

3.1 Introduction

A FBG comprises a periodic modulation of the refractive index in the core of the optical fiber, in which the phase fronts are perpendicular to the longitudinal axis of the fiber. When a broadband light source is injected into a uniform FBG, constructive interference occurs at a particular resonant wavelength and a portion of light at that wavelength is reflected as other wavelengths are transmitted. A single resonant wavelength exists for a SMF, whereas a number of resonant wavelengths can be achieved for the few-mode or multimode fibers. Hereafter the particular resonant wavelength is called the Bragg Wavelength, a product of the effective refractive index, n_{eff} of the fiber, and period of the grating structure inscribed in the fiber. The effective refractive index depends on the core diameter and dopant composition in the core. Ge is a commonly used index riser and photosensitive material for photosensitive fibers. Highly photosensitive fibers can be attained with a high concentration of Ge dopant in the fiber core (Medvedkov, Vasiliev, Gnusin, & Dianov, 2012). However, such fibers suffer from several disadvantages, such as high attenuation, brittleness, and high splicing loss with common SMFs (Gillooly, 2011). The core refractive index can be lowered by co-doping Boron, an index depressor, into the core glass. The composition of B-Ge can be optimized to tailor the refractive index of the fiber closer to that of SMF-28 fibers. These fibers can be further photosensitized through a post-treatment process as in hydrogen loading, wherein the fibers are soaked in a highly pressurized H_2 gas chamber for a week or a couple of days at high temperature (80 °C to 100 °C).

In determining the grating period, both periods of the grating and phase mask can be easily assumed to be the same if the phase mask technique is used in writing the FBG. However, the inscribed grating period can be slightly different from that of the phase mask because of the condition of the fabrication rig, UV ray geometry, and orientation of the fibers with respect to the phase mask. In a different approach, the grating period can be calculated from the Bragg wavelength, as measured using an Optical Spectrum Analyzer (OSA), and an assumed value for n_{eff} that can be numerically calculated provided that the important parameters such as cladding, core radii, and NA are known (Snyder & Young, 1978). However, the accuracy of the calculation is subjected to the numerical method and parameters used. The refractive index of the fiber can be affected by the internal stresses in the fibers caused by elasto-optical effects (Yablon, 2004). Generally, two types of internal stresses occur in optical fibers, namely, the thermo-elastic and frozen-in stresses. Thermo-elastic stress is initiated by the difference in thermal-expansion coefficients between core and cladding (Sceats, Atkins, & Poole, 1993). Frozen-in stresses are the result of non-uniform temperature and strain distribution in the heated fiber during the drawing process. The residual stresses are permanently trapped in the fiber because of the rapid cooling of the fiber (Hermann, Hutjens, & Wiechert, 1989; Ky, Limberger, Salathé, & Cochet, 1998). As a result, stress-induced index change is produced, and the magnitude of the index change can be as high as 10^{-3}, which leads to an uncertainty of ±0.7 nm in the calculation of grating period. Some studies have indicated that hydrogen loading can reduce axial stress in the fiber core (Ky, Limberger, Salathé, Cochet, & Dong, 1999). The degree of stress reduction varies in accordance with the drawing force and types of dopant in the fibers. Nonetheless, the effect is reversible for certain types of fibers when H_2 out-diffuses from the fibers. The combination of all these factors may result in larger uncertainty in the estimation of grating period.

In this work, a more accurate measurement technique based on optical imaging and digital image processing algorithm is proposed to measure the grating period. Optical imaging technique is a direct approach to determine the period of the grating structure with the assistance of DIC and a high-resolution digital CCD camera (Dragomir et al., 2003; Kouskousis et al., 2006; K.-S. Lim et al., 2013). Dragomir et al. proposed the direct observation of the grating structure under normal temperature and no applied strains on FBG (Dragomir et al., 2003). The optical images reveal complex grating structures in the fiber, which can be attributed to the different order of diffractions by the phase mask (Kouskousis et al., 2006).

The gratings structures are written on several pre-strained photosensitive fibers. The grating period of the FBG can be tuned by inscribing the grating on a pre-strained photosensitive fiber (Zhang et al., 1994), and it will be reduced when the external applied axial stress on the fibers is released. Afterward, high-resolution microscope images of the grating structures are taken and processed using digital image processing algorithm, and the grating period is estimated by calculating the average spacing of the fringes. The fabrication of FBGs in different grating periods is discussed. The optical imaging technique for the period measurement of pre-strained FBG is presented along with the sample images taken for SMF and FMFs tested to verify the technique.

3.2 Photosensitivity of Fibers and its Enhancement with Hydrogen loading

Photosensitivity is a significant feature of optical fibers that enables the fabrication of Bragg gratings and devices based on gratings. The intrinsic photosensitivity in standard SMF used in telecommunication is typically low ($\Delta n \sim 3 \times 10^{-5}$). Therefore, different techniques for improving the photosensitivity of fibers have been proposed by different researchers in past few decades (Hill, Fujii, Johnson, & Kawasaki, 1978; Hill, Malo, Bilodeau, & Johnson, 1993; Raman Kashyap, 2010a). The FBGs can be categorized into three different types based on photosensitive response.

Type I: Type I photosensitive materials show a monotonic increase in refractive index along with time when exposed to UV. This class of photosensitivity is commonly used to create FBGs.

Type IIA: Following a type I positive index change, the extended exposure of some materials can inhibit the refractive index increase and increase the time-varying negative index change.

Type II: The third group of photosensitivity is the result of exposing the material in question to high intensity light. Sufficiently high exposure causes physical damage, which has an associated index change. Such changes in refractive index can be of the order 1×10^{-2}, which remains stable up to high temperatures because of the nature of their formation.

Photosensitivity level is increased by various types of dopants, such as Ge, Sn, N, Eu, and Ce (Broer, Cone, & Simpson, 1991; Butov, Dianov, & Golant, 2006;

Ebendorff-Heidepriem & Ehrt, 2000; Raman Kashyap, 1994). Using Ge as dopant is convenient because it allows the increase of the refractive index of silica with better design and ease of fabrication. By increasing the Ge dopant level, the number of defects in silica increases, which results the enhancement of photosensitivity. However, excessively high dopant levels result in higher refractive index than desired, with higher optical loss and less mechanical strength. To avoid the unwanted effects of high Ge dopant levels, the co-dopants can be added to compensate for the refractive index value of silica and increase the photosensitivity (e.g., B).

In germanosilicate glasses, instead of increasing the dopant levels, alternative techniques have been developed to enhance photosensitivity without changing the physical properties of the glass. Hydrogen loading is the most commonly used method first reported by Lemaire *et al.* (Lemaire, Atkins, Mizrahi, & Reed, 1993), where optical fibers were kept under high pressure for the diffusion of hydrogen into the silicate matrix. The UV-induced maximum refractive index change has been reported as 2×10^{-2} in hydrogen-loaded glass (Svalgaard & Færch, 2005).

3.3 Bragg Gratings Inscription in the Fiber Core

In this section, the inscription of Bragg gratings in the fiber core is presented in detail. SMF-28, B-Ge co-doped photosensitive fiber (Fibercore Ltd: PS1250/1500), and FMF, as well as two-mode step index (OFS, Denmark) and four-mode step index fibers (OFS, Denmark), are used in this study. The commonly used techniques for inscribing the Bragg gratings inside the fiber core include interferometric, point by point inscription, and standard phase mask technique (Raman Kashyap, 2010b). The interferometric technique for the inscriptions of FBGs is quite complicated and the alignment is hard to achieve because of its sensitivity, particularly when the gratings have to be inscribed precisely for certain Bragg wavelength. In the point to point inscription technique, each writing plane inscribed into a fiber by a focused single-laser pulse; therefore this technique needs a precise translation stage, which is relatively difficult and costly. The phase mask technique is relatively simple and more precise for inscribing the gratings. Additionally, the mask with phase grating can be used to generate the two laser beams and make interference patterns used to print the grating pattern inside the fiber core.

3.3.1 The Laser Source for the Inscription of FBG

Several types of laser sources can be used for the inscription of FBGs by inducing the refractive index modulation inside the fiber core, which can be classified as continuous wave (CW) lasers and pulse lasers. The most common UV pulse sources used to fabricate FBGs with a phase mask are KrF excimer laser with the wavelength of 248 nm and ArF excimer laser with the wavelength of 193 nm. Argon ion CW laser with a wavelength of 244 nm can also be used because of its high spatial and temporal coherence; however, this laser has smaller power and beam diameter compared with the excimer lasers. The inscription is relatively difficult with CW laser because of the alignment problems caused by the smaller beam size and laser power. In the present work, FBGs have been written by CW and UV excimer lasers for the investigation of exact grating periods by optical imaging technique. In other works, the UV excimer lasers CL 5100 (Optosytems Ltd.) with specifications mentioned in Table 3.1, have been used for the FBG inscription. The beam profile of the excimer laser has a Gaussian distribution profile along with the vertical and horizontal axes. Laser power or energy can be controlled through the laser control panel, and the pulse repetition rate can be adjusted for better quality in FBG inscription. The laser control and gas mixture panels are as shown in Figure 3.1.

Table 3.1: Parameters of used UV CL 5100 excimer lasers (Optosystems Ltd.)

Parameter	**ArF Laser**	**KrF Laser**
Wavelength	193 nm	248 nm
Nominal Pulse Energy	20 mJ	40 mJ
Average Power CL 5100	2 W	4 W
Max repetition rate	100 Hz	
Pulse Duration	8 ns to 10 ns	9 ns to 11 ns
Stability of pulse energy	sigma < 2%	
Beam Size at FWHM	12 mm × 5 mm	
Beam Divergency at FWHM	4 mrad × 2 mrad	
Dimensions, mm^3	780L × 330W × 583H	
Weight, kg	80	
Cooling	Air	
Power Consumption	220 V, 50 Hz, 1.5 kW	
Gas	1 premix cylinder	
Control	RS 232, Window	

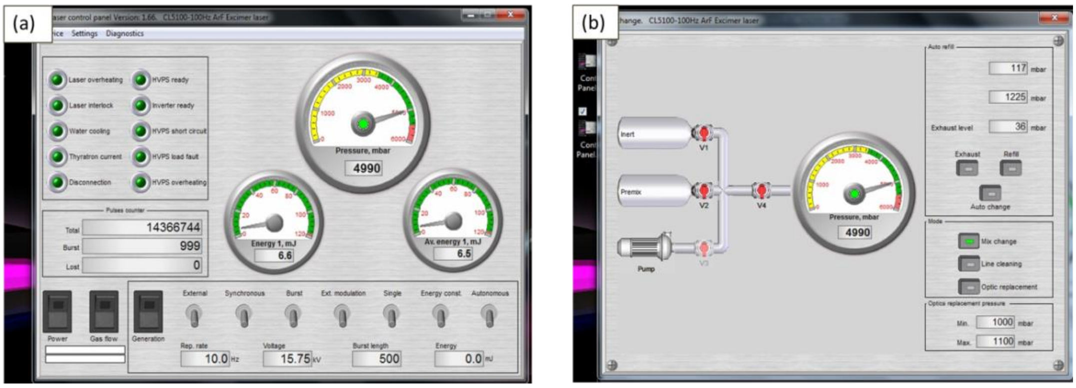

Figure 3.1: Graphical user interface (GUI) for the laser control panel and gas mixture.

3.3.2 Experimental Setup for FBG inscription

A schematic of the FBG writing setup is shown in Figure. The output of the KrF laser operating at 248 nm wavelength is reflected by mirrors to change the level of beams by matching the height of setup, expanding the first lens, filtering using the vertical slit, converging to the line source using cylindrical lenses, and then passing through a phase mask before the fiber is irradiated. The schematic of the experimental setup is shown in Figure 3.2. A vertical slit is placed between the first two lenses to spatially filter the sides of the Gaussian beam, which results in approximately uniform beam size of the laser. The focal lengths of first two lenses are 25 and 200 mm to expand the beam size from about 6 mm to 45 mm when placed approximately 225 mm apart. The third lens focuses the beam before it strikes the phase mask. According to the lens specifications, the spacing between the third lens and the target optical fiber must be approximately 67 mm. Phase mask is used just before the target optical fiber which induces the interference pattern laterally on the target fiber where the grating structure is inscribed. The target fiber is held by a pair of fiber clampers mounted on a rail and separated by approximately 6 cm. The spacing and alignment of the fiber with respect to the phase mask can be adjusted during the precision translation stage. The target fiber should be placed in contact with the fine corrugation of the phase mask before writing. Moreover, the fiber in contact with the phase mask should be properly cleaned and no coating or coating particles should be found on the part irradiated by UV laser; this may cause a permanent burn mark or damage on the surface of the phase mask. The real-time experimental setup used for the fabrication of FBGs is shown in detail in Figure 3.3 (a)-(c).

However, the photosensitive Ge-doped hydrogen-loaded target fiber is connected to the ASE broadband laser source via circulator through bare fiber adaptor. The other side is connected to OSA via a fiber patch cord. Thus, the transmission spectrum is continuously monitored until the FBG becomes saturated before the laser is stopped. After the writing process, the FBG is gently removed from the setup is properly tagged in terms of reflectivity, length of gratings, and type of fiber.

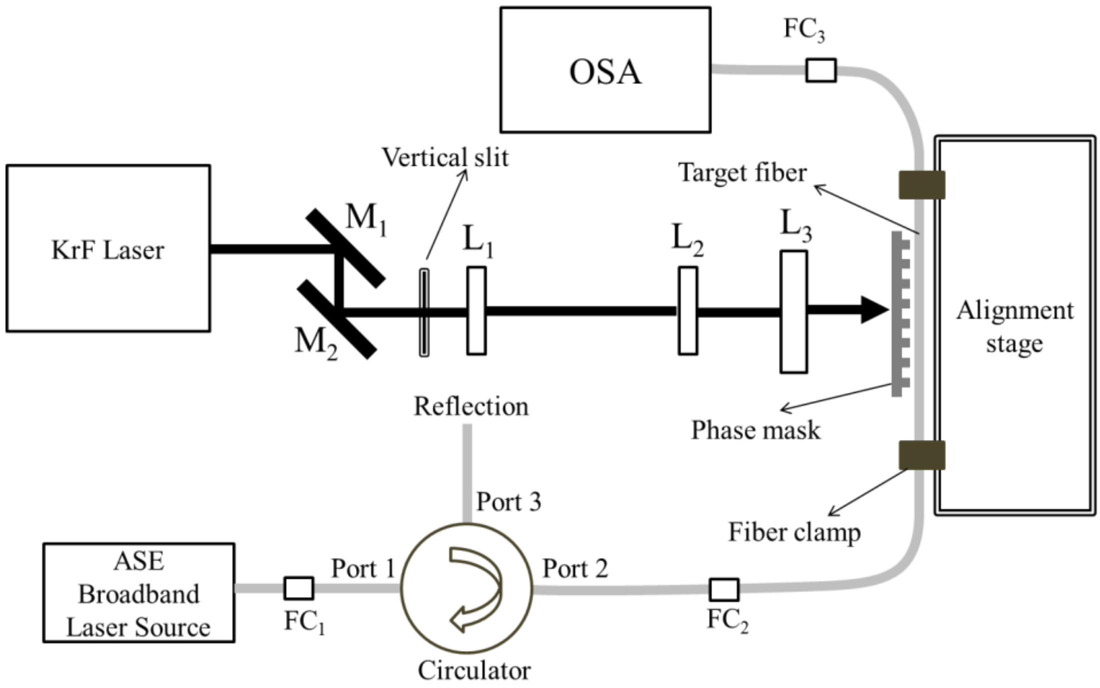

Figure 3.2: Schematic of FBG fabrication setup using phase mask technique. M_1 and M_2: reflection mirrors; L_1, L_2, and L_3: lenses; FC_1, FC_2, and FC_3: fiber connectors; OSA: optical spectrum analyzer.

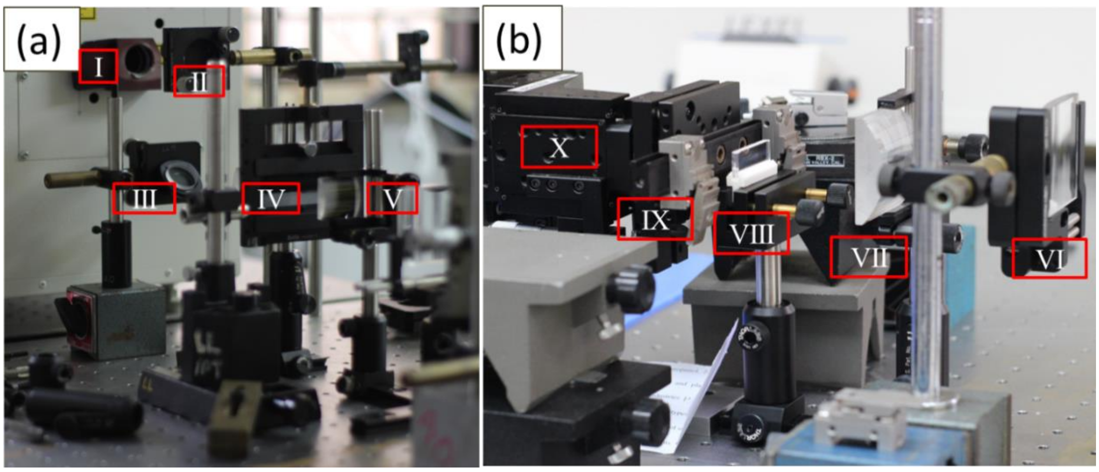

Figure 3.3: Experimental rig in the laboratory used for FBG fabrication (a) from laser side (b) from fiber alignment stage. I: Aperture of excimer laser; II and III: reflective UV mirrors; IV: spatial filter using slit; V: First lens; VI: Second lens; VII: Third lens; VIII: Phase mask; IX: Target fiber with fiber holders; X: Fiber alignment stage.

3.3.2.1 Stage Alignment for Inscription of FBGs

The quality of FBGs depends on various factors, such as the resolution of the phase mask, quality of UV beam profile, alignment of optical setup, and alignment of target fiber fixed with stage. The alignment of the stage is critical with respect to the position of the phase mask and beam profile. In this work, the employed manual stage has five degrees of freedom (DoF) such as x, y, and z axes, rotation along y-axis by angle θ, and rotation along y-axis by angle ϕ, as shown in Figure 3.4 (a). The Optical rail is mounted on the stage where the fiber holders are fixed firmly 6 cm to 7 cm apart. The target fiber is aligned in such a way that the optical beam should be perfectly coupled with the fiber axis and the symmetric diffraction pattern is formed and detected using a piece of white paper behind, as shown in Figure 3.4 (b). Before inscribing the FBG on the desired fiber, the stage is perfectly aligned and verified through the dummy fiber, which is placed near the phase through fiber holders. Laser power is increased and frequency is set at higher value to see the brighter and symmetric diffraction pattern.

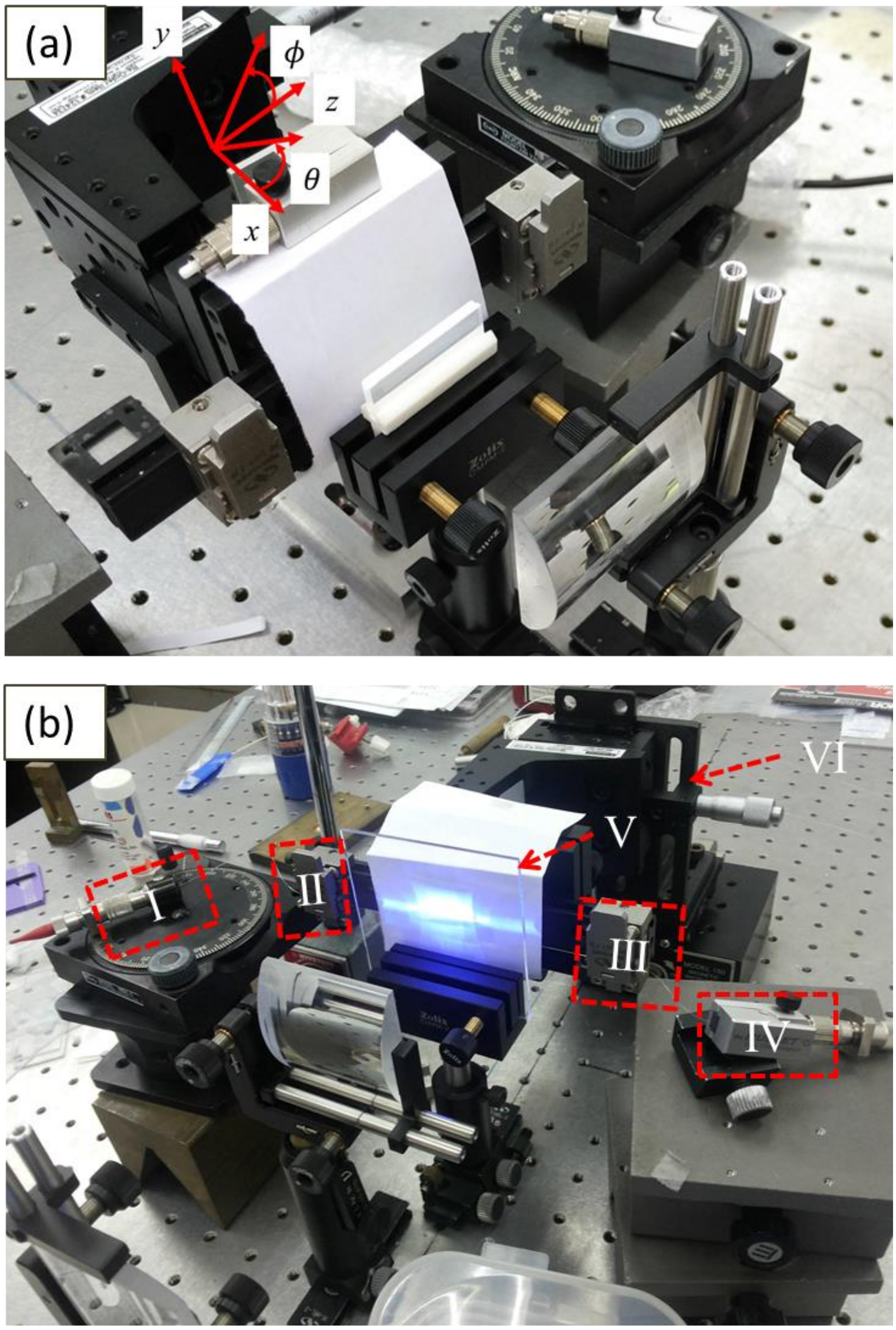

Figure 3.4: (a) Illustration of stage alignment with five axes and phase mask position before UV illumination (b) The diffraction pattern after UV illumination on target fiber perfectly aligned by manual stage with reference to the phase mask. I, IV: bare fiber adapters; II, III: fiber holders; V: phase mask; VI: manual stage with five degrees of freedom (DoF).

3.3.2.2 Phase Mask

The phase mask is the main part of the fabrication of FBGs. The phase mask is a one-dimensional periodic surface relief grating. Phase masks are usually fabricated using e-beam lithography on a fused silica plate. The phase masks used herein for KrF and ArF lasers are manufactured by companies Ibsen Photonics, Denmark, and O/E Lands Inc., respectively, and their specifications are given in Table 3.2.

Table 3.2: Features of the Phase Masks used for Inscription of FBG.

Features	**248 nm illumination (KrF Laser)**	**193 nm illumination (ArF Laser)**
Manufacturer	Ibsen Photonics, Denmark	O/E Land Inc.
Material of Phase Mask	UV-grade Fused Silica	Silica (SiO_2)
Phase Mask Period	1068.80 nm	1067.00 nm
Grating period accuracy and uniformity	±0.01 nm	0.001 nm
Max. Grating size	50 mm x 10 mm	30 mm x 3 mm
Substrate size	3" x 3" x 2 mm	
0^{th} order suppression	< 4% (Typically 1-2%)	<3.05 % Typically

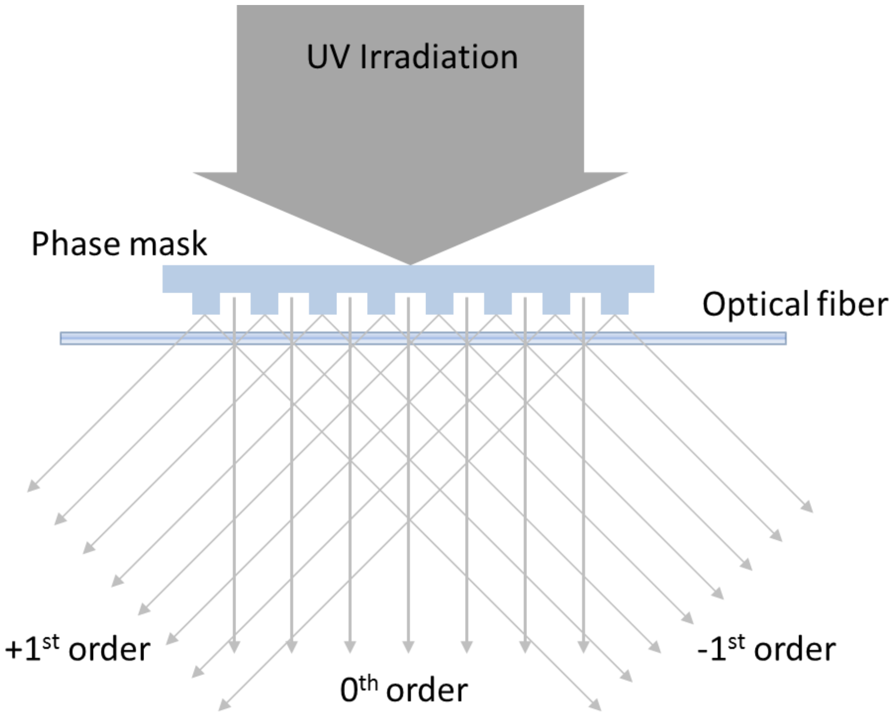

Figure 3.5: Illustrative diagram of UV irradiated beam diffraction through phase mask with diffraction orders for the inscription of FBGs inside the core of optical fiber.

The UV laser beam passing through the phase mask is diffracted to form a three-dimensional interference pattern to inscribe the grating inside the fiber. With the UV irradiation at normal incidence, the diffracted radiations are split into different orders (i.e., 0th order and +1/-1 order) as shown in Figure 3.5. This interference pattern induces periodic refractive index change, i.e., refractive index modulation in the core of UV photosensitive fiber.

The UV light is normally present on the grating when the phase mask is used in the +1/-1 order configuration. The angles of diffraction θ_0, θ_{+1}, θ_{-1}, θ_{+2}, and θ_{-2} are given in terms of the UV wavelength λ_{UV} and phase mask period Λ_M as follows

$$sin\theta_m = m \frac{\lambda_{UV}}{\Lambda_M} \qquad \textbf{(3-1)}$$

where m represents the order and interference of the +1 and -1 beams, which creates the fringe pattern with exactly one half of the period of the phase mask, regardless of the wavelength of the incident radiation given by

$$\Lambda_f = \frac{\Lambda_M}{2} \qquad \textbf{(3-2)}$$

Therefore the phase mask design is optimized in such a way that the intensity of the +1st and -1st orders is maximized, whereas the intensity carried in the 0th order is minimized. Moreover, the intensity in any higher orders (m = ±2, ±3, etc.), if such orders are present, is also minimized. Because of its simplicity and low mechanical sensitivity, the phase mask technique is more preferred over point-to-point method and interferometric technique.

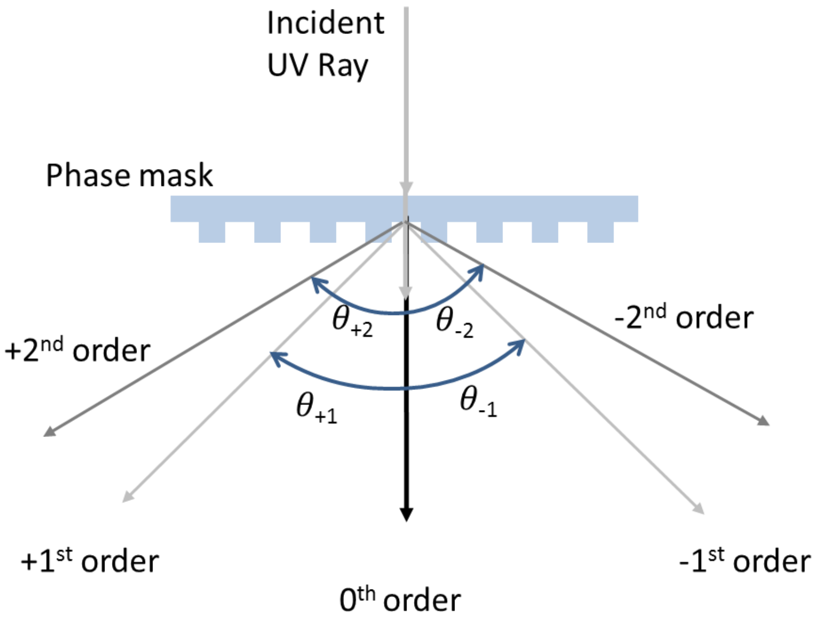

Figure 3.6: Ray diagram for +1/-1 order and +2/-2 order diffraction with angles.

3.3.3 Spectrum Growth during Inscription of FBG

The spectrum growth of FBGs during inscription has been monitored with the OSA, controlled using LabVIEW, and recorded for further analysis and characterization. The spectral growth of different FBGs is shown in Figure 3.7. The growth rate depends on the photosensitivity and nature of dopants in the fiber core, the laser pulse rate and energy, and the fiber alignment with reference to phase mask. The growth rate is further increased if the fibers are loaded with hydrogen. The transmission spectra for the four-mode FBGs have been recorded and are shown in Figure 3.7. The value of Bragg transmission loss in each resonant wavelength dip increases until the fundamental mode and other higher order modes become saturated. The reflection spectra of fabricated Bragg gratings in SMF, FMFs, and MMFs have been shown in Figure 3.8 to Figure 3.13.

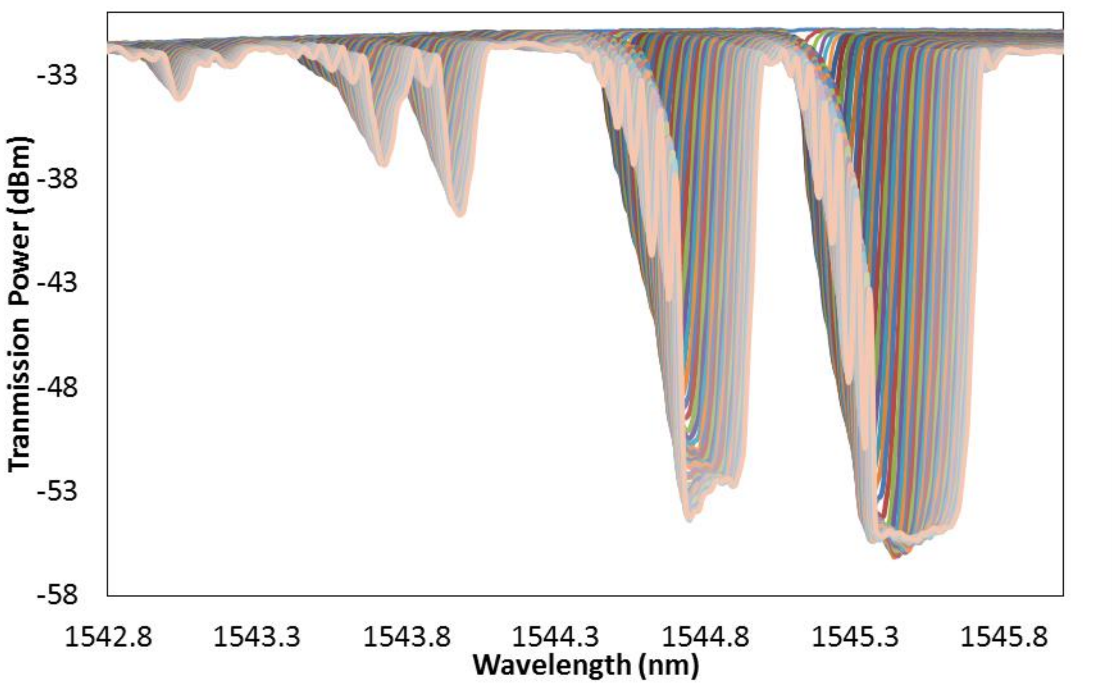

Figure 3.7: Transmission spectrum growth during inscription of FBG in 4-mode step index fiber.

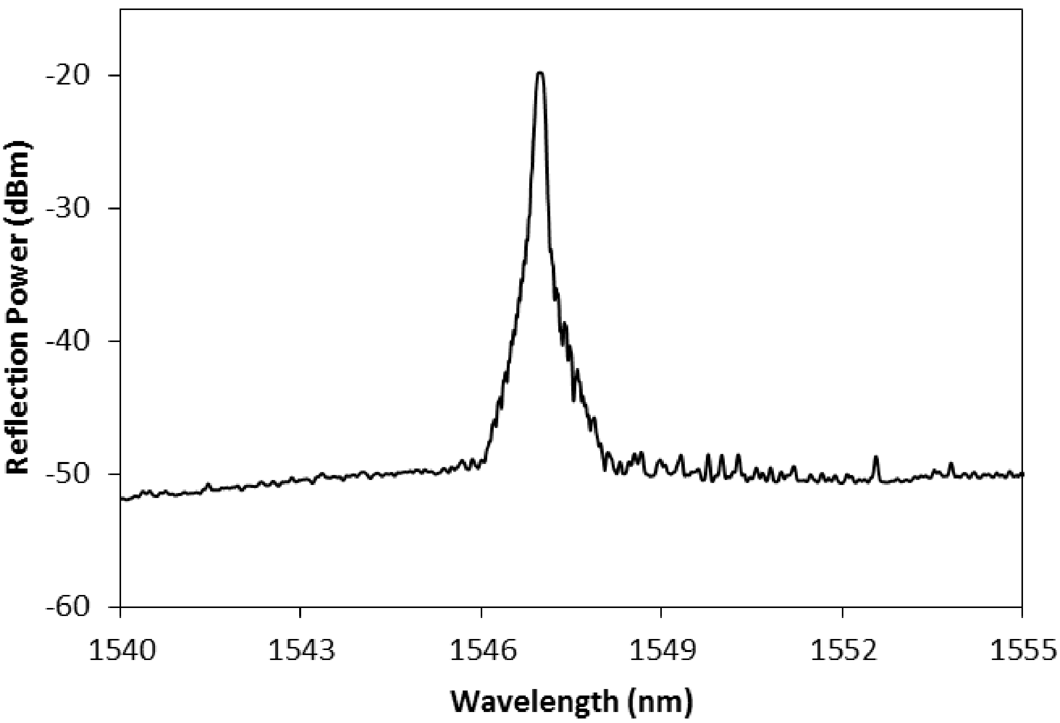

Figure 3.8: Reflection spectrum of single mode fiber (SMF) Bragg grating with grating period of 534.4 nm.

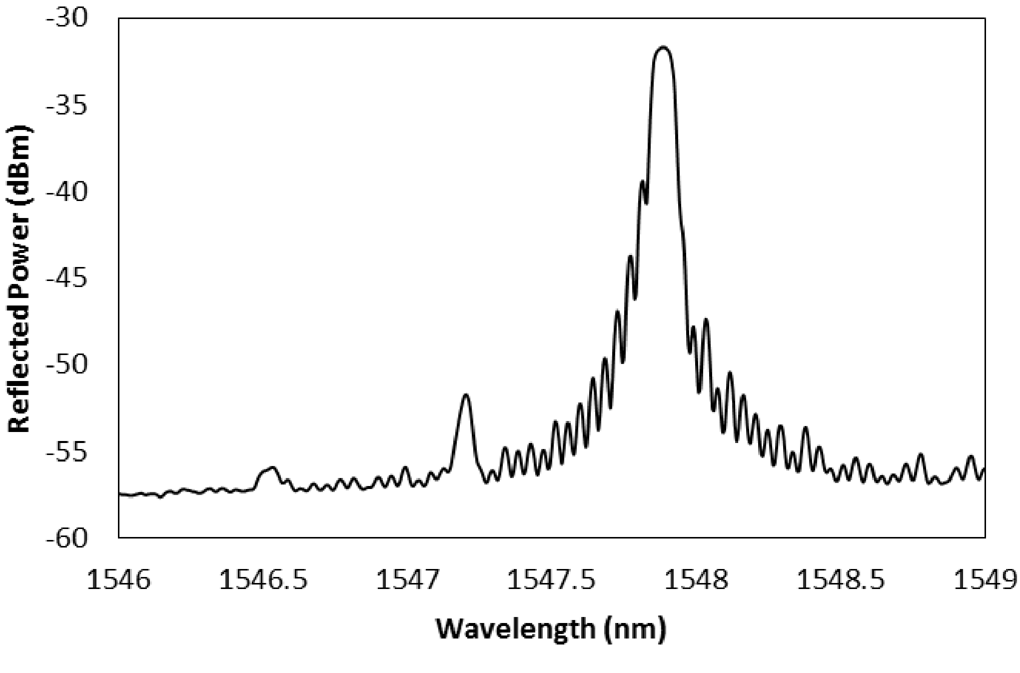

Figure 3.9: Reflection spectrum of fabricated two-mode step index fiber with core radius as 9.75 µm and grating period as 534.4 nm.

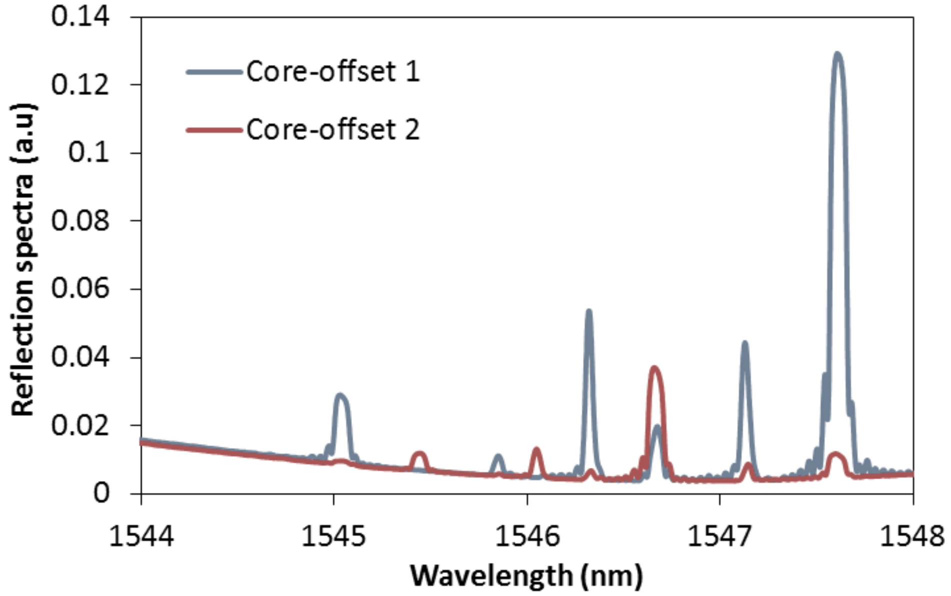

Figure 3.10: Reflection spectra obtained by core offset of four-mode step index FBG with core radius of 12.5 µm and grating period of 534.4 nm.

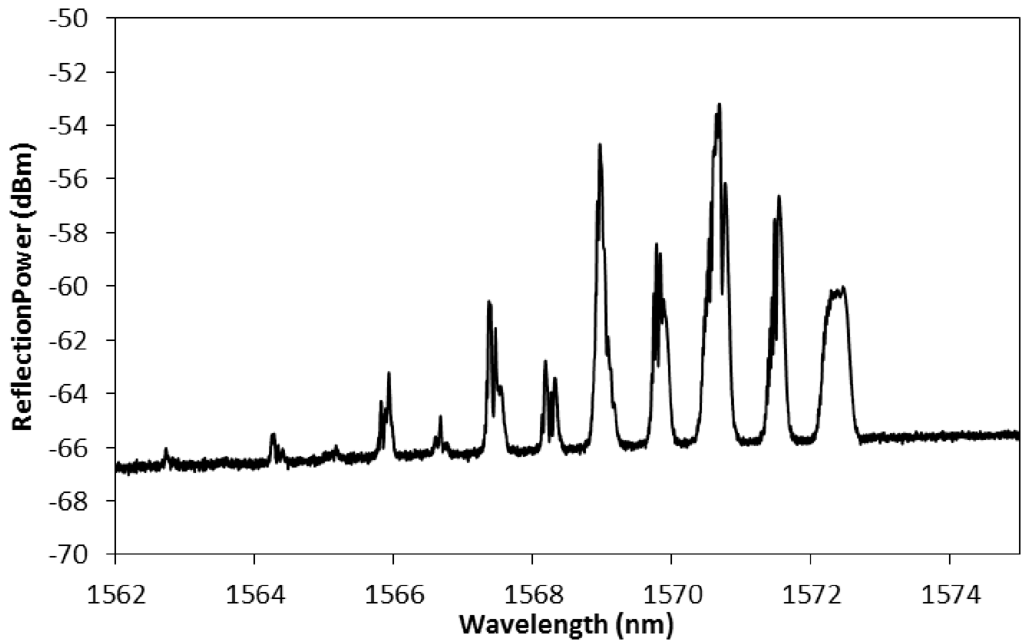

Figure 3.11: Reflection spectrum of fabricated Graded index (GI) multimode fiber (MMF) with core radius of 62.5 ± 2.5 µm and grating period of 534.4 nm.

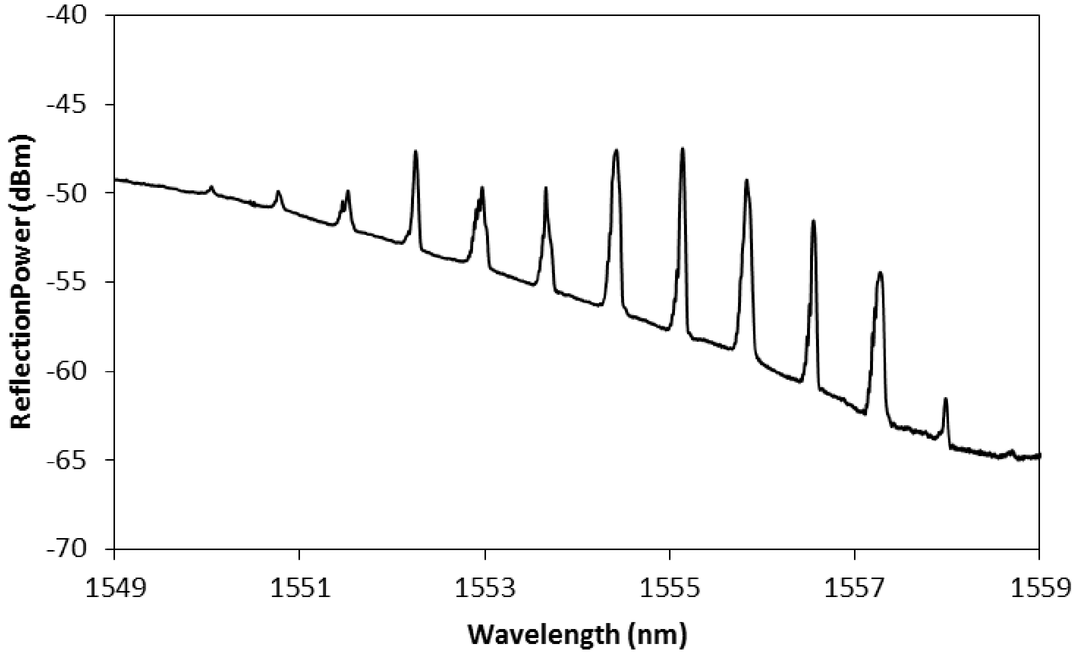

Figure 3.12: Reflection spectrum of fabricated step index (SI) multimode fiber (MMF) Bragg grating with core radius of 50 μm and grating period of 534.4 nm.

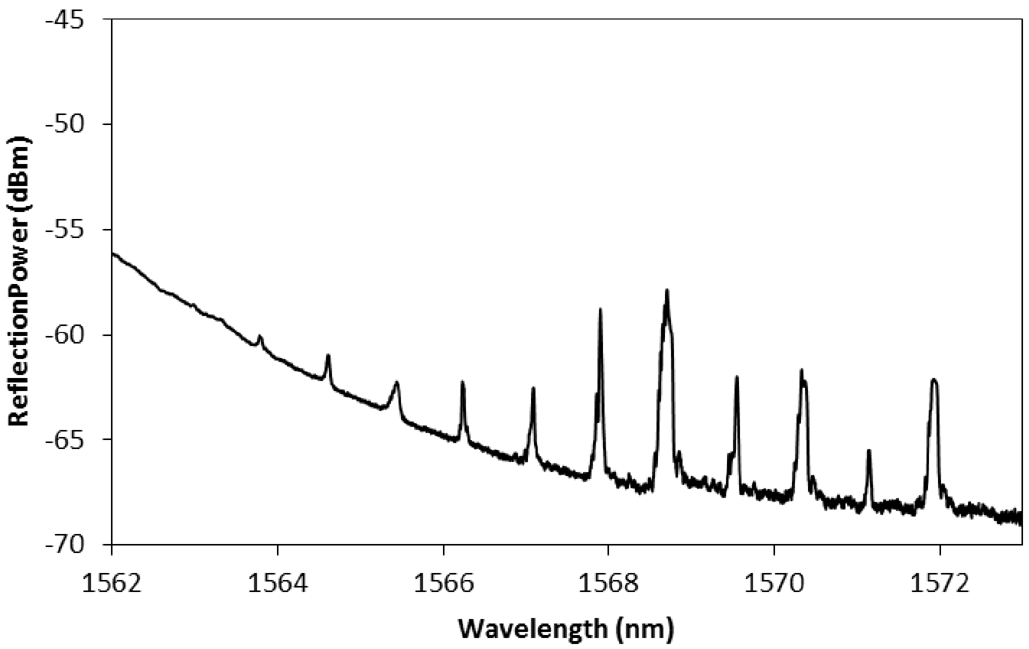

Figure 3.13: Reflection spectrum of fabricated step index (SI) multimode fiber (MMF) Bragg grating with core radius of 62.5 μm and grating period of 534.4 nm.

3.4 Bragg Wavelength Stabilization after Inscription of FBG

The inscription of FBGs involves the "excitation" of the optical fiber material (i.e., glass) to a metastable state, such as when the electron is displaced to a trapping site or a structural change is quenched into the glass as a result of UV illumination. The decay of the electron states is caused by the thermal variations, which depicts that the UV-induced defects inside the fiber core are not thermodynamically stable. Therefore, some sites that can reverse their states resulting in a decay of refractive index exist, as shown in Figure 3.14 (a). Treatment for such sites should be given so that the activation energy barrier becomes large enough to avoid decay as illustrated in Figure 3.14 (b). The activation energies of different defect sites during grating formation can be defined in the order of $E_{a1} < E_{a2} < E_{a3}$. The defects may possibly return to low energy states by decaying the energy, that is, when it overcomes the activation energy barrier caused by thermal effect. When a defect overcomes its activation energy barrier with thermal assistance, the contribution of the site to the refractive index modulation (Δn) is lost and grating decay occurs. The defect sites with less activation energy (i.e., E_{a1}) decay faster than those with high activation energies (i.e., E_{a3}). The presence of residual hydrogen in regions unexposed to UV can cause instability; therefore, the FBGs are thermally treated by annealing them in an oven at 80 °C for 10 hours to remove the residual hydrogen and become more stable. A blue spectral shift has been observed at approximately 1 nm, and reflectivity has been found to decrease by approximately 3 dB. If FBGs are to be used in ultrahigh temperature applications, the gratings need to be regenerated or reborn by thermally annealing them at higher temperatures. In this way, the reflectivity decreases and at a certain temperature rises again. A new Bragg wavelength that is more stable for use in ultrahigh temperature environment then appears.

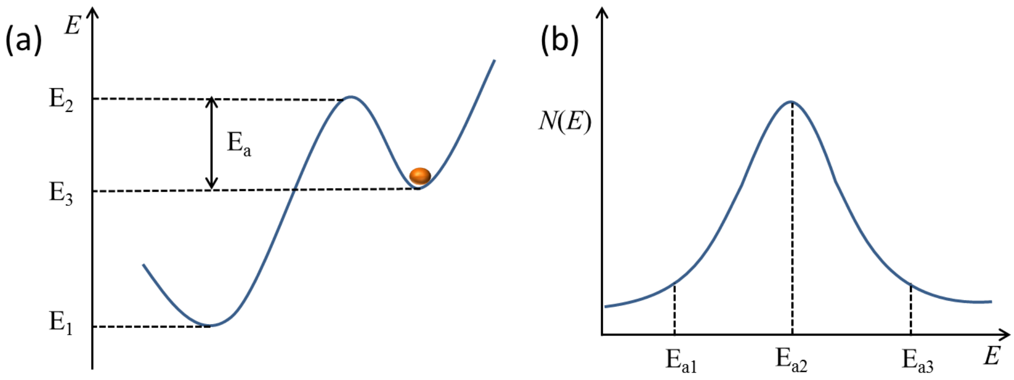

Figure 3.14: (a) Illustrative diagram of energy levels of different UV-induced defect sites and energy of activation, resulting in the refractive index modulation in FBGs; (b) the amorphous nature of the glass leads to a distribution in the UV-induced defect sites (Kannan, Guo, & Lemaire, 1997; Poumellec, 2001).

3.5 Birefringence Induced during Inscription of FBGs

During exposure, the absorption of the UV-light on the side of the fiber results in an asymmetric index change profile in the photosensitive areas. Considering the illumination along the x-axis and in the absence of saturation for all fibers, the refractive index change is assumed to present an exponential decay across the photosensitive area of the fibers. The optical fiber usually has circularly symmetric refractive index profiles before UV illumination e.g., for step index optical fiber, it can be written as

$$n^2(x,y) = \begin{cases} {n_1}^2 & for\ 0 \le r < a \\ {n_2}^2 = {n_1}^2 - \Delta n^2 & for\ a < r < R \end{cases} \qquad \textbf{(3-3)}$$

where $r = \sqrt{x^2 + y^2}$, and (x, y) are the Cartesian coordinates in the plane of cross section of optical fiber. The region for the range of $0 \le r < a$ represents the core of the optical fiber whereas the region for the range of $a < r < R$ represents the cladding of the optical fiber and $\Delta n^2 = {n_1}^2 - {n_2}^2$. Such refractive index profile is realized by homogeneous Ge doping of the core of the optical fiber. As a result, the fiber core is assumed with homogeneous photosensitivity and no photosensitivity of the cladding. When the optical fiber is illuminated by UV laser beam from two sides, then the refractive index profile can be modeled as,

$$n_{UV}{}^2(x,y) = n^2(x,y) + \delta n_R{}^2(x,y) + \delta n_L{}^2(x,y) \qquad \textbf{(3-4)}$$

where the terms $\delta n_R{}^2(x,y)$ and $\delta n_L{}^2(x,y)$ represent the refractive index change in the profile induced from the right side and the left side of UV illuminations. The change in refractive index profile is exponential in nature if the fiber is illuminated from one direction. The mathematical form is given as

$$\delta n_{\substack{R\\L}}{}^2(x,y) = \begin{cases} A_{\substack{R\\L}}{}^2 \quad e^{\left\{-2\alpha\left(\pm x+\sqrt{a^2-y^2}\right)\right\}} & for\ 0 \leq r < a \\ 0 & for\ a < r < R \end{cases} \qquad \textbf{(3-5)}$$

where A is the maximum change in refractive index profile caused by UV illumination, and 2α is the power attenuation constant of the UV laser light for fiber medium. If fiber is illuminated by UV laser from the right-hand side, then $\delta n_L = 0$, the refractive index profile will not be symmetric, and the birefringence inside the core of fiber is formed. Birefringence is the optical property of the guiding medium, which depends on the polarization and propagation direction of light. Consequently, for a given LP mode, different polarization states of the modes are coupled with each other and this phenomenon is considered as self-mode coupling whereas the coupling of two different LP modes is stated as cross-mode coupling. The illustration of asymmetric refractive index profile and birefringence with respect to exposure time are shown in Figure 3.15 (a) and (b), respectively. Atomic force microscopy (AFM) was used to observe the asymmetry of refractive index profile in (Inniss et al., 1994), and Vengsarkar *et al.* found that the UV-induced birefringence can be reduced by two-side illumination of the fiber (Vengsarkar, Zhong, et al., 1994). Various numerical methods have been presented for calculating the birefringence (Belhadj, LaRochelle, & Dossou, 2004; Renner, 2001).

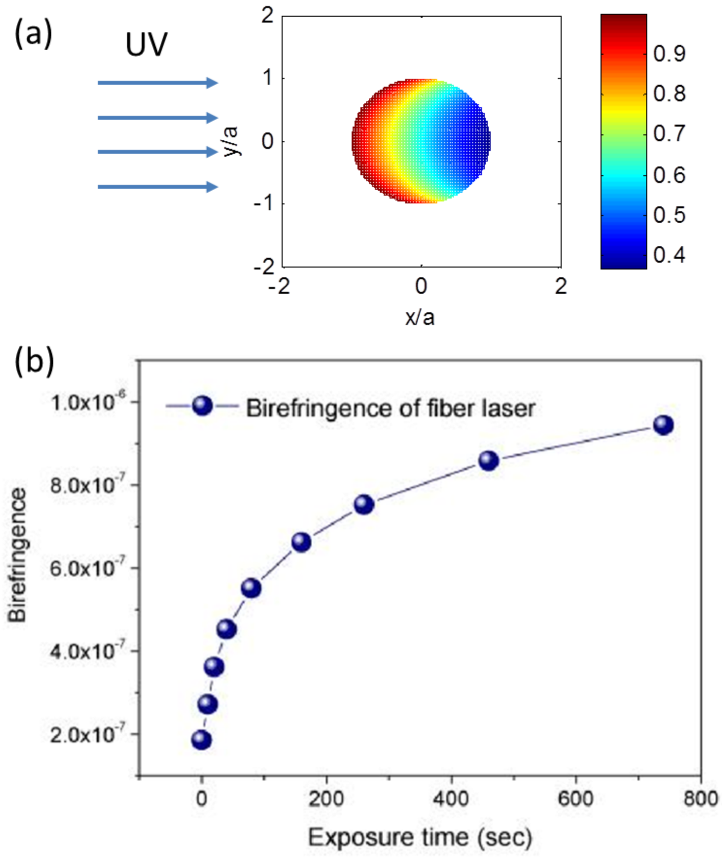

Figure 3.15: (a) Illustration of UV-induced asymmetric refractive index profile with multiplication factor of 10^{-4}; (b) birefringence induced in fiber core through UV laser-side illumination (T. Guo et al., 2011).

3.6 Tuning Grating Period by Writing Grating on Pre-strained Fibers

The B-Ge co-doped optical fiber has been used for the fabrication of FBG with specifications given in Figure 3.16 (a). For the fabrication of FBG on H_2-loaded fiber, one end of the fiber was fixed and tensile stress was applied on the other end as shown in Figure 3.16 (b). The figure shows that the fiber is elongated along its axial axis.

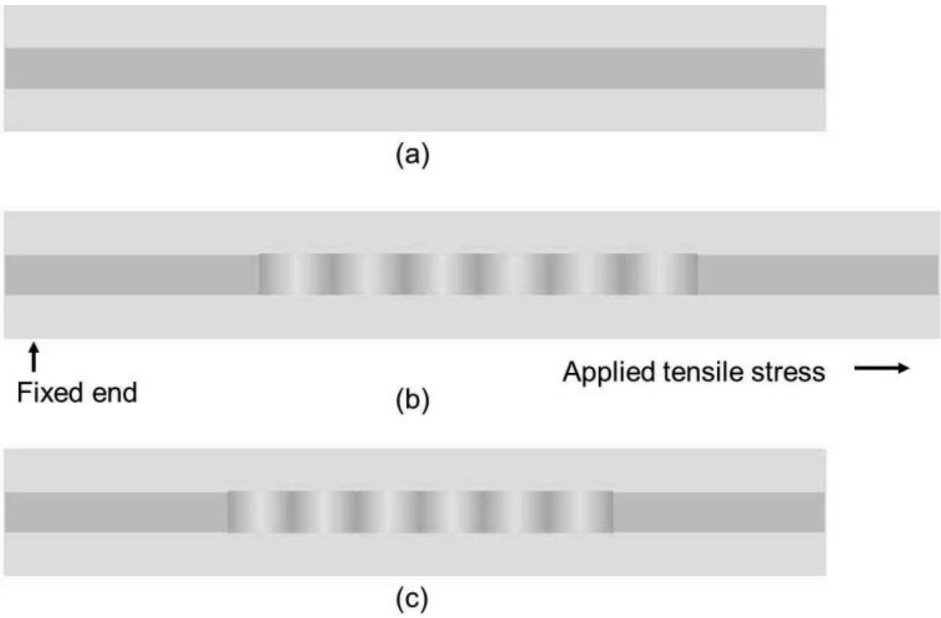

Figure 3.16: (a) A photosensitive fiber PS1250/1500 (Fibercore Ltd) with the specifications as: fiber diameter of 125.3 µm, core-cladding index contrast of 0.5%, 10 mol% of GeO_2, and 14–18 mol% of B_2O_3; (b) Writing an FBG on pre-strained fiber by using phase mask technique. (c) When the stress is removed, the grating period is reduced (Ali et al., 2013).

The FBG structure was inscribed into the fiber core by a CW UV laser at 244 nm with an average output power of 4 mW using phase mask technique where phase mask period was 1072.6 nm. A Bragg reflectivity of 99.97% is obtained at 1552 nm. The transmission and reflection spectra were measured using an OSA at the resolution of 0.05 nm. Transmission loss of 0.4 dB was observed at the Bragg wavelength after the fiber was exposed to 244 nm laser irradiation for a total fluence of 17 J/cm². Afterward, the applied stress was removed and the grating structure was contracted in the axial dimension. As a result, variations occur in the Bragg wavelength λ_B, grating period Λ, and in effective refractive index n_{eff}. Their relationship is given by,

$$\frac{\Delta\lambda}{\lambda_B} = \frac{\Delta n}{n_{eff}} + \frac{\Delta\Lambda}{\Lambda} \quad \textbf{(3-6)}$$

The notation Δ denotes the change of the respective parameter. The linear relationship between wavelength shift and axial strain $\Delta\Lambda/\Lambda$ is given by,

$$\frac{\Delta\lambda}{\lambda_B} = \eta \frac{\Delta\Lambda}{\Lambda} \qquad \textbf{(3-7)}$$

where η is constant and $\eta \epsilon\ [0.74, 0.78]$.

Considering the low UV fluence on the fiber, the change of stress profile and amplitude can be neglected, whereas the change of refractive index is dominated by color-center effect. The Bragg wavelength of the grating red-shifted during grating inscription, confirming that Type-I grating was formed.

3.6.1 Optical Imaging Technique for Grating Period Measurement

Optical imaging technique is a direct approach for the measurement of grating period. The accuracy of the measurement relies on the quality of the images taken and on the image processing algorithm technique. In this work, a Zeiss Axioplan DIC microscope equipped with a 10MP CCD camera is used to capture high-resolution digital images of grating structures. The magnification factor of the DIC microscope lens was set at $50\times$. The dimension of the image is $H \times W \equiv 2716 \times 3664$ pixels, and the spatial resolution of the image is 31.98 nm/pixel.

To calculate the period of pre-strained FBGs, the image processing algorithm is implemented:

i. A clear image of the grating structure in the horizontal orientation is captured. The pixel intensities $I(x, y)$ can be described in an $H \times W$ matrix,

$$I(x,y) = \begin{bmatrix} i_{0,0} & i_{0,1} & \cdots & i_{0,k} & \cdots & i_{0,k+L-1} & \cdots & i_{0,W-1} \\ i_{1,0} & i_{1,1} & \cdots & i_{1,k} & \cdots & i_{1,k+L-1} & \cdots & i_{1,W-1} \\ \vdots & \vdots & \ddots & \vdots & \ddots & \vdots & \ddots & \vdots \\ i_{j,0} & i_{j,1} & \cdots & i_{j,k} & \cdots & i_{j,k+L-1} & \cdots & i_{j,W-1} \\ \vdots & \vdots & \ddots & \vdots & \ddots & \vdots & \ddots & \vdots \\ i_{j+M-1,0} & i_{j+M-1,1} & \cdots & i_{j+M-1,k} & \cdots & i_{j+M-1,k+L-1} & \cdots & i_{j+M-1,W-1} \\ \vdots & \vdots & \ddots & \vdots & \ddots & \vdots & \ddots & \vdots \\ i_{H-1,0} & i_{H-1,1} & \cdots & i_{H-1,k} & \cdots & i_{H-1,k+L-1} & \cdots & i_{H-1,W-1} \end{bmatrix} \quad \textbf{(3-8)}$$

where spatial coordinates (x, y) represent the rows and columns of the image pixels.

ii. The grating profile can be obtained from the pixel intensities in the fiber core region. To improve the quality of the grating profile, a sample image with size $M \times W$ $(M > 1)$ is taken from (j)th row to $(j + M - 1)$th row. A smooth sinusoidal grating profile is produced by calculating the average M pixel intensities in every column of the sample image, which is given by

$$P(j,k) = \frac{1}{M} \sum_{l=j}^{j+M-1} i_{l,k} \quad \textbf{(3-9)}$$

where $j \in [0, H - M]$ and $k \in [0, W - 1]$

iii. The noise of grating profile can be filtered by passing the profile through a row-wise moving average filter, the size of L is given by

$$\tilde{P}(j,k) = \frac{1}{L} \sum_{m=k}^{k+L-1} P(j,m) \quad \textbf{(3-10)}$$

where $j \in [0, H - M]$ and $m \in [0, H - L]$.

Figure 3.17 illustrates the periodic grating structure and the filtered grating profile. The filter size L is kept below 33.6 [1076 (grating period) / 31.98nm/pixel (spatial resolution) = 33.6]; otherwise, the frequency component of the grating period will be filtered out or attenuated by the moving average filter.

iv. A better estimation of the period can be achieved by taking the average period from a bulk grating length with a large number of periods to overcome the error introduced by the image spatial resolution of 31.98 nm/pixel. The standard deviation of the calculation is used as an indicator for the estimation.

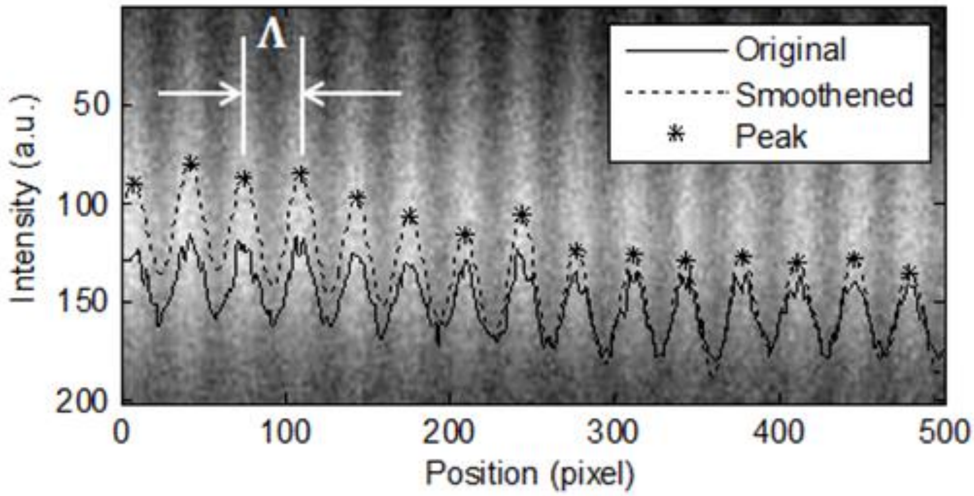

Figure 3.17: The fabricated grating structure image acquired by DIC microscope with a clear visibility of the fringes. The sample size used to plot the grating profile (original) from the sample image was M=15. A moving average filter with the size of 13 was used to make smoothened grating profile. The grating period Λ space between two nearby peaks (*) of the grating profile (Ali et al., 2013).

v. Procedures ii-iv are repeated vertically across the entire microscope image. The calculated average of the peak-to-peak spacing with low standard deviations provides the optimal estimation for the measurement. The grating period Λ is estimated by taking the sample mean and sample standard deviation calculated from the 10 optimal sets of data.

3.6.2 Algorithm Implementation for Grating Period Measurement

Figure 3.18 (a) shows a microscope image of a grating structure. The periodic fringes are clearly shown in the enlarged image in the inset. From the digital pixel intensity, the sinusoidal profile of the grating structure is obtained and the spacing between two adjacent peaks corresponds to a grating period. Figure 3.18 (b) shows that the curve of standard deviation corresponds to the vertical spatial position of the image in Figure 3.18 (a) based on the aforementioned procedures i—v in Section 3. The estimated grating period in the region with low-standard deviation is approximate to the actual one. The dot distribution map in Figure 3.18 (c) provides an alternative way to interpret the relationship between estimated grating periods against its standard deviation. Most of the data are scattered within the vicinity of 1000 nm and bounded between 1×10^5 and 2×10^5 in standard deviation. The calculated grating periods with the smallest standard deviation enclosed in a red box in the figure provide the nearest estimation to the actual grating period.

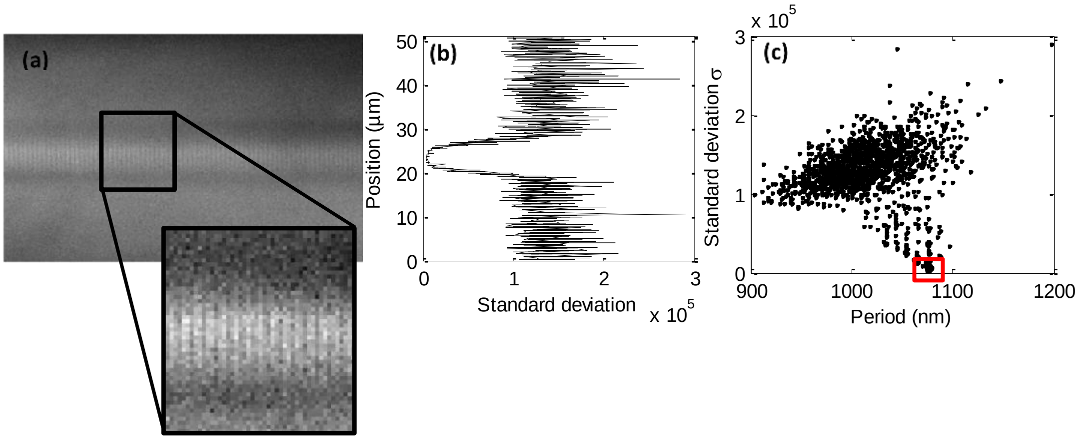

Figure 3.18: (a) The image of FBG structure acquired by DIC microscope showing the clear dark and bright regions perpendicular to fiber core axis. The inset indicates the enlarged image of the grating structure from the core region of the fiber. (b) The graph of standard deviation calculated from the corresponding intensity profile. (c) Dot distribution map of standard deviation against grating period. The red box marks the data with smallest standard deviation (Ali et al., 2013).

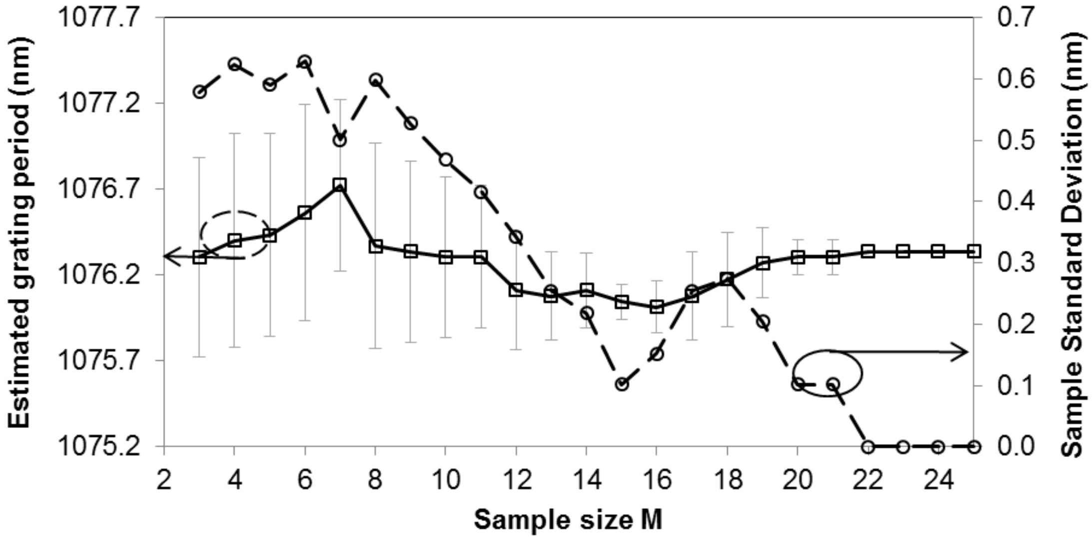

Figure 3.19: Graphical interpretation of calculated grating period with respect to the sample size M. The error bar (sample standard deviation) decreases with increasing sample size M (Ali et al., 2013).

The sample size M is an important parameter that influences the accuracy of the estimation. As shown in Figure 3.19, the sample deviation decreases with increasing sample size and eventually approaches zero when the size is larger than 21. Moreover, the estimated grating period fluctuates between 1076.70 and 1076.00 nm. The estimation converges to 1076.34 nm when M > 21. This clearly shows that larger sample size helps improve the SNR of the grating period and reduces the uncertainty in the estimation of grating period. The rate of the convergence relies on the image quality and orientation of the grating structure in the image. In the investigation, the microscope image of the grating structure at different angles in the range of [–3.5°, 3.5°] are taken and processed for grating period measurement. Figure 3.20 shows the measurement performance for different rotational angle θ of the fiber longitudinal axis with respect to the image horizontal axis. The estimated grating period increases with increasing rotation angle in both positive and negative directions. The variation is in agreement with the function Λ/cos θ. The general trend of the standard deviation can be described by the shaded region in the figure. The result indicates that the minimum uncertainty ± 0.36 nm (sample standard deviation) occurs at θ=0˚ where the longitudinal axis of the FBG is parallel with the horizontal axis of the image. The uncertainty is higher when the magnitude of rotation angle is larger, and the uncertainty is ±1.39 nm at θ=3.5°. This finding indicates the necessity to ensure that the grating structure is parallel with the horizontal axis of the image for the grating period measurement.

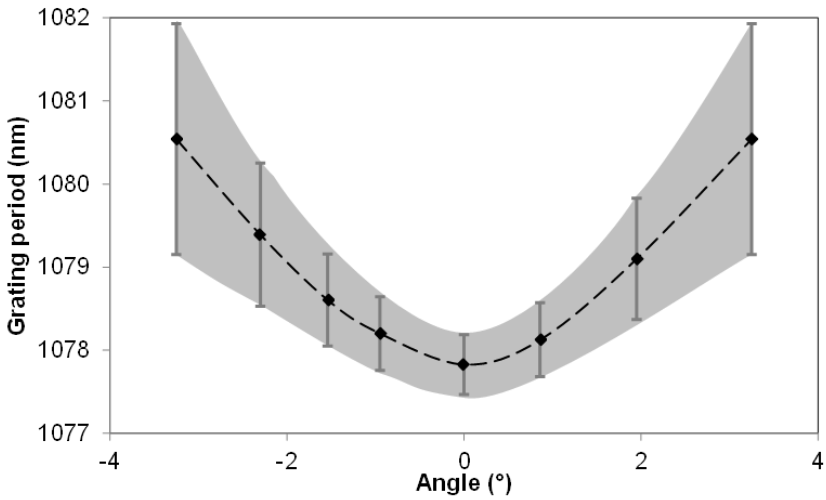

Figure 3.20: The effect of the rotation angle of fiber core axis θ in degrees on the period of fiber Bragg gratings Λ. The shaded region is bounded by the measured standard deviation of the results acquired at the sample size of 10 (Ali et al., 2013).

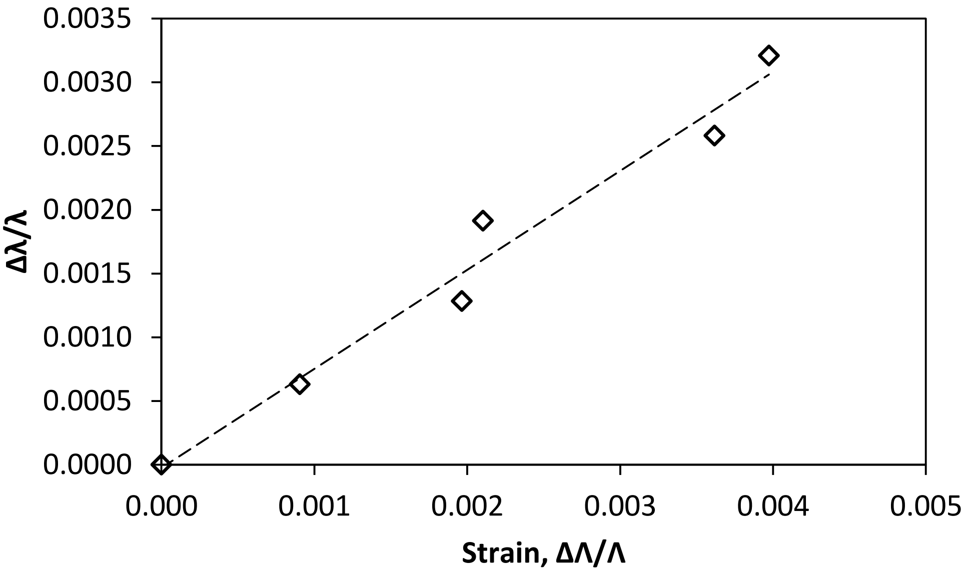

Figure 3.21: The graph illustrating the relation of fractional Bragg wavelength shift Δλ/λ with respect to the strain ΔΛ/Λ (Ali et al., 2013).

Figure 3.21 shows the relationship between the fractional Bragg wavelength shift and the applied axial strain $\Delta\Lambda/\Lambda$ on the FBG. The measured slope of the graph is 0.776 with a linear correlation coefficient of 0.98. Based on the expression in equations (3-6) and (3-7), the linear slope between $\Delta n/n_{eff}$ and strain is −0.224, which is the typical strain-optic coefficient for the SMF-28 fiber. This result indicates that the proposed technique is in complete agreement with the literature and is accurate for the measurement of FBG period [13].

The grating period of FM-FBG has also been measured using the optical imaging technique. The cross sectional images and sample grating images are shown in Figure 3.22 and Figure 3.23, respectively. The calculated period is verified with the phase mask period.

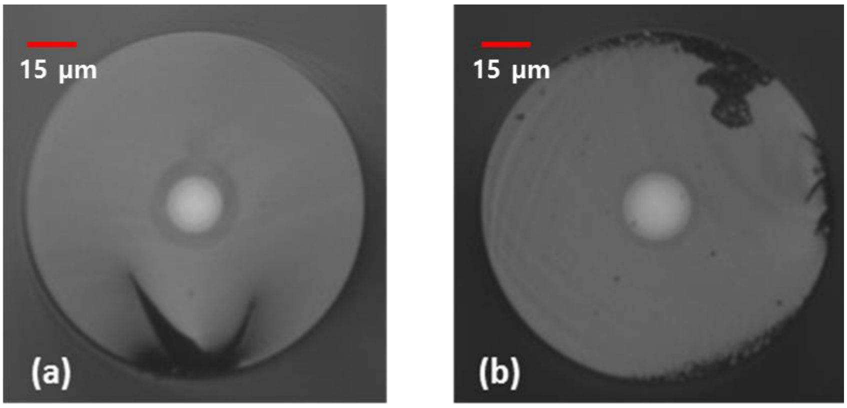

Figure 3.22: Cross-sectional optical images of two-mode and four-mode fibers.

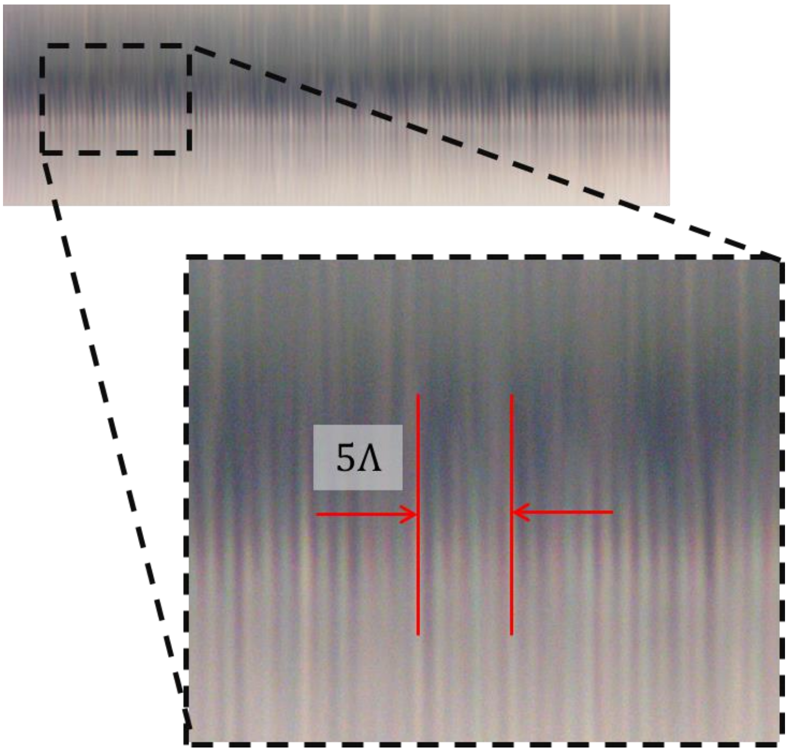

Figure 3.23: Optical image showing the grating region inside the core of two-mode step index fiber. The inset indicates the enlarged image of the grating structure from the core region of the fiber. 5Λ represents the total length of five grating fringes, each with a period of Λ.

3.7 Numerical Simulations for FMFs and FM-FBGs

The numerical simulations for the detailed analysis of FMFs and FM-FBGs are discussed in this section.

3.7.1 The Intensity Profile of LP Modes Guided by FMF

The intensity profiles of the linearly polarized modes supported by FMF have been plotted by MATLAB using the modal field equations presented in Chapter 2 as shown in Figure 3.24 to Figure 3.31. To better illustrate the three ways of representing the modes, 3D, contour, and 2D were used. The values of core refractive and cladding refractive index used to plot the mode intensity profiles are 1.4483 and 1.4433, respectively. These values have been chosen by keeping the core-cladding refractive contrast value at 5×10^{-3}, which has been provided by the manufacturer of FMF (OFS, Denmark). In addition, the core and cladding radii are 9.75 and 125 µm, respectively.

The LP_{01} has a beam profile-like Gaussian shape and signal power is focused at the center. The intensity profiles of LP_{11a} and LP_{11b} modes with x- and y-polarization have been plotted in Figure 3.25 and Figure 3.26, respectively. However if the polarization modes LP_{11a} and LP_{11b} are combined, the mode intensity profile assumes a doughnut-like shape shown in Figure 3.27. Furthermore, this research focuses on the spatial modes instead of the mode polarizations; therefore, the LP_{11} mode is used in the succeeding chapters. Similarly the LP_{21} mode also has x- and y-polarized modes at LP_{21a} and LP_{21b} as shown in Figure 3.28 and Figure 3.29, respectively. If these modes are combined, the net LP_{21} mode will assume a doughnut shape shown in Figure 3.30, the only difference of this mode to that of LP_{11} mode is the thickness of the doughnut ring, which is clearly seen in the contours and 2D shapes of the modes.

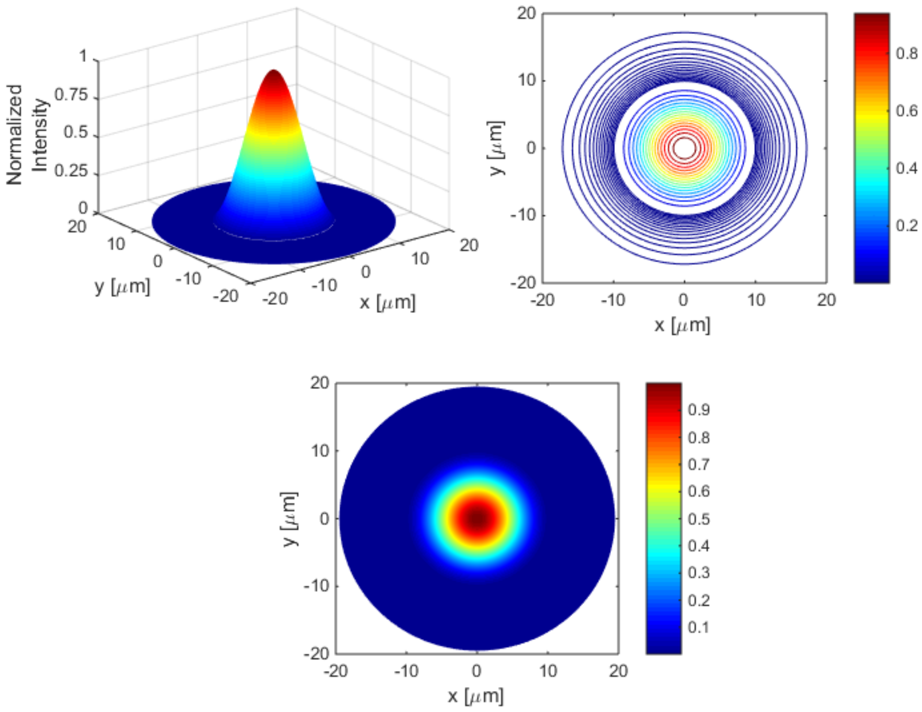

Figure 3.24: 3D, contour, and 2D simulated plots of mode intensity profile for LP_{01} mode of FMF.

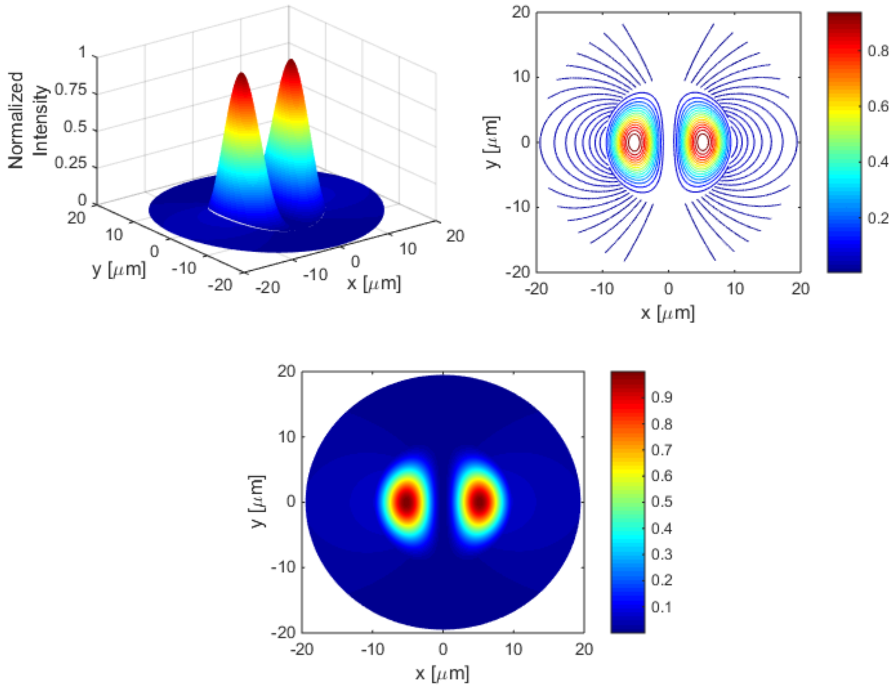

Figure 3.25: 3D, contour, and 2D simulated plots of mode intensity profile for LP_{11a} mode of FMF.

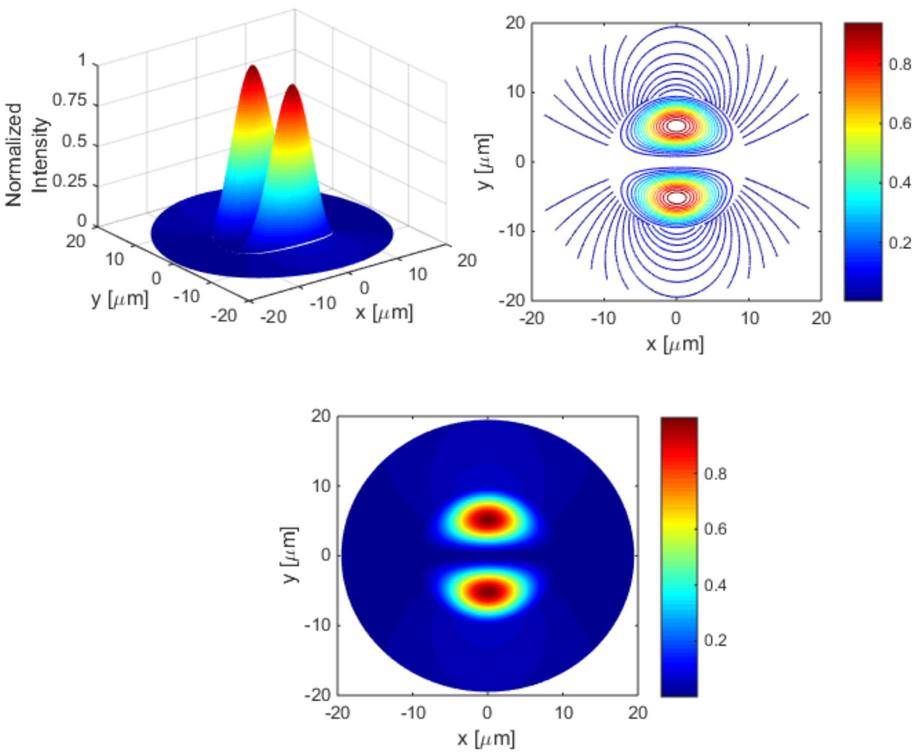

Figure 3.26: 3D, contour, and 2D simulated plots of mode intensity profile for LP_{11b} mode of FMF.

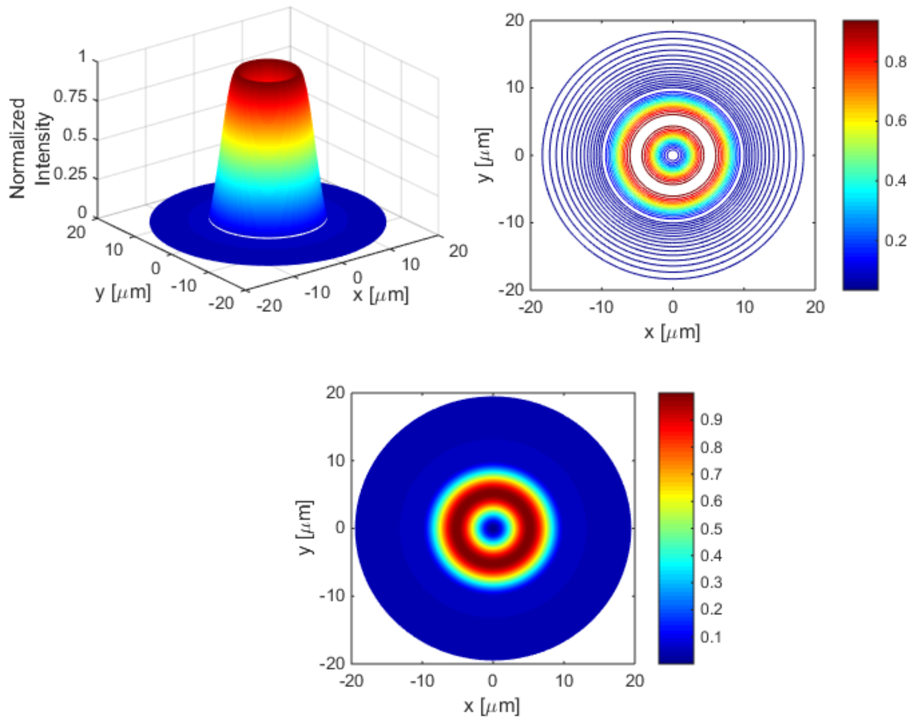

Figure 3.27: 3D, contour, and 2D simulated plots of mode intensity profile for LP_{11} mode (combination of LP_{11a} and LP_{11b} modes) of FMF.

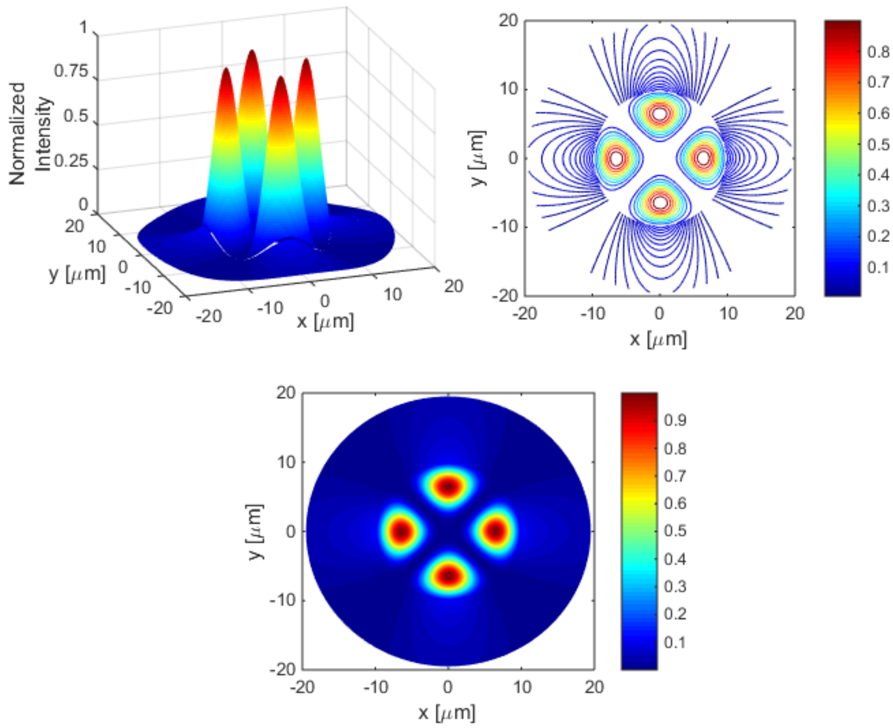

Figure 3.28: 3D, contour, and 2D simulated plots of mode intensity profile for LP_{21a} mode of FMF.

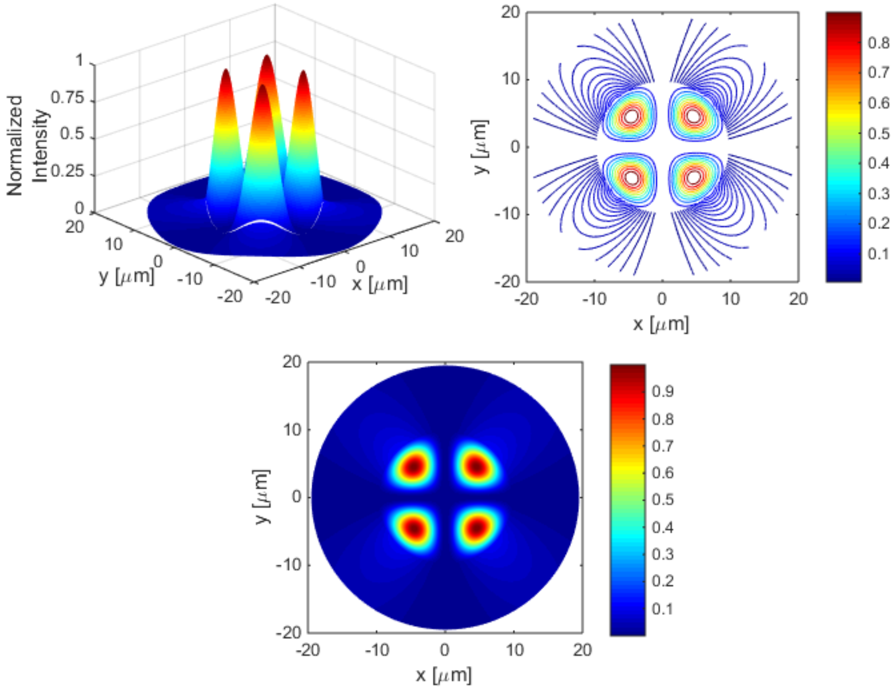

Figure 3.29: 3D, contour, and 2D simulated plots of mode intensity profile for LP_{21b} mode of FMF.

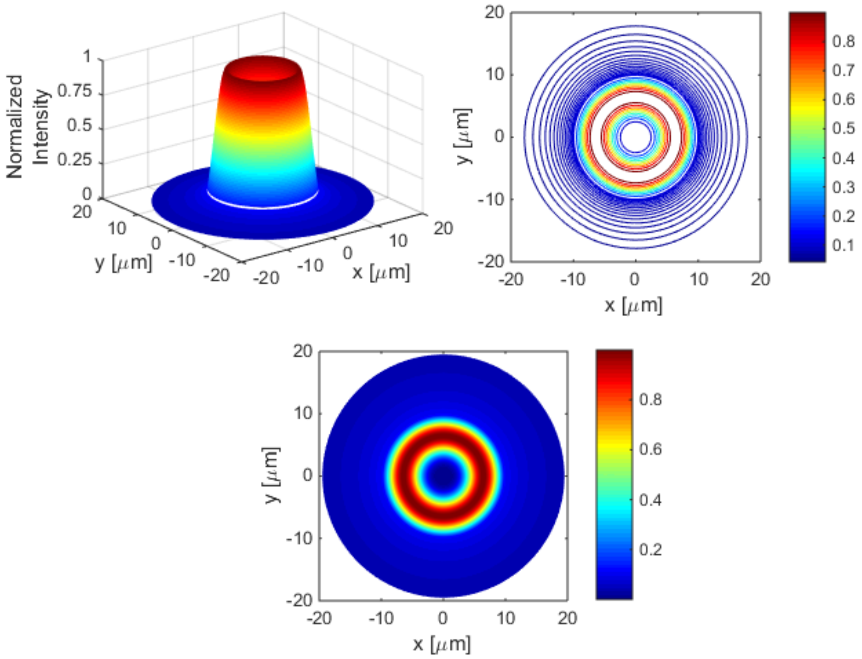

Figure 3.30: 3D, contour, and 2D simulated plots of mode intensity profile for LP_{21} mode of FMF

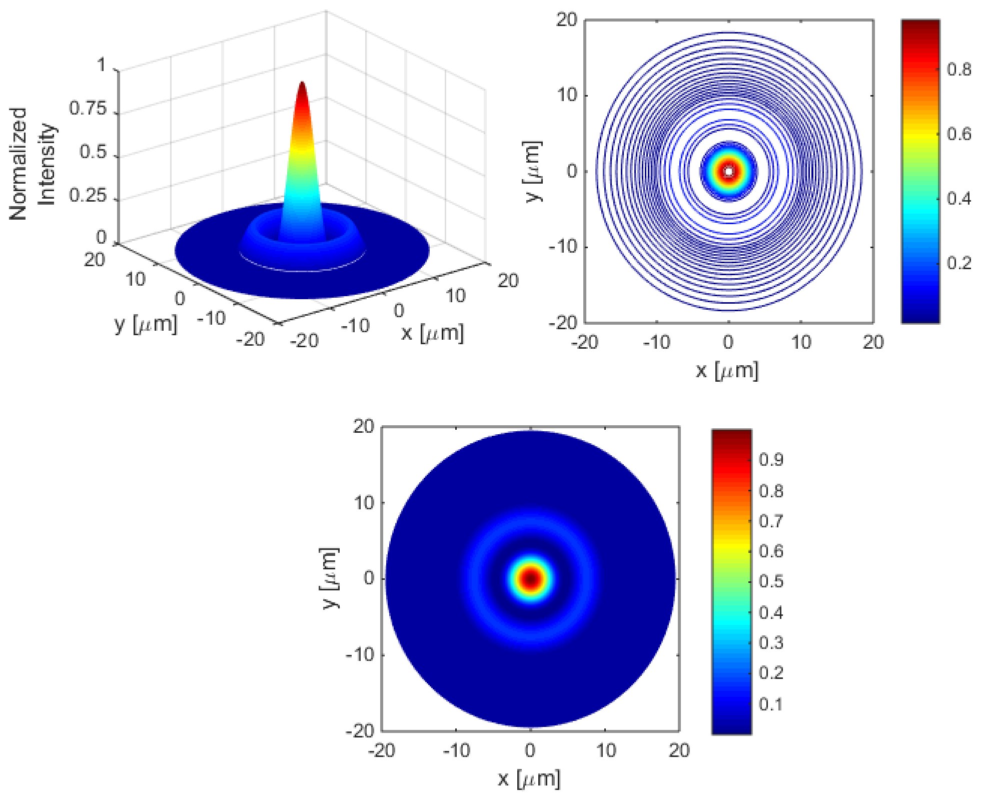

Figure 3.31: 3D, contour, and 2D simulated plots of mode intensity profile for LP_{02} mode of FMF.

3.7.2 Effective Refractive Index of LP modes and theoretical investigation of FMF Bragg Wavelengths

The effective refractive index of the modes can be calculated using mode propagation constants, which are numerically found from the characteristic equations of the optical fiber presented in Chapter 2. The effective refractive index values of the weakly guided linearly polarized (LP) modes are further used to find the Bragg wavelengths and verify the mode coupling of different modes in FBGs. For the aforementioned specifications of FMF, the numerically calculated effective refractive index values for broad and narrow wavelength range are shown in Figure 3.32 (a) and (b), respectively. The MATLAB code is given in the Appendix A.1 section.

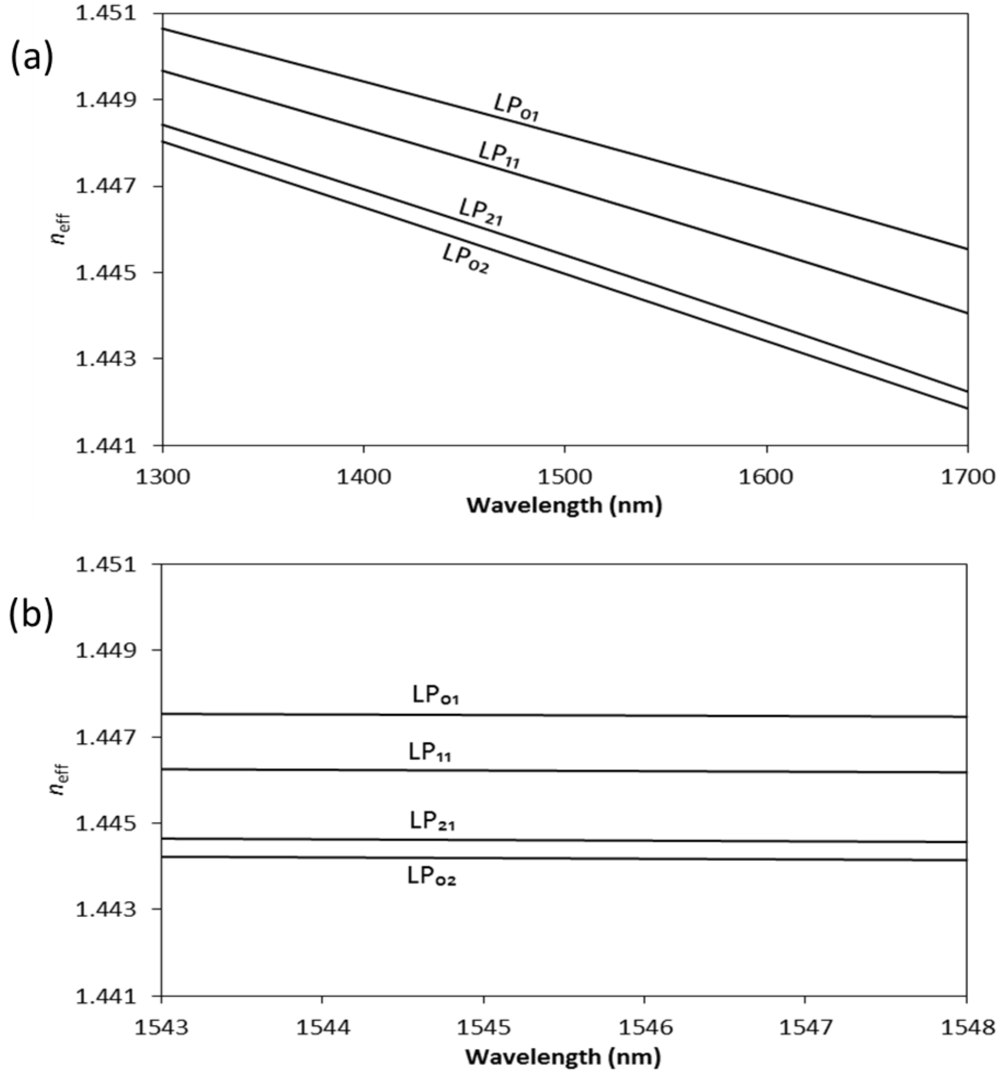

Figure 3.32: Numerically calculated values of effective refractive index of LP modes guided by FMF (a) long span of wavelength and (b) short span of wavelength.

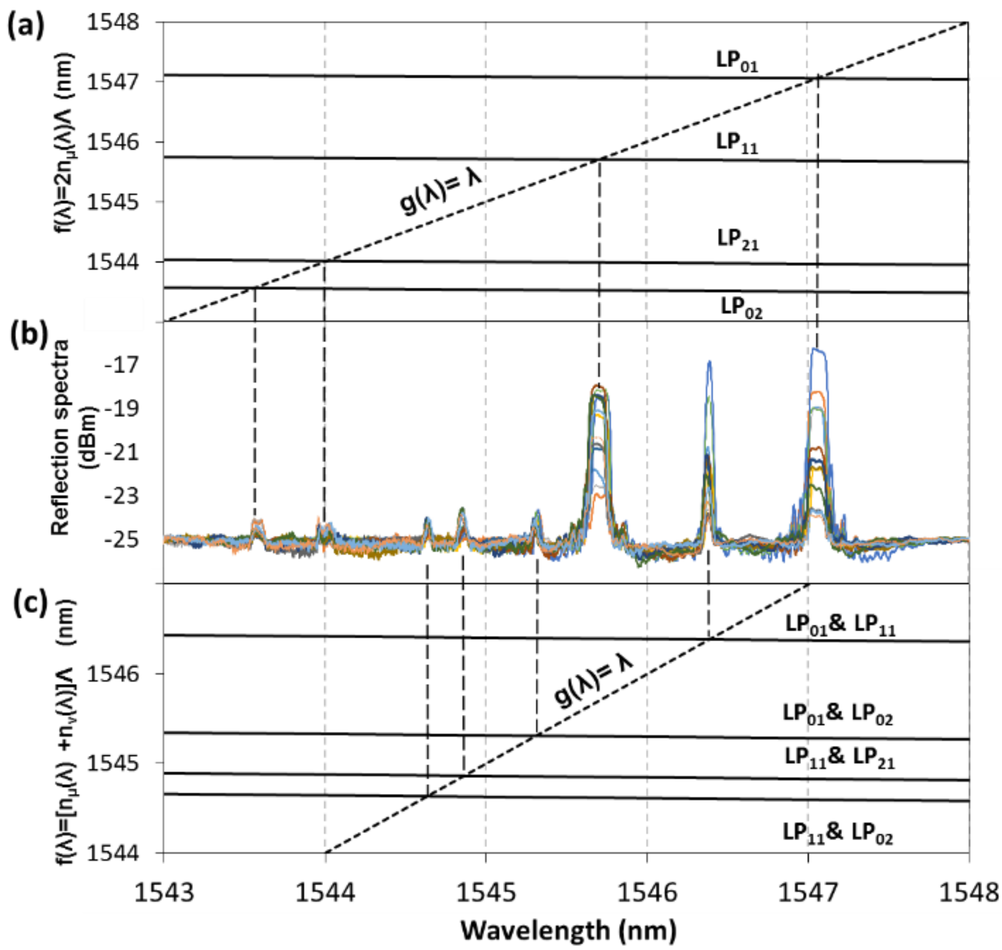

Figure 3.33: Theoretically estimated Bragg wavelengths mapped with the reflection spectra of 2M-FBG (a) Calculated curves of $f(\lambda) = 2n_{\mu}(\lambda)\Lambda$, (b) reflection spectra of the FM-FBG, and (c) calculated curves of $f(\lambda) = [n_{\mu}(\lambda) + n_{\nu}(\lambda)]\Lambda$ (K. S. Lim et al., 2014).

For the fabricated FM-FBG, considering the phase mask period Λ_{PM} = 1068.8 nm or grating period Λ = 534.4 nm, the function $f(\lambda) = 2n_{\mu}\Lambda$ for self-coupled modes and the function g (λ) = λ are defined and plotted together to determine the reflected Bragg wavelengths. Similar to the real spectrum of FM-FBG, the additional reflected Bragg wavelengths appear as a result of cross-mode coupling in FM-FBGs. For those peaks, the function $f(\lambda) = [n_{\mathrm{eff},\mu}(\lambda) + n_{\mathrm{eff},\nu}(\lambda)]\Lambda$ has been defined and plotted together to determine the cross-coupled wavelengths. The plotted functions along with the reflected spectra of FM-FBGs are shown in Figure 3.33. The multiple spectra shown in Figure 3.33 (b) have been obtained through the same FM-FBG using offset technique.

The core offset technique can be used to control the fundamental power mode and higher order modes.

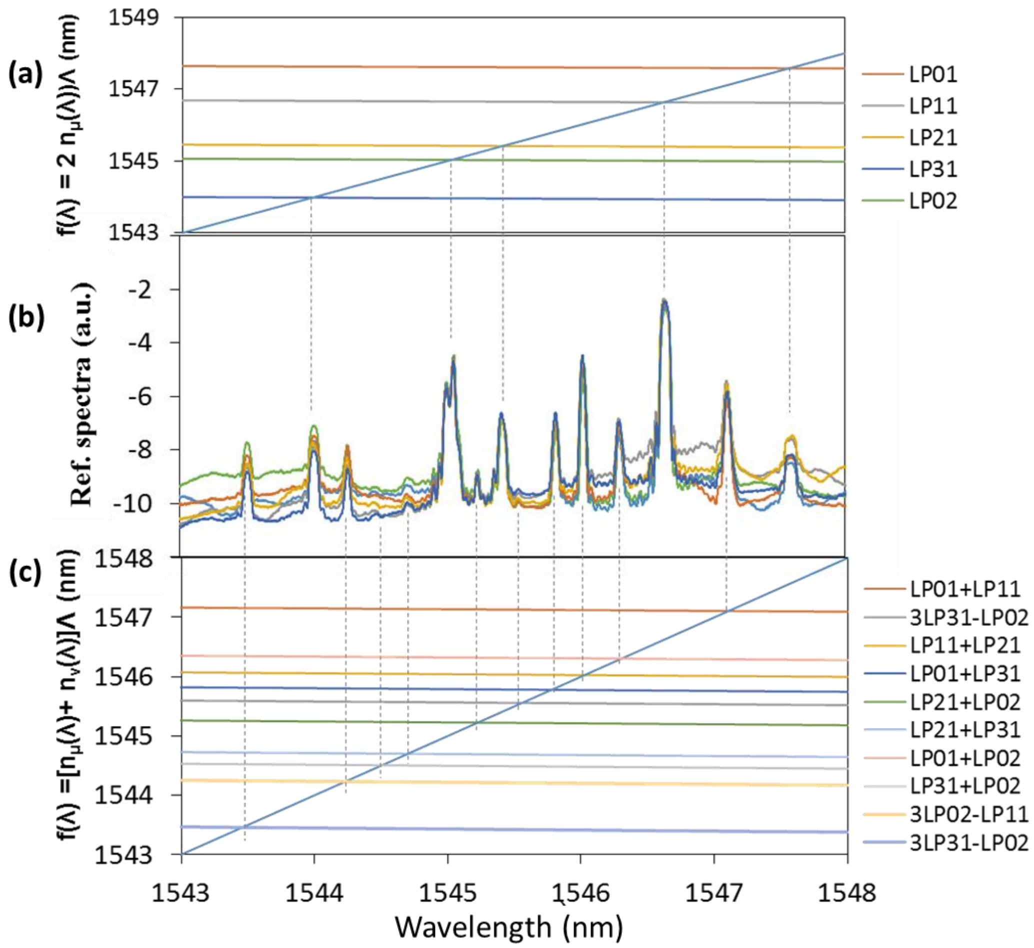

Figure 3.34: Theoretically estimated Bragg wavelengths mapped with the reflection spectra of 4M-FBG (a) Calculated curves of $f(\lambda) = 2n_{\mu}(\lambda)\Lambda$, (b) reflection spectra of the FM-FBG, and (c) calculated curves of $f(\lambda) = [n_{\mu}(\lambda) + n_{v}(\lambda)]\Lambda$.

The method for the comparison of the simulated phase matching curve f(λ) and output spectrum of the FM-FBG is similar to that of a previously reported study (Mizunami et al., 2000). Therefore, all the resonant wavelengths from the experiment can be accurately estimated from the simulation results. The simulations have been conducted using the parameters (core diameter ‘a’ and core-cladding index difference ‘Δn’) provided by the manufacturer of the FMFs (OFS, Denmark). The spacing between two adjacent resonant wavelengths will be greatly affected if the parameters used in the simulation do not agree with the actual physical parameters of the fiber. Matching the resonant wavelengths between the experimental data and simulation results would be close to impossible. Furthermore, the self-coupled and cross-coupled Bragg wavelengths for the higher order modes in the four-mode fiber have also been investigated and verified with the experimentally obtained reflection spectra shown in Figure 3.34. The different spectra were obtained by core offset of 4M-FBG.

3.7.3 Numerical Simulation of Transmission and Reflection Spectra of FM-FBG

The coupled mode equations presented in Chapter 2 are used to obtain the transmission and reflection spectra of FM-FBG. In this section, the two-mode fiber is numerically solved to obtain the spectra, and the MATLAB code is given in Appendix A.2. The peak finder code from the spectra of the fabricated FBGs is given in Appendix A.3, whereas the parameters used for the calculation are given in Table 3.3.

Table 3.3: Parameters with their values used for simulations of 2M-FBG

Parameter	Value of the parameter
Core radius (μm)	9.75
Cladding radius (μm)	62.5
Grating length (cm)	2.0
Grating period (nm)	534.4
$n_{\mathrm{eff},01}$	1.447527732
$n_{\mathrm{eff},11}$	1.446247196
Refractive index modulation (δn)	1.0×10^{-4}
Full width at half maximum (FWHM)	0.0085
Wavelength range (nm)	1544-1548

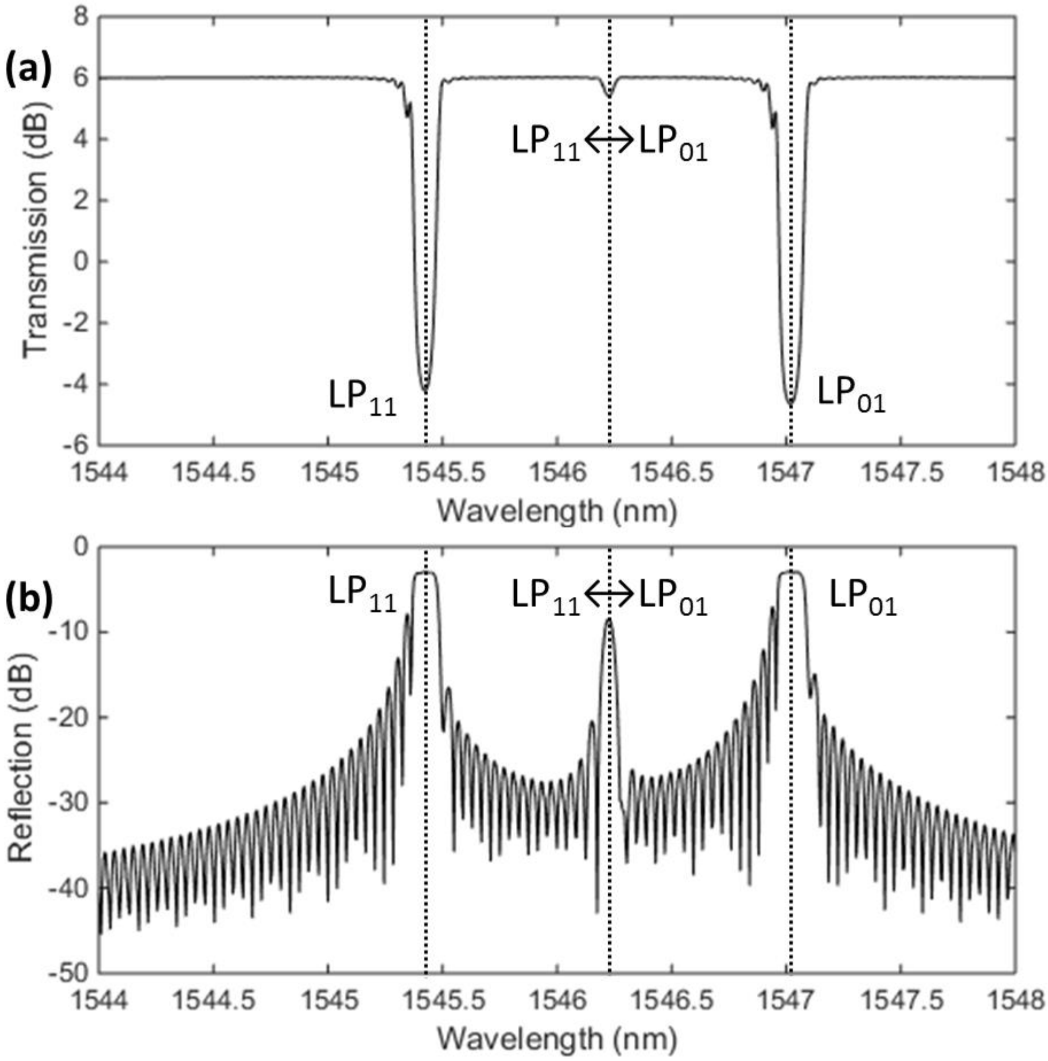

Figure 3.35: Numerical simulation of 2M-FBG. (a) Transmission spectrum and (b) reflection spectrum when both LP_{01} and LP_{11} modes are excited equally and cross-coupling parameter was set as d_c=0.09.

The transmission and reflection spectra of 2M-FBG are shown in Figure 3.35 to Figure 3.39. In Figure 3.35, the transmission and reflection spectra are numerically plotted when both LP_{01} and LP_{11} modes are excited equally and the cross-coupling parameter has been set as d_c=0.09. Figure 3.36 and Figure 3.37 show the cross-coupling values set as d_c=0.02 and zero. Evidently, when the cross-coupling parameter is reduced, the power at cross-coupled wavelength also decreases. Similarly, the spectra plots for selective mode excitation are also presented by keeping the value of cross-coupling parameter constant at 0.02. Figure 3.38 represents the transmission and reflection spectra when the LP_{01} mode has been excited and the power of LP_{11} mode is set to zero. For LP_{11} excitation, the power of LP_{01} mode is set to zero, and the spectra are plotted in Figure 3.39.

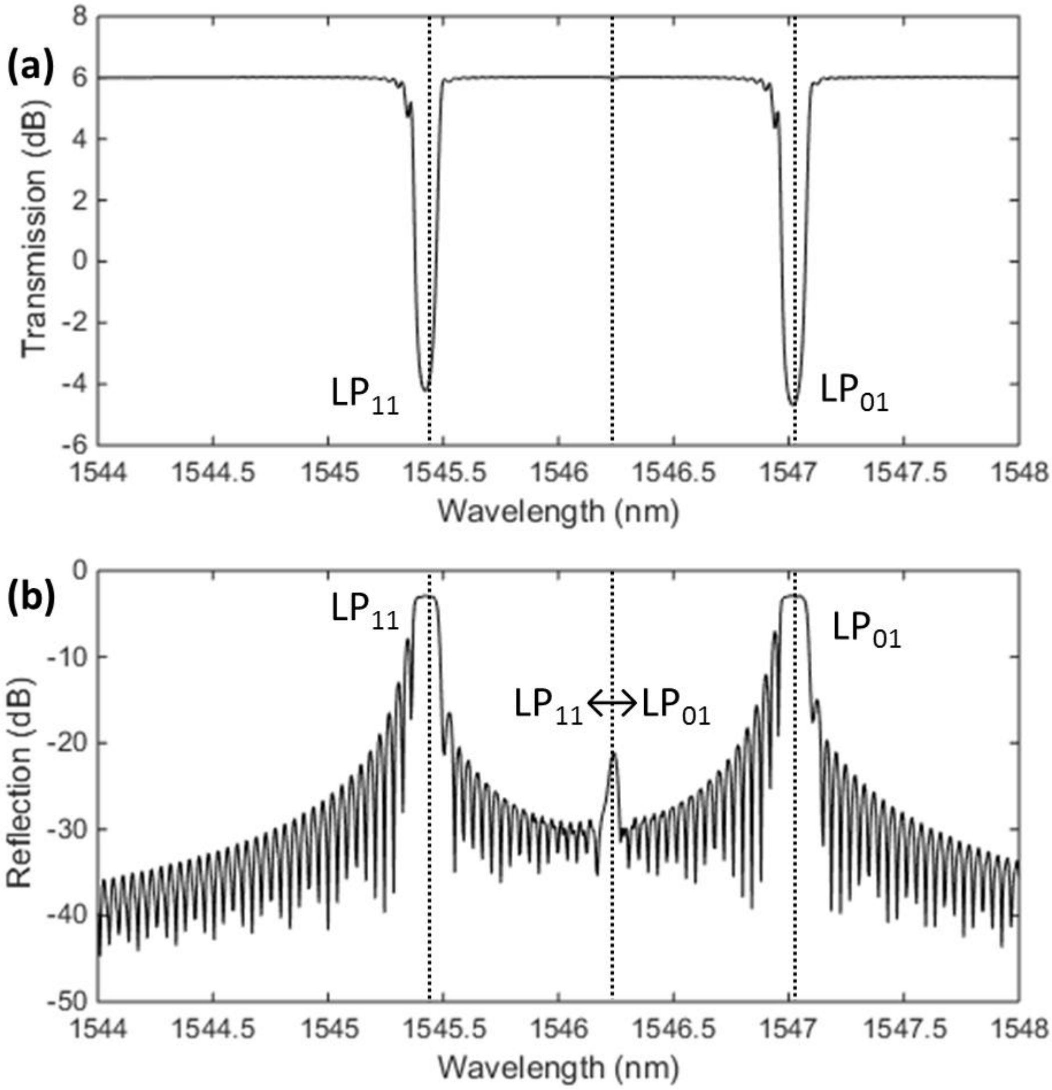

Figure 3.36: Numerical simulation of 2M-FBG. (a) Transmission spectrum and (b) reflection spectrum when both LP_{01} and LP_{11} modes are excited equally and cross-coupling parameter is set at d_c=0.02.

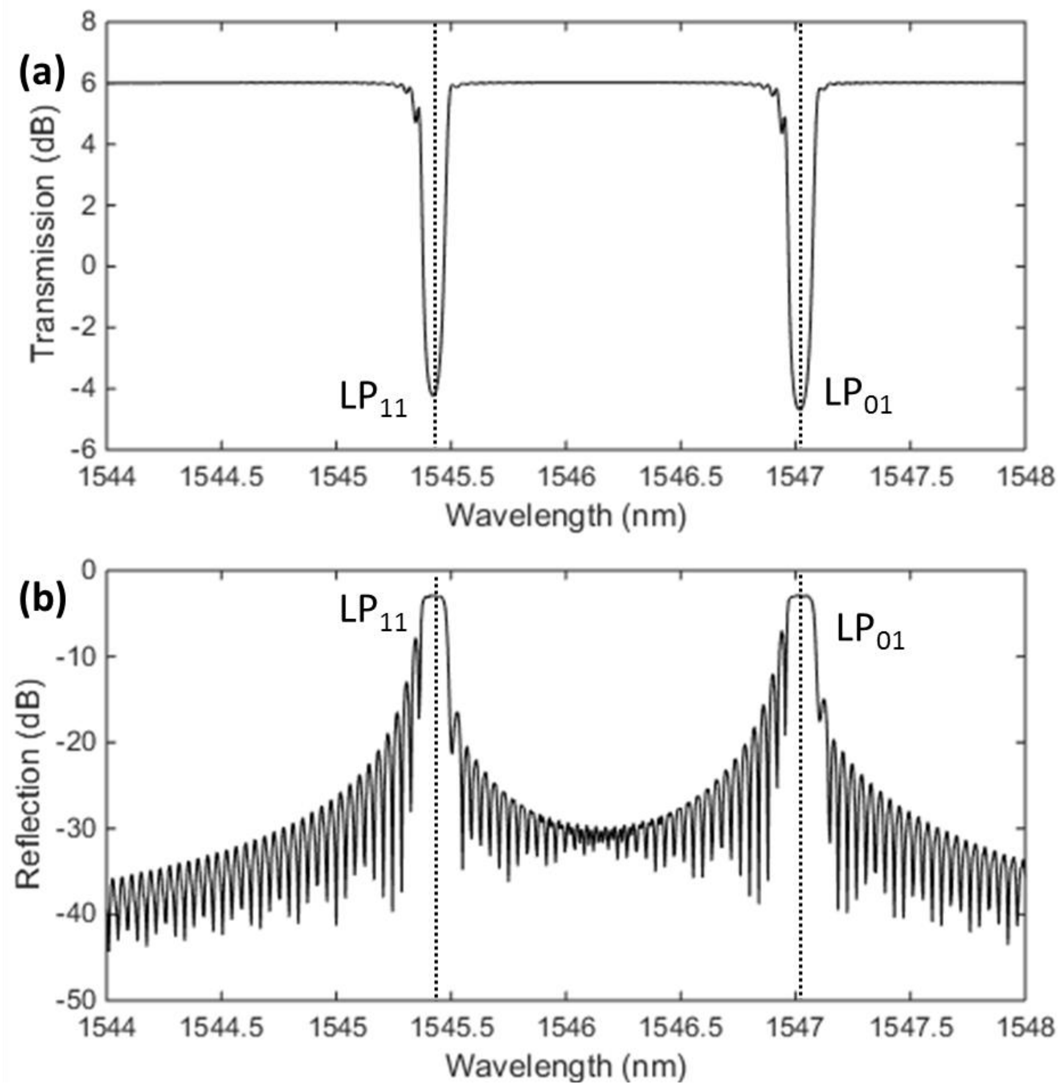

Figure 3.37: Numerical simulation of 2M-FBG. (a) Transmission spectrum and (b) reflection spectrum when both LP_{01} and LP_{11} modes are excited equally and cross-coupling parameter is set at d_c=0.

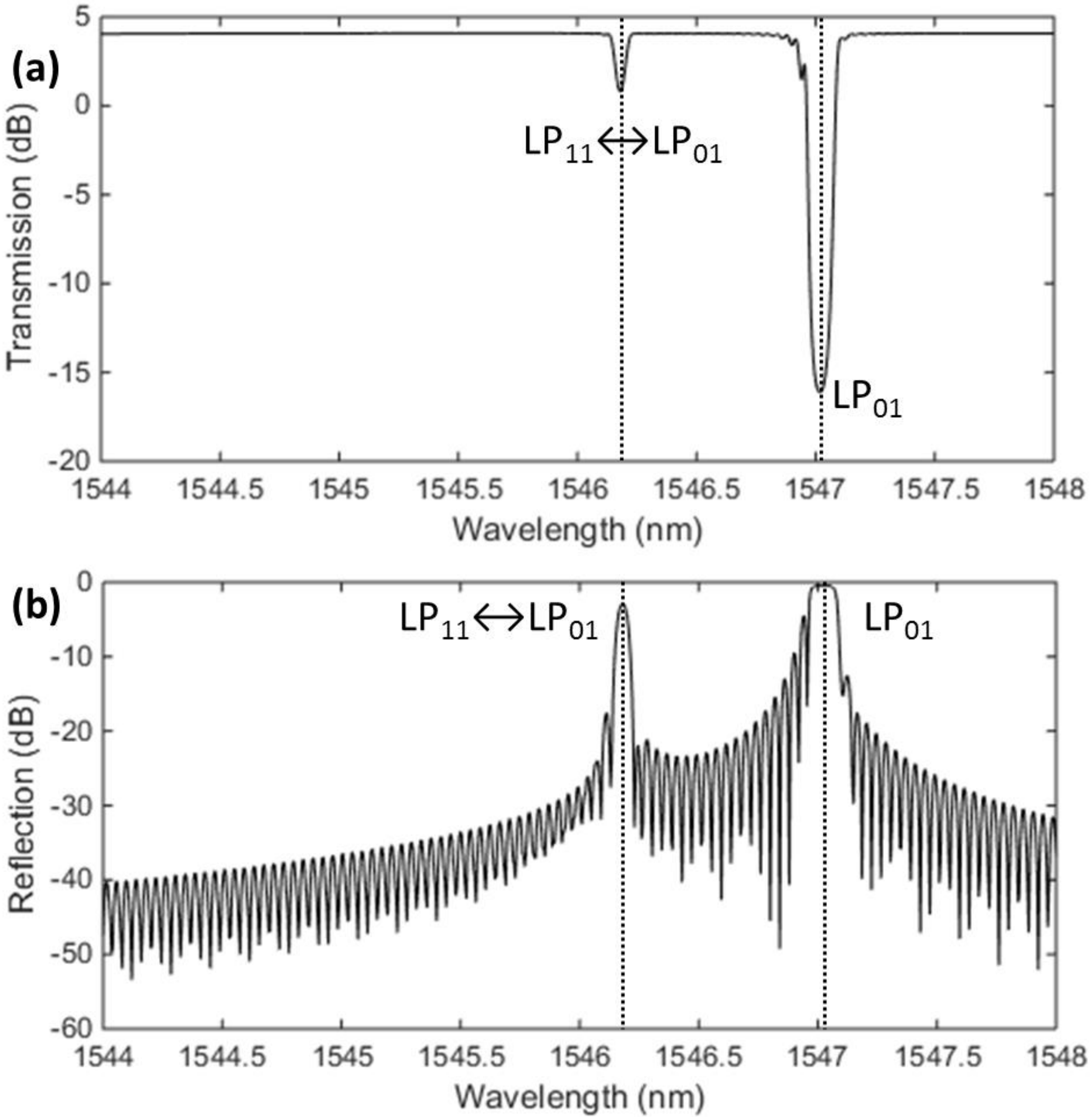

Figure 3.38: Numerical simulation of 2M-FBG. (a) Transmission spectrum and (b) reflection spectrum when LP_{01} mode is excited, LP_{11} power is set to zero, and cross-coupling parameter is set at d_c=0.02.

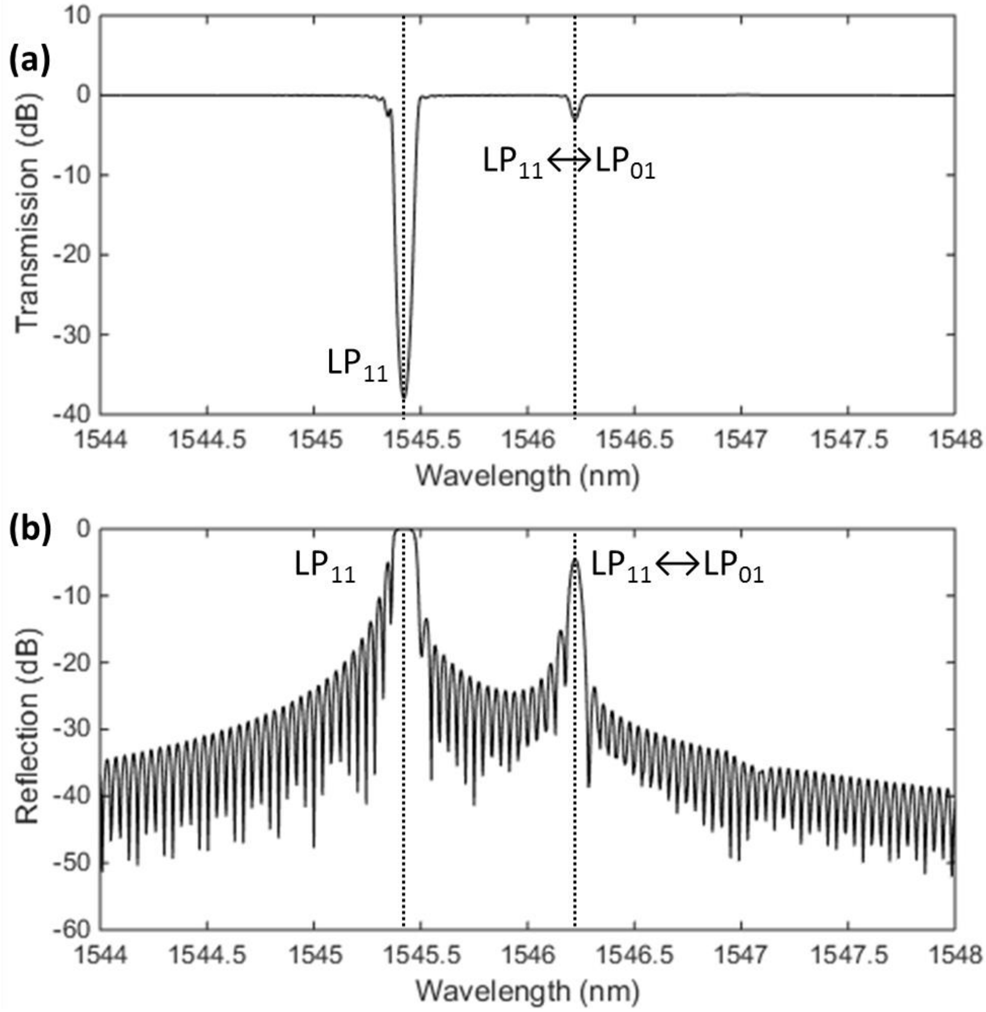

Figure 3.39: Numerical simulation of 2M-FBG. (a) Transmission spectrum and (b) reflection spectrum when LP_{11} mode is excited, LP_{01} power is set to zero, and cross-coupling parameter is set at d_c=0.02.

3.7.4 Power Confinement Ratios and Refractive Index Sensitivities of Cladless FMF Bragg Grating

FM-FBGs can work as sensing devices because of their sensitivity to changes in the ambient environment, such as temperature and concentration of the solution. To increase its sensitivity for solution concentration, the cladding of FM-FBG is removed, and the Bragg wavelength difference of the modes increases during the etching process. Figure 3.40 shows that when the optical fiber radius is decreased by etching, the wavelength difference increases and the power of higher order mode decreases. Therefore, the simulation for the refractive index sensitivities with different etched radii and power confinement ratio in the core, as well as the power ration for evanescent field, should be numerically simulated for clearer investigation and optimization of etched fiber radius.

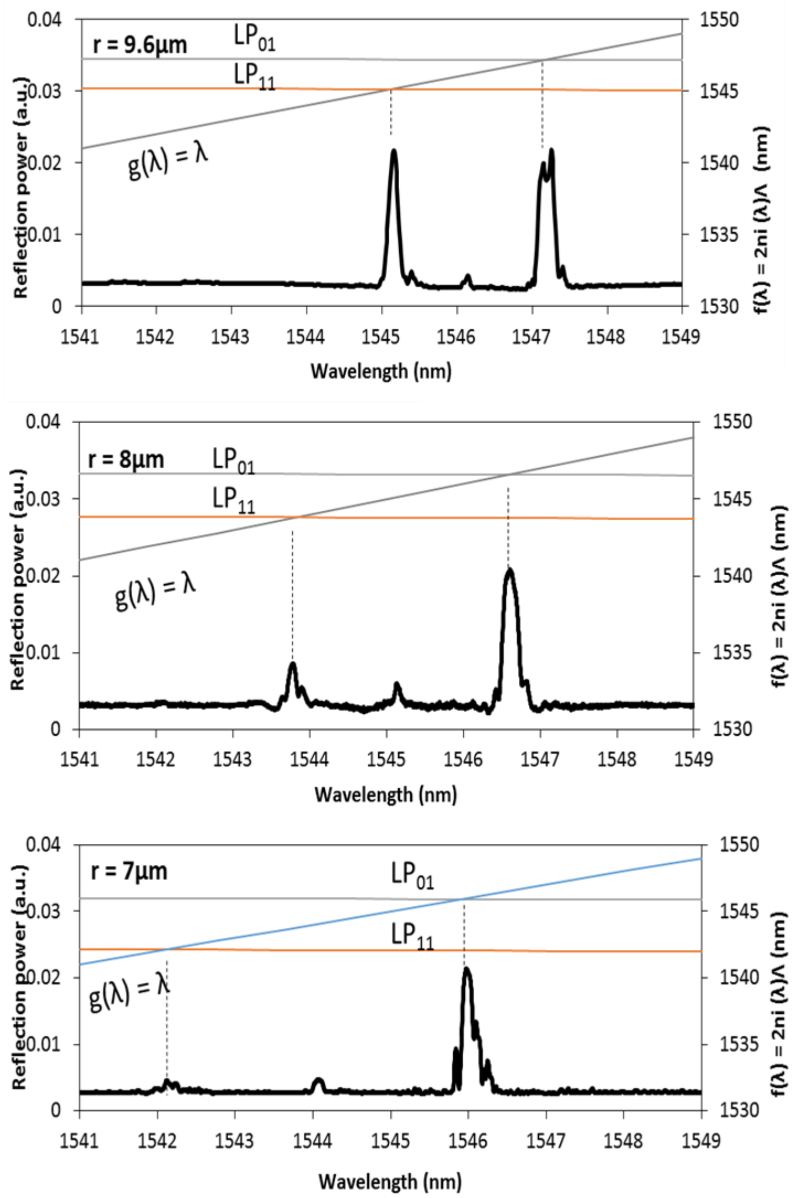

Figure 3.40: Theoretical estimation of the Bragg wavelengths of two-mode FM-FBG, and variation of peak wavelength difference versus reduced fiber radius in air media, i.e., air (n=1).

Similar to the result of cladding removal, the evanescent wave is excited at the etched core-ambient boundary. Evanescent wave can be further enhanced by reducing the etched fiber radius at the expense of reducing the ratio of power confined within the core (Ghatak & Thyagarajan, 1998), as illustrated in Figure 3.41(a) and (b). Compared with the LP_{01} mode, LP_{11} presents a greater gain in the evanescent wave power during fiber radius reduction, as depicted by the blue curves in Figure 3.41 (a). However, the medium RI affects the evanescent wave generation. The ambient medium with RI closer to that of fiber glass produces stronger evanescent wave as a result of smaller etched fiber NA. This finding explains the increase in the etched fiber's ratio of power in evanescent wave when the medium is changed from air (solid curves in Figure 3.41(b)) to water (dotted curves in Figure 3.41 (b)). The MATLAB code for the numerical calculation of refractive index sensitivities and power confinement ratios are given in Appendix A.4.

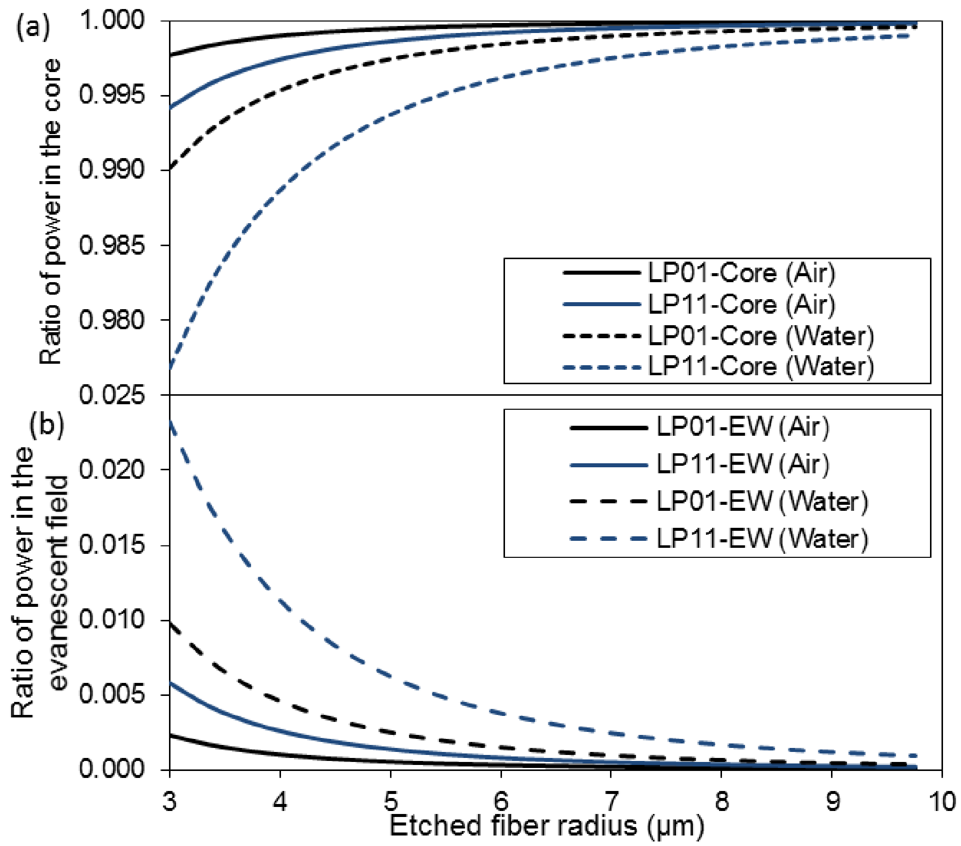

Figure 3.41: Relationships between ratios of power in the (a) core and (b) evanescent field with the etched fiber radius. EW: Evanescent wave (H. Z. Yang et al., 2015).

Figure 3.42 shows the simulation results on the sensitivity of Bragg wavelengths λ_{01} and λ_{11} in the function of etched fiber radius. The high RI sensitivity of λ_{11} can be attributed to the extended mode profile and relatively higher power ratio in evanescent wave for LP_{11} mode. Therefore, LP_{11} mode has stronger interaction with the ambient medium compared with the LP_{01} mode.

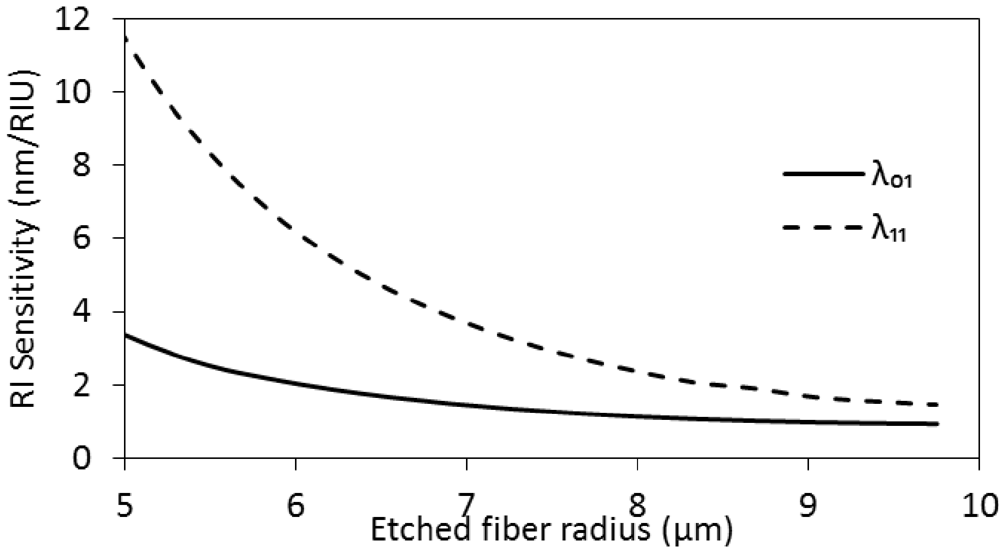

Figure 3.42: RI sensitivity of Bragg wavelengths λ_{01} and λ_{11} to ambient RI (simulation) (H. Z. Yang et al., 2015).

3.8 Summary

In this chapter, the photosensitivity of optical fibers, and fabrication of FBGs using phase mask technique have been presented in detail. The optical imaging technique was investigated for accurate measurement of grating period of FBGs. Image processing was performed on the acquired microscope images to obtain low noise grating profiles for measuring the grating period. A good linearity between the measured Bragg wavelengths and grating periods is observed and the measured strain-optics coefficient was found to be in agreement with reported literature. Furthermore, numerical simulations have been performed to investigate the intensity profiles of optical fibers and numerical calculations of effective indices of FMF have been done to verify the corresponding self- and cross- coupling Bragg wavelengths in fabricated FM-FBGs. In addition the chemical etching effect on Bragg wavelength difference, the power ratio of modes and RI sensitivity were analyzed numerically.

CHAPTER 4: CHARACTERIZATION OF MODE COUPLING IN FEW-MODE FIBER BRAGG GRATING AND MODE CONVERSION

In this chapter, the characterization of few-mode fiber Bragg gratings (FM-FBGs) inscribed in two-mode and four-mode step-index fibers has been carried out in detail. Under conditions of selective input mode launching, coupling between specific modes of interest can be selectively excited and the self-coupling and cross-coupling properties at the associated resonant wavelengths can be clearly identified and verified by observing the reflected mode intensity profiles. Such FM-FBGs can potentially be used as reflective mode-converters for mode division multiplexed data transmission systems.

4.1 Introduction

Few-mode fiber (FMF) based Mode division multiplexing (MDM) has emerged as a promising new technology for the realization of higher data transmission capacities in optical communication networks following on from the successful prior exploitation of time division multiplexing (TDM) and wavelength division multiplexing (WDM) technologies in standard single mode fibers (SMFs) (Essiambre et al., 2010; Richardson et al., 2013; Sleiffer et al., 2013). Unlike SMF, FMFs are capable of supporting more than one spatial mode in the fiber core by virtue of a larger core size, and each spatial mode can be employed as an individual transmission channel. Compared to conventional multimode fiber (MMF), FMFs support much fewer spatial modes and are typically designed to have a low differential mode group delay (DMGD) in order to reduce the complexity of digital signal processing (DSP) required at the system output to correct for the inevitable mode coupling that occurs during transmission. Hence, there is an increasing interest in the study of FMFs and other associated devices fabricated from FMF, for example in the properties of few-mode fiber Bragg gratings (FM-FBGs) (Mizunami et al., 2000), FMF long-period gratings (Youngquist, Brooks, & Shaw, 1984), FMF modal couplers (Ismaeel et al., 2014; Y Jung et al., 2013), adaptive mode control in FMF (Peng Lu & Xu, 2016) and FMF amplifiers (Yongmin Jung, Kang, et al., 2014; Yongmin Jung, Lim, et al., 2014).

The inscription of Bragg grating structures in FMFs leads to the generation of multiple resonant wavelengths in both reflection and transmission spectra due to the presence of multiple core modes that satisfy viable phase matching conditions. This multi-peak reflection property has been previously used for wavelength/mode selective components in FMF laser cavities, e.g. to realize a multi-wavelength fiber laser or a transverse mode switchable fiber laser (Daniel et al., 2011; Moon et al., 2004). Recently FM-FBG research has been revisited as a mean to allow spatial mode conversion for MDM applications (Fang & Jia, 2014a; K. S. Lim et al., 2014; Wu et al., 2012). Core-offset launching was used to excite the higher order spatial modes in a FM-FBG. Strasser et al. proposed a mode convertor ($LP_{01} \rightarrow LP_{11}$) based on a tilted grating in two-mode fiber. It is found that the reflections of coupling strength and mode conversion vary with the tilt angle of the grating. The angle can be carefully controlled to achieve mode conversion without the undesired LP_{01} reflection (Strasser, Pedrazzani, & Andrejco, 1997).

In this chapter, the uniform Bragg gratings, in both a step-index two-mode fiber (2MF, OFS Denmark) supporting LP_{01} and LP_{11} mode groups and in a four-mode fiber (4MF, OFS Denmark) supporting LP_{01}, LP_{11}, LP_{21}, and LP_{02} mode groups, have been characterized which were inscribed using an ArF excimer laser operating at 193nm. Through selective mode excitation using binary phase plates, we analyzed the mode coupling of the fabricated 2M-FBGs and 4M-FBGs. The measured transmission and reflection spectra are compared with the simulation results and the mode intensity profiles at every resonant wavelength under different mode excitation conditions are analyzed to confirm the spatial modes involved.

4.2 Characterization Setup for Mode coupling in FM-FBG

4.2.1 Fabrication of FM-FBGs

Few-mode fiber Bragg gratings were inscribed in the hydrogenated FMFs by using an ArF excimer laser and a phase-mask. The length for each FBG was fixed at 20 mm and the grating period was fixed at 533.5 nm. After that, the FM-FBG produced was annealed in a hot oven at 80 °C for 12 hours to allow the residual hydrogen to out-diffuse from the fibers.

4.2.2 Phase Plate Fabrication and Optimization

Selective mode excitation is more popularly achieved using planar phase plates and free space optical systems i.e. (objective lenses and beam splitters, etc.) (Igarashi, Souma, Tsuritani, & Morita, 2014). The modification of the spatial phase distribution of the beam can be done by binary phase plates placed across a collimated beam in free space, generating a desired selective mode when re-focused in the optical fiber. In this study the binary phase plates made by polymer and glass have been used which are fabricated by the use of the process of UV curing as well as glass etching. The operating wavelength of the fabricated binary phase plates is 1550 nm in this study. Selective excitation of higher order modes with the aid of binary phase plates is commonly used method in recent FMF based MDM transmission systems due to its simplicity and high modal purity (routinely achieved modal extinction ratios are greater than 20dB) (Y Jung et al., 2013; Roland Ryf, Sebastian Randel, et al., 2012; VAJM Sleiffer et al., 2012).

4.2.2.1 Fabrication of Binary Phase Plates

The design of phase plates is generally based on a binary phase which can generate the desired phase and spatial intensity pattern at the focus of the coupling lens. A beam with the cross-sectional size of 4 mm^2 is used for avoiding the excessive truncation of the Gaussian radial profile, whereas the area of the spatial field patterns is extended up to 10 mm^2. Figure 4.1 represents the layout for different binary phase plates designed for the selective excitation of higher order modes.

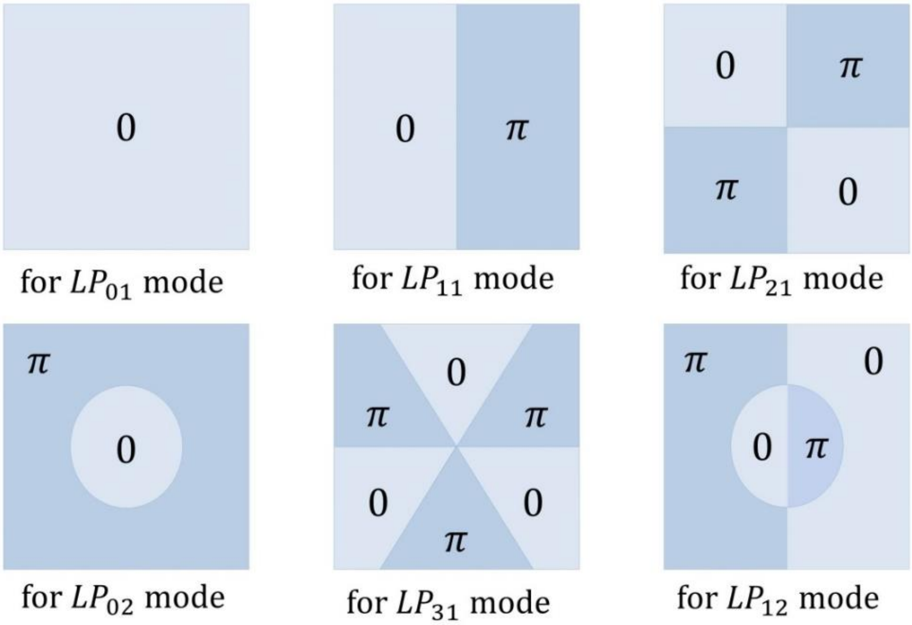

Figure 4.1: Schematic of binary phase plate used for selective higher order mode excitation; 0 and π are the phase differences induced by the change of thickness of phase plate.

On the basis if the binary phase plates illustrated in Figure 4.1, a photolithographic mask is fabricated, this is then used for making a 4 inch Silicon wafer master. Afterwards the polymer replicas can be formed by the Silicon wafer master. The oxide layer thickness is chosen as 1.53 μm for the realization of π phase shift. The polymer material had the similar value of the refractive index as that of the oxide layer and therefore only a small error was expected in the optical path length from the process of replication. The thickness (d) can be formulated as

$$d = \frac{\lambda}{2(n-1)}(1+\delta) \qquad \textbf{(4-1)}$$

where λ represents the operating wavelength i.e., 1550 nm, n is the refractive index of the silicon substrate and δ is considered as normalized phase-difference error.

The silicon master patterns are replicated in UV curable cement (Norland Optical Adhesives NOA 63), as shown in Figure 4.2. The master is then pressed against the glass substrate after the surface treatment of the Si/oxide with an anti-adhesive layer. The Silicon master was separated after UV curing process. Here it is mentioned that the spacer is used to enable the separation from the Silicon master by maintaining the adhesion to the substrate, as shown in Figure 4.2.

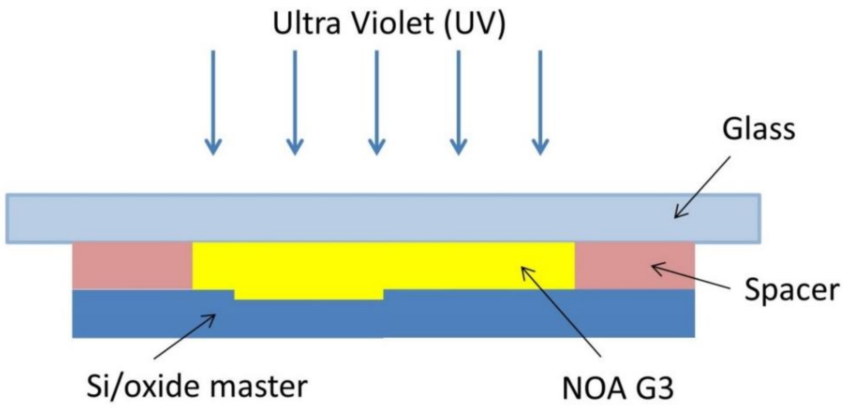

Figure 4.2: UV curing process for fabrication of polymer based binary phase plate.

4.2.2.2 Characterization of Binary Phase Plates

Mode conversion based on phase plates is well known technique and has been extensively used in recent mode-division multiplexed transmission experiments to excite higher-order modes in FMF due to its simplicity and the high modal purity. Therefore it is very essential to characterize the binary phase plates in terms of mode conversion efficiency or extinction ratio. The theoretical coupling efficiency and modal extinction ratio is well described by Roland Ryf *et al*. (Roland Ryf, Sebastian Randel, et al., 2012). The phase plate thickness error and lateral alignment error are very important in achieving high quality mode excitation. As a calibration on the sensitivity, 1% error in thickness difference can induce a crosstalk less than -35dB for LP_{01} to LP_{11} launching. This approach experimentally has been validated by the authors in ref. (VAJM Sleiffer et al., 2012) and a good mode-selectivity of more than 25 dB has been demonstrated.

However the efficiency of the binary phase plate for mode conversion can be measured by a simple scheme using higher-order mode stripper. Firstly, for the generation of LP_{11} mode from an incident LP_{01} mode, a binary phase plate $(0, \pi)$ is used. Secondly, the combination of collimating lens with the binary phase plate is used for the excitation of the LP_{11} mode inside the FMF which is then bent tightly to introduce a high leakage loss for the LP_{11} mode. By using this method, it is possible to quantify the mode conversion efficiency as well as the extinction ratio (ER) of the LP_{01} and LP_{11} modes for the given binary phase plates.

4.3 Characterization of Mode Coupling in FM-FBGs

Figure 4.3 shows the characterization setup for the analysis of mode coupling in FM-FBGs by selective mode excitation. An amplified spontaneous emission (ASE) source centred at 1550 nm and an optical spectrum analyzer (OSA) were used for measuring the transmission and reflection spectra of the FM-FBGs. Three collimating lenses with a focal length as f = 4.5 mm and a non-polarizing beam splitter (BS) are used for coupling the converted beam to the FM-FBG and to recirculate the reflected beam from the FM-FBG to an FMF (similar to the host fiber used for the FM-FBG) for analysis using the OSA. The mode conversion phase plate is positioned in the region between the two collimating lenses where the beam size is large and positional tolerances are largest.

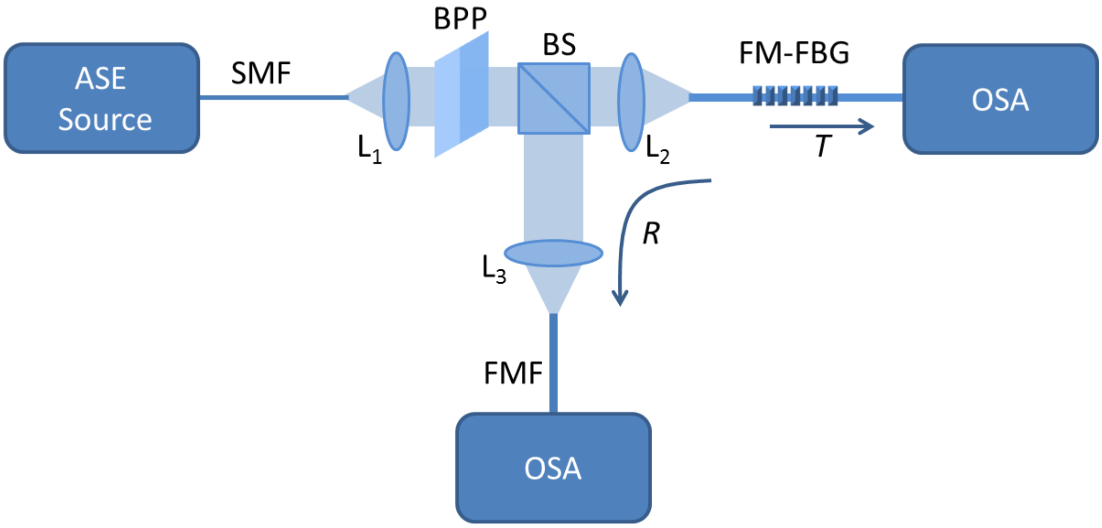

Figure 4.3: The block diagram of the experimental setup used for the mode coupling analysis of an FM-FBG by the selective mode excitation. SMF: single mode fiber, BPP: binary phase plate, BS: non-polarizing beam splitter, T: transmission, R: reflection, OSA: optical spectrum analyzer.

The relationship between the two counter-propagating waves in a FM-FBG is given by (Raman Kashyap, 1999)

$$\beta_\mu^+ + \beta_v^- = \frac{2\pi}{\Lambda} \quad \textbf{(4-2)}$$

where and are the propagation constants of the two counter-propagating waves in the FM-FBG, μ, v $\in\{01,11,21,02\}$ and Λ is the grating period (Igarashi et al., 2014). For the scenario of self-coupling, both counter-propagating waves are on the same mode ($\mu = v$), hence the equation (4-2) can be simplified as

$$\lambda_\mu = 2n_{eff.\mu}\Lambda \quad \textbf{(4-3)}$$

where λ_μ is the resonant wavelength, and $n_{eff.\mu}$ is effective refractive index of the corresponding spatial mode, LP_μ. The decreasing UV laser intensity across the fiber core due to absorption leads to the formation of an asymmetric index profile in the grating. This contributes to a non-zero overlap integral between various spatial modes that would not otherwise couple (Wu et al., 2012). Hence, cross couplings are excited and new reflection wavelengths are produced. The relationship between the excited resonant wavelength and the two cross-coupled spatial modes is given by (Raman Kashyap, 1999)

$$\lambda_{\mu,\nu} = [n_{eff.\mu} + n_{eff.\mu}]\Lambda \qquad \textbf{(4-4)}$$

where μ, ν ε {01,11,21,02} and $\mu \neq \nu$.

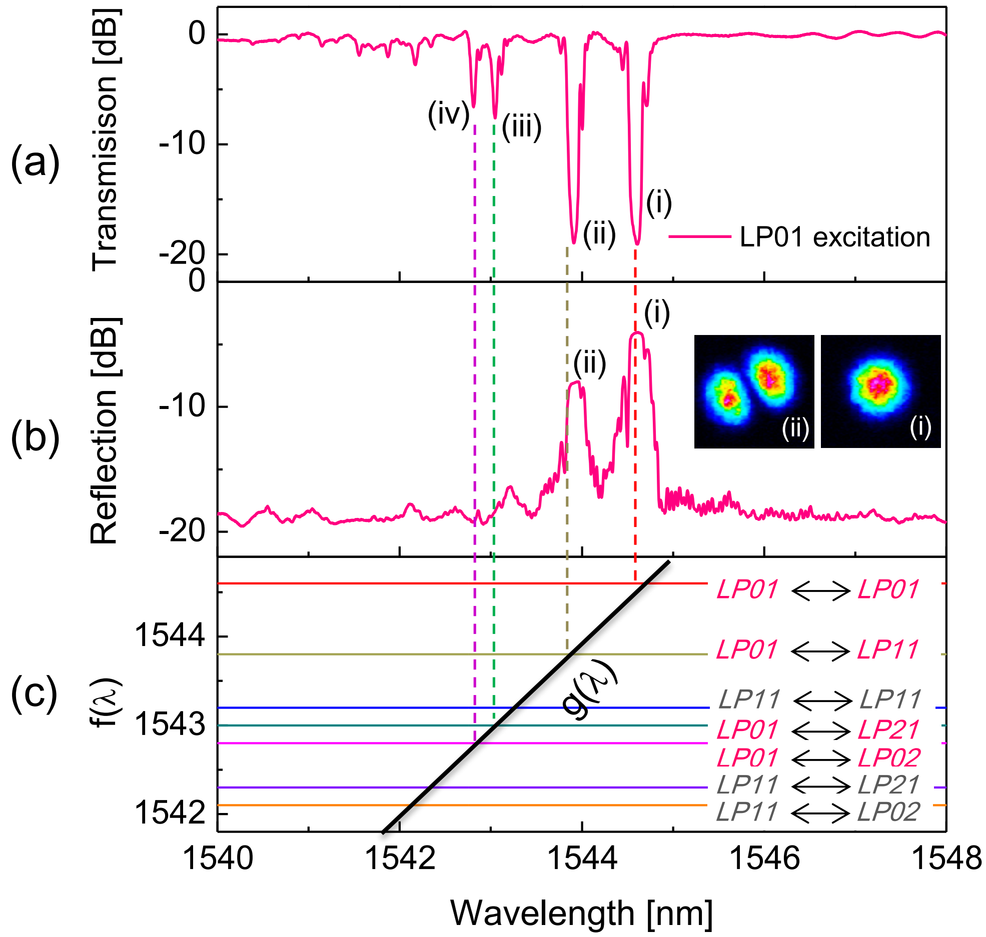

Figure 4.4: (a) Transmission spectra and (b) reflection spectra of the 2-mode FBG under pure LP_{01} excitation. The insets are the beam profiles at the wavelengths of interest (see notations (i) – (ii)). (c) Theoretical estimation of the resonant wavelengths of the corresponding modes are given by the intersections between $f(\lambda) = [n_\mu(\lambda) + n_\nu(\lambda)]\Lambda$ or $f(\lambda) = 2n_\mu(\lambda)\Lambda$ and $g(\lambda) = \lambda$ (Ali et al., 2015).

Figure 4.4 and Figure 4.5, the output spectra have been shown under LP_{01} and LP_{11} excitations, respectively for the 2M-FBG which has a core diameter of 19.5 μm and an index contrast of ~0.005 under the selective input mode excitation of the LP_{01} and LP_{11} modes, the two lowest modes in the fiber. The resonant wavelength for each spatial mode can be theoretically estimated from the position of intersection between the two functions, $f(\lambda)$ and $g(\lambda) = \lambda$, where $f(\lambda) = 2n_{eff,\mu}\Lambda$ for the self-coupling, and $f(\lambda) = [n_{eff,\mu} + n_{eff,\nu}]\Lambda$ is for the cross coupling as illustrated in Figure 4.4(c) and Figure 4.5(c) (Chuang et al., 2012). It is also to be noted that the cross couplings and share similar coupling characteristics and a reflection peak at the same wavelength. For the convenience of representation, the notation $LP_u \leftrightarrow LP_v$ is employed to represent the cross coupling between the two modes.

Under LP_{01} mode excitation, four resonant wavelengths are observed in transmission, denoted as (i), (ii), (iii) and (iv) in Figure 4.4(a). The highest reflections are achieved at peaks (i) and (ii) which correspond to the self-coupling $LP_{01}\leftrightarrow LP_{01}$ and the cross-coupling $LP_{01}\leftrightarrow LP_{11}$, respectively. These reflection peaks are centred at the wavelengths λ_μ = 1544.61 nm and 1543.92 nm respectively. The appearance of the other two resonant wavelengths (iii) and (iv) correspond to $LP_{01}\leftrightarrow LP_{21}$ (1543.04 nm) and $LP_{01}\leftrightarrow LP_{02}$ (1542.81 nm) cross-coupling. Note that only LP_{01} mode is excited, the self-coupling $LP_{11}\leftrightarrow LP_{11}$ and the other cross-coupling related to an input LP_{11} mode are not observed as expected.

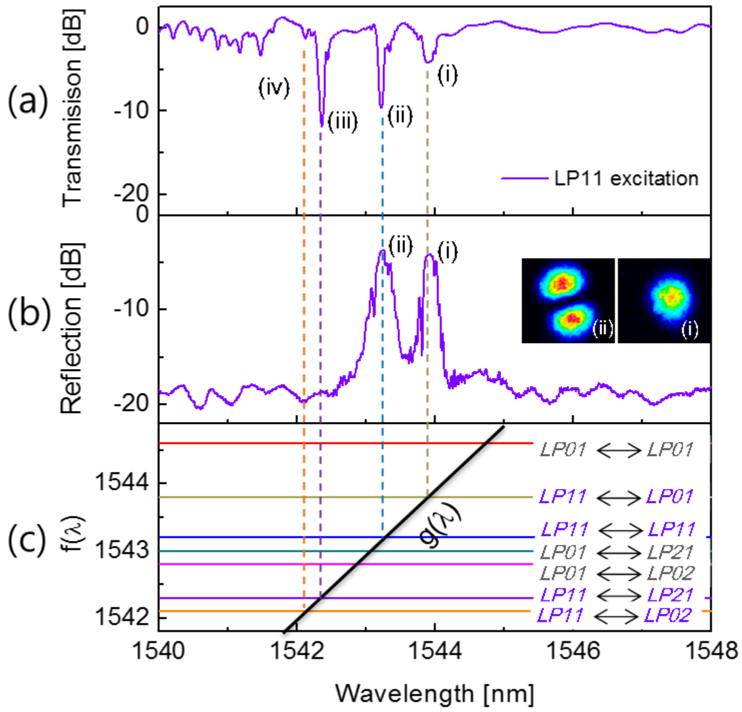

Figure 4.5: (a) Transmission spectra and (b) reflection spectra of the 2-mode FBG under pure LP_{11} excitation. The insets are the beam profiles at the wavelengths of interest (see notations (i) – (ii)). (c) Theoretical estimation of the resonant wavelengths of the corresponding modes are given by the intersections between $f(\lambda)=[n_\mu(\lambda)+n_\nu(\lambda)]\Lambda$ or $f(\lambda)=2n_\mu(\lambda)\Lambda$ and $g(\lambda)=\lambda$ (Ali et al., 2015).

At the cross-coupling wavelength (ii) between the LP_{01} and LP_{11} mode, a strong intermodal coupling is achieved of more than -18.9dB, which corresponds to a mode conversion efficiency of 98.7%. Thus at this particular cross-coupling wavelength, this device can be used as a reflective $LP_{01}\leftrightarrow LP_{11}$ mode converter. The full width at half maximum (FWHM) of the peak is about 0.23nm. The 2MF in our experiment has been developed to support the two lowest-order guided modes for long-haul transmission but the LP_{21} and LP_{02} are still guided over a short length of fiber due to a relatively large V-number (~4.3). To experimentally verify the LP_{21} mode guidance along the fiber, we launched the LP_{21} mode at the fiber input (away from a Bragg resonance) and the output mode profile was examined at the end of the fiber (fiber length = 1 m). As expected, the weakly confined LP_{21} guided mode was clearly observed at the output fiber end, though it shows high propagation loss and bend sensitivity. This can be attributed to the high propagation losses for the higher order modes. The measured resonant wavelengths in the transmission and reflection spectra are in good agreement with simulation results of the fiber refractive index profile as shown by the vertical lines in Figure 4.4(c).

Under LP_{11} mode excitation, another four resonant wavelengths are observed as shown in Figure 4.5(a). These wavelengths denoted by (i), (ii), (iii) and (iv) correspond to the following mode couplings respectively $LP_{11}\leftrightarrow LP_{01}$, $LP_{11}\leftrightarrow LP_{11}$, $LP_{11}\leftrightarrow LP_{21}$ and $LP_{11}\leftrightarrow LP_{02}$. The high transmission dip (iii) in Figure 4.5(a) indicates that there is a strong excitation of $LP_{11}\leftrightarrow LP_{21}$ cross-coupling in the FM-FBG but low reflected power in Figure 4.5(b). The high propagation loss is held to be responsible for the attenuation and absence of the LP_{21} mode in the reflection, where the fiber grating is located at a distance of about 3 m away from the input end of the 2MF. As the existence of higher order modes (HOMs) in 2MF has been proved by launching the LP_{21} mode using a phase plate, the LP_{21} mode after 3 m length of propagation whereas the mode profile for LP_{02} mode was very difficult to see due very high loss and the optical alignment of phase plate is quite delicate. The acquired mode profile for LP01, LP11 and LP21 supported by two mode fiber are shown in Figure 4.6.

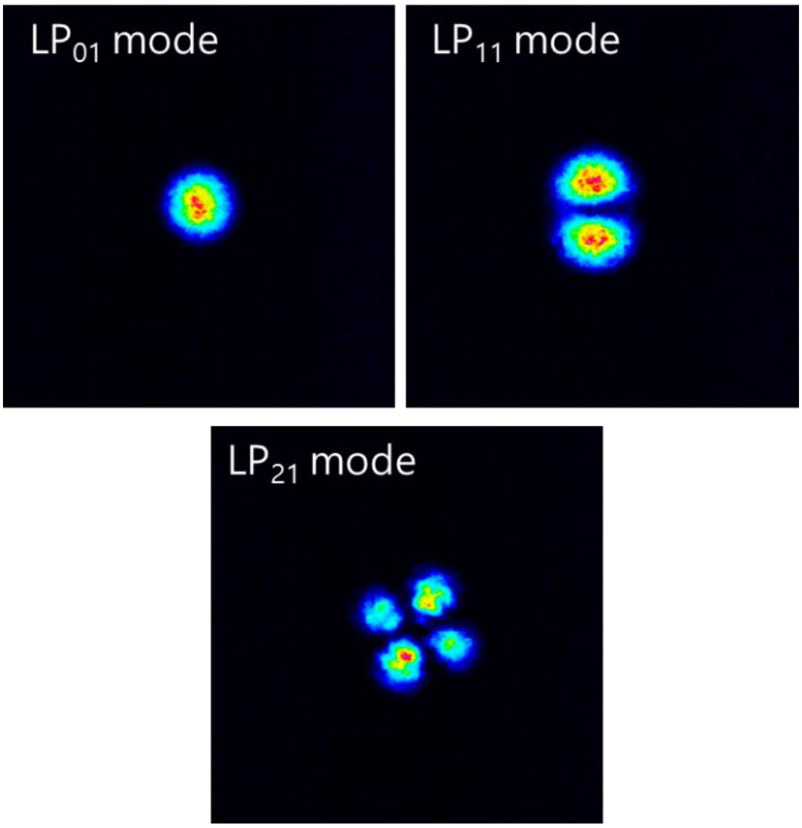

Figure 4.6: Acquired CCD images of mode profiles for the confirmation of higher order modes at the end of 3 m long TMF by exciting LP_{01}, LP_{11} and LP_{21} mode using phase plate, it is was hard to get the LP_{02} mode for TMF.

Furthermore, the mode intensity profile analysis was conducted with a tunable laser source (TLS) replacing the ASE in the experimental setup. The insets in Figure 4.4(b) show the mode profiles of the reflected beam at different peak wavelengths. The LP_{01} mode profile was observed at (i) and the LP_{11} mode profile at (ii) as expected. A potential useful phenomenon is observed at the cross-coupling $LP_{01}\leftrightarrow LP_{11}$ peak wavelength where the LP_{11} mode profile is attained under LP_{01} mode excitation (refer (ii) in Figure 4.4(b)) whereas the LP_{01} mode profile is attained at the wavelength under LP_{11} mode excitation (refer (i) in Figure 4.5(b)). Thus at this cross-coupling wavelength, this device can serve as a reflective $LP_{01}\leftrightarrow LP_{11}$ mode converter.

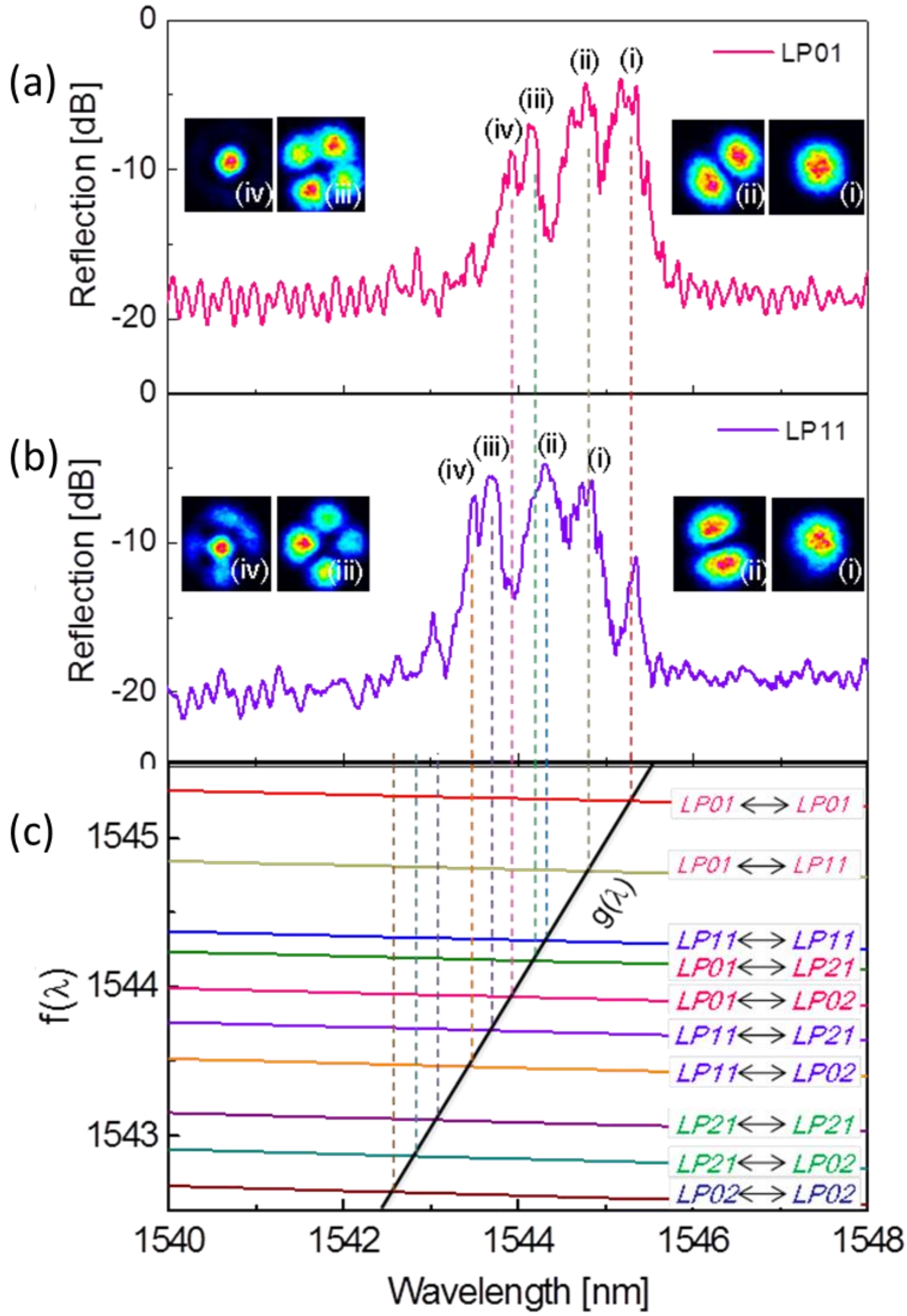

Figure 4.7: Reflection spectra of 4M-FBG under selective mode excitation of (a) LP_{01} mode (b) LP_{11} mode. The insets show the intensity profiles of the reflected beam at the wavelengths of interest (see notations (i) – (iv)). (c) The resonant wavelengths of the corresponding modes can be determined from the intersections between $f(\lambda) = [n_{\mu}(\lambda) + n_{\nu}(\lambda)]\Lambda$ or $f(\lambda) = 2n_{\mu}(\lambda)\Lambda$ and $g(\lambda) = \lambda$ (Ali et al., 2015).

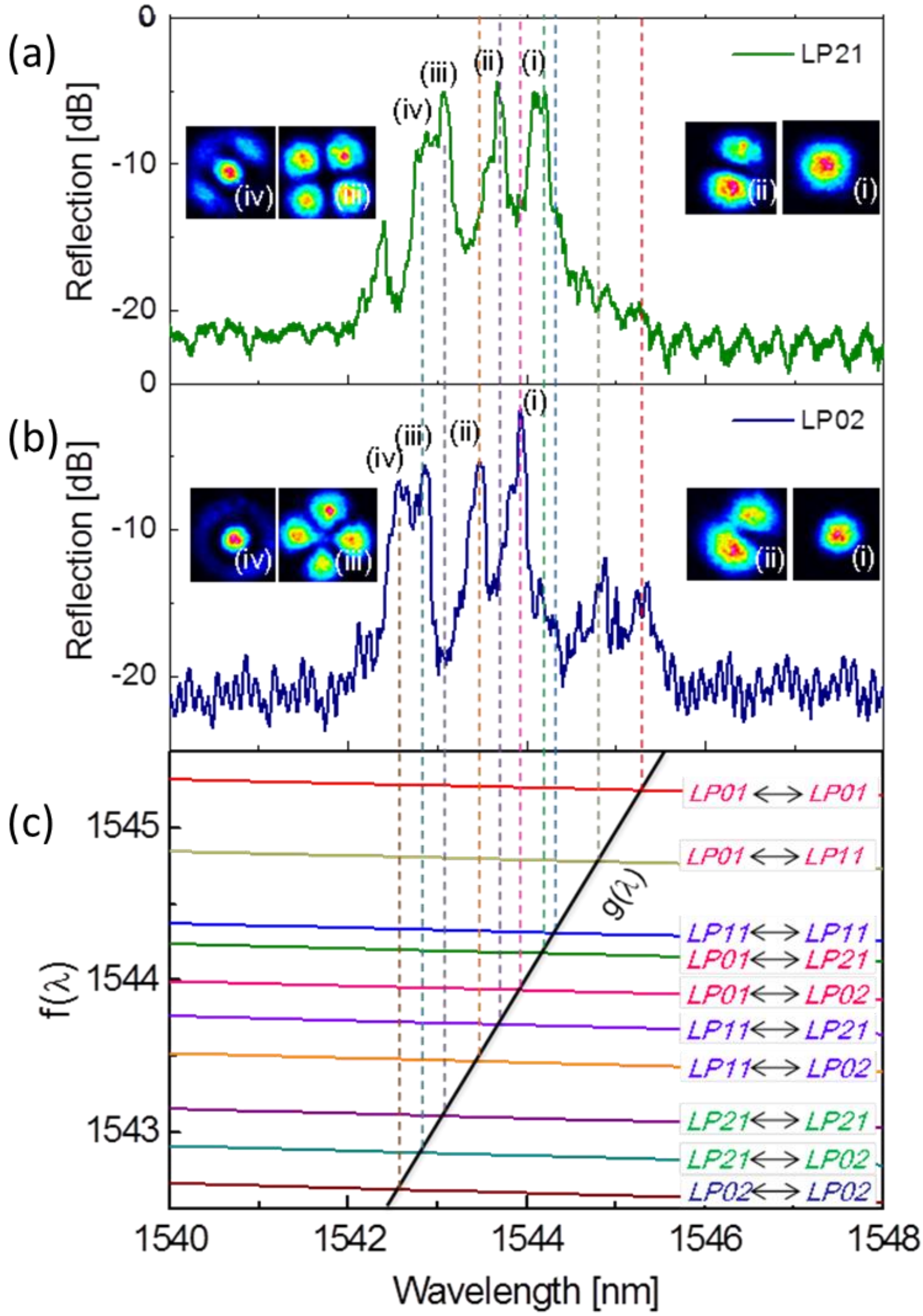

Figure 4.8: Reflection spectra of 4M-FBG under selective mode excitation of (a) LP_{21} mode (b) LP_{02} mode. The insets show the intensity profiles of the reflected beam at the wavelengths of interest (see notations (i) – (iv)). (c) The resonant wavelengths of the corresponding modes can be determined from the intersections between $f(\lambda)=[n_{\mu}(\lambda)+n_{\nu}(\lambda)]\Lambda$ or $f(\lambda)=2n_{\mu}(\lambda)\Lambda$ and $g(\lambda)=\lambda$ (Ali et al., 2015).

Similar experiments were performed with the 4M-FBG. The 4MF has a larger core diameter ~25 μm and index contrast of 0.005. The higher V-number (~6) suggests that more spatial modes will be supported in the fiber. Figure 4.7(a), (b) and Figure 4.8 (a), (b) show the reflection spectra of the FM-FBG under different selective mode excitation conditions. Similar to the analysis in Figure 4.4 and Figure 4.5, the identification of the reflection peaks with their corresponding mode coupling assignments is achieved by referring to the simulation results in Figure 4.7(c) and Figure 4.8(c). The peaks (i) – (iv) in Figure 4.7(a) correspond to the self-coupling $LP_{01} \leftrightarrow LP_{01}$, and the cross-coupling $LP_{01} \leftrightarrow LP_{11}$, $LP_{01} \leftrightarrow LP_{21}$ and $LP_{01} \leftrightarrow LP_{02}$, are centred at the wavelengths of 1545.27, 1544.79, 1544.17, and 1543.95 nm respectively. The recorded mode intensity profiles show that all four spatial modes, namely LP_{01}, LP_{11}, LP_{21} and LP_{02} are attained at their corresponding peak wavelengths (see insets) and in agreement with the predicted cross-coupling. Similar to the observation in Figure 4.4 and Figure 4.5, the mode profiles of the reflected beam from the self-coupled peaks are unaffected by the choice of mode excitation. The same observation is achieved in the investigations of LP_{11} mode excitation as presented in Figure 4.7(b), LP_{21} excitation in Figure 4.8(a) and LP_{02} mode excitation in Figure 4.8(b). This result suggests that 6 different bidirectional mode conversions can be realized by exploiting the cross-coupling properties of the FM-FBG. The maximum achievable number of bidirectional mode conversions for 4M-FBG can be formulated as ${}^{4}C_{2} = 6$(Bogart, 1989) However, the conversion is restricted to a small bandwidth of ~0.05 - ~0.2nm at the associated cross-coupling resonant wavelengths depending on the cross mode overlap integral. This shortcoming can be addressed by spectral tuning (through temperature or strain) to achieve wider wavelength coverage (Qiu et al., 2013). This also provides the convenience of dynamic mode conversion in MDM transmission applications.

4.4 Tunable Mode Converter using FM-FBG

In previous section, it is obvious that the FM-FBGs can be used as mode converters by utilizing the cross-coupling resonant wavelengths. Nevertheless it is limited to the small bandwidth at resonant wavelengths which can be overcome by tuning the FM-FBGs via applied strain or controlling the temperature as the FM-FBG is sensitive to the strain and temperature.

FM-FBGs firstly have been characterized for applied strain and temperature and by investigating their corresponding sensitivities. Figure 4.10 shows the strain response of FM-FBG for tunability of mode converter. The measured average strain sensitivity for self-coupling as well as cross-coupling modes is ~ 0.535 (pm/με). Typical tuning range of 5nm can be achieved. Maximum achievable range is ~8nm.

FM-FBG has been also characterized for applied temperature for the range of 22 ^{o}C to 80 ^{o}C and the measured average temperature sensitivity of each mode is as ~ 9.57 ± 0.12 pm/^{o}C.

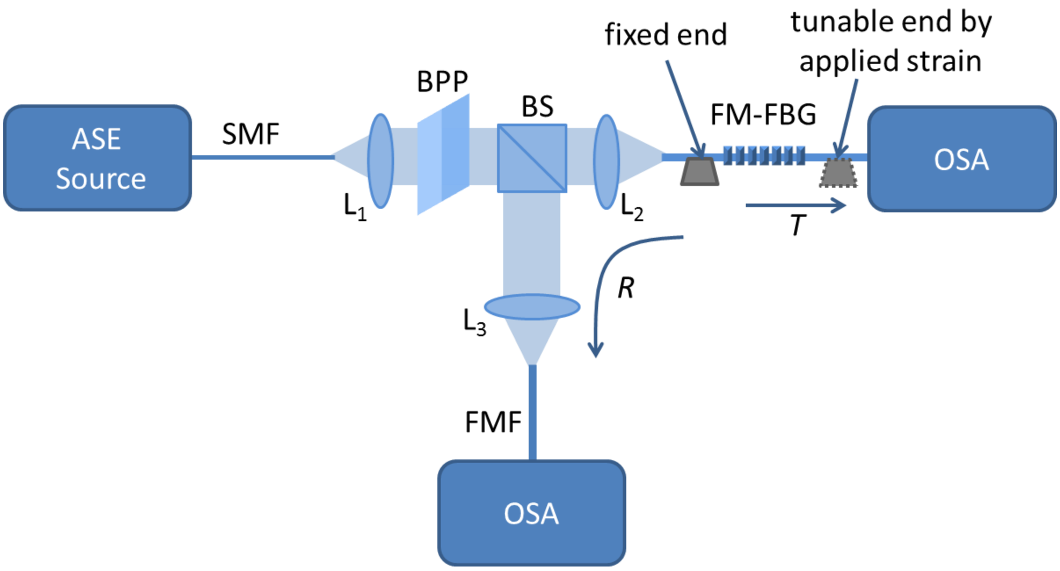

Figure 4.9: Experimental Setup for the characterization of tunable mode converter by applying strain on FM-FBG.

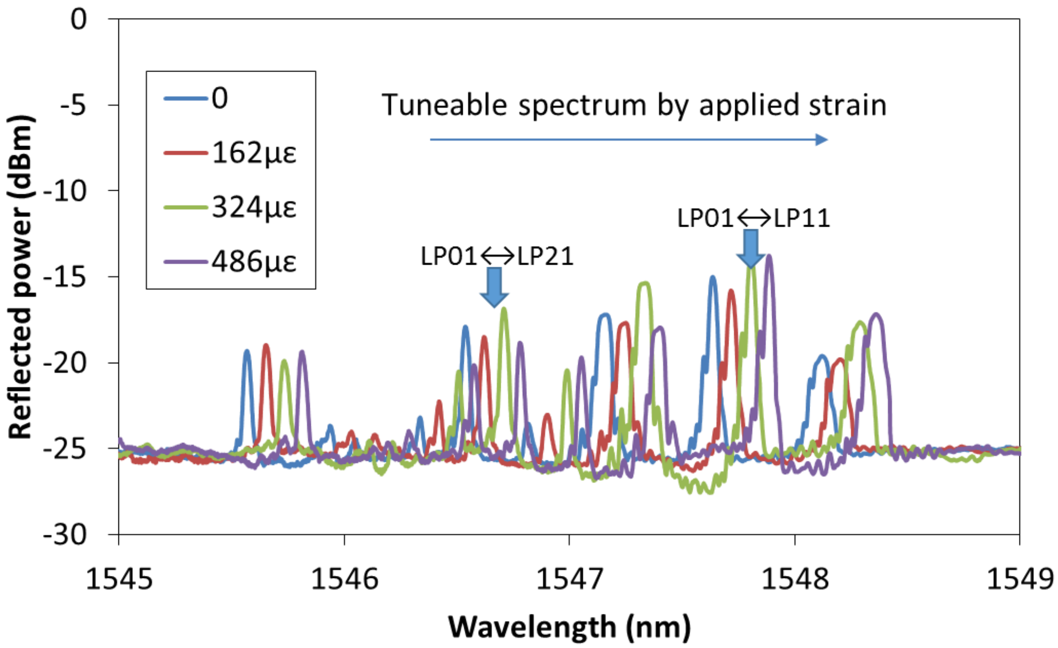

Figure 4.10: Reflection spectra of FM-FBG under strain for the characterization of tunable mode converter.

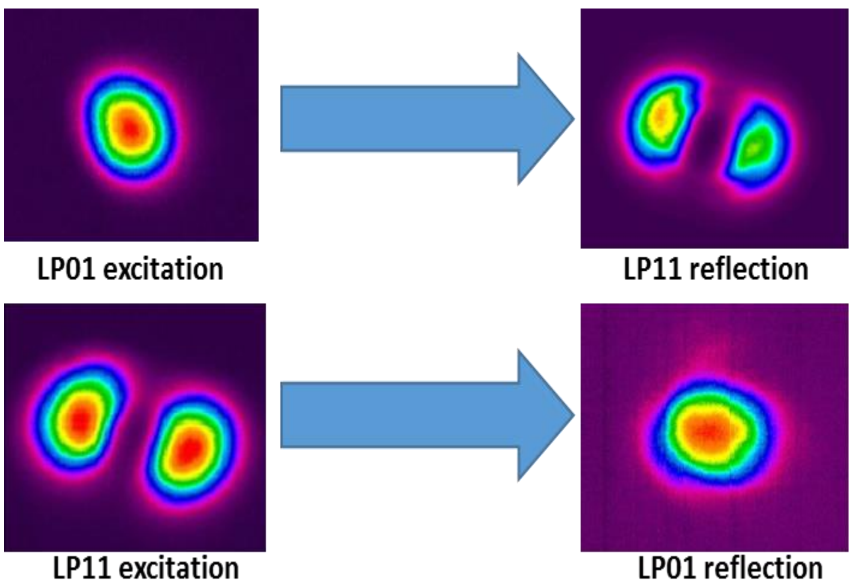

Figure 4.11: The experimentally obtained reflected mode intensity profile at cross-coupling wavelength ($LP_{01}\leftrightarrow LP_{11}$).

4.5 Summary

In this chapter the detailed characterization of modal coupling in FM-FBGs has been studied. The binary phase plates were used for the characterization of FM-FBGs inscribed in 2MF and 4MF. Thereafter it was investigated that the mode conversions can be achieved on the cross coupling wavelengths. The mode converter can be made as tunable by using the wavelength tunability properties of FM-FBGs with the application of strain or temperature. These mode converters can be used in the optical communication set up for the implementation of SDM technology.

CHAPTER 5: FABRICATION AND CHARACTERIZATION OF CLADLESS FEW-MODE FIBER BRAGG GRATING SENSOR

The fabrication and spectral characteristics of cladless few-mode fiber grating to refractive index (RI) and temperature is investigated in this chapter. The grating device is fabricated from an etched few-mode Fiber Bragg Grating (FM-FBG) that can support two Bragg wavelengths, in which the sensitivities for each Bragg wavelength to the changes of RI and temperature are different. Dispersion relation of circular waveguide is used to describe the wavelength characteristics of the proposed sensor and the simulation result indicates that an etched diameter of 14.1 μm can produce an optimal performance for both power confinement and RI sensitivity for all Bragg wavelengths of the FM-FBG. Experimental results show that the grating device has the RI sensitivities for both λ_{01} and λ_{11} are estimated to be 1.183 nm/RIU and 4.816 nm/RIU respectively, and temperature sensitivities for λ_{01} and λ_{11} are 9.62 ± 0.08 pm/°C and 9.52 ± 0.13 pm/°C respectively. With the assistance of 3 × 3 characteristic matrix, discrimination measurements of temperature and RI has been demonstrated and the deviations in RI and temperature measurements are ±8 × 10^{-4} RIU and ±1 ºC respectively.

5.1 Introduction

Various types of structures using optical fibers have been proposed by different researchers for the achievement of simultaneous sensing of parameters (Ping Lu & Chen, 2008; Qiangzhou et al., 2012; Squillante, 1998; Yu, Tam, Chung, & Demokan, 2000). The continual development of these kinds of sensors have eventually led to the commercialization of various devices for the applications of measurement of blood glucose level and detection of glutamate, aspartame, sulfite, lactose and, ethanol in food and water products (Squillante, 1998). The biosensor and chemical sensor industry is holding a great promise for addressing the need for simple, fast, and continuous in-situ monitoring techniques. Generally, most of the optical biosensors and chemical sensors are based on the detection of the fluorescence intensity or the measurement of the analyte RI.

In the sensing of liquid RI, a sensor comprises of a single FBG with pigtail fiber was proposed for temperature and refractive index measurement in which a pair of incoherent waves from the FBG and the facet end due to Fresnel reflection can be obtained for sensing (Meng, Shen, Zhang, Tan, & Huang, 2010). Similarly, many researchers have proposed other fiber optic based sensors like as tilted FBGs (Wong, Chung, Tam, & Lu, 2011; C.-L. Zhao, Yang, Demokan, & Jin, 2006), LPGs (Y.-J. Kim, Paek, & Lee, 2002), double cladding fibers (DCFs) (Liu et al., 2010) and interferometry based sensors as (S. Gao et al., 2013; Iadicicco, Campopiano, Cutolo, Giordano, & Cusano, 2005; Ping Lu et al., 2012; Xiong et al., 2014), for simultaneous measurement of temperature and RI. Meanwhile, several techniques have been proposed to improve the RI sensitivity of the normal FBG by accessing the evanescent field of the fundamental mode in the optical fiber, such as chemical etching, Iadicicco et al. (Iadicicco et al., 2005) proposed an intriguing approach for simultaneous sensing of RI and temperature in which a portion of an FBG is etched to produce a Bragg wavelength that is sensitive to both changes of ambient refractive index and temperature of a solution whereas the unetched part of the FBG can provide a different Bragg wavelength that is only sensitive to ambient temperature change. Accurate measurements of refractive index can be attained via cancellation of temperature based on the data from both Bragg wavelengths. Considering the fact that the etched-core grating is sensitive to both temperature and RI, a temperature insensitive sensor based on partial cone-shaped FBG is proposed (Chryssis, Lee, Lee, Saini, & Dagenais, 2005; Sang et al., 2007) in which the constituent of temperature from wavelength reading of the etched part of the FBG is eliminated based on the reading from the un-etched part of the FBG, which is insensitive to ambient RI change. In (Chryssis et al., 2005) the refractive index sensitivities of 7.8×10^{-2} and 3.4×10^{-3} are reported in the range of 1.45 and 1.33, respectively and temperature sensitivities of 6.15×10^{-6}/ºC and 5.66×10^{-6}/ºC are achieved in the range of 15-50ºC. Yang et al. (Yang, Guang, Rajibul, Kok-Sing, & Ahmad, 2014) proposed a device with the similar concept but different structure, in which the FBG part of the fiber was chemically etched to achieve taper shape has and the minimum etched diameter is 4.4 μm.

Generally, etched-core FBGs in SMF with excessive etched diameter (~2-5μm) are fragile and difficult to handle. Considering the factors of mechanical stability and life span of the etched-core FBG, larger etched diameter is preferred. On the other hand, the RI sensitivity of the device is significantly reduced if the etched diameter is greater than the original core diameter of the fiber. FM-FBG has more than one Bragg wavelength in the spectrum due to the inherit properties of supporting more than mode transverse mode in the fiber. Cladless few-mode FBG offers good RI sensitivities even at considerably larger etched core diameter particularly for the Bragg wavelengths associated with higher order modes. Qiu et al. had investigated the temperature and strain characteristics of a single few-mode grating inscribed on a polymer optical fiber. Multiple Bragg wavelengths are observed from the grating. They share similar strain sensitivities but different temperature sensitivities for different orders of modes. These properties are exploited for discrimination measurement between temperature and strain (Hang Zhou Yang et al., 2015). In case of our proposed sensor, the FM-FBG is written on the glass based few-mode fiber (FMF) by UV laser to do the simultaneous measurement RI and temperature. A chemical etching technique is used to produce the FM-FBG with two Bragg wavelengths, in which the etched core diameter is ~14.1 μm which is mechanically more stable and easy to fabricate than the etching of normal

FBG. The etching diameter of 14.1 μm is based on the simulation result for optimal the power confinement of etched FM-FBG.

On the other hand, the consideration of cross sensitivity between parameters is crucially important for simultaneous measurement. The negligence of this factor in simultaneous sensing may lead to imprecise measurement. Particularly, single element sensors with multi-parameter sensing ability, in which the sensitivities of each parameter are the functions of other parameters. For accurate discriminative measurement, cross sensitivity should be taken into measurement with the aid of 3x3 characteristic matrix (Hang Zhou Yang et al., 2015). In this chapter, simulation is performed on our proposed sensor to identify the transverse mode of each Bragg wavelengths. The property of cross sensitivity between temperature and RI is investigated. Discrimination measurement using 3x3 characteristic matrix is also presented.

5.2 Fabrication of Cladless Few-mode Fiber Bragg Grating Sensor

In this section, the fabrication details of cladless FM-FBG are presented. The fabrication of proposed sensor can be divided into two standard steps as inscription of Bragg gratings inside FMF core and chemical etching for removing the fiber cladding.

5.2.1 Inscription of Bragg Gratings inside FMF core

The fabrication begins with inscription of Bragg grating structure inside the core of an FMF. The FMFs used are germanosilicate fibers (OFS, Denmark) with a core diameter of 19.5μm, RIs of cladding and core are 1.444 and 1.449 respectively which gives an NA of ~0.12.

Cladless FM-FBG sensor is fabricated from FMF through simple fabrication processes – UV grating inscription and chemical etching. KrF excimer laser and standard phase mask with period 1068.80 nm, were used to produce 2 cm long grating in the core of hydrogen loaded FMF. After the fabrication, FM-FBGs were annealed in a hot oven at 80 °C for 10 hours to remove the residue hydrogen. Figure 5.1 shows the schematic diagrams of FMF before gratings inscription and after gratings inscription. Whereas after FM-FBG inscription, it has been cleaved in such a way that grating part is much closed to the fiber end so that it can interact with ambient environment and the cleaving point is indicated in Figure 5.1.

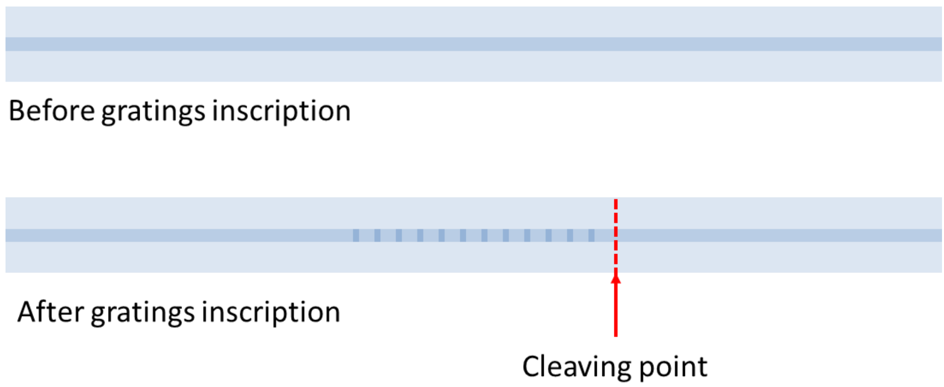

Figure 5.1: Schematic diagram of FMF before inscription and after inscription of FBG inside the core and cleaving point to make fiber end sensor

5.2.2 Chemical etching of FM-FBG

After that, chemical etching was performed to remove the cladding of the fiber to enhance the evanescent wave of the core modes and to enable interaction between the core mode and ambient medium. For fast and better etching, two steps were performed. In first step the fiber end was dipped into the HF solution (48% in water) in which the silica glass is etched at a rate of ~3.05 µm/min from an original diameter of 125µm until it approaches a few µm from the cladding-core boundary. Fast etching rate may results to less desired glass surface roughness. This problem can be alleviated by continuing the etching at slower rate. In the second step, Buffered Oxide Etchant (BOE) solution with the volume ratio of NH_4F solution (40% in water) and HF solution (48% in water) was used as the etchant. The observed etching rate was 0.3 µm/min and smoother glass surface was produced. In addition, it also offers the advantage of better control in etched core fiber and reduces the risk of excessive reduction in fiber radius, an irreversible process. In Figure 5.2, the graph illustrates the reduction of fiber radius during the etching process with HF solution at the rate of ~3.05 µm/min in the first 34 min followed by slower etching process with BOE at the rate of 0.3 µm/min. The etchant is covered with a thin layer silicon oil to prevent the evaporation of the etchant solution. After achieving the desired fiber shape, the FM-FBG is rinsed with distilled water to remove the residual etchant. The illustration of fiber etching using etchant covered with and without the layer of oil is shown in Figure 5.3. It is clear that the boundary between etched and un-etched part of fiber is smooth and continuous for oil covered etchant whereas for that of uncovered with oil the boundary is discontinuous and rough. Also in case of uncovered etchant, the surface un-etched part of fiber has become rough. The microscope image of original FMF end with FBG and the etched FM-FBG end is shown in Figure 5.4. For the ease of understanding, an illustrative diagram of device structure is presented in Figure 5.4 (c).

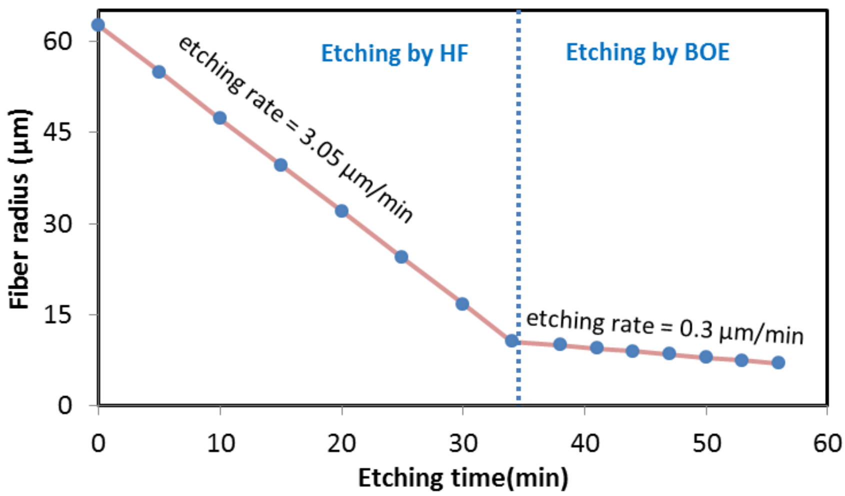

Figure 5.2: Illustration of fiber radius reduction after chemical etching by HF for and BOE.

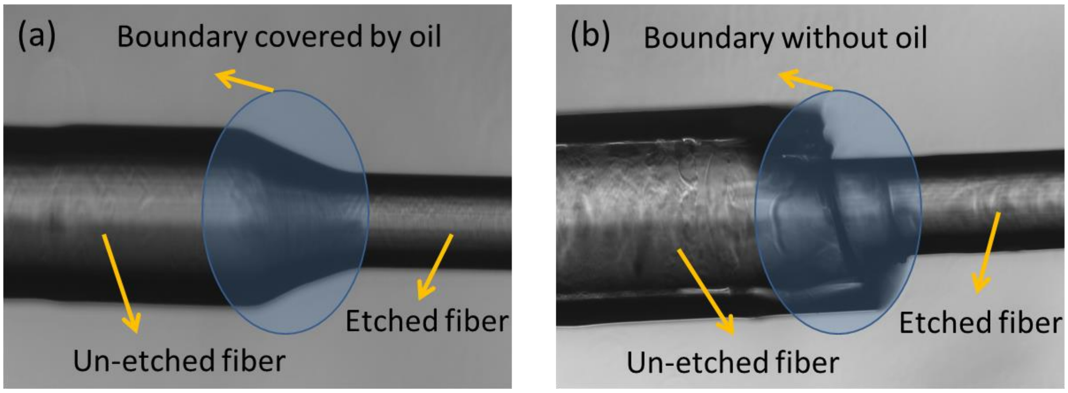

Figure 5.3: Optical images of etched fiber using etchant (a) covered with oil (b) without covering with oil.

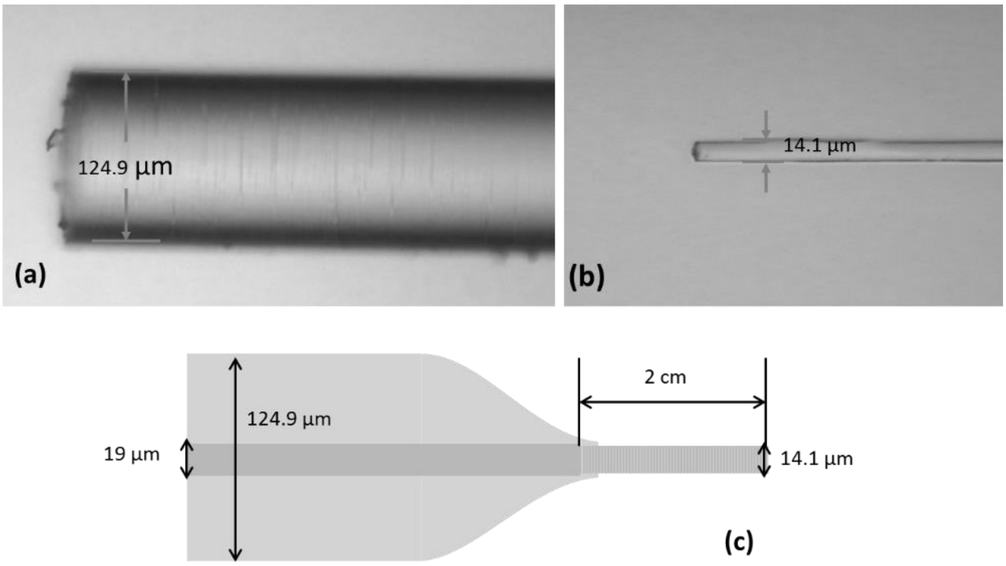

Figure 5.4: Microscope images of the FMF (a) before etching (b) after etching and (c) graphical image of the cladless FM-FBG with a grating length of 2 cm (H. Z. Yang et al., 2015).

5.3 Experimental Setup

In the sensor calibration experiment, the broadband laser source from an erbium doped fiber amplifier (EDFA) is used to launch the light into a circulator before it enters the FM-FBG which is placed in the solution as shown in Figure 5.5. A digital hot plate is used to heat up the solution, which has a temperature resolution of 0.1 ºC. Meanwhile, a thermocouple is placed as close as to the FM-FBG to get the temperature information of the solution. The reflection spectrum of the FBG is analysed by an optical spectrum analyser (OSA) at the resolution of 0.01nm.

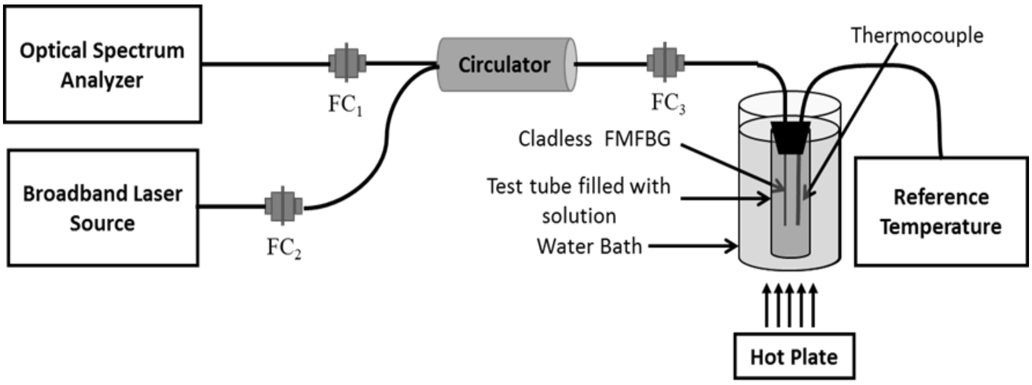

Figure 5.5: Experimental setup for simultaneous sensing of refractive index and temperature. FC: fiber connector (H. Z. Yang et al., 2015).

5.4 Results and Discussion

Figure 5.6 shows the output response of the proposed sensor in the air (n = 1) and water (n = 1.3159) at different etched fiber radii. As shown in the graph, the wavelength spacing between λ_{01} and λ_{11}, denoted as $\Delta\lambda$ increases with increasing fiber radius. The experimental results are in good agreement with the simulation results of etched few-mode FBG (See dotted curve in Figure 5.6).

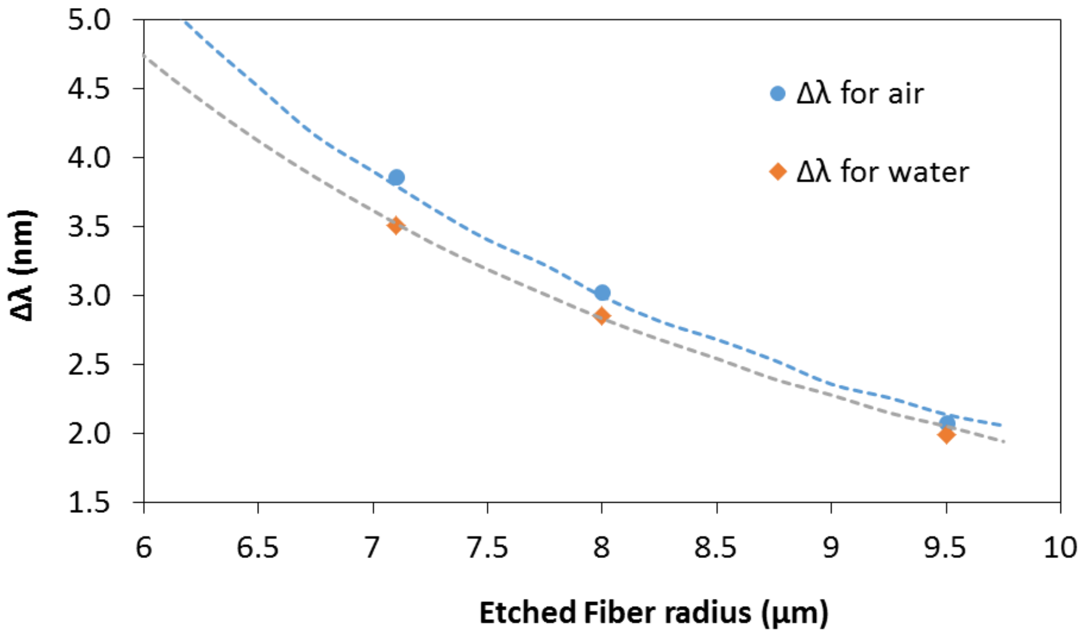

Figure 5.6: The relationship between wavelength difference Δλ and the etched fiber radius in the air (n=1) and water (n=1.3159). The dotted lines represent the simulation results (H. Z. Yang et al., 2015).

The etched few-mode FBG is also characterized with sodium chloride (NaCl(aq)) solutions with concentrations range from 0 to 32 g/100ml. The measured RIs of the solutions using prism coupler at 1550 nm are in the range of 1.3159-1.3620. The solution RI is linearly increasing at the rate of 0.001445 RIU/(g/100ml) with the NaCl(aq) solution concentration (g/ml).

In the measurements, the grating device is placed inside a test tube filled with salinity solution. The test tube is sealed and dipped into the water bath heater to control the temperature of the liquid solution. At same time, a thermocouple is sealed into the test tube also which located as close as possible but not in physical contact with the sensor probe for temperature measurement as depicted by Figure 5.5. The heating temperature of the water bath heater is kept for 15 mins at each step point to ensure that the temperature is well-distributed in the water. It is worth noting that as a precautionary measure, clean and pure solution with no adhesive properties was used in this experiment to minimize the risk of contamination due to foreign impurities or extraneous coating on the sensor.

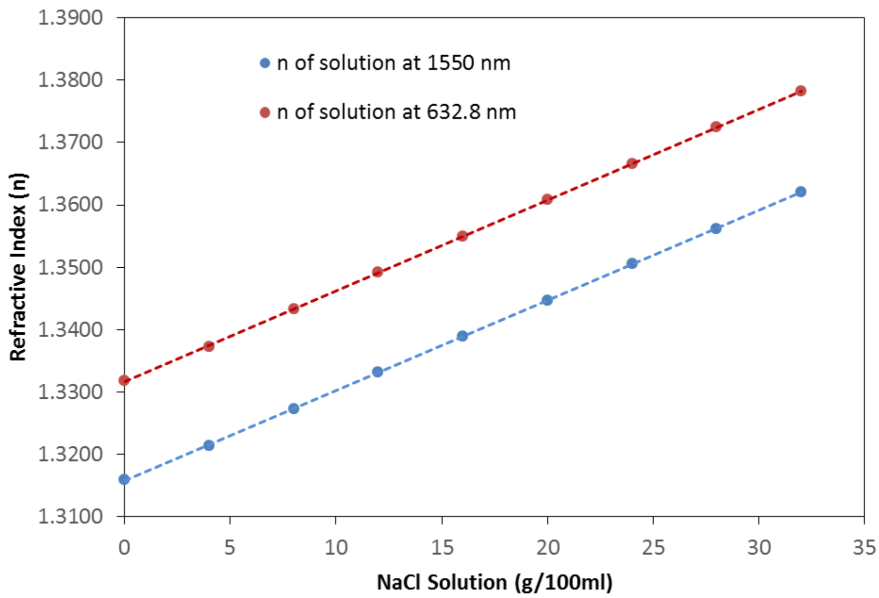

Figure 5.7: Refractive index of NaCl solution (grams dissolved in 100 ml of water) obtained by prism coupler method at the wavelengths of 632.8nm and 1550nm, used for the characterization of proposed sensor.

For characterization of cladless sensor, the reference refractive indices of the used NaCl solutions were considered, which were achieved using prism coupler method. Prism coupler method is used at the wavelengths of 632.8 nm and 1550 nm for the measurement of refractive index of NaCl solution (grams dissolved in 100 ml of water) as shown in Figure 5.7.

Figure 5.8 (a) shows the output spectra of the proposed sensor in the solutions with different RIs (see legend). A small reflection peak situated at the middle between λ_{01} and λ_{11} is the result of the intermodal coupling between LP_{01} and LP_{11} modes. In the observation, both Bragg wavelengths λ_{01} and λ_{11} linearly shift with the change of solution RI, Δn in the range of 0.000 – 0.046. The RI sensitivities for both λ_{01} and λ_{11} are estimated to be 1.183 nm/RIU and 4.816 nm/RIU respectively with good linearity, R^2 > 94%. It is also observed that the RI sensitivity for mode-coupled wavelength is ~3.000 nm/RIU, which is the average of the aforesaid sensitivities.

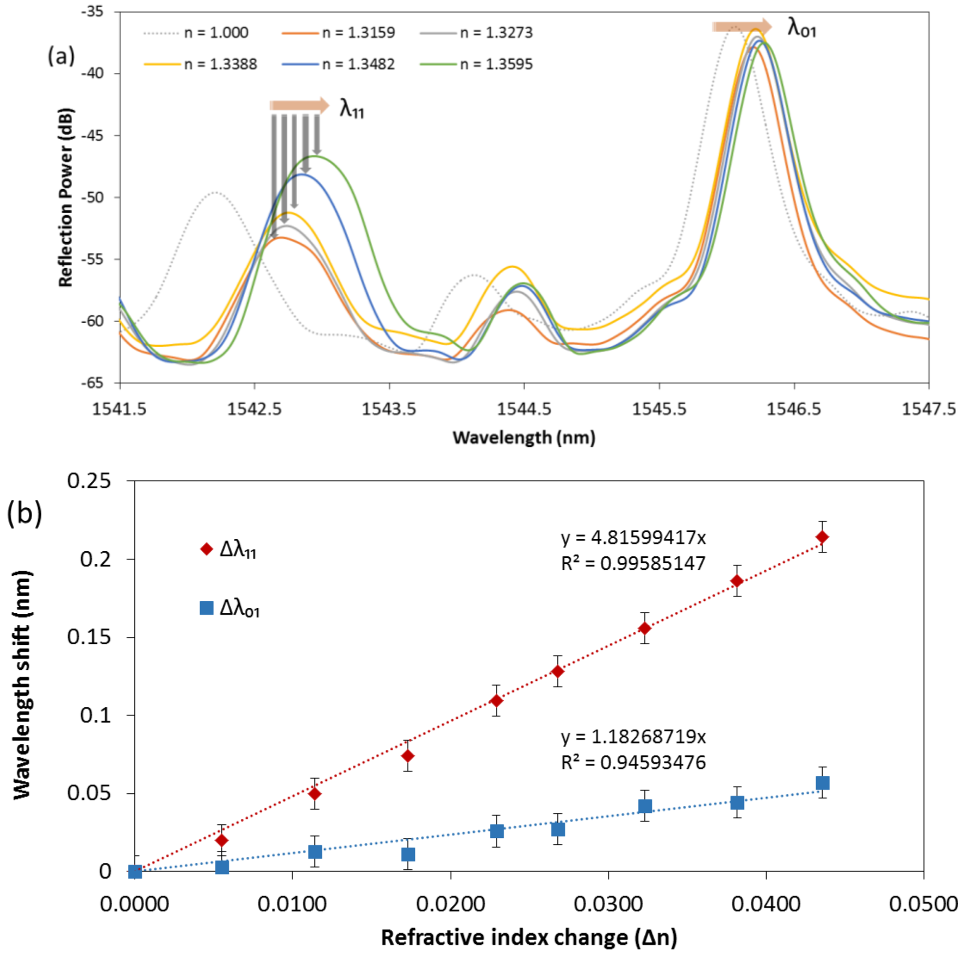

Figure 5.8: (a) Reflection spectra of the proposed sensor in the solution of different refractive indices (room temperature ~ 22°C). The grey dotted curve represents the reflection spectra of sensor in air (n= 1). (b) The relationship between wavelength shifts of λ_{01} and λ_{11} and the change in solution RI (H. Z. Yang et al., 2015).

Figure 5.9 shows the temperature response of the proposed sensor in the range of 22 °C~70 °C, for the solution with RI of 1.3159 at 22 °C. The measured temperature sensitivities for λ_{01} and λ_{11} are 9.62 ± 0.08 pm/°C and 9.52 ± 0.13 pm/°C respectively. The same characterization was repeated with solutions of different RIs, *n* as listed in the legend of Figure 5.10. In Figure 5.10 (a) and (b), the relationships between wavelength shifts $\Delta\lambda_{01}$ and $\Delta\lambda_{11}$ with the change of temperature has been shown. Based on the temperature sensitivity from each linear graph in Figure 5.10 (a) and (b), the variation of temperature sensitivity with RI change is obtained and as presented in Figure 5.11.

These variations indicate that the temperature sensitivities of λ_{01} and λ_{11} are weak functions of RI and the influence of this cross sensitivity should not be neglected. Nevertheless, it should be included in the characterization and measurement. The tests were repeated six times to acquire average temperature sensitivities at different reflective indices as presented in Figure 5.11. The error bars in the figure denote the deviations of sensitivities which are taken from the sensitivity slope uncertainties.

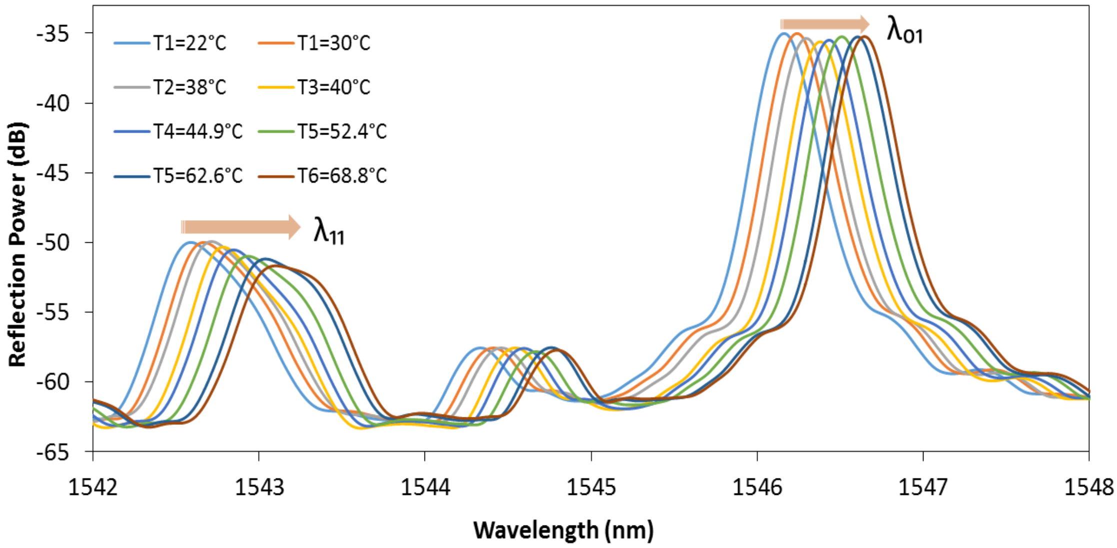

Figure 5.9: Reflection spectra of the sensor at different temperature (solution RI, n_o = 1.3159) (H. Z. Yang et al., 2015).

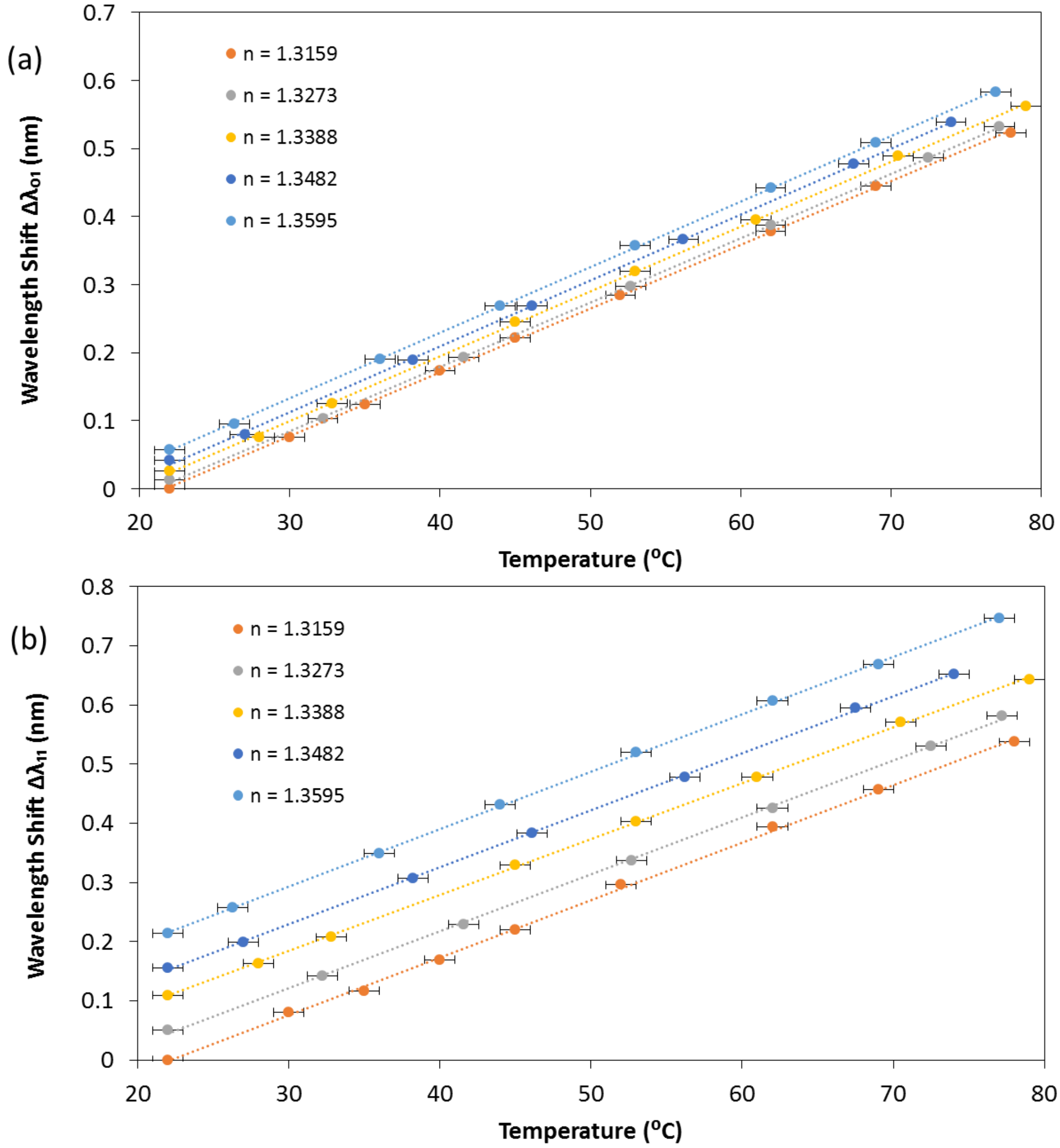

Figure 5.10: The relationship between wavelength shifts (a) $\Delta\lambda_{01}$ and (b) $\Delta\lambda_{11}$, and changes in temperature T (°C) and solution RI (n); the dotted lines show the linear curve fit for the experimental data and the error bar shows the uncertainty in temperature within ±1°C (H. Z. Yang et al., 2015).

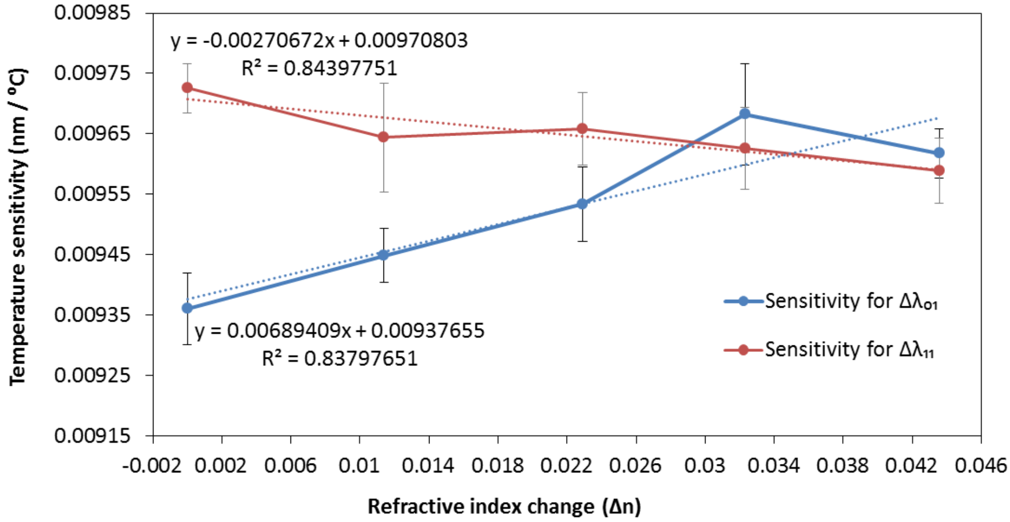

Figure 5.11: The variation of temperature sensitivities (nm/°C) of λ_{01} and λ_{11} with the change of solution RI with reference to n_o. The error bars represent the uncertainty in temperature sensitivities at different refractive indices (H. Z. Yang et al., 2015).

From the obtained results as shown in Figure 5.8 (b) and Figure 5.10, it is clear that the proposed sensor can be used for simultaneous temperature and RI measurement. It can be realized with the aid of simultaneous linear equations which can be presented in matrix form as follow (Hang Zhou Yang et al., 2015)

$$\begin{bmatrix} \Delta\lambda_{01} \\ \Delta\lambda_{11} \\ \Delta\lambda \end{bmatrix} = \begin{bmatrix} \kappa_{\alpha(\lambda_{01})} & \kappa_{\alpha(\lambda_{01})} & \kappa_{n(\lambda_{01})} \\ \kappa_{\alpha(\lambda_{11})} & \kappa_{\alpha(\lambda_{11})} & \kappa_{n(\lambda_{11})} \\ 0 & 0 & \kappa_{n(\lambda_{01})} - \kappa_{n(\lambda_{11})} \end{bmatrix} \begin{bmatrix} \Delta\alpha \\ \Delta T \\ \Delta n \end{bmatrix} \quad \textbf{(5-1)}$$

where κ_T and κ_n are the calibrated sensitivities of temperature and RI, $\Delta\lambda_{01}$ and $\Delta\lambda_{11}$ are the wavelength shifts of λ_{01} and λ_{11}. κ_α is the cross sensitivity between temperature and RI and it depends on the other physical parameters like turbidity, temperature gradient and etc. Some precautions have been applied to minimize the influence of the aforementioned factors. As depicted in Figure 5.10, the error bars are very small; it is fair to assume that those effects can be negligible. ΔT and Δn represent the change in temperature and ambient RI, respectively. Hence, the temperature and RI of the solution can be measured by inverting the matrix in (5-1),

$$\begin{bmatrix}\Delta\alpha\\ \Delta T\\ \Delta n\end{bmatrix}=\begin{bmatrix}\kappa_{\alpha(\lambda_{01})} & \kappa_{\alpha(\lambda_{01})} & \kappa_{n(\lambda_{01})}\\ \kappa_{\alpha(\lambda_{11})} & \kappa_{\alpha(\lambda_{11})} & \kappa_{n(\lambda_{11})}\\ 0 & 0 & \kappa_{n(\lambda_{01})}-\kappa_{n(\lambda_{11})}\end{bmatrix}^{-1}\begin{bmatrix}\Delta\lambda_{01}\\ \Delta\lambda_{11}\\ \Delta\lambda\end{bmatrix} \quad \textbf{(5-2)}$$

The elements in the 3×3 characteristic matrix in Eq (5.2) can be obtained from experimental results in Figure 5.8 and Figure 5.11. These are given as,

$\kappa_{\alpha(\lambda_{01})} = 6.894 \times 10^{-3}$nm/^{o}C.RIU,

$\kappa_{T(\lambda_{01})} = 9.377 \times 10^{-3}$nm/^{o}C,

$\kappa_{\alpha(\lambda_{11})} = -2.707 \times 10^{-3}$ nm/^{o}C.RIU,

$\kappa_{T(\lambda_{11})} = 9.708 \times 10^{-3}$ nm/^{o}C,

$\kappa_{n(\lambda_{01})} = 1.1827$ nm/RIU, and

$\kappa_{n(\lambda_{11})} = 4.8160$ nm/RIU.

After getting the values of ΔT and Δn, the actual values of T and n can be easily determined from

$$T\ (°\mathrm{C}) = \mathrm{T}_0 + \Delta T \quad \textbf{(5-3)}$$

$$n = \mathrm{n}_0 + \Delta n \quad \textbf{(5-4)}$$

where T_0 = 22°C and n_0 = 1.3159. The characterized equations of experimental results of the sensor and actual values of temperature and refractive indices acquired from thermocouple (at the time of measurements) and prism coupler (at room temperature) are in good agreement as in Figure 5.12, with the temperature range from 22 °C to ~75 °C at a fixed ambient RI (1.3159) and then repeated for the other ambient RI values up to 1.3595. Here it is mentioned that the cross sensitivity factor that has been included in the characterized model has reduced the expected deviations of refractive index due to dependence on temperature. The deviations in the RI and temperature measurement presented in Figure 5.11, are ±8×10^{-4} and ±1 °C respectively. It should be noted that in the experimental results each data point is the mean of five readings with error bar representing the deviation from mean value. By considering the similar methods for the measurement of the accuracy, sensitivity, and the repeatability as in (Golnabi, 2004; Golnabi & Azimi, 2007), it has been investigated that the proposed sensor is more accurate (0.5 % error) due to the inclusion of cross-sensitivity factor, and high sensitive (specifically for higher order mode for RI measurement as shown in Figure 5.8) and exhibits the high repeatability with deviations of $\pm 8\times 10^{-4}$ and ±1 °C in the measurement of RI and temperature respectively.

The image of final designed packaged sensor is shown in Figure 5.13 along with the graphical measurements illustrations. In addition, the investigation has indicated that the sensor is suitable for simultaneous measurement of refractive index and temperature with good sensitivity and repeatability. Nevertheless, the proposed sensor has some limitations for instance the concentration inhomogeneity in the tested solution may cause erroneous measurement. Other factors such as mechanical instability and fragility may contribute to the uncertainty in the measurement. It is suggested that the proposed sensor should be properly packaged to eliminate the aforementioned factors and to prolong the lifespan of the sensor. The potential applications include food processing, drug synthesis, water treatment, biomedical and chemical solutions.

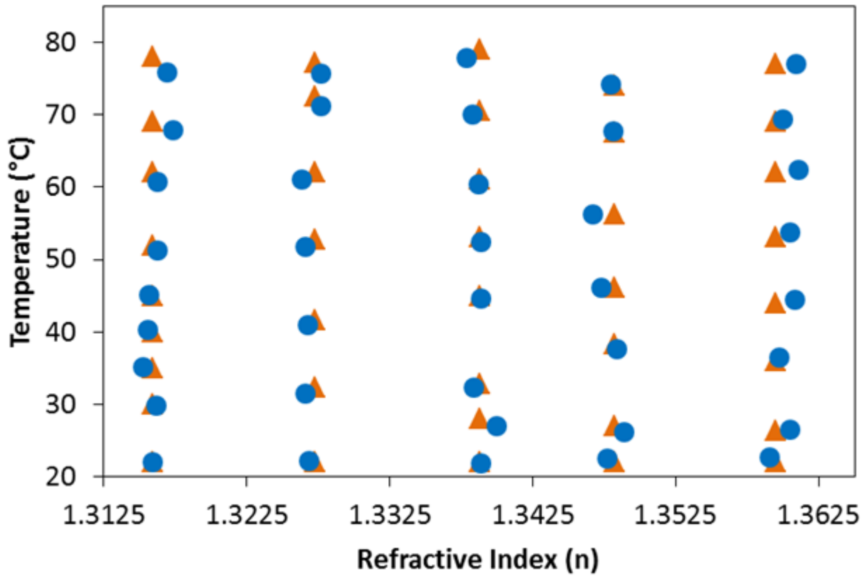

Figure 5.12: Comparison between measured data using the proposed sensor (●) and reference data (▲) acquired from thermocouple (at the time of measurements) and prism coupler (at room temperature) for temperature and refractive index measurements (H. Z. Yang et al., 2015).

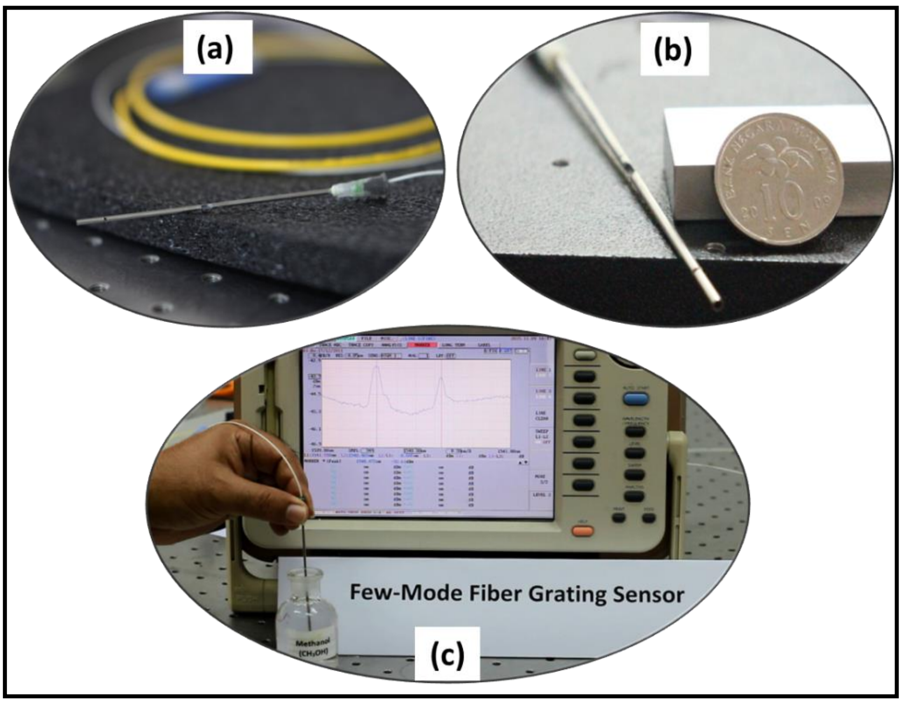

Figure 5.13: Packaged cladless few-mode fiber Bragg grating sensor and measurements illustrations.

5.5 Summary

In this chapter, the FM-FBGs were used for the investigation of modal sensitivities. Two-mode FM-FBGs were chemically etched to make sensitive to the ambient environment such as refractive index and temperature. Dispersion relation of circular waveguide is used to describe the wavelength characteristics of the proposed sensor and the simulation result indicates which were performed in chapter 3, section 3.7 that an etched diameter of 14.1 μm can produce an optimal performance for both power confinement and RI sensitivity for all Bragg wavelengths of the FM-FBG. Experimental results have indicated that the grating device has the RI sensitivities for both λ_{01} and λ_{11} were estimated to be 1.183 nm/RIU and 4.816 nm/RIU respectively, and temperature sensitivities for λ_{01} and λ_{11} are 9.62 ± 0.08 pm/°C and 9.52 ± 0.13 pm/°C respectively. With the assistance of 3 × 3 characteristic matrix, discrimination measurements of temperature and RI were demonstrated and the deviations in RI and temperature measurements were $\pm 8 \times 10^{-4}$ RIU and ±1 ºC respectively. Furthermore, the fabricated sensor was packaged which was more stable and easy to handle for the measurements. The maximum RI of the solution which was considered in the study is 1.3595 (max refractive index of NaCl solution prepared in laboratory). However it can be further increased for other solutions. Also the sensor performance is similar for temperature range as that of normal FBG But in case of ultra-high temperature the FBG can be regenerated first before etching and then can be used .

CHAPTER 6: CONCLUSION AND FUTURE WORK

This thesis focuses on theoretical, numerical, and experimental analyses of FM-FBGs. This research is divided into five chapters, and the summary of each chapter is given below. Following the conclusion, perspectives on future work are given to recommend further developments for the present study.

6.1 Conclusion

The historical background of fiber-optic technology and the recent developments in the field of FMF, as well as the motivation for the presented research, study objectives, and thesis outlines, are presented briefly in Chapter 1. Furthermore, a brief theoretical background on optical fibers with the modal characteristic equation and coupled mode theory is discussed in Chapter 2. The applications of FMFs in the implementation of SDM and sensing technologies are also presented. In Chapter 3, the photosensitivity enhancement of optical fiber through hydrogen loading and the details of UV lasers are discussed. FM-FBGs were fabricated with high-reflective mode resonant wavelengths. Moreover, simulations for the reflection and transmission spectra of FM-FBGs were conducted, and the findings agree with the real spectra of FM-FBGs. Considering the imperfections, environmental changes during the fabrication of FBGs, or the pre-strained condition of the fiber during grating inscription, the grating period should be accurately measured. A novel optical imaging technique is introduced in this work. Investigations have revealed that the proposed approach is more appealing and accurate. In the image processing of the acquired images of grating structure inside the optical fiber, the sample size M was an important parameter that monitored the accuracy of estimating the grating period. The findings indicated that larger sample sizes yield grating profiles with better SNR of optical images, which help reduce the uncertainty of the grating period measurement. However, the accuracy of the proposed technique relies on the parallelism between the grating structure and the image's horizontal axis. The optimal estimation was attained when the angle of rotation was zero. Moreover, the linear slope of the graph of fractional Bragg wavelength shift $\Delta\lambda / \lambda$ against the strain applied $\Delta\Lambda / \Lambda$ was found to be 0.776, whereas the strain-optic coefficient was 0.224. These findings agree with those reported in the literature. The grating period of the inscribed FM-FBGs was also measured and verified. In the last section of Chapter 3, numerical simulations are varied for FM-FBGs. The mode intensity profiles and the transmission and reflection spectra of 2M-FBG with mode coupling and selective mode excitation were investigated. Furthermore, the effects of chemical etching on the modal sensitivities and power confinement ratios inside 2M-FMF were numerically simulated.

The mode-coupling properties for 2M-FBGs and 4M-FBGs with the selective mode excitation were investigated using binary phase plates in Chapter 4. The resonant wavelengths were found to be associated with a particular excitation for both self-coupling and cross-coupling, which can be excited and observed in the output spectra. The mode-coupling properties of the resonant wavelengths were identified using the simulation results. Mode conversion at the cross-coupling-associated resonant wavelengths have been demonstrated and verified with the reflected mode intensity profile. Lastly, the results indicate that two different bidirectional mode conversions can be realized with a 2M-FBG, whereas six different bidirectional mode conversions can be realized with a 4M-FBG. By considering the bandwidth limitation of FM-FBGs at cross-mode coupling wavelengths at which the mode conversion can be conducted, the tunability methods of FM-FBGs were presented. The applied strain and temperature variation were the possible solutions to tune the Bragg wavelengths to the desired positions. The temperature sensitivities of all FM-FBG modes were in the range of approximately 9.57 ± 0.12 pm/°C, which is comparable with standard single-mode FBGs. The observed mean of the strain sensitivities for all FM-FBG modes lie within the range of approximately 0.535 (pm/με). Therefore, FM-FBGs can be considered as the optimal solution for mode converters in all fiber MDM or SDM technologies.

The modal sensitivities of cladless FM-FBG sensor to the temperature and refractive index were experimentally investigated in Chapter 5. Chemical etching technique was used to reduce the fiber diameter of two FBG modes to access the evanescent field of the fundamental and higher order mode in the optical fiber. Simulations were performed to investigate the refractive index sensitivities of the reflective modes of FM-FBGs at different etched diameters. The simulation results show that an etched diameter of 14.1 μm can exhibit better performance for optimal power confinement of etched FM-FBG without losing the higher order mode. The measured RI sensitivities of cladless FM-FBG were 1.183 nm/RIU and 4.816 nm/RIU for λ_{01} and λ_{11} wavelengths, which correspond to self-mode couplings of LP_{01} and LP_{11} modes, respectively. The sensitivities for temperature were in the range between 9.57 ± 0.12 pm/°C. For accurate and simultaneous measurement besides those of temperature and RI sensitivities for LP_{01} and LP_{11} modes, the element of cross sensitivity between temperature and RI was also included using 3 × 3 characteristic matrix. The deviations in RI and temperature were found to be $\pm 8 \times 10^{-4}$ and $\sim\pm 1^{o}$C respectively. Through these investigations, the sensor was found to be suitable for simultaneous measurement of refractive index and temperature with good sensitivity and repeatability. Nevertheless, the proposed sensor has some limitations; for instance, the concentration inhomogeneity in the tested solution may cause erroneous measurement. Other factors such as mechanical instability and fragility of the device may contribute to uncertainties in the measurement. Thus, the proposed sensor should be properly packaged to eliminate the aforementioned factors and to prolong the lifespan of the sensor. The potential applications include food processing, drug synthesis, and water treatment.

In conclusion, the fabrication of FM-FBGs and the characterization of modal coupling and modal sensitivities have been experimentally demonstrated and further adopted for mode conversion and sensing applications. FM-FBGs with high reflectivity and stability were fabricated, and an exact grating period measurement technique was developed. Characteristic equations of optical fibers and coupled mode equations for FMFs from the theoretical model were reviewed. The experimental and theoretical results were analyzed to achieve in-depth understanding on these FM-FBGs devices. Several characteristics of FM-FBGs devices, particularly mode extinction ratio, modal sensitivities to physical changes, and modal coupling, were observed and exploited in multi-wavelength laser systems and sensor applications in this research. The experiments have shown promising results. Overall, this research on FM-FBG devices has achieved a great success.

6.2 Future Work

In the future, more advanced modeling and analysis techniques of the FMF-based devices should be developed to simplify the digital signal processing complexities in SDM technology. The ultimate goal of developing this field is to develop economical and affordable all-fiber SDM technology. Various specialty fibers should be designed and fabricated so that the main requirements of the MDM systems can be achieved, such as low MDL, low IL, low intermodal coupling, and low DMGD. However, mode converters using FM-FBGs require high mode extinction ratio, large wavelength band, and strong mode coupling to make them tunable and more efficient. Therefore, photonic integration of FMF to the existing communication system in its initial stages will be essential. Moreover, FMF fiber-based devices can be produced at a reasonable cost and scaled to high-volume manufacturing relative to SMFs. Most network operators will only consider deploying SDM if it lowers the cost-per-bit, provides the routing flexibility needed for efficient photonic mesh networks, and allows a reasonable transitional strategy from systems based on standard SMF. Regardless of the ultimate outcome, the next few years will appear to be a busy and exciting time for research on optical fiber communications.

Various properties of FM-FBG structures should be explored and exploited for different applications to enrich the list of FMF devices, such as chirped FM-FBGs and super-structured FM-FBGs. Chirped FBGs present larger FWHM; hence, more interesting results are expected and should be investigated for mode conversions. Super-structured FM-FBGs may help achieve the add drop multi-wavelength and modal filters. Furthermore, FM-FBGs establish a good scope in the field of multi-parameter sensing; therefore, the effort should be dedicated into expanding and improving the functionalities of these FM-FBG-based sensors. Multi-parameter sensing provides considerable potential for medical applications, particularly in body or structure health monitoring, as well as in chemical, petrol, and gas industries. Thermally regenerated FBGs are other important and interesting devices that should be investigated, which may enable multi-parameter sensing in ultrahigh temperature environments.

REFERENCES

Agrawal, G. P. (2007). *Nonlinear fiber optics*: Academic press.

Agrawal, G. P. (2012). *Fiber-optic communication systems* (Vol. 222): John Wiley & Sons.

Ali, M. M., Lim, K. S., Yang, H. Z., Chong, W. Y., Lim, W. S., & Ahmad, H. (2013). Direct period measurement for fiber Bragg grating using an optical imaging technique. *Applied optics, 52*(22), 5393-5397.

Ali, M. M., Yongmin, J., Kok-Sing, L., Islam, M. R., Alam, S. U., Richardson, D. J., & Ahmad, H. (2015). Characterization of Mode Coupling in Few-Mode FBG With Selective Mode Excitation. *Photonics Technology Letters, IEEE, 27*(16), 1713-1716.

Andermahr, N., & Fallnich, C. (2010). Optically induced long-period fiber gratings for guided mode conversion in few-mode fibers. *Optics express, 18*(5), 4411-4416.

Annamalai, M., & Vasilyev, M. (2012). Phase-sensitive multimode parametric amplification in a parabolic-index waveguide. *Photonics Technology Letters, IEEE, 24*(21), 1949-1952.

Bai, N., Ip, E., Huang, Y.-K., Mateo, E., Yaman, F., Li, M.-J., . . . Montero, C. (2012). Mode-division multiplexed transmission with inline few-mode fiber amplifier. *Optics express, 20*(3), 2668-2680.

Belhadj, N., LaRochelle, S., & Dossou, K. (2004). Form birefringence in UV-exposed photosensitive fibers computed using a higher order finite element method. *Optics express, 12*(8), 1720-1726.

Berdagué, S., & Facq, P. (1982). Mode division multiplexing in optical fibers. *Applied optics, 21*(11), 1950-1955.

Bigot, L., Le Cocq, G., & Quiquempois, Y. (2015). Few-Mode Erbium-Doped Fiber Amplifiers: A Review. *Journal of Lightwave Technology, 33*(3), 588-596.

Bogart, K. P. (1989). *Introductory combinatorics*: Saunders College Publishing.

Bosco, G., Carena, A., Curri, V., Poggiolini, P., & Forghieri, F. (2010). Performance limits of Nyquist-WDM and CO-OFDM in high-speed PM-QPSK systems. *Photonics Technology Letters, IEEE, 22*(15), 1129-1131.

Boys, C. V. (1887). On the production, properties, and some suggested uses of the finest threads. *Philosophical Magazine, 23*(45), 489-499.

Boys, C. V. (1889). Quartz fibres. *Nature*, 247–251.

Broer, M., Cone, R., & Simpson, J. R. (1991). Ultraviolet-induced distributed-feedback gratings in Ce 3+-doped silica optical fibers. *Optics letters, 16*(18), 1391-1393.

Bullington, A. L., Pax, P. H., Sridharan, A. K., Heebner, J. E., Messerly, M. J., & Dawson, J. W. (2012). Mode conversion in rectangular-core optical fibers. *Applied optics, 51*(1), 84-88.

Burns, R. W. (2004). *Communications: an international history of the formative years* (Vol. 32): IET.

Butov, O., Dianov, E., & Golant, K. (2006). Nitrogen-doped silica-core fibres for Bragg grating sensors operating at elevated temperatures. *Measurement science and technology, 17*(5), 975.

Cai, J.-X., Cai, Y., Davidson, C., Lucero, A., Zhang, H., Foursa, D., . . . Mohs, G. (2011). *20 Tbit/s capacity transmission over 6,860 km.* Paper presented at the Optical Fiber Communication Conference.

Cappellini, G., & Trillo, S. (1991). Third-order three-wave mixing in single-mode fibers: exact solutions and spatial instability effects. *JOSA B, 8*(4), 824-838.

Chen, D., Wu, C., Tse, M., & Tam, H.-Y. (2011). Hydrostatic pressure sensor based on mode interference of a few mode fiber. *Progress In Electromagnetics Research, 119*, 335-343.

Chen, X., Li, A., Ye, J., Al Amin, A., & Shieh, W. (2013). Demonstration of few-mode compatible optical add/drop multiplexer for mode-division multiplexed superchannel. *Lightwave Technology, Journal of, 31*(4), 641-647.

Chester, A. N., Martellucci, S., & Scheggi, A. V. (2012). *Optical fiber sensors* (Vol. 132): Springer Science & Business Media.

Choi, S.-K., Li, R.-D., Kim, C., & Kumar, P. (1997). Traveling-wave optical parametric amplifier: investigation of its phase-sensitive and phase-insensitive gain response. *JOSA B, 14*(7), 1564-1575.

Chryssis, A. N., Lee, S. M., Lee, S. B., Saini, S. S., & Dagenais, M. (2005). High sensitivity evanescent field fiber Bragg grating sensor. *Photonics Technology Letters, IEEE, 17*(6), 1253-1255.

Chuang, W., Zhengyong, L., Kit Man, C., Tse, M. L. V., Chan, F. Y. M., Lau, A. P. T., . . . Haw-Yaw, T. (2012). Strong LP_{01} and LP_{11} Mutual Coupling Conversion in a Two-Mode Fiber Bragg Grating. *Photonics Journal, IEEE, 4*(4), 1080-1086.

Daniel, J. M. O., Chan, J. S. P., Kim, J. W., Sahu, J. K., Ibsen, M., & Clarkson, W. A. (2011). Novel technique for mode selection in a multimode fiber laser. *Optics express, 19*(13), 12434-12439.

Desurvire, E. (2002). *Erbium-doped fiber amplifiers: principles and applications*: Wiley-Interscience.

Dong, J., & Chiang, K. S. (2015). Temperature-Insensitive Mode Converters With CO 2-Laser Written Long-Period Fiber Gratings. *Photonics Technology Letters, IEEE, 27*(9), 1006-1009.

Dong, X., Tam, H., & Shum, P. (2007). Temperature-insensitive strain sensor with polarization-maintaining photonic crystal fiber based Sagnac interferometer. *Applied Physics Letters, 90*(15), 151113.

Dragomir, N. M., Rollinson, C., Wade, S. A., Stevenson, A. J., Collins, S. F., Baxter, G. W., . . . Roberts, A. (2003). Nondestructive imaging of a type I optical fiber Bragg grating. *Optics letters, 28*(10), 789-791.

Ebendorff-Heidepriem, H., & Ehrt, D. (2000). Formation and UV absorption of cerium, europium and terbium ions in different valencies in glasses. *Optical Materials, 15*(1), 7-25.

Ellis, A., & Doran, N. (2013). Are few-mode fibres a practical solution to the capacity crunch?

Ellis, A. D., & Suibhne, N. M. (2012). *The MODE-GAP Project.* Paper presented at the Frontiers in Optics.

Essiambre, R.-J., Kramer, G., Winzer, P. J., Foschini, G. J., & Goebel, B. (2010). Capacity limits of optical fiber networks. *Journal of Lightwave Technology, 28*(4), 662-701.

Essiambre, R.-J., & Tkach, R. W. (2012). Capacity trends and limits of optical communication networks. *Proceedings of the IEEE, 100*(5), 1035-1055.

Fang, L., & Jia, H. (2014a). Coupling analyses of LP 0m modes with optical fiber gratings in multimode fiber and their application in mode-division multiplexing transmission. *Optics Communications, 322*, 118-122.

Fang, L., & Jia, H. (2014b). Mode add/drop multiplexers of LP 02 and LP 03 modes with two parallel combinative long-period fiber gratings. *Optics express, 22*(10), 11488-11497.

Feng, X., Liu, Y., Fu, S., Yuan, S., & Dong, X. (2004). Switchable dual-wavelength ytterbium-doped fiber laser based on a few-mode fiber grating. *Photonics Technology Letters, IEEE, 16*(3), 762-764.

Ferreira, F. M., Fonseca, D., & da Silva, H. J. (2014). Design of few-mode fibers with M-modes and low differential mode delay. *Lightwave Technology, Journal of, 32*(3), 353-360.

Fontaine, N. K., Ryf, R., Bland-Hawthorn, J., & Leon-Saval, S. G. (2012). Geometric requirements for photonic lanterns in space division multiplexing. *Optics express, 20*(24), 27123-27132.

Gabet, R., Le Cren, E., Jin, C., Gadonna, M., Ung, B., Jaouen, Y., . . . La Rochelle, S. (2014). *Characterization of Few Mode Fibers by OLCI Technique.* Paper presented at the Optical Communication (ECOC 2014), 40th European Conference and Exhibition on, At Cannes (France).

Gao, S., Zhang, W., Zhang, H., Geng, P., Lin, W., Liu, B., . . . Xue, X. (2013). Fiber modal interferometer with embedded fiber Bragg grating for simultaneous measurements of refractive index and temperature. *Sensors and Actuators B: Chemical, 188*, 931-936.

Gao, Y., Sun, J., Chen, G., & Sima, C. (2015). Demonstration of simultaneous mode conversion and demultiplexing for mode and wavelength division multiplexing systems based on tilted few-mode fiber Bragg gratings. *Optics express, 23*(8), 9959-9967.

Genevaux, P., Simonneau, C., Le Cocq, G., Quiquempois, Y., Bigot, L., Boutin, A., & Charlet, G. (2016). A Five-Mode Erbium-Doped Fiber Amplifier for Mode-Division Multiplexing Transmission. *Journal of Lightwave Technology, 34*(2), 456-462.

Ghatak, A., & Thyagarajan, K. (1998). *An introduction to fiber optics*: Cambridge university press.

Giles, I., Obeysekara, A., Chen, R., Giles, D., Poletti, F., & Richardson, D. (2012). Fiber LPG mode converters and mode selection technique for multimode SDM. *Photonics Technology Letters, IEEE, 24*(21), 1922-1925.

Gillooly, A. (2011). Photosensitive fibres: Growing gratings. *Nature Photonics, 5*(8), 468-469.

Golnabi, H. (2004). Design and operation of a fiber optic sensor for liquid level detection. *Optics and Lasers in Engineering, 41*(5), 801-812.

Golnabi, H., & Azimi, P. (2007). Design and performance of a plastic optical fiber leakage sensor. *Optics & Laser Technology, 39*(7), 1346-1350.

Gong, M., Yuan, Y., Li, C., Yan, P., Zhang, H., & Liao, S. (2007). Numerical modeling of transverse mode competition in strongly pumped multimode fiber lasers and amplifiers. *Optics express, 15*(6), 3236-3246.

Grüner-Nielsen, L., & Nicholson, J. W. (2012). *Stable mode converter for conversion between LP01 and LP11 using a thermally induced long period grating.* Paper presented at the Proceedings of IEEE Summer Topical Meeting.

Grüner-Nielsen, L., Sun, Y., Nicholson, J. W., Jakobsen, D., Jespersen, K. G., Lingle Jr, R., & Pálsdóttir, B. (2012). Few mode transmission fiber with low DGD, low mode coupling, and low loss. *Journal of Lightwave Technology, 30*(23), 3693-3698.

Grüner-Nielsen, L., Wandel, M., Kristensen, P., Jorgensen, C., Jorgensen, L. V., Edvold, B., . . . Jakobsen, D. (2005). Dispersion-compensating fibers. *Journal of Lightwave Technology, 23*(11), 3566.

Guo, P., Rao, Y., Li, D., Gong, Y., Peng, G., Wu, Y., . . . Wu, H. (2013). Inscription of Bragg gratings in few-mode optical fibers. *Chinese Optics Letters, 11*(2), 020606.

Guo, T., Wong, A. C., Liu, W.-S., Guan, B.-O., Lu, C., & Tam, H.-Y. (2011). Beat-frequency adjustable Er 3+-doped DBR fiber laser for ultrasound detection. *Optics express, 19*(3), 2485-2492.

Hamel, P., Jaouen, Y., Gabet, R., & Ramachandran, S. (2007). Optical low-coherence reflectometry for complete chromatic dispersion characterization of few-mode fibers. *Optics letters, 32*(9), 1029-1031.

Hansryd, J., Andrekson, P., Westlund, M., Li, J., & Hedekvist, P.-O. (2002). Fiber-based optical parametric amplifiers and their applications. *Selected Topics in Quantum Electronics, IEEE Journal of, 8*(3), 506-520.

Hanzawa, N., Saitoh, K., Sakamoto, T., Matsui, T., Tomita, S., & Koshiba, M. (2011). *Demonstration of mode-division multiplexing transmission over 10 km two-mode fiber with mode coupler.* Paper presented at the Optical Fiber Communication Conference.

Hayashi, T., Taru, T., Shimakawa, O., Sasaki, T., & Sasaoka, E. (2011). *Ultra-low-crosstalk multi-core fiber feasible to ultra-long-haul transmission.* Paper presented at the National Fiber Optic Engineers Conference.

Hecht, J. (2004). *City of light: the story of fiber optics*: Oxford university press.

Hellwig, T., Schnack, M., Walbaum, T., Dobner, S., & Fallnich, C. (2014). Experimental realization of femtosecond transverse mode conversion using optically induced transient long-period gratings. *Optics express, 22*(21), 24951-24958.

Hellwig, T., Walbaum, T., & Fallnich, C. (2013). Optically induced mode conversion in graded-index fibers using ultra-short laser pulses. *Applied Physics B, 112*(4), 499-505.

Herbster, A. F., & Romero, M. A. (2014). Few-mode erbium-doped fiber amplifier design method based on the signal-pump overlap integral. *Optical Engineering, 53*(9), 096101-096101.

Hermann, W., Hutjens, M., & Wiechert, D. U. (1989). Stress in optical waveguides. 3: Stress induced index change. *Applied optics, 28*(11), 1980-1983.

Hill, K., Fujii, Y., Johnson, D. C., & Kawasaki, B. (1978). Photosensitivity in optical fiber waveguides: Application to reflection filter fabrication. *Applied Physics Letters, 32*(10), 647-649.

Hill, K., Malo, B., Bilodeau, F., & Johnson, D. (1993). Photosensitivity in optical fibers. *Annual Review of Materials Science, 23*(1), 125-157.

Hill, K., Malo, B., Vineberg, K., Bilodeau, F., Johnson, D., & Skinner, I. (1990). Efficient mode conversion in telecommunication fibre using externally written gratings. *Electronics Letters, 26*(16), 1270-1272.

Huang, T., Fu, S., Ke, C., Shum, P. P., & Liu, D. (2014). Characterization of Fiber Bragg Grating Inscribed in Few-Mode Silica-Germanate Fiber. *Photonics Technology Letters, IEEE, 26*(19), 1908-1911.

Iadicicco, A., Campopiano, S., Cutolo, A., Giordano, M., & Cusano, A. (2005). Nonuniform thinned fiber Bragg gratings for simultaneous refractive index and temperature measurements. *Photonics Technology Letters, IEEE, 17*(7), 1495-1497.

Igarashi, K., Souma, D., Takeshima, K., & Tsuritani, T. (2015). Selective mode multiplexer based on phase plates and Mach-Zehnder interferometer with image inversion function. *Optics express, 23*(1), 183-194.

Igarashi, K., Souma, D., Tsuritani, T., & Morita, I. (2014). Performance evaluation of selective mode conversion based on phase plates for a 10-mode fiber. *Optics express, 22*(17), 20881-20893. doi:10.1364/OE.22.020881

Inniss, D., Zhong, Q., Vengsarkar, A., Reed, W., Kosinski, S., & Lemaire, P. (1994). Atomic force microscopy study of uv‐induced anisotropy in hydrogen‐loaded germanosilicate fibers. *Applied Physics Letters, 65*(12), 1528-1530.

Ip, E., Li, M.-J., Bennett, K., Huang, Y.-K., Tanaka, A., Korolev, A., . . . Hu, J. (2014). 146λ× 6× 19-Gbaud wavelength-and mode-division multiplexed transmission over 10× 50-km spans of few-mode fiber with a gain-equalized few-mode EDFA. *Journal of Lightwave Technology, 32*(4), 790-797.

Ip, E., Li, M.-j., Montero, C., & Yano, Y. (2013). *6x28-Gbaud Few-Mode Recirculating Loop Transmission with Gain-Equalized Inline Few-Mode Fiber Amplifier*. Paper presented at the Optical Fiber Communication Conference.

Ismaeel, R., Lee, T., Oduro, B., Jung, Y., & Brambilla, G. (2014). All-fiber fused directional coupler for highly efficient spatial mode conversion. *Optics express, 22*(10), 11610-11619.

James, S. W., & Tatam, R. P. (2003). Optical fibre long-period grating sensors: characteristics and application. *Measurement science and technology, 14*(5), R49-R61.

Jung, Y., Chen, R., Ismaeel, R., Brambilla, G., Alam, S.-U., Giles, I., & Richardson, D. (2013). Dual mode fused optical fiber couplers suitable for mode division multiplexed transmission. *Optics express, 21*(20), 24326-24331.

Jung, Y., Kang, Q., Sahu, J. K., Corbett, B., Winfield, R., Poletti, F., . . . Richardson, D. J. (2014). Reconfigurable modal gain control of a few-mode EDFA supporting six spatial modes. *IEEE Photon. Technol. Lett, 26*(11), 1100-1103.

Jung, Y., Lim, E., Kang, Q., May-Smith, T., Wong, N., Standish, R., . . . Richardson, D. (2014). Cladding pumped few-mode EDFA for mode division multiplexed transmission. *Optics express, 22*(23), 29008-29013.

Kahn, J. M., & Ho, K.-P. (2004). Spectral efficiency limits and modulation/detection techniques for DWDM systems. *Selected Topics in Quantum Electronics, IEEE Journal of, 10*(2), 259-272.

Kang, Q., Lim, E.-L., Jung, Y., Sahu, J. K., Poletti, F., Baskiotis, C., . . . Richardson, D. J. (2012). Accurate modal gain control in a multimode erbium doped fiber amplifier incorporating ring doping and a simple LP 01 pump configuration. *Optics express, 20*(19), 20835-20843.

Kannan, S., Guo, J. Z., & Lemaire, P. J. (1997). Thermal stability analysis of UV-induced fiber Bragg gratings. *Journal of Lightwave Technology, 15*(8), 1478-1483.

Kashyap, R. (1994). Photosensitive optical fibers: Devices and applications. *Optical Fiber Technology, 1*(1), 17-34.

Kashyap, R. (1999). *Fiber bragg gratings*: Academic press.

Kashyap, R. (2010a). Chapter 2 - Photosensitivity and Photosensitization of Optical Fibers. In R. Kashyap (Ed.), *Fiber Bragg Gratings (Second Edition)* (pp. 15-51). Boston: Academic Press.

Kashyap, R. (2010b). Chapter 3 - Fabrication of Bragg Gratings. In R. Kashyap (Ed.), *Fiber Bragg Gratings (Second Edition)* (pp. 53-118). Boston: Academic Press.

Kashyap, R., & Blow, K. (1988). Observation of catastrophic self-propelled self-focusing in optical fibres. *Electronics Letters, 24*(1), 47-49.

Kawano, K., & Kitoh, T. (2004). *Introduction to Optical Waveguide Analysis: Solving Maxwell's Equation and the Schrödinger Equation*: John Wiley & Sons.

Kikuchi, K. (2006). Phase-diversity homodyne detection of multilevel optical modulation with digital carrier phase estimation. *Selected Topics in Quantum Electronics, IEEE Journal of, 12*(4), 563-570.

Kim, B. Y., Blake, J. N., Huang, S.-Y., & Shaw, H. J. (1987). Use of highly elliptical core fibers for two-mode fiber devices. *Optics letters, 12*(9), 729-731.

Kim, Y.-J., Paek, U.-C., & Lee, B. H. (2002). Measurement of refractive-index variation with temperature by use of long-period fiber gratings. *Optics letters, 27*(15), 1297-1299.

Kim, Y. H., & Song, K. Y. (2014). Mapping of intermodal beat length distribution in an elliptical-core two-mode fiber based on Brillouin dynamic grating. *Optics express, 22*(14), 17292-17302.

Kirkendall, C. K., & Dandridge, A. (2004). Overview of high performance fibre-optic sensing. *Journal of Physics D: Applied Physics, 37*(18), R197.

Koizumi, Y., Toyoda, K., Yoshida, M., & Nakazawa, M. (2012). 1024 QAM (60 Gbit/s) single-carrier coherent optical transmission over 150 km. *Optics express, 20*(11), 12508-12514.

Kouskousis, B. P., Rollinson, C. M., Kitcher, D. J., Collins, S. F., Baxter, G. W., Wade, S. A., . . . Roberts, A. (2006). Quantitative investigation of the refractive-index modulation within the core of a fiber Bragg grating. *Optics express, 14*(22), 10332-10338.

Krummrich, P. M. (2012). *Efficient optical amplification for spatial division multiplexing.* Paper presented at the SPIE OPTO.

Kumar, A., Goel, N. K., & Varshney, R. (2001). Studies on a Few-Mode Fiber-Optic Strain Sensor Based on LP01-LP 02 Mode Interference. *Journal of Lightwave Technology, 19*(3), 358.

Ky, N. H., Limberger, H. G., Salathé, R. P., & Cochet, F. (1998). Effects of drawing tension on the photosensitivity of Sn–Ge-and B–Ge-codoped core fibers. *Optics letters, 23*(17), 1402-1404.

Ky, N. H., Limberger, H. G., Salathé, R. P., Cochet, F., & Dong, L. (1999). Hydrogen-induced reduction of axial stress in optical fiber cores. *Applied Physics Letters, 74*(4), 516-518.

Le Cocq, G., Bigot, L., Le Rouge, A., Bigot-Astruc, M., Sillard, P., Koebele, C., . . . Quiquempois, Y. (2012). Modeling and characterization of a few-mode EDFA supporting four mode groups for mode division multiplexing. *Optics express, 20*(24), 27051-27061.

Lee, K. S., & Erdogan, T. (2001). Fiber mode conversion with tilted gratings in an optical fiber. *JOSA A, 18*(5), 1176-1185.

Lemaire, P. J., Atkins, R., Mizrahi, V., & Reed, W. (1993). High pressure H2 loading as a technique for achieving ultrahigh UV photosensitivity and thermal sensitivity in GeO2 doped optical fibres. *Electronics Letters, 29*(13), 1191-1193.

Leon-Saval, S., Birks, T., Bland-Hawthorn, J., & Englund, M. (2005). Multimode fiber devices with single-mode performance. *Optics letters, 30*(19), 2545-2547.

Leon-Saval, S. G., Fontaine, N. K., Salazar-Gil, J. R., Ercan, B., Ryf, R., & Bland-Hawthorn, J. (2014). Mode-selective photonic lanterns for space-division multiplexing. *Optics express, 22*(1), 1036-1044.

Li, A., Al Amin, A., Chen, X., & Shieh, W. (2011). *Reception of mode and polarization multiplexed 107-Gb/s CO-OFDM signal over a two-mode fiber.* Paper presented at the National Fiber Optic Engineers Conference.

Li, A., Wang, Y., Hu, Q., & Shieh, W. (2015). Few-mode fiber based optical sensors. *Optics express, 23*(2), 1139-1150.

Li, G., Bai, N., Zhao, N., & Xia, C. (2014). Space-division multiplexing: the next frontier in optical communication. *Advances in Optics and Photonics, 6*(4), 413-487.

Li, H.-N., Li, D.-S., & Song, G.-B. (2004). Recent applications of fiber optic sensors to health monitoring in civil engineering. *Engineering structures, 26*(11), 1647-1657.

Li, M.-J., Hoover, B., Li, S., Bickham, S., Ten, S., Ip, E., . . . Wang, T. (2012). *Low delay and large effective area few-mode fibers for mode-division multiplexing.* Paper presented at the 2012 17th Opto-Electronics and Communications Conference.

Li, S., Mo, Q., Hu, X., Du, C., & Wang, J. (2015). Controllable all-fiber orbital angular momentum mode converter. *Optics letters, 40*(18), 4376-4379.

Li, T. (1993). The impact of optical amplifiers on long-distance lightwave telecommunications. *Proceedings of the IEEE, 81*(11), 1568-1579.

Liao, P. (2012). *Theory of Dielectric Optical Waveguides 2e*: Academic press.

Lim, K.-S., Yang, H.-Z., Chong, W.-Y., Cheong, Y.-K., Lim, C.-H., Ali, N. M., & Ahmad, H. (2013). Axial contraction in etched optical fiber due to internal stress reduction. *Optics express, 21*(3), 2551-2562.

Lim, K. S., Ali, M. M., Loo, C. C., Chong, W. Y., & Ahmad, H. (2014). *Observation of mode-coupling in few mode fiber Bragg gratings*.

Liu, H., Pang, F., Guo, H., Cao, W., Liu, Y., Chen, N., . . . Wang, T. (2010). In-series double cladding fibers for simultaneous refractive index and temperature measurement. *Optics express, 18*(12), 13072-13082.

Lobato, A., Ferreira, F., Kuschnerov, M., van den Borne, D., Jansen, S. L., Napoli, A., . . . Lankl, B. (2012). Impact of mode coupling on the mode-dependent loss tolerance in few-mode fiber transmission. *Optics express, 20*(28), 29776-29783.

Lobato Polo, A. P., Ferreira, F., Kuschnerov, M., van den Borne, D., Jansen, S., Spinnler, B., & Lankl, B. (2012). *Impact of Mode Coupling on the Mode-Dependent Loss Tolerance in Few-Mode Fiber Transmission.* Paper presented at the European Conference and Exhibition on Optical Communication.

Lu, C., & Cui, Y. (2006). Fiber Bragg grating spectra in multimode optical fibers. *Journal of Lightwave Technology, 24*(1), 598.

Lu, P., & Chen, Q. (2008). Fiber Bragg grating sensor for simultaneous measurement of flow rate and direction. *Measurement science and technology, 19*(12), 125302.

Lu, P., Harris, J., Xu, Y., Lu, Y., Chen, L., & Bao, X. (2012). Simultaneous refractive index and temperature measurements using a tapered bend-resistant fiber interferometer. *Optics letters, 37*(22), 4567-4569.

Lu, P., & Xu, Y. (2016). *Adaptive Mode Control in a Few-Mode Fiber.* Paper presented at the Optical Fiber Communication Conference.

Ma, Y., Sych, Y., Onishchukov, G., Ramachandran, S., Peschel, U., Schmauss, B., & Leuchs, G. (2009). Fiber-modes and fiber-anisotropy characterization using low-coherence interferometry. *Applied Physics B, 96*(2-3), 345-353.

Mac Suibhne, N., Watts, R., Sygletos, S., Garcia Gunning, F. C., Grüner-Nielsen, L., & Ellis, A. (2012). *Nonlinear pulse distortion in few-mode fiber.* Paper presented at the European Conference and Exhibition on Optical Communication.

Marcuse, D. (1974). Theory of Dielectric Optical Waveguides: Academic Press, Inc, New York.

Medvedkov, O. I., Vasiliev, S. A., Gnusin, P. I., & Dianov, E. M. (2012). Photosensitivity of optical fibers with extremely high germanium concentration. *Optical Materials Express, 2*(11), 1478-1489.

Méndez, A., & Morse, T. F. (2011). *Specialty optical fibers handbook*: Academic Press.

Meng, H., Shen, W., Zhang, G., Tan, C., & Huang, X. (2010). Fiber Bragg grating-based fiber sensor for simultaneous measurement of refractive index and temperature. *Sensors and Actuators B: Chemical, 150*(1), 226-229.

Miller, D. A. B. (2013). Reconfigurable add-drop multiplexer for spatial modes. *Optics express, 21*(17), 20220-20229.

Miller, S. (2012). *Optical fiber telecommunications*: Elsevier.

Mitra, P. P., & Stark, J. B. (2001). Nonlinear limits to the information capacity of optical fibre communications. *Nature, 411*(6841), 1027-1030.

Mizunami, T., Djambova, T. V., Niiho, T., & Gupta, S. (2000). Bragg gratings in multimode and few-mode optical fibers. *Journal of Lightwave Technology, 18*(2), 230.

Mizuochi, T. (2006). Recent progress in forward error correction and its interplay with transmission impairments. *Selected Topics in Quantum Electronics, IEEE Journal of, 12*(4), 544-554.

Mondanos, M., Lloyd, P., Giles, I., Badcock, R., & Weir, K. (2000). *Damage detection in composite structures using polarimetric low coherence interferometry.* Paper presented at the Proceedings of SPIE, the International Society for Optical Engineering.

Montero-Orille, C., Moreno, V., Prieto-Blanco, X., Mateo, E. F., Ip, E., Crespo, J., & Liñares, J. (2013). Ion-exchanged glass binary phase plates for mode-division multiplexing. *Applied optics, 52*(11), 2332-2339.

Moon, D. S., Paek, U.-C., & Chung, Y. (2004). Multi-wavelength lasing oscillations in an erbium-doped fiber laser using few-mode fiber Bragg grating. *Optics express, 12*(25), 6147-6152.

Nielsen, M., Jacobsen, C., Mortensen, N., Folkenberg, J., & Simonsen, H. (2004). Low-loss photonic crystal fibers for transmission systems and their dispersion properties. *Optics express, 12*(7), 1372-1376.

Okamoto, K. (2010). *Fundamentals of optical waveguides*: Academic press.

Onishi, M., Okuno, T., Kashiwada, T., Ishikawa, S., Akasaka, N., & Nishimura, M. (1998). Highly nonlinear dispersion-shifted fibers and their application to broadband wavelength converter. *Optical Fiber Technology, 4*(2), 204-214.

Pan, Z., Weng, Y., & Wang, J. (2015). Investigation of nonlinear effects in few-mode fibers. *Photonic Network Communications*, 1-11.

Poumellec, B. (2001). Time Decay Modelling of UV-Induced Refractive Index Change of Silica Glasses for Optical Applications *Ageing Studies and Lifetime Extension of Materials* (pp. 429-435): Springer.

Pradhan, P., Sengupta, D., Rehouma, H., Francois, V., Tremblay, C., & Ung, B. (2015). *Excitation of vector modes in few-mode fiber using wire-based mechanical long period fiber grating.* Paper presented at the Photonics North, 2015.

Qian, D., Huang, M.-F., Ip, E., Huang, Y.-K., Shao, Y., Hu, J., & Wang, T. (2011). *101.7-Tb/s (370× 294-Gb/s) PDM-128QAM-OFDM transmission over 3× 55-km SSMF using pilot-based phase noise mitigation.* Paper presented at the Optical Fiber Communication Conference.

Qian, D., Ip, E., Huang, M.-F., Li, M.-j., Dogariu, A., Zhang, S., . . . Wang, T. (2012, 2012/10/14). *1.05Pb/s Transmission with 109b/s/Hz Spectral Efficiency using Hybrid Single- and Few-Mode Cores.* Paper presented at the Frontiers in Optics 2012/Laser Science XXVIII, Rochester, New York.

Qiangzhou, R., Xueguang, Q., Jing, Z., Ruohui, W., Manli, H., & Zhongyao, F. (2012). Simultaneous Measurement for Displacement and Temperature Using Fiber Bragg Grating Cladding Mode Based on Core Diameter Mismatch. *Lightwave Technology, Journal of, 30*(11), 1645-1650.

Qiu, W., Cheng, X., Luo, Y., Zhang, Q., & Zhu, B. (2013). Simultaneous Measurement of Temperature and Strain Using a Single Bragg Grating in a Few-Mode Polymer Optical Fiber. *Journal of Lightwave Technology, 31*(14), 2419-2425.

Ramachandran, S. (2003). *Novel photonic devices in few-mode fibres.* Paper presented at the Circuits, Devices and Systems, IEE Proceedings-.

Ramachandran, S. (2005). Dispersion-tailored few-mode fibers: a versatile platform for in-fiber photonic devices. *Journal of Lightwave Technology, 23*(11), 3426.

Ramachandran, S., Ghalmi, S., Wang, Z., & Yan, M. (2002). Band-selection filters with concatenated long-period gratings in few-mode fibers. *Optics letters, 27*(19), 1678-1680.

Ramachandran, S., Kristensen, P., & Yan, M. F. (2009). Generation and propagation of radially polarized beams in optical fibers. *Opt Lett, 34*(16), 2525-2527.

Ramachandran, S., Wang, Z., & Yan, M. (2002). Bandwidth control of long-period grating-based mode converters in few-mode fibers. *Optics letters, 27*(9), 698-700.

Randel, S., Magarini, M., Ryf, R., Gnauck, A., Winzer, P., Hayashi, T., . . . Sasaki, T. (2011). *MIMO-based signal processing of spatially multiplexed 112-Gb/s PDM-QPSK signals using strongly-coupled 3-core fiber.* Paper presented at the European Conference and Exposition on Optical Communications.

Randel, S., Ryf, R., Gnauck, A., Mestre, M. A., Schmidt, C., Essiambre, R., . . . Sureka, A. (2012). *Mode-multiplexed 6× 20-GBd QPSK transmission over 1200-km DGD-compensated few-mode fiber.* Paper presented at the Optical Fiber Communication Conference.

Randel, S., Ryf, R., Sierra, A., Winzer, P. J., Gnauck, A. H., Bolle, C. A., . . . Lingle, R. (2011). 6× 56-Gb/s mode-division multiplexed transmission over 33-km few-mode fiber enabled by 6× 6 MIMO equalization. *Optics express, 19*(17), 16697-16707.

Renner, H. (2001). Effective-index increase, form birefringence and transition losses in UV-side-illuminated photosensitive fibers. *Optics express, 9*(11), 546-560.

Richardson, D., Fini, J. M., & Nelson, L. E. (2013). Space-division multiplexing in optical fibres. *Nature Photonics, 7*(5), 354-362.

Ryf, R., Essiambre, R., von Hoyningen-Huene, J., & Winzer, P. (2012). *Analysis of mode-dependent gain in Raman amplified few-mode fiber.* Paper presented at the Optical Fiber Communication Conference.

Ryf, R., Fontaine, N. K., Guan, B., Essiambre, R.-J., Randel, S., Gnauck, A., . . . Ercan, B. (2014). *1705-km transmission over coupled-core fibre supporting 6 spatial modes.* Paper presented at the 2014 The European Conference on Optical Communication (ECOC).

Ryf, R., Mestre, M., Randel, S., Schmidt, C., Gnauck, A., Essiambre, R.-J., . . . Sureka, A. (2012). Mode-multiplexed transmission over a 209-km DGD-compensated hybrid few-mode fiber span. *Photonics Technology Letters, IEEE, 24*(21), 1965-1968.

Ryf, R., Mestre, M. A., Gnauck, A., Randel, S., Schmidt, C., Essiambre, R., . . . Sureka, A. (2012). *Low-loss mode coupler for mode-multiplexed transmission in few-mode fiber.* Paper presented at the Optical Fiber Communication Conference.

Ryf, R., Randel, S., Fontaine, N. K., Montoliu, M., Burrows, E., Chandrasekhar, S., . . . Winzer, P. (2013). *32-bit/s/Hz spectral efficiency WDM transmission over 177-km few-mode fiber.* Paper presented at the National Fiber Optic Engineers Conference.

Ryf, R., Randel, S., Gnauck, A. H., Bolle, C., Essiambre, R.-J., Winzer, P., . . . Lingle, R. (2011). *Space-division multiplexing over 10 km of three-mode fiber using coherent 6× 6 MIMO processing.* Paper presented at the Optical Fiber Communication Conference.

Ryf, R., Randel, S., Gnauck, A. H., Bolle, C., Sierra, A., Mumtaz, S., . . . Winzer, P. J. (2012). Mode-division multiplexing over 96 km of few-mode fiber using coherent 6 6 MIMO processing. *Lightwave Technology, Journal of, 30*(4), 521-531.

Ryf, R., Sierra, A., Essiambre, R.-J., Randel, S., Gnauck, A., Bolle, C. A., . . . Pupalaikis, P. (2011). *Mode-equalized distributed Raman amplification in 137-km few-mode fiber*. Paper presented at the European Conference and Exposition on Optical Communications.

Sakata, H., Sano, H., & Harada, T. (2014). Tunable mode converter using electromagnet-induced long-period grating in two-mode fiber. *Optical Fiber Technology, 20*(3), 224-227.

Saleh, B. E. A., & Teich, M. C. (2007). Fundamentals of Photonics: John Wiley & Sons, Inc., Hoboken, New Jersey.

Salsi, M., Koebele, C., Sperti, D., Tran, P., Brindel, P., Mardoyan, H., . . . Sillard, P. (2011). *Transmission at 2x100Gb/s, over two modes of 40km-long prototype few-mode fiber, using LCOS based mode multiplexer and demultiplexer.* Paper presented at the Optical Fiber Communication Conference.

Sang, X., Yu, C., Mayteevarunyoo, T., Wang, K., Zhang, Q., & Chu, P. L. (2007). Temperature-insensitive chemical sensor based on a fiber Bragg grating. *Sensors and Actuators B: Chemical, 120*(2), 754-757.

Sano, A., Kobayashi, T., Yamanaka, S., Matsuura, A., Kawakami, H., Miyamoto, Y., . . . Masuda, H. (2012). *102.3-Tb/s (224 x 548-Gb/s) C-and extended L-band all-Raman transmission over 240 km using PDM-64QAM single carrier FDM with digital pilot tone.* Paper presented at the National Fiber Optic Engineers Conference.

Savory, S. J., Gavioli, G., Killey, R. I., & Bayvel, P. (2007). *Transmission of 42.8 Gbit/s polarization multiplexed NRZ-QPSK over 6400km of standard fiber with no optical dispersion compensation.* Paper presented at the Optical Fiber Communication Conference.

Sceats, M., Atkins, G., & Poole, S. (1993). Photolytic index changes in optical fibers. *Annual Review of Materials Science, 23*(1), 381-410.

Schulze, C., Brüning, R., Schröter, S., & Duparré, M. (2015). Mode Coupling in Few-Mode Fibers Induced by Mechanical Stress. *Journal of Lightwave Technology, 33*(21), 4488-4496.

SeGall, M., Divliansky, I., Jollivet, C., Schülzgen, A., & Glebov, L. B. (2015). Holographically encoded volume phase masks. *Optical Engineering, 54*(7), 076104-076104.

SeGall, M., Divliansky, I. B., & Glebov, L. (2013). *Simultaneous laser mode conversion and beam combining using multiplexed volume phase elements.* Paper presented at the Advanced Solid State Lasers.

SeGall, M., Rotar, V., Lumeau, J., Mokhov, S., Zeldovich, B., & Glebov, L. B. (2012). Binary volume phase masks in photo-thermo-refractive glass. *Optics letters, 37*(7), 1190-1192.

Sillard, P., Bigot-Astruc, M., & Molin, D. (2014). Few-mode fibers for mode-division-multiplexed systems. *Journal of Lightwave Technology, 32*(16), 2824-2829.

Sleiffer, V., Chen, H., Jung, Y., Leoni, P., Kuschnerov, M., Simperler, A., . . . Richardson, D. (2013). Field demonstration of mode-division multiplexing upgrade scenarios on commercial networks. *Optics express, 21*(25), 31036-31046.

Sleiffer, V., Jung, Y., Inan, B., Chen, H., van Uden, R., Kuschnerov, M., . . . Koonen, T. (2012). *Mode-division-multiplexed 3x112-Gb/s DP-QPSK transmission over 80 km few-mode fiber with inline MM-EDFA and Blind DSP.* Paper presented at the European Conference and Exhibition on Optical Communication.

Sleiffer, V., Jung, Y., Veljanovski, V., Van Uden, R., Kuschnerov, M., Chen, H., . . . Richardson, D. J. (2012). 73.7 Tb/s (96 x 3 x 256-Gb/s) mode-division-multiplexed DP-16QAM transmission with inline MM-EDFA. *Optics express, 20*(26), B428-B438.

Smit, M., Van der Tol, J., & Hill, M. (2012). Moore's law in photonics. *Laser and photonics Reviews, 6*(1), 1.

Snitzer, E. (1961). Cylindrical dielectric waveguide modes. *JOSA, 51*(5), 491-498.

Snitzer, E., & Osterberg, H. (1961). Observed Dielectric Waveguide Modes in the Visible Spectrum*. *JOSA, 51*(5), 499-505.

Snyder, A. W., & Young, W. R. (1978). Modes of optical waveguides. *JOSA, 68*(3), 297-309.

Soma, D., Takeshima, K., Igarashi, K., & Tsuritani, T. (2014). *Degenerate modes multiplexer/demultiplexer using Mach-Zehnder interferometer with image inversion.* Paper presented at the Optical Communication (ECOC), 2014 European Conference on.

Song, D.-R., Su Park, H., Kim, B. Y., & Song, K. Y. (2014). Acoustooptic Generation and Characterization of the Higher Order Modes in a Four-Mode Fiber for Mode-Division Multiplexed Transmission. *Journal of Lightwave Technology, 32*(23), 3932-3936.

Squillante, E. (1998). Applications of fiber-optic evanescent wave spectroscopy. *Drug development and industrial pharmacy, 24*(12), 1163-1175.

Stacey, C., & Jenkins, J. (2005). *Demonstration of fundamental mode propagation in highly multimode fibre for high power EDFAs.* Paper presented at the CLEO/Europe. 2005 Conference on Lasers and Electro-Optics Europe, 2005.

Stolen, R. H., & Bjorkholm, J. E. (1982). Parametric amplification and frequency conversion in optical fibers. *Quantum Electronics, IEEE Journal of, 18*(7), 1062-1072.

Strasser, T., Pedrazzani, J. R., & Andrejco, M. (1997). *Reflective-mode conversion with UV-induced phase gratings in two-mode fiber*. Paper presented at the Optical Fiber Communication. OFC 97., Conference on.

Suibhne, N. M., Watts, R., Sygletos, S., Gunning, F. C. G., Grüner-Nielsen, L., & Ellis, A. D. (2012). *Nonlinear soliton propagation in a few mode optical fibre.* Paper presented at the Opto-Electronics and Communications Conference (OECC), 2012 17th.

Sun, N.-H., Liau, J.-J., Kiang, Y.-W., Lin, S.-C., Ro, R.-Y., Chiang, J.-S., & Chang, H.-W. (2009). Numerical analysis of apodized fiber Bragg gratings using coupled mode theory. *Progress In Electromagnetics Research, 99*, 289-306.

Suzuki, S., Schülzgen, A., & Peyghambarian, N. (2008). Single-mode fiber laser based on core-cladding mode conversion. *Optics letters, 33*(4), 351-353.

Svalgaard, M., & Færch, K. U. (2005, 2005). *High index contrast UV-written waveguides.* Paper presented at the 12th European Conference on Integrated Optics, France.

Takenaga, K., Sasaki, Y., Guan, N., Matsuo, S., Kasahara, M., Saitoh, K., & Koshiba, M. (2012). Large effective-area few-mode multicore fiber. *Photonics Technology Letters, IEEE, 24*(21), 1941-1944.

Takenaga, K., Sasaki, Y., Guan, N., Matsuo, S., Kasahara, M., Saitoh, K., & Koshiba, M. (2012, 9-11 July 2012). *A large effective area few-mode multi-core fiber.* Paper presented at the Photonics Society Summer Topical Meeting Series, 2012 IEEE.

Udd, E., & Spillman Jr, W. B. (2011). *Fiber optic sensors: an introduction for engineers and scientists*: John Wiley & Sons.

Vengsarkar, A. M., Michie, W. C., Jankovic, L., Culshaw, B., & Claus, R. O. (1994). Fiber-optic dual-technique sensor for simultaneous measurement of strain and temperature. *Lightwave Technology, Journal of, 12*(1), 170-177.

Vengsarkar, A. M., Zhong, Q., Inniss, D., Reed, W., Lemaire, P. J., & Kosinski, S. (1994). Birefringence reduction in side-written photoinduced fiber devices by a dual-exposure method. *Optics letters, 19*(16), 1260-1262.

Vuong, J., Ramantanis, P., Frignac, Y., Salsi, M., Genevaux, P., Bendimerad, D. F., & Charlet, G. (2015). Mode coupling at connectors in mode-division multiplexed transmission over few-mode fiber. *Optics express, 23*(2), 1438-1455.

Weng, Y., Ip, E., Pan, Z., & Wang, T. (2015). Single-end simultaneous temperature and strain sensing techniques based on Brillouin optical time domain reflectometry in few-mode fibers. *Optics express, 23*(7), 9024-9039.

Winzer, P. J. (2011). Energy-efficient optical transport capacity scaling through spatial multiplexing. *IEEE Photonics Technology Letters*, *13*(23), 851-853.

Wong, A. C., Chung, W., Tam, H.-Y., & Lu, C. (2011). Single tilted Bragg reflector fiber laser for simultaneous sensing of refractive index and temperature. *Optics express*, *19*(2), 409-414.

Wu, C., Liu, Z., Chung, K. M., Tse, M.-L. V., Chan, F. Y., Lau, A. P. T., . . . Tam, H.-Y. (2012). Strong and mutual coupling conversion in a two-mode fiber Bragg grating. *Photonics Journal, IEEE, 4*(4), 1080-1086.

Xia, C., Amezcua-Correa, R., Bai, N., Antonio-Lopez, E., Arrioja, D. M., Schulzgen, A., . . . Mateo, E. (2012). Hole-assisted few-mode multicore fiber for high-density space-division multiplexing. *Photonics Technology Letters, IEEE, 24*(21), 1914-1917.

Xiong, R., Meng, H., Yao, Q., Huang, B., Liu, Y., Xue, H., . . . Huang, X. (2014). Simultaneous measurement of refractive index and temperature based on modal interference. *Sensors Journal, IEEE*, *14*(8), 2524-2528.

Yablon, A. D. (2004). Optical and mechanical effects of frozen-in stresses and strains in optical fibers. *Selected Topics in Quantum Electronics, IEEE Journal of, 10*(2), 300-311.

Yaman, F., Bai, N., Zhu, B., Wang, T., & Li, G. (2010). Long distance transmission in few-mode fibers. *Optics express*, *18*(12), 13250-13257.

Yang, H. Z., Ali, M. M., Islam, M. R., Lim, K.-S., Gunawardena, D. S., & Ahmad, H. (2015). Cladless few mode fiber grating sensor for simultaneous refractive index and temperature measurement. *Sensors and Actuators A: Physical, 228*(0), 62-68.

Yang, H. Z., Guang, Q. X., Rajibul, I. M., Kok-Sing, L., & Ahmad, H. (2014). Simultaneous measurement of aliphatic alcohol concentration and temperature based on etched taper FBG. *Sensors and Actuators B: Chemical, 202*, 959-963.

Yang, H. Z., Qiao, X. G., Wang, Y. P., Ali, M. M., Lai, M. H., Lim, K. S., & Ahmad, H. (2015). In-Fiber Gratings for Simultaneous Monitoring Temperature and Strain in Ultrahigh Temperature. *Photonics Technology Letters, IEEE, 27*(1), 58-61.

Yariv, A. (1973). Coupled-mode theory for guided-wave optics. *Quantum Electronics, IEEE Journal of, 9*(9), 919-933.

Youngquist, R., Brooks, J., & Shaw, H. J. (1984). Two-mode fiber modal coupler. *Optics letters, 9*(5), 177-179.

Yu, Y., Tam, H., Chung, W., & Demokan, M. S. (2000). Fiber Bragg grating sensor for simultaneous measurement of displacement and temperature. *Optics letters, 25*(16), 1141-1143.

Yung, Y., Alam, S.-u., Li, Z., Dhar, A., Giles, D., Giles, I., . . . Richardson, D. (2011). *First demonstration of multimode amplifier for spatial division multiplexed transmission systems.* Paper presented at the European Conference and Exposition on Optical Communications.

Zaitsev, V. F., & Polyanin, A. D. (2002). *Handbook of exact solutions for ordinary differential equations*: CRC Press.

Zhang, Q., Brown, D., Reinhart, L., Morse, T., Wang, J., & Xiao, G. (1994). Tuning Bragg wavelength by writing gratings on prestrained fibers. *Photonics Technology Letters, IEEE, 6*(7), 839-841.

Zhao, C.-L., Yang, X., Demokan, M., & Jin, W. (2006). Simultaneous temperature and refractive index measurements using a 3 slanted multimode fiber Bragg grating. *Journal of Lightwave Technology, 24*(2), 879.

Zhao, N., Huang, B., Amezcua-Correa, R., Li, X., & Li, G. (2013). *Few-mode fiber optical parametric amplifier.* Paper presented at the Optical Fiber Communication Conference.

Zhu, X., Schülzgen, A., Li, H., Wei, H., Moloney, J., & Peyghambarian, N. (2010). Coherent beam transformations using multimode waveguides. *Optics express, 18*(7), 7506-7520.

Zou, W., He, Z., & Hotate, K. (2009). Complete discrimination of strain and temperature using Brillouin frequency shift and birefringence in a polarization-maintaining fiber. *Optics express, 17*(3), 1248-1255.

APENDICES

A. MATLAB CODES

This section provides some of the important MATLAB source codes written during the course of this research. Most of the codes written are for the plots and graphs in the result of numerical solutions of the analytical expressions and experimental data in this work.

A.1 Numerical Calculations of Propagation Constants and Mode Effective Refractive Index of Few-mode Fiber

```
%%%%%%%%%%%%Numerical Calculations of Mode Propagation Constants
%%%%%%%%%%%%and Effective Refractive index using Characteristics
%%%%%%%%%%%%equations of weakly guided/simplified equations

clc;
clear all;
format long;
tic
W = input('Enter the number of Wavelength Points ='); %Number of
wavelength points = 100
M = input('Enter the number of modes =');  % no of modes = 4;
lambda = linspace(1543e-9,1548e-9,W);
a = input('Enter the Core radius (um) ='); ;   %core radius = 10.75
b = input('Enter the Core radius (um) =');     % cladding radius =
62.5;
bk = zeros(W,M); % Define the matrix for mode propagtion constatnts
values
neff = zeros(size(bk)); % Define the matrix for mode effective
refractive index values

%%%%%%%%%%%%%%%%%% Newton Raphson Method for Numerical Calculation of
%%%%%%%%%%%%%%%%%% Mode Effective Refratcive index Values

for m=1:M %mode
        for w=1:W  %lambda
            nb = n_sellmeier_um(lambda(w)*1e6)-0.000724;
            na = n_sellmeier_um(lambda(w)*1e6)-0.000724+ 0.0050;
            NA(m,w) = sqrt(na^2-nb^2);
            V = 2*pi*10^-6*a.*NA(m,w)/lambda(w);
            clear f dx x;
            syms x;
            e = 5e-5;                      % setting the tolerance value
            dx = 1;
            f = V*((1-x)^0.5)*besselj(m-2,V*((1-x)^0.5))/besselj(m-
1,V*((1-x)^0.5))...
               + V*x^0.5*besselk(m-2,V*x^0.5)/besselk(m-1,V*x^0.5);
% enter your function here;
            x = 0.99999;
            if m > 5
```

```
                clear f x;
                syms x;
                f = V*((1-x)^0.5)*besselj(m-7,V*((1-
x)^0.5))/besselj(m-6,V*((1-x)^0.5))...
                + V*x^0.5*besselk(m-7,V*x^0.5)/besselk(m-6,V*x^0.5);
% enter your function here;
                x = 0.60;
            elseif m > 10
                clear f x;
                syms x;
                f = V*((1-x)^0.5)*besselj(m-12,V*((1-
x)^0.5))/besselj(m-11,V*((1-x)^0.5))...
                + V*x^0.5*besselk(m-12,V*x^0.5)/besselk(m-11,V*x^0.5);
% enter your function here;
                x = 0.20;
            end
            % initially assumed value of x
            count = 0; % setting counter to know the no. of iterations
            p = zeros(1,1);
            while (abs(dx) > e)             % initialising the
iteration and continue until the error is less than tolerance
                dx = real(0.25*eval(f/(diff(f))));     % calculating
dx, diff is used for finding the differentiation of the fuction
                x = x - dx ;                % updating the value of x
                count = count + 1;          % incrimenting the counter
                p(count) = x;
                if (count > 35)
                    fprintf('Error...! Solution not converging !!!
\n');  % printing the error message
                    break;
                end
            end
            bk(w,m)=x;
            if x > 0
                neff(w,m)=sqrt(nb.^2 + bk(w,m).*NA(m,w).^2);
                Lb(w,m)=1068.8.*neff(w,m);
            end

        end
        hold on
        plot(lambda, neff(:,m))
        hold off
end
```

A.2 Numerical Analysis Few-mode Fiber Bragg Gratings

```
%%%%Numerical Analysis of Few-mode Fiber Bragg Gratings (FM-FBGs)%%%%
clear all
close all
clc
tic
n01 = input('Enter the Effective refractive index  at Bragg wavelength
of LP01 ='); %2MF-FBG effective index for LP01
n11 = input('Enter the Effective refractive index  at Bragg wavelength
of LP11 ='); %2MF-FBG effective index for LP01
dd = 0.0058;       %For the equally adjustment of effective refractive
index of teh modes
n01 = n01-dd;
n11 = n11-dd;
dn = input('Enter the core refractive index modulation parameter =');
```

```
% dn=1.0E-04; %Index modulation
N_lamb = 801; % No. of sample point for lambda  1001
N_z = 800;   % Discrete number of points in z-direction
L = input('Enter the value grating length ='); %L=0.02 m or 0.0090m ;
lamb = linspace(1542E-9,1548E-09,N_lamb); % wavelength range lambda
disp = linspace(-L/2,L/2,N_z);  %displacement
disp_G = linspace(0,L,N_z);  %for gaussian
dz = disp(2)-disp(1);
FWHM = 0.0085;
%%%%%%%%%%%%%%%%%%% Lossless FM-FBG %%%%%%%%%%%%%%%%%%%%
period0 = input('Enter the value grating period ='); % Grating period;
period = period0*1e-9;
dp = 0;
m = 1;
Pa = 0.73;   %LP01 / LP11 intensity ratio
a = sqrt(Pa);
b = sqrt(1-Pa)*exp(-i*3.8);
c = 'k';     %graph colour
%%%%%%%%%%%% Runge Kutta Method for the Numerical solution of coupled
%%%%%%%%%%%% mode equations of FM-FBGs
I = [1 0 0 0; 0 1 0 0; 0 0 1 0; 0 0 0 1]; %4x4 order Identity Matrix
% dn_z = dn; %uniform
dn_z = dn*exp(-((disp_G-L/2)./FWHM).^2/2); %  Gaussian
d11 = 0.20;
dc = 0.02; % coupling parameter
for l=lamb;
    F = I;
    Z = 1;
    for z = disp
        %%%%%%%%%%%%%%%%%%%%%LP01%%%%%%%%%%%%%%%%%%%%%%%%
        del1 = 2*pi*n01*(1/l) - pi./period;
        del2 = 2*pi*n01*(1/l) - pi./(period+dp/2);
        del4 = 2*pi*n01*(1/l) - pi./(period+dp);
        s01 = 2*pi*dn_z(Z)./l;
        k01 = pi*dn_z(Z)/l;
         %%%%%%%%%%%%%%%%%%%%%LP11%%%%%%%%%%%%%%%%%%%%%%%%%
        Del1 = 2*pi*n11*(1/l) - pi./period;
        Del2 = 2*pi*n11*(1/l) - pi./(period+dp/2);
        Del4 = 2*pi*n11*(1/l) - pi./(period+dp);
        s11 = d11*2*pi*dn_z(Z)./l;
        k11 = d11*pi*dn_z(Z)/l;
        kc = dc*pi*dn_z(Z)/l;
        K1 = dz*i*[-(s01 + del1) 0 -k01 -kc;
                   0 -(s11 + Del1) -kc -k11;
                   k01 kc (s01 + del1) 0;
                   kc k11 0 (s11 + Del1)];
        K2 = dz*i*[-(s01 + del2) 0 -k01 -kc;
                   0 -(s11 + Del2) -kc -k11;
                   k01 kc (s01 + del2) 0;
                   kc k11 0 (s11 + Del2)]*(I+K1/2);
        K3 = dz*i*[-(s01 + del2) 0 -k01 -kc;
                   0 -(s11 + Del2) -kc -k11;
                   k01 kc (s01 + del2) 0;
                   kc k11 0 (s11 + Del2)]*(I+K2/2);
        K4 = dz*i*[-(s01 + del4) 0 -k01 -kc;
                   0 -(s11 + Del4) -kc -k11;
```

```
                    k01 kc (s01 + del4) 0;
                    kc k11 0 (s11 + Del4)]*(I+K3);
           R = I + (K1 + 2*K2 + 2*K3 + K4)/6;
           F = R*F;
           Z = Z + 1;
       end
       G11 = [F(1,1) F(1,2); F(2,1) F(2,2)];
       G12 = [F(1,3) F(1,4); F(2,3) F(2,4)];
       G21 = [F(3,1) F(3,2); F(4,1) F(4,2)];
       G22 = [F(3,3) F(3,4); F(4,3) F(4,4)];
       B0 = G22^-1*G21*[a;b]; %A(LP01;LP11)
       AL = (G11-G12*G22^-1*G21)*[a;b];
       r01(m) = B0(1);
       r11(m) = B0(2);
       t01(m) = AL(1);
       t11(m) = AL(2);
       m=m+1;
   end
   RL = 10*log10((abs(r01)+abs(r11)).^2);% Transmission Spectra of FM-FBG
   TL = 10*log10((abs(t01)+abs(t11)).^2); % Reflection Spectrum of FM-FBG
   %%%%%%% Plots of Reflection and Transmission Spectra of FM-FBG%%%%%%
   toc
   figure(1)
   subplot(211)
   hold on
   plot(lamb*1e9,(RL),c)
   hold off
   ylabel('Reflection (dB)')
   xlabel('Wavelength (nm)');
   subplot(212)
   hold on
   plot(lamb*1e9,TL,c)
   hold off
   ylabel('Transmission (dB)')
   xlabel('Wavelength (nm)');
```

A.3 Peak Finder for Experimentally Acquired Reflection Spectra of FBGs

```
clc;
close all;
clear all;
format long;
%%%%%Set path of Excel Sheet excel for Reflection Spectra
A = xlsread('Reflection Spectrum Data.xlsx','Sheet1','A2:R5002');
wl=A(:,1);
for k = 2:5
x = A(:,k);
yy1 = smooth(wl,x,0.02,'loess');
[pks,locs] = findpeaks(yy1,'THRESHOLD',0.00008);
hold on
plot(wl,yy1)
hold off
hold on
plot(wl(locs),pks,'ro')
hold off
disp(num2str(wl(locs)'))
end
```

A.4 Power Confinement Ratios and Refractive index Sensitivities for Cladless (Etched) FM-FBG

```
%%%%%Power Confinement Ratios and Refractive index Sensitivities for
Cladless (Etched) FM-FBG%%%%
clc;
clear all;
close all;
format long;
tic
W = 1;                              %Number of wavelength points
M = 4;                              % no of modes
R = 2;                              % no of RI steps
RHO = 20;
lambda = linspace(1538e-9,1548e-9,W);
RI = [1 1.3157 1.31575];                    %[1 linspace(1.3157,1.371,
R)];
a = linspace( 3, 9.75, RHO);          % core radius 7.19
b = 62.5;                              % cladding radius
bk = zeros(RHO,W,M);
neff = zeros(size(bk));
for rho = 1:RHO                        % radius
    for rr = 1:(R+1)
        for m=1:M                   % mode
            for w=1:W               % lambda
                nb = RI(rr);% (n_sellmeier_um(lambda(w)*1e6)-0.00050);
                na = (n_sellmeier_um(lambda(w)*1e6) + 0.0050);
                NA(m) = sqrt(na^2-nb^2);
                V = 2*pi*10^-6*a(rho).*NA(m)/lambda(w);
                clear A B f dx x;
                syms f x A B;
                dx = 1;
                A = - besselj(m,V*((1-x)^0.5))./(V*((1-
x)^0.5)*besselj(m-1,V*((1-x)^0.5))) + (m-1)/(V^2*(1-x));
                B = - besselk(m,V*(x^0.5))./(V*(x^0.5)*besselk(m-
1,V*(x^0.5))) + (m-1)/(V^2*(x));
%                f = (A + B)*(A + (nb/na)^2*B) - (m-1)^2*(nb^2 +
x*NA(m,w)^2)/(x^2*(1-x)^2); % enter your function here;
                f = (A + B)*(A + (nb/na)^2*B) - (m-1)^2*(1/(V*(1-
x)^0.5)^2 + 1/(V*(x)^0.5)^2)*(1/(V*(1-x)^0.5)^2 +
(nb/na)^2/(V*(x)^0.5)^2); % enter your function here;
                x = 0.998;
                if m > 3 && m <= 6
                    clear f x A B;
                    syms f x A B;
                    A = - besselj(m-3,V*((1-x)^0.5))./(V*((1-
x)^0.5)*besselj(m-4,V*((1-x)^0.5))) + (m-4)/(V^2*(1-x));
                    B = - besselk(m-
3,V*(x^0.5))./(V*(x^0.5)*besselk(m-4,V*(x^0.5))) + (m-4)/(V^2*(x));
                    %f = (A + B)*(A + (nb/na)^2*B) - (m-4)^2*(nb^2 +
x*NA(m,w)^2)/(x^2*(1-x)^2); % enter your function here;
                    f = (A + B)*(A + (nb/na)^2*B) - (m-4)^2*(1/(V*(1-
x)^0.5)^2 + 1/(V*(x)^0.5)^2)*(1/(V*(1-x)^0.5)^2 +
(nb/na)^2/(V*(x)^0.5)^2); % enter your function here;
                    x = 0.995;
                elseif m > 6
                    clear f x A B;
                    syms f x A B;
```

```
                    A = - besselj(m-6,V*((1-x)^0.5))./(V*((1-
x)^0.5)*besselj(m-7,V*((1-x)^0.5))) + (m-7)/(V^2*(1-x));
                    B = - besselk(m-
6,V*(x^0.5))./(V*(x^0.5)*besselk(m-7,V*(x^0.5))) + (m-7)/(V^2*(x));
                    %f = (A + B)*(A + (nb/na)^2*B) - (m-7)^2*(nb^2 +
x*NA(m,w)^2)/(x^2*(1-x)^2); % enter your function here;
                    f = (A + B)*(A + (nb/na)^2*B) - (m-7)^2*(1/(V*(1-
x)^0.5)^2 + 1/(V*(x)^0.5)^2)*(1/(V*(1-x)^0.5)^2 +
(nb/na)^2/(V*(x)^0.5)^2); % enter your function here;
                    x = 0.993;
                end

                % initially assumed value of x
                e = 1e-4;                       % setting the
tolerance value
                count = 0;                      % setting counter to
know the no of iterations taken
                p = zeros(1,1);

                while (abs(dx) > e)             % initialising the
iteration and continue until the error is less than tolerance
                    dx = real(0.20*eval(f/(diff(f))));     %
calculating dx, diff is used for finding the differentiation of the
fuction
                    x = x - dx ;                % updating the value
of x
                    count = count + 1;          % incrimenting the
counter
                    p(count) = x;
                    if (count > 30)
                        fprintf('Error...! Solution not converging !!!
\n');  % printing the error message
                        break;
                    end
                end
                bk(m)=x;
                if x > 0
                    neff(rho,rr,m)=sqrt(nb.^2 + bk(m).*NA(m).^2);
                    Lb(rho,rr,m)=1068.8.*neff(rho,rr,m);
                end
            end
        end
    end
end
figure(1)
subplot(311)
plot(a,neff(:,1,2),a,neff(:,1,3)) % plot LP01 and LP11 in air
subplot(312)
plot(a,1068.8.*neff(:,1,2),a,1068.8.*neff(:,1,3))
data_air = [a' 1068.8.*neff(:,1,2) 1068.8.*neff(:,1,3) ];
data_water = [a' 1068.8.*neff(:,2,2) 1068.8.*neff(:,2,3) ];

dLam01 = 1068.8.*neff(:,3,2) - 1068.8.*neff(:,2,2); % sensitivity of
Bragg wl for LP01 in water
dLam01 = dLam01/0.00005;

dLam11 = 1068.8.*neff(:,3,3) - 1068.8.*neff(:,2,3); % sensitivity of
Bragg wl for LP11 in water
dLam11 = dLam11/0.00005;
subplot(313)
plot(a, dLam01,'b--', a, dLam11, 'k--');
ylabel('RI sensitivity (nm/RIU)');
Sensitivity = [a'*1e6 dLam01 dLam11];
```

```
lambda = 1538e-9;
k = 2*pi./lambda;
a = a*10^-6;
for r_N = 1:RHO

    % in the air
    na = (n_sellmeier_um(lambda*1e6) + 0.0050);
    U01 = k*sqrt(na^2 - neff(r_N,1,2)^2)*a(r_N);
    V01 = k*a(r_N).*sqrt(na^2-1);
    W01 = k*sqrt(neff(r_N,1,2)^2 - 1)*a(r_N);  % in air
    P01_clad(r_N) = (U01/V01)^2*(1-besselk(0,W01)^2./(besselk(-
1,W01)*besselk(1,W01)));
    P01_core(r_N) = 1 - P01_clad(r_N);

    U11 = k*sqrt(na^2 - neff(r_N,1,3)^2)*a(r_N);
    V11 = k*a(r_N).*sqrt(na^2-1);
    W11 = k*sqrt(neff(r_N,1,3)^2 - 1)*a(r_N);  % in air
    P11_clad(r_N) = (U11/V11)^2*(1-
besselk(1,W11)^2./(besselk(0,W11)*besselk(2,W11)));
    P11_core(r_N) = 1 - P11_clad(r_N);
      % in the water
    na = (n_sellmeier_um(lambda*1e6) + 0.0050);
    U01 = k*sqrt(na^2 - neff(r_N,2,2)^2)*a(r_N);
    V01 = k*a(r_N).*sqrt(na^2-1.3157^2);
    W01 = k*sqrt(neff(r_N,2,2)^2 - 1.3157^2)*a(r_N);  % in water
    P01_clad_H2O(r_N) = (U01/V01)^2*(1-besselk(0,W01)^2./(besselk(-
1,W01)*besselk(1,W01)));
    P01_core_H2O(r_N) = 1 - P01_clad_H2O(r_N);

    U11 = k*sqrt(na^2 - neff(r_N,2,3)^2)*a(r_N);
    V11 = k*a(r_N).*sqrt(na^2-1.3157^2);
    W11 = k*sqrt(neff(r_N,1,3)^2 - 1.3157^2)*a(r_N);  % in water
    P11_clad_H2O(r_N) = (U11/V11)^2*(1-
besselk(1,W11)^2./(besselk(0,W11)*besselk(2,W11)));
    P11_core_H2O(r_N) = 1 - P11_clad_H2O(r_N);

%      r = linspace(0, a(r_N),100);
%      r2 = linspace(a(r_N), 40,100);
%      P01_core(r_N) = trapz(r, r.*(besselj(0,
U.*r./a(r_N))./besselj(0, U)).^2);
%      P01_clad(r_N) = trapz(r2, r2.*(besselk(0,
W.*r2./a(r_N))./besselk(0, W)).^2);
%      conf01(r_N) = P01_core(r_N)/ (P01_core(r_N) + P01_clad(r_N));
%      syms r r2 theta;
%      P11_core = eval(int(int(r.*(besselj(0, U.*r./a(r_N))./besselj(0,
U)*cos(theta)).^2,r ,0, a(r_N)),theta,0,2*pi));
%      P11_clad = eval(int(int(r2.*(besselk(0,
W.*r2./a(r_N))./besselk(0, W)*cos(theta)).^2, r2 ,a(r_N),
40),theta,0,2*pi));
%      conf11(r_N) = P11_core / (P11_core + P11_clad);
end
figure(2)
subplot(211)
plot(a, P11_core,'k--', a, P01_core, 'b--')
ylabel('Power Confinement ratio inside the core')
xlabel('Etched fiber radius (\mum)')
subplot(212)
plot(a, P11_clad,'k--', a, P01_clad, 'b--')
ylabel('Power Confinement ratio outside the core')
xlabel('Etched fiber radius (\mum)')

figure(3)
subplot(211)
```

```
plot(a, P11_core_H2O,'k--', a, P01_core_H2O, 'b--')
ylabel('Power Confinement ratio inside the core')
xlabel('Etched fiber radius (\mum)')
subplot(212)
plot(a, P11_clad_H2O,'k--', a, P01_clad_H2O, 'b--')
ylabel('Power Confinement ratio outside the core')
xlabel('Etched fiber radius (\mum)')

Confine = [P01_clad' P01_core' P11_clad' P11_core'];
Confine_H2O = [P01_clad_H2O' P01_core_H2O' P11_clad_H2O'. . .
P11_core_H2O'];
```

LIST OF PUBLICATIONS AND PAPERS PRESENTED

Candidate's Journal Publications for Thesis

1. **M. M. Ali,** Y. Jung, K. S. Lim, Md. R. Islam, S. Alam, D. J. Richardson, and H. Ahmad, "Characterization of mode coupling in few mode fiber Bragg gratings with selective mode Excitation," IEEE Photon. Tech. Lett., vol. 27, no. 16, pp. 1713 – 1716, 2015.
2. H. Z. Yang, **M. M. Ali,** Md. R. Islam, K. -S. Lim, X. G. Qiao, and H. Ahmad, "Cladless Few Mode Fiber Grating Sensor for Simultaneous Measurement of Refractive Index and Temperature," Sensors and Actuators A: Physical, vol. 228, pp. 62–68, 2015.
3. **M. M. Ali,** K. S. Lim, H. Z. Yang, W. Y. Chong, W. S. Lim, H. Ahmad, "Direct period measurement for fiber Bragg grating using an optical imaging technique," Applied Optics, vol. 52, no. 22, pp. 5393-5397, 2013.

Patents on Fabricated Devices Included in Thesis

1. Few-Mode Fibre Grating Sensor, Patent filed no. PI 2014703282, Filing date: 5 NOVEMBER 2014. (National, Malaysia)
2. A Fiber-Based System as a Spatial Mode Converter, A Method for Forming Few Mode Fiber Bragg Gratings and Use Therefor, Patent filed no. PI 2015701694, Filing date: 26 MAY 2015. (National, Malaysia)

Candidate's work presented in Conferences/Colloquium/Seminar

1. **M. M. Ali,** Md. R. Islam, K. S. Lim, H. Ahmad, E. Lewis, "Few Mode Fiber Bragg Grating Sensors for Multi-parameter Sensing," Poster presentation in the Winter College on Optics at ICTP, Trieste, Italy, 2016.
2. **M. M. Ali,** Y. Jung, Md. R. Islam, K. S. Lim, S. Alam, D. J. Richardson, and H. Ahmad, "Optical Mode-converters based on Few Mode Fiber for Mode Division Multiplexing," The 5th International Conference on Solid State Science and Technology (ICSSST) 2015, Langkawi, Kedah, Malaysia, 2015.
3. **M. M. Ali,** K. S. Lim, Y. K. Maheshwari, H. Ahmad, "Few Mode Fiber Bragg Grating for Pressure Sensing," International Conference on Engineering & Technology, Computer, Basic & Applied Sciences-ECBA-2016, Istanbul, Turkey, 2016.
4. **M. M. Ali,** Few mode fiber Bragg gratings and its recent developed applications, Optical Fibre Sensors Research Centre (OFSRC) and Mobile & Marine Robotics Research Centre (MMRRC) Annual Colloquium 2015, University of Limerick, 18th December 2015.
5. K. S. Lim, **M. M. Ali,** Md. R. Islam, H. Ahmad and L. Y. Sen, Few-Mode Fiber Grating Sensor, The International Conference and Exposition on Inventions by Institute of Higher Learning (PECIPTA 2015), Kuala Lumpur Convention Centre, December 2015.
6. **M. M. Ali,** Fabrication and characterization of few mode fiber Bragg gratings with mode conversion and sensing applications, presented in Institute of Graduate Studies Postgraduate Research Findings Seminar for the partial fulfilment of Ph.D Candidature, 23rd September 2015.

7. **M. M. Ali,** Fabrication and characterization of few mode fiber Bragg gratings with mode conversion and sensing applications, presented in Institute of Graduate Studies Postgraduate Candidature Defence for the partial fulfilment of Ph.D Candidature, 2nd July 2015.
8. **M. M. Ali,** Fabrication and characterization of few mode fiber Bragg gratings with mode conversion and sensing applications, presented in Institute of Graduate Studies Postgraduate Seminar for the partial fulfilment of Ph.D Candidature, 10th February 2015.
9. **M. M. Ali,** K. S. Lim and H. Ahmad, "Fabrication of Few Mode Fiber Bragg Gratings and Characterization of Modal Coupling," presented in Annual Physics Colloquium 2015, University of Malaya, Malaysia, 2015.
10. **M. M. Ali,** K. S. Lim, Md. R. Islam, and H. Ahmad, "Few Mode Fiber Bragg Gratings for Sensing Applications," presented in 28th Regional Conference on Solid State Science and Technology (RCSSST2014), Cameron Highland, Pahang, Malaysia, 2014.
11. K. S. Lim, **M. M. Ali,** C. C. Loo, W. Y. Chong and H. Ahmad, "Observation of mode-coupling in few mode fiber Bragg gratings," 2014 IEEE Summer Topical Meeting Series, Canada, 2014.

Candidate's Related Publications during Candidature

1. **M. M. Ali,** Md. R. Islam, K.-S. Lim, D. S. Gunawardena, H. Z. Yang, and H. Ahmad, "PCF-cavity FBG Fabry-Perot resonator for simultaneous measurement of pressure and temperature," *IEEE Sensors Journal*, vol. 15, no. (12), 6921-6925, 2015.

2. Md. R. Islam , M. Bagherifaez, **M. M. Ali,** H. K. Chai, K. S. Lim, H. Ahmad "Tilted Fiber Bragg Grating Sensors for Reinforcement Corrosion Measurement in Marine Concrete Structure," IEEE Transactions on Instrumentation & Measurement, vol. 64, no. 12, pp. 3510-3516, 2015.
3. M. R. Islam, **M. M. Ali,** M. H. Lai, K. S. Lim, and H. Ahmad, "A High Sensitive in-fiber Fabry-Perot Resonator for Ultrasonic Sensing," *IET Optoelectronics*, vol.9, no.3, pp.136-140, 2015.
4. **M. M. Ali,** K. S. Lim, A. Becir, M. H. Lai, and H. Ahmad, "Optical Gaussian notch filter based on periodic microbent fiber Bragg grating," *IEEE Photonics Journal*, vol.6, no.1, pp.1-8, 2014.
5. Md. R. Islam , M. Bagherifaez, **M. M. Ali,** H. K. Chai, K. S. Lim, H. Ahmad, "Optical Fiber Sensors for Reinforcement Corrosion Monitoring in Marine Concrete Structure," The 7th Asia and Pacific Young Researchers and Graduates Symposium (YRGS 2015), Kuala Lumpur, Malaysia; 2015.
6. H. Z. Yang, X. G. Qiao, Y. P. Wang, **M. M. Ali,** M. H. Lai, K. S. Lim, and H. Ahmad, "In-fiber gratings for simultaneous monitoring temperature and strain in ultra-high temperature," *IEEE Photonic Technology Letters*, vol. 27, no. 1, pp 58-61, 2014.
7. D. S. Gunawardena, M. -H. Lai, K. -S. Lim, M. M. Ali and H. Ahmad, "Measurement of grating visibility of an FBG based on bent-spectral analysis," *Applied Optics*, vol. 54, no. 5, pp. 1146-1151, 2015.
8. H. Z. Yang, X. G. Qiao, **M. M. Ali,** Md. R. Islam and K. S. Lim, "Optimized tapered optical fiber for ethanol (C2H5OH) concentration sensing" *IEEE/OSA Journal of Lightwave Technology*, vol. 32, no. 9, pp. 1777-1783, 2014.

9. K. S. Lim, H. Z. Yang, A. Becir, M. H. Lai, **M. M. Ali,** X. Qiao, and H. Ahmad, "Spectral analysis of bent fiber Bragg gratings: theory and experiment," *Optics Letters*, vol. 38, no. 21, pp. 4409-4412, 2013.
10. **M. M. Ali,** K. S. Lim and H. Ahmad, "Fabrication Techniques for Superstructure Fiber Bragg Gratings and Their Applications" presented in Annual Physics Colloquium 2014, University of Malaya, Malaysia, 2014.
11. **M. M. Ali,** K. S. Lim, and H. Ahmad, "Mechanically Induced Periodic Microbending of Fiber Bragg Grating for Vibration Sensing," presented in The 9th Mathematics and Physical Science Graduate Congress 2014, University of Malaya, Malaysia, 8th – 10th January 2014.

Candidate's Honors and Awards during Candidature

1. Selected for attending **Research Opportunities Week (ROW), 2016** Organized by **Technical University of Munich (TUM), Germany**, 2016.
2. Selected for attending the **Winter College on Optics** at the Abdus Salam International Centre for Theoretical Physics **(ICTP), Trieste, Italy, 2016.**
3. **Was awarded conference travel grant** to attend the international conference ECBA-2016, Istanbul, **Turkey, 2016.**
4. Selected for **Visiting Ph.D. Research Fellow** at **University of Limerick Ireland under Erasmus Mundus**, INTACT Programme funded by European Union for 12 months started from Dec. 2015.
5. **Won Bronze Medal** in The International Conference and Exposition on Inventions by Institute of Higher Learning **(PECIPTA 2015), Kuala Lumpur Convention Centre, Dec. 2015.**

6. **Awarded conference travel grant** to attend the international conference (RCSSST2014), Cameron Highland, Pahang, Malaysia, 2014.
7. Selected for **Summer School on Lasers and Laser Applications (SSOLLA 2014)** held at APRI, Gwangju Institute of Science and Technology, **Korea.**
8. **Was awarded by IPPP grant** by University of Malaya for Ph.D. research under grant no. **PG029-2013A.**
9. Fully Funded **Bright Sparks Scholarship** for Ph.D. (2013-2016) Research at University of Malaya Kuala Lumpur, Malaysia.